Development of a Multivariate Wall Function Approach for Momentum, Heat and Mass Transfer in the Wall Condensation Regime

Entwicklung eines multivariaten Wandfunktionsansatzes für den Impuls-, Wärme- und Stoffübergang im Wandkondensationsregime

Von der Fakultät für Maschinenwesen der Rheinisch-Westfälischen Technischen Hochschule Aachen zur Erlangung des akademischen Grades eines Doktors der Ingenieurwissenschaften genehmigte Dissertation

vorgelegt von

Henrik Müller

Berichter: Univ.-Prof. Dr. rer. nat. Hans-Josef Allelein
Univ.-Prof. Dr.-Ing. Reinhold Kneer
Univ.-Prof. Dr.-Ing. Eckart Laurien

Tag der mündlichen Prüfung: 05. Oktober 2022

Zusammenfassung

Der Einsatz numerischer Methoden zur Sicherheitsanalyse von Kernkraftwerken hilft Lieferanten, Betreibern und Sicherheitsbehörden, die Auslegung der Anlage zu begründen, das Verhalten der Anlage bei verschiedenen Störfallszenarien zu verstehen, Maßnahmen zur Störfallbegrenzung zu definieren und Potenziale zur Verbesserung der Anlagensicherheit aufzuzeigen. Ergänzend zu den etablierten Lumped-Parameter- oder System-Codes werden zunehmend auch Computational Fluid Dynamics (CFD) Programme für diese Aufgabe eingesetzt. CFD-Codes bieten die Möglichkeit, zusätzliche Erkenntnisse über lokale oder dreidimensionale Strömungsphänomene im Verlauf eines Störfalls zu gewinnen. Eine Anwendung von großem Interesse für den Einsatz von CFD-Codes ist die Strömung im Sicherheitseinschluss während eines Kühlmittelverluststörfalls (LOCA), insbesondere im Hinblick auf die Wasserstoffverteilung und die Bildung zündfähiger Gemische. Aufgrund des Vorhandenseins von Phänomenen wie Wandkondensation erfordert die Analyse der Strömung im Sicherheitseinschluss während eines LOCA eine feine Gitterauflösung an der Wandoberfläche, um die Strömung genau vorherzusagen. Mit einem solch feinen Gitter benötigen die Berechnungen jedoch eine prohibitiv große Rechenzeit. Daher müssen Subgittermodelle, so genannte Wandfunktionen, eingesetzt werden, um die erforderliche Gitterauflösung und damit die Rechenzeit zu reduzieren.

Die derzeit verfügbaren Wandfunktionen sind für die Modellierung von Strömungen im Sicherheitsbehälter unter LOCA-Bedingungen nicht geeignet. Insbesondere, weil sie die Effekte des statischen Auftriebs und der kondensationsbedingten Wandnormalgeschwindigkeit, allgemein als 'suction effect' bezeichnet, nicht berücksichtigen.

Der in dieser Arbeit vorgestellte Wandfunktionsansatz besteht aus einer Reihe von empirischen Funktionen, die auf experimentellen Daten basieren, welche durch hochauflösende numerische Daten ergänzt werden. Zusätzlich zu den typischerweise in Wandfunktionen auftretenden Effekten deckt der Ansatz auch den Einfluss von Auftrieb und Wandnormalströmung ab. Um diese Effekte zu berücksichtigen, wird ein abdeckender Satz von dimensionslosen Parametern hergeleitet und die Eingangsdaten werden zu multivariaten algebraischen Funktionen kombiniert, die das Konzept der radialen Basisfunktionen nutzen. Dies ermöglicht eine einfache und rechenzeitsparende Integration der Wandfunktion in verschiedene CFD-Codes. Eine beispielhafte Implementierung in den CFD-Code ANSYS CFX wird vorgestellt. Eine erste Validierung wird anhand von Separateffekt- und Integraleffekt-Tests durchgeführt.

Die Validierung anhand der Separateffekt-Tests zeigt, dass der neu entwickelte Wandfunktionsansatz im Vergleich zu einer Standard-Wandfunktion verbesserte Ergebnisse liefert, insbesondere unter containmentähnlichen Strömungsbedingungen. Allerdings zeigen die Integraleneffekt-Tests in größerem Maßstab keine solche Verbesserung, was auf den begrenzten Anwendungsbereich des neuen Modells zurückzuführen ist, der sich aus der begrenzten Menge an verfügbaren Eingabedaten ergibt. Nichtsdestotrotz zeigen die Ergebnisse, dass der neu entwickelte Wandfunktionsansatz das Potenzial hat, rechenzeit technisch erschwingliche CFD-Berechnungen eines vollständigen Containments unter LOCA-Bedingungen mit einer genauen Vorhersage des wandnahen Impuls-, Wärme- und Stofftransfers zu ermöglichen, auch wenn noch einige Arbeit zu leisten ist.

Abstract

The use of numerical methods for the safety analysis of nuclear power plants helps suppliers, operators and safety authorities to justify the plant layout, understand the plant behavior in different accident scenarios, to define accident mitigation measures and to identify potentials for the improvement of the plant safety. Complementary to the well-established lumped parameter or system codes, there is an increasing demand to use computational fluid dynamics (CFD) codes for this task. CFD codes offer the ability to gain additional insights into, for example, localized or three-dimensional flow phenomena in the course of an accident, especially the distribution of hydrogen and the formation of combustible mixtures. One application of great interest for the use of CFD-codes is the containment flow during a loss of coolant accident (LOCA). Due to the presence of phenomena such as wall condensation, the analysis of the containment flow during a LOCA requires a fine mesh resolution at the wall surface to accurately predict the flow. However, with such a fine mesh, the calculations require a prohibitive large amount of computation time. Therefore, subgrid models, so called wall functions, need to be employed to reduce the required grid resolution and thus the computational time.

Currently available wall functions are not suitable for modeling containment flows under LOCA conditions. In particular, they do not include the effects of buoyancy and condensation-induced wall normal velocity, commonly referred to as the suction effect.

The wall function approach presented in this thesis consists of a set of empirical functions based on experimental data supplemented by high resolution numerical data. In addition to the effects typically encountered in wall functions, the approach includes the influence of buoyancy and wall normal flow. To account for these effects, a covering set of non-dimensional parameters is derived and the input data are combined into multivariate algebraic functions using the concept of radial basis functions. This allows an easy and computationally fast integration of the wall function into different CFD codes. An exemplary implementation in the CFD code ANSYS CFX is presented. A first validation is performed based on separate and integral effect tests.

The separate effect test validation demonstrates that the newly developed wall function approach provides improved results compared to a standard wall function, especially under containment-like flow conditions. However, larger scale integral effect tests do not show such improvement due to the limited application range of the new model resulting from the limited amount of available input data. Nevertheless, the results show that the newly developed wall function approach has the potential to enable computationally affordable CFD calculations of a full containment under LOCA conditions with an accurate prediction of the near wall momentum, heat and mass transfer, although some work remains to be done.

Contents

1. Introduction **12**

2. Condensation and the Boundary-Layer in the Wall Condensation Regime **15**
2.1. Condensation . . . 15
2.2. The boundary layer in the wall condensation regime . . . 18
2.2.1. Conservation equations for the boundary layer . . . 19
2.2.2. Influence of wall condensation on the boundary layers . . . 21

3. Existing Boundary Layer Models **25**
3.1. Boundary layer modeling approaches and examples . . . 25
3.1.1. Different boundary layer modeling approaches . . . 25
3.1.2. The logarithmic law of the wall . . . 26
3.1.3. Kader's wall function . . . 31
3.1.4. Popovac's wall function . . . 33
3.1.5. FIBULA . . . 35
3.2. The SETCOM test facility and data base . . . 35
3.2.1. Simulation Model of SETCOM . . . 40
3.2.2. Comparison of SETCOM measurement and fine mesh simulation data . . . 44

4. Model Development and Implementation **53**
4.1. New non-dimensional Parameters . . . 53
4.2. Non-equilibrium Factors . . . 59
4.3. Implementation via Radial Basis Functions . . . 69

5. Verification and Validation **75**
5.1. Qualitative analysis of the new wall function . . . 75
5.2. Comparison with SETCOM results . . . 88
5.3. Integral tests . . . 100
5.3.1. TOSQAN ISP47 . . . 101
5.3.2. THAI HM2 . . . 111

6. Summary and Conclusion **122**
6.1. Summary . . . 122
6.2. Outlook . . . 123

7. References **126**

Appendices

A. Boundary Conditions of the SETCOM Experiments used in this Thesis **132**

B. Data Centers, RBF Coefficients and Scales of the New Wall Function Approach **138**

C. Integration of the New Wall Function into ANSYS CFX **155**

D. Additional Validation Results **165**
D.1. Additional SETCOM validation cases 165
D.2. Additional THAI HM2 validation results 173

Nomenclature

Latin Symbols

$\dot{m}''$	Mass flux density
$\dot{q}''$	Heat flux density
$\dot{q}^+$	Dimensionless heat flux
$\vec{x}$	Data point where the approximation function is evaluated
a_1	Coefficient of turbulence model
B	Basis function
B	Buoyancy indicator
C_1	Integrational constant
C_2	Integrational constant
c_p	Specific heat capacity at constant pressure
C_u	Non-equilibrium constant
CM	Collocation matrix
D	Mass diffusivity
DM	Distance matrix
FG^+	Dimensionless gravity force
Gr_L	Grashof number
h_t	Latent heat also called enthalpie of transformation
k	Turbulent kinetic energy
L_τ	Shear length
p	Pressure
$P_f(\vec{x})$	Approximation function
p_{sat}	Saturation pressure
Pr	Prandtl number
Re_D	Reynolds number
Sc	Schmidt number

T	Temperature
t	Time
T^+	Dimensionless temperature
u	Velocity
u^+	Dimensionless velocity
u_τ	Shear velocity
x	Location
Y	Mass Fraction
y^+	Dimensionless wall distance
Y_s^+	Dimensionless steam mass fraction
c	Coefficient of the approximation function

Greec Symbols

α	Integrational constant
Δ	Difference
δ	Partial differenciation
ϵ	Scaling factor
κ	von Kármán constant
λ	Thermal conductivity
μ	Dynamic viscosity
μ_t	Eddy viscosity
μ_t^+	Eddy viscosity ratio
ν	Kinematic viscosity
ω	Turbulent eddy frequency
ϕ	Arbitrary flow quantity
ρ	Density
τ_W	Wall shear stress
C	Integrational constant

Subscripts and Superscripts

$''$	Fluctuation of a Favre averaged quantity or area related quantity
$+$	Dimensionless quantity
$Cond$	Condensation
Err	Error
i	Spacial direction
j	Spacial direction
L	Non-condensable gas
n	Wall normal direction
p	Wall parallel direction
S	Steam
Sen	Sensible
SWF	Standard wall function
t	Turbulent
Tot	Total
v	Viscous
k	Running index

1. Introduction

Condensation is a physical phenomenon commonly observed in everyday life. One example is clouds, which are made up of countless small water droplets that form when warm, humid air rises to a higher, colder layer of the atmosphere. Another everyday example is the condensate on a bathroom mirror after a hot shower or bath. In this case, water vapor from the warm, humid air condenses on the cold surface of the mirror. Based on these two common examples, one can already distinguish two 'types' of condensation, each of which requires a specific approach to condensation modeling: Condensation inside a gaseous volume and condensation on the surface of a wall.

Condensation also plays an important role in nuclear reactor safety, especially in, but not limited to, the reactor containment under loss of coolant accident (LOCA) conditions. In case of a LOCA, there are a multitude of processes relevant to the integrity of the containment, and thus to the protection of the environment from the release of radioactive material, which are influenced by condensation. One example of such a process is the pressurization of the containment due to the heat and mass release from the reactor's primary coolant system. This pressurization is countered by condensation due to the much smaller specific volume of liquid water ($0.001\,\mathrm{m^3\,kg^{-1}}$) compared to steam ($1.72\,\mathrm{m^3\,kg^{-1}}$ at $100\,^{\circ}\mathrm{C}$ and $1\,\mathrm{bar}$).

Another example is the inertization of the containment atmosphere by steam in the event of a hydrogen release from the damaged reactor core. If the steam condenses, the containment atmosphere can become locally or globally combustible. In addition, evaporation in the reactor core and condensation on the containment structures is a very efficient way to remove the decay heat from the reactor core under LOCA conditions. These examples show that condensation is a very important phenomenon in the containment of a nuclear reactor under LOCA conditions and can be both beneficial and detrimental to the integrity of the containment under these conditions. Thus, simulation tools used to investigate the containment under LOCA conditions must be able to accurately predict condensation.

The ability of both lumped parameter (LP) and computational fluid dynamics (CFD) codes to predict complex containment flows, like the formation and dissolution of a light gas stratification, was thoroughly tested in the framework of the ISP47 [Allelein et al., 2007]. One of the findings of the ISP was that the CFD codes in particular needed further development to improve their prediction of condensation processes, including wall condensation. This triggered extensive research efforts on the topic of wall condensation, both experimental and theoretical. On the experimental side, especially the separate effect tests CONAN [Ambrosini et al., 2014] and it's successor the SETCOM [Belt, 2019] test facility have provided new insights into the physics of wall condensation. On the theoretical side, the SARNET benchmark [Ambrosini et al., 2014] has provided a thorough comparison of different wall condensation models. Bucci [Bucci, 2009] continued this work in his Ph.D. thesis providing an in-depth evaluation of the CONAN test results. Lehmkuhl [Lehmkuhl, 2018] developed a new comprehensive approach to wall condensation modeling with his FIBULA model. Nevertheless, there are still issues, especially in terms of computational time, that need to be addressed regarding wall

condensation modeling for containment scale CFD applications.

Today, LP codes are the main tool for the investigation of containment flows under LOCA conditions due to their fast computation time and proven accuracy. However, as a result of their modeling approach, they cannot be used to investigate localized or highly three-dimensional phenomena. Thus, CFD codes, which are well suited for predicting these phenomena and generally offer a better resolution of the containment flow, are increasingly being used for containment analysis. Nonetheless, due to the multitude of physics involved in a containment flow and the need to resolve gradients in space and time with a suitable computational grid, CFD calculations of a full containment under LOCA conditions (up to 70 000 m^3 of volume and 3 days of transient time) require large amounts of computational time up to the point where such an analysis is prohibitively expensive. Therefore, solutions are needed to reduce the computational time required for such a calculation.

There are a multitude of possible approaches to speed up CFD calculations for containment scale problems. One would be to couple a CFD and an LP code, as for example Götz [Götz et al., 2017] has done for the CFD code ANSYS CFX and the LP code COCOSYS. In this way, only the area of interest can be calculated with the computationally expensive CFD code, while the rest of the containment is calculated with the much faster LP code. However, this approach is only applicable if the finer resolution of the CFD code is only required for some areas of the containment. If the resolution of the CFD code is required for the entire containment, this approach offers no advantage.

The near wall flow field, also known as the boundary layer, often needs to be resolved with a large number of cells, and thus requires a large amount computation time, in CFD calculations due to the large gradients present in this region. Hence, reducing the necessary resolution in the boundary layer yields a great potential for speeding up the calculations. This can be achieved by using subgrid models, so called wall functions, which model the flow phenomena that are no longer resolved by the mesh. This is common practice in the industrial application of CFD codes [Popovac et al., 2007]. However, Lehmkuhl [Lehmkuhl, 2018] showed that the currently available wall functions are not suitable for modeling the flows in the containment under LOCA conditions. In particular, they do not include the effects of buoyancy and condensation induced wall normal velocity, commonly called the suction effect.

The goal of this thesis is the development, prototypical implementation, and first validation of a wall function approach for the momentum, heat, and mass transfer processes inside a boundary layer in the wall condensation regime suitable for containment scale applications.

The wall function approach presented in this thesis consists of a set of empirical functions based on experimental data where available and supplemented by high resolution numerical data where necessary. In addition to the effects typically encountered in wall functions it also covers the influence of buoyancy and wall normal flow. To include these effects, a covering set of non-dimensional parameters is derived and the input data are combined into multivariate algebraic functions utilizing the concept of radial basis functions. This allows for an easy and computationally fast integration of the wall function into different CFD codes. An exemplary implementation in the CFD code

ANSYS CFX is presented. A validation is performed based on separate and integral effect tests.

The main source of experimental data for model development and validation used in this thesis is the SETCOM test facility, which was specifically designed to investigate the behavior of the boundary layer in the wall condensation regime. The facility, located at the research center Jülich, was designed, constructed and commissioned by Belt [Belt, 2019] and extensive experimental work was carried out by Hundhausen [Hundhausen et al., 2017b] [Hundhausen et al., 2017a]. In addition, experiments from the TOSQAN and THAI facilities are used for the verification and validation of the new model, since the conditions in these facilities resemble the natural or mixed convection conditions in a containment under LOCA conditions.

This thesis consists of six sections including this introduction. In section 2 the basic physics of condensation as well as the boundary layer are discussed. It also introduces the concept of different boundary layers for different physical quantities like velocity, temperature and steam mass. The differential equations describing these boundary layers are presented and the influence of wall condensation on these boundary layers and their interaction is elucidated.

In section 3 different approaches to boundary layer modeling and different existing wall function concepts relevant for the boundary layer in the wall condensation regime are summarized and further development potential is identified. Additionally, the SETCOM test facility, which has been extensively used for model development and the validation of the new wall function, is presented.

In section 4 the development of the new wall function is described. The development process is divided into three steps: First, the derivation of the necessary variables to fully describe the boundary layer in the wall condensation regime, then the derivation of the actual model by extending Popovac's [Popovac et al., 2007] idea of the non-equilibrium factor and finally the transfer of the model into a form usable by CFD codes via approximation with radial basis functions.

In section 5 a first validation of the new wall function approach is presented. In a first step, a qualitative assessment of the new wall function regarding the expected behavior of the boundary layers is conducted. In a second step, coarse mesh simulations of the SETCOM experiment with the standard and the new wall function are compared with fine mesh best estimate simulations of these experiments. Finally, coarse mesh simulations of the TOSQAN ISP47 and THAI HM2 experiments with the new wall function are compared to the experimental results as well as to fine mesh best estimate simulations.

In section 6 the work is summarized and an outlook on future work is given.

2. Condensation and the Boundary-Layer in the Wall Condensation Regime

2.1. Condensation

Condensation describes the phase transition of a fluid from gas to liquid. On a macroscopic scale, the phases can be distinguished by their different behavior when poured into a finite volume: Gases always fill such a volume completely, while a liquid can form a surface that isolates it from the remainder of the volume [Perrot, 1998]. At this scale, a condensation mass transfer can only be observed from the gas to the liquid phase. At the microscopic scale, the phases can be distinguished by the way the molecules interact with each other: While the molecules in the gas phase show no interaction except for collisions, a weak electromagnetic interaction can be observed in the liquid phase [Perrot, 1998]. At this scale, a constant exchange of molecules between the two phases can be observed. Thus, the direction of the overall mass flow is determined by the probability of a molecule changing from the gaseous to the liquid state and vice versa. The modeling effort in this work is focused on the macroscopic scale because CFD, as a continuum mechanics method, does not resolve the microscopic scale.

Two of the most important phenomena associated with condensation are saturation pressure and latent heat. The saturation pressure p_{sat} is the pressure the gas phase above the flat surface of a pure liquid or solid substance in a closed system assumes if both phases are in thermodynamic equilibrium [Perrot, 1998]. However, the saturated state does not only appear under these rigorous conditions, it can also play an important role, for example, in multi-component processes which are not in thermodynamic equilibrium. Wall condensation in the presence of non-condensable gases is one such process. Here, the steam partial pressure at the phase interface is often equal to the saturation pressure [Kelm, 2010] and the saturation pressure can thus be used as a boundary condition in a condensation model.

Latent heat, also called enthalpy of transformation h_t, is the heat a substance absorbs or releases when it undergoes a phase change [Perrot, 1998]. It is the energy required to break the electromagnetic bonds between molecules in the liquid phase to evaporate a fluid, or the energy released by the formation of these bonds when a fluid condenses. Due to the comparatively large latent heat of water, for example it takes about 5 times the energy to vaporize a given amount of water than to heat it from 0 °C to 100 °C, evaporation in the reactor core and condensation on the containment walls is an efficient way to cool the reactor core under severe accident conditions [Rosa et al., 2009].

Condensation can occur under a variety of different physical conditions. Often these conditions require an unique approach on condensation modeling for CFD. One particular important distinction for the model is where the condensation takes place. Examples of different locations are:

- Inside the volume of a gas, a liquid or a porous solid
- On the surface of a solid (wall condensation) or a liquid

The difference the location makes to the condensation process can be seen, for example, by comparing the condensation inside a gas volume and on the surface of a wall. For the volume condensation, influences like the presence of condensation seeds, the subcooling of the gas, and the transport of the droplets are of great importance. Whereas, wall condensation is governed by effects like the near wall flow, the surface temperature of the wall, and the behavior of the condensate on the wall surface. Consequently, a dedicated wall condensation model is required in CFD codes, even though the basic physical process of condensation does not differ based on the location.

Another influence that has to be accounted for in a condensation model is that the gas (and liquid) may contain multiple substances. In this case, one or more of the substances may be condensable while others are non-condensable. The term condensable herein describes the fact that a gas can condense under the given thermodynamic conditions. The presence of multiple condensable gases poses a challenge to condensation modeling because the composition of the gas phase and the liquid phase are unequal in the equilibrium state. A property used for example in the process of distillation [Perrot, 1998]. The main effect of the presence of non-condensable gases on the condensation process is the possible accumulation of these gases at the phase interface. This can hinder the transport of vapor to the phase interface and thus slow down the overall condensation process [Lehmkuhl, 2018] [Kelm, 2010]. The relevant gas mixture for the containment under severe accident conditions, and thus the focus of this work, is a mixture of one condensable gas (water vapor) with multiple non-condensable gases (nitrogen, oxygen, hydrogen).

Wall condensation in the presence of non-condensable gases is essentially determined by two physical phenomena: The transport of steam to the phase interface and the transport of heat in the condensate wetting the wall [Kelm, 2010]. These processes are shown on the left side of figure 2.1. It can be clearly seen that the transport of the steam (see steam mass fraction Y_S) to the phase interface (index I) is primarily influenced by the non-condensable gases accumulating at the phase interface (non-condensable gas mass fraction Y_L). These must be penetrated by the steam on its way from the main flow to the phase boundary.

The main influence of the condensate film on the condensation process is its thermal resistance which hinders the transport of the latent heat into the wall [Kelm, 2010]. This resistance is mainly determined by two factors: The liquids thermal conductivity and the films thickness. In addition, the thermal resistance is influenced by the velocity and waviness of the film [Dupont, 2017] as well as the type of wetting of the wall (index W in figure 2.1), which can be in the form of droplets, rivulets or a closed film. However, since the condensate film is often very thin, if a contiguous film exists at all, and thus offers only a small resistance to the heat flux it is commonly ignored in CFD wall condensation models (see e.g. [Kelm, 2010] [Zschaeck et al., 2014] [Lehmkuhl, 2018]). This is also the case for the new model presented in this thesis. Nonetheless, the new model can relatively easy be combined with a film model if such a model is deemed necessary.

The transport of steam to the phase interface is strongly influenced by the near wall flow, also called the boundary layer. In particular, the transport of steam to the phase boundary, but also the behavior of the film, is significantly influenced by the

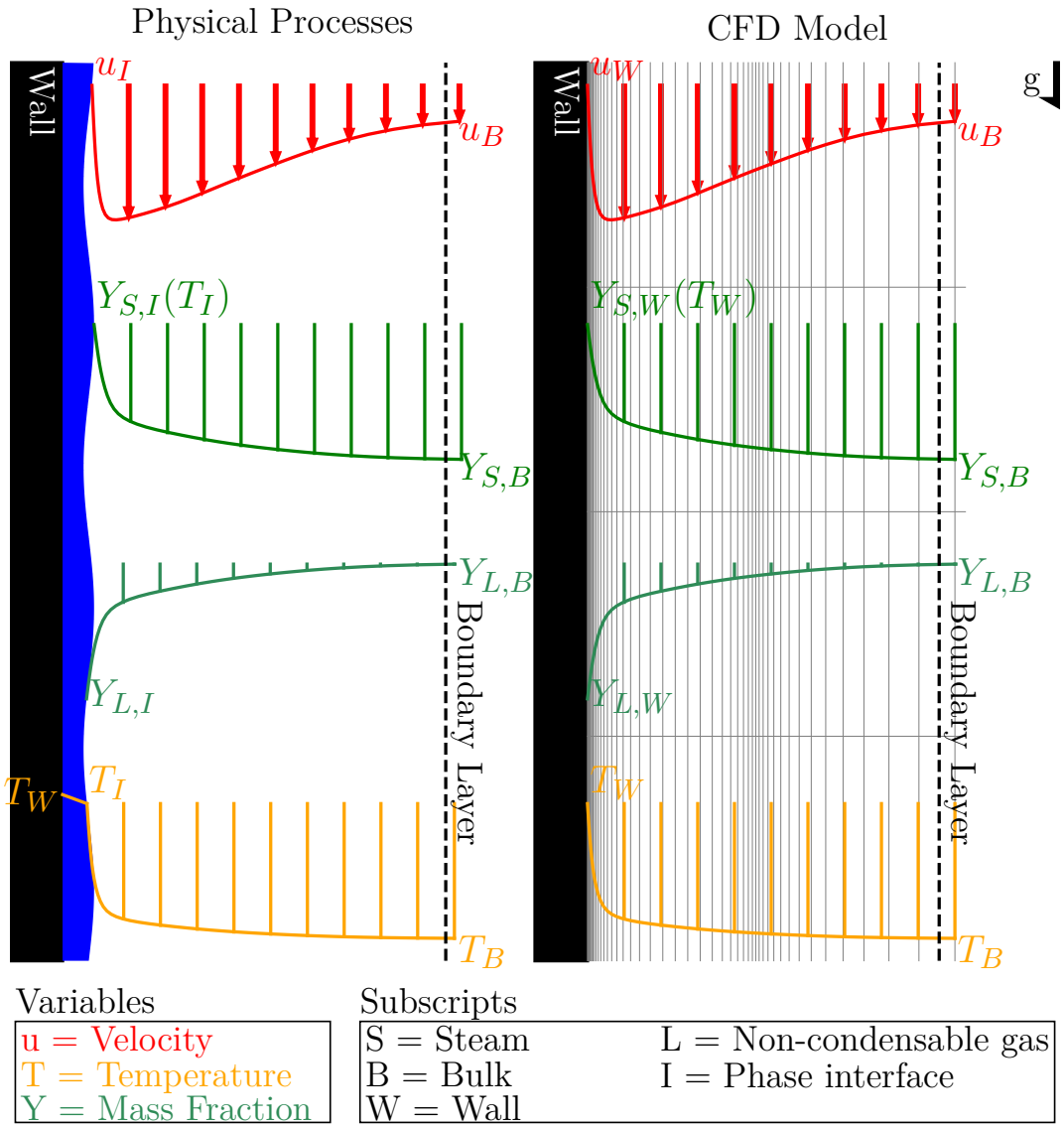

Figure 2.1: Wall condensation: Physical processes and CFD model

interaction with the velocity (u) and the temperature (T) boundary layer. Therefore, these boundary layers are also shown in figure 2.1. The interaction is primarily based on three effects: Buoyancy, turbulence, and the wall normal velocity induced by the condensation (see 'suction' effect) [Lehmkuhl, 2018]. Since this interaction significantly influences both the condensation and the different flow boundary layers, a complete model of wall condensation must include not only the condensation model itself, but also a complete description of all flow boundary layers: Velocity, temperature, species

mass, and turbulence. This model approach, as already applied in a CFD calculations, is depicted on the right hand side of figure 2.1 together with a computational mesh with a sufficient resolution to resolve the gradients of the flow. The new boundary layer model developed in the framework of this thesis aims to accurately describe these physics without the need for such a fine computational mesh.

2.2. The boundary layer in the wall condensation regime

The concept of the boundary layer was developed by Ludwig Prandtl [Prandtl, 2010]. It was his idea to split a flow into two parts: The friction free bulk flow and the viscous boundary layer close to the surface of a body. Prandtl showed that friction can play an important role in the flow of a fluid with low viscosity, especially when the flow is bounded by a wall. With this idea, Prandtl drastically improved the ability of theoretical fluid dynamics to predict real flows [Schlichting et al., 2006]. Thus, he was able to close the gap between theoretical and experimental fluid dynamics of his time.

As can be seen from the description above, the boundary layer is an area of a flow where friction cannot be neglected due to the influence of a wall. Figure 2.2 shows a sketch of a boundary layer for a flow over a flat plate. As can be seen in the figure, the boundary layer contains a velocity gradient between the main flow and the wall surface, which gets steeper the closer one gets to the wall. This gradient exists because the flow has to satisfy the no slip boundary condition at the wall surface and thus has the same speed as the surface at the location of the surface, which differs from the main flow velocity. These gradients lead to the strong friction influence in the boundary layer. In addition, velocity gradients tend to induce turbulence in a flow, and thus turbulence can also play an important part in the behavior of a boundary layer.

In the containment under loss of coolant accident conditions the boundary layer is expected to be turbulent. Thus, this type of boundary layer will be investigated in this thesis. In the literature (see e.g. [Craft et al., 2004], [Popovac et al., 2007], [Lehmkuhl et al., 2016] or [Han et al., 1997]) the turbulent boundary layer is typically split into three parts: The viscous sublayer, the buffer layer, and the turbulent layer. While viscosity is one of the determining factors of a boundary layer, its actual influence on the flow is limited to two of these regions: The viscous sublayer, directly at the wall surface, where viscosity is the sole relevant mechanism of momentum transfer and the the buffer layer, where viscous and turbulent momentum transfer are of equal magnitude.

In the outermost region of the boundary layer, the turbulent layer, turbulence is such an efficient momentum transfer mechanism that viscosity is no longer relevant. Turbulence in the boundary layer is influenced by two main factors: The production of turbulence due to the velocity gradient and the damping of turbulent fluctuations in the vicinity of the wall surface. The mutual presence of these factors immediately explains the structure of the turbulent boundary layer. In the outer part of the layer, the production of turbulence is already large, while the damping effect is still relatively minor. Hence, turbulence is responsible for nearly the whole wall normal momentum transfer in this area. Closer to the wall surface damping becomes more and more dominant as the wall blocks turbulent fluctuations. Therefore, viscosity at first takes an equal share of

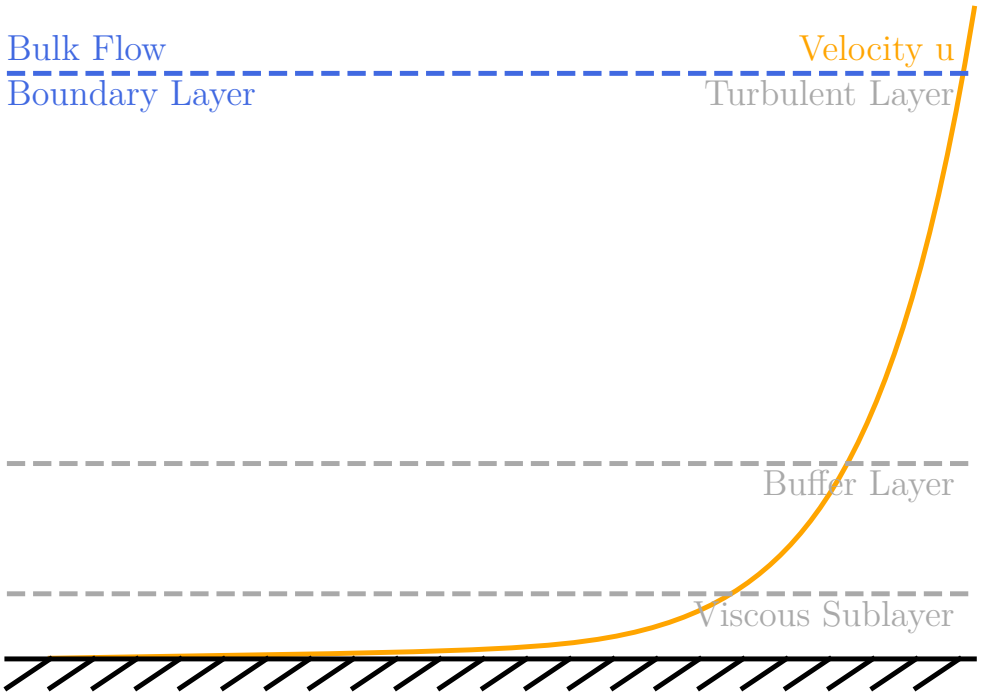

Figure 2.2: Sketch of a boundary layer

the wall normal momentum transfer in the buffer layer and finally becomes the dominant transport mode in the viscous sublayer.

For flows with wall condensation there is also a temperature and a vapor mass boundary layer [Lehmkuhl, 2018]. For these quantities, the thermal conductivity respectively the molecular diffusivity are the effects that cannot be neglected close to the wall surface. The gradient between the main flow and the wall, or more precisely the surface of the condensate, is present due to the surface temperature of the film and the saturation pressure at the surface of the condensate. Thus, the two main elements of the velocity boundary layer, molecular transport and a gradient between the main flow and the wall surface, also exist for the temperature of the flow and the vapor mass concentration. Consequently, boundary layers also exist for these quantities and must be considered in a boundary layer model for condensing flows.

2.2.1. Conservation equations for the boundary layer

The transport equations for mass, momentum, energy, and vapor mass form the basis for the modeling of the boundary layers in the wall condensation regime. In the following,

these equations are used in their Favre averaged forms. Favre averaging builds up on the concept of of Reynolds averaging of the equations, which enables a better handling of turbulence by splitting quantities ϕ, subjected to turbulence, into a time averaged part $\overline{\phi}$, representing the mean flow, and a fluctuating part ϕ', representing the turbulent fluctuations. The process is demonstrated in equation 2.1. As the Reynolds averaging process is only applicable to incompressible flows, the quantity ϕ can be subjected to a mass averaging, called Favre averaging, to extend the range of applicability to compressible flows. The process of Favre averaging is depicted in equation 2.2 and the notation for a Favre averaged quantity is given in equation 2.3. Here, the Favre averaged quantity is written as $\tilde{\phi}$ and the associated fluctuation as ϕ''. The resulting Favre averaged transport equations for mass, momentum, energy, and vapor mass, as given by [Oertel, 2017], are presented in equations 2.4 to 2.7.

In equations 2.4 to 2.7 u_i, T and Y_s stand for the velocity, temperature and steam mass fraction respectively, as already described in section 2.1. The indices i and j indicate the spacial direction and can take values from one to three. In the equations, the spacial position is indicated by x and the time by t. The pressure is described by p and the density by ρ. The molecular transport properties are described by μ, λ and D for the dynamic viscosity, the thermal conductivity, and the mass diffusivity, respectively. The specific heat capacity at constant pressure is given by c_p.

$$\phi = \overline{\phi} + \phi' \tag{2.1}$$

$$\tilde{\phi} = \frac{\overline{\rho\phi}}{\overline{\rho}} \tag{2.2}$$

$$\phi = \tilde{\phi} + \phi'' \tag{2.3}$$

$$\frac{\partial\overline{\rho}}{\partial t} + \frac{\partial\overline{\rho}\tilde{u}_i}{\partial x_i} = 0 \tag{2.4}$$

$$\frac{\partial\overline{\rho}\tilde{u}_i}{\partial t} + \frac{\partial\overline{\rho}\tilde{u}_i\tilde{u}_j}{\partial x_j} = -\frac{\partial\overline{p}}{\partial x_i} + \frac{\partial}{\partial x_j}(\mu(\frac{\partial\tilde{u}_i}{\partial x_j} + \frac{\partial\tilde{u}_j}{\partial x_i}) - \rho\overline{u''_i u''_j} + \mu(\frac{\partial\overline{u''}_i}{\partial x_j} + \frac{\partial\overline{u''}_j}{\partial x_i})) + \overline{\rho}g_i \tag{2.5}$$

$$\frac{\partial\overline{\rho}c_p\tilde{T}}{\partial t} + \frac{\partial\overline{\rho}c_p\tilde{T}\tilde{u}_i}{\partial x_i} = \frac{\partial}{\partial x_i}(\lambda\frac{\partial\tilde{T}}{\partial x_i} - \overline{\rho}c_p\overline{T''u''_i} + \lambda\frac{\partial\overline{T''}}{\partial x_i}) \tag{2.6}$$

$$\frac{\partial\overline{\rho}\tilde{Y}_s}{\partial t} + \frac{\partial\overline{\rho}\tilde{Y}_s\tilde{u}_i}{\partial x_i} = \frac{\partial}{\partial x_i}(\overline{\rho}D\frac{\partial\tilde{Y}_s}{\partial x_i} - \overline{\rho}\overline{Y''_s u''_i} + \overline{\rho}D\frac{\partial\overline{Y''}_s}{\partial x_i}) \tag{2.7}$$

In order to gain a better understanding of the boundary layers, the following simplifications, commonly used in boundary layer modeling (see e.g. [Lehmkuhl et al., 2016] [Popovac et al., 2007]), are introduced into the equations: The flow is in a steady state, it is two dimensional, and relevant gradients exist only in a wall normal direction, except for the pressure gradient. Introducing these assumptions into equations 2.4 to 2.7 yields equations 2.8 to 2.11 as the transport equations for the turbulent boundary layer in the wall condensation regime. In the equations, the indices p and n represent the wall parallel and wall normal direction, respectively. The overline and tilde representing the

averaging processes have been dropped here and in future equations in this thesis, for the sake of legibility.

$$\underbrace{\frac{\partial \rho u_n}{x_n}}_{Suction} = 0 \tag{2.8}$$

$$\underbrace{\frac{\partial \rho u_p u_n}{\partial x_n}}_{Suction} = \frac{\partial}{\partial x_n}(\underbrace{\mu \frac{\partial u_p}{\partial x_n}}_{Diffusion} \underbrace{- \rho \overline{u''_p u''_n} + \mu \frac{\partial \overline{u''_p}}{\partial x_n}}_{Turbulence}) + \underbrace{\rho g_p - \frac{\partial p}{\partial x_p}}_{Buoyancy} \tag{2.9}$$

$$\underbrace{\frac{\partial \rho c_p T u_n}{\partial x_n}}_{Suction} = \frac{\partial}{\partial x_n}(\underbrace{\lambda \frac{\partial T}{\partial x_n}}_{Diffusion} \underbrace{- \rho c_p \overline{T'' u''_n} + \lambda \frac{\partial \overline{T''}}{\partial x_n}}_{Turbulence}) \tag{2.10}$$

$$\underbrace{\frac{\partial \rho Y_s u_n}{\partial x_n}}_{Suction} = \frac{\partial}{\partial x_n}(\underbrace{\rho D \frac{\partial Y_s}{\partial x_n}}_{Diffusion} \underbrace{- \rho \overline{Y'_s u'_n} + \rho D \frac{\partial \overline{Y''}_s}{\partial x_n}}_{Turbulence}) \tag{2.11}$$

It can be seen from equations 2.8 to 2.11 that there are four factors that influence the boundary layers in the wall condensation regime:

- The molecular transport processes in the fluid
- Turbulent fluctuations
- The wall normal flow also known as the suction effect [Lehmkuhl et al., 2016]
- The buoyancy forces on the fluid as combination of the hydro static pressure gradient and the gravitational force [Turner, 1973]

As has been explained earlier, molecular transport is a determining factor for all boundary layers and thus must be present in all boundary layer models. Turbulence is also a common effect in boundary layers and is therefore incorporated in many boundary layer models. In contrast, suction and buoyancy only appear in a boundary layer under very specific conditions, such as wall condensation, and are thus neglected in most boundary layer models. Thus, these two effects are one of the focuses of the new boundary layer model developed in this thesis. Therefore, the influence of buoyancy and suction on the boundary layers will be discussed in the following.

2.2.2. Influence of wall condensation on the boundary layers

The differential equations for the boundary layer, presented in equations 2.4 and 2.9 to 2.11, share three different properties through which they can interact. These are the density ρ, the wall normal velocity u_n, and the turbulent fluctuations. An additional interaction could take place via the influence of pressure, temperature and gas composition on the molecular transport properties. However, as it is difficult to integrate the changes

of these transport properties into a wall function, this influence will not be discussed here. In the following, the interaction of the boundary layers via density, wall normal velocity, and turbulence will be discussed. In doing so, it should be kept in mind that these different effects also influence each other.

Density changes in the boundary layer with wall condensation appear due to the changing temperature and gas composition in the layer (see section 2.1). However, Lehmkuhl [Lehmkuhl, 2018] showed that in the absence of gravity, the influence of the density differences on the boundary layer can be neglected under typical containment flow conditions. In the presence of gravity, density changes in the boundary layer become relevant as they give rise to buoyancy forces. Buoyancy forces are the result of the difference between the hydrostatic pressure and the gravitational force acting on a fluid element [Turner, 1973]. Hence, they directly effect only the momentum transport in the boundary layer, as can be seen from equations 2.4 and 2.9 to 2.11. However, buoyancy also directly and indirectly affects turbulence [Kim et al., 2008] and therefore also the energy and species transport in the boundary layer, as will be described in the following paragraphs.

The direct influence of buoyancy is limited to the velocity boundary layer because buoyancy acts as a momentum source. The importance of buoyancy increases with a decreasing bulk velocity and buoyancy is one of the main drivers [Rosa et al., 2009] of the flow in the containment under loss of coolant accident conditions. The exact nature of the buoyancy influence on the velocity boundary layer depends on many factors like the magnitude and direction of the bulk flow, the gas composition of the bulk flow and the temperature difference between the bulk and the wall surface. The focus of this thesis is on downward facing flows of steam air mixtures along a cool vertical wall. Under these conditions, buoyancy accelerates the flow, leading to a thinner boundary layer with steeper gradients close to the wall surface [Lehmkuhl, 2018]. For very low bulk flow velocities, a velocity maximum appears near the wall surface and the flow exhibits a wall jet like behavior. Measurement data on this behavior are presented, for example, by Hundhausen [Hundhausen et al., 2017a].

While buoyancy does not directly influence the species mass and energy transport in the boundary layer, as can be seen from equations 2.10 and 2.11, buoyancy does influence the turbulent transport and thus indirectly influences the species mass and energy transfer. The influence of buoyancy on turbulence also occurs in a direct and indirect manner, as described by Kim [Kim et al., 2008], for example.

The direct influence of buoyancy can enhance as well as diminish turbulence. Stable stratifications, where the density increases in the direction of gravity, diminish turbulence while unstable stratifications, where the density decreases in the direction of gravity, enhance turbulence [Arya, 1975]. This is explained by Turner [Turner, 1973] as follows: In both stratifications a fluid element experiences a pressure force which equals its own weight in its resting position. Now a turbulent fluctuation displaces the fluid element from its resting position. In a stable stratification, the fluid element experiences a pressure force smaller than its own weight if driven upward and larger the its own weight if driven downward. Thus, it experiences a force driving it back to its resting position in both cases. Hence the turbulent fluctuation is diminished. In an unstable stratified flow, the

forces drive the fluid element away from its resting position, thus enhancing turbulence. An illustration of these processes can be found in figure 2.3.

This behavior can be depicted as an additional source term for the turbulent kinetic energy and eddy dissipation ratio in two equation turbulence models. For example, ANSYS CFX [ANSYS, 2016b] uses the equation 2.12 for the production of turbulent kinetic energy P_{kb} and the equation 2.13 for the production of the eddy dissipation rate $P_{\epsilon b}$. The direct influence of buoyancy on turbulence is especially important in stratified flows and flows along inclined walls, as large density gradients in gravity direction are present in these flows. For flows along vertical walls, which are the focus of this thesis, the direct influence of buoyancy on turbulence is of lesser importance because only small density gradients in the direction of gravity are present in these flows [Kim et al., 2008].

$$P_{kb} = -\frac{\mu_t}{\rho \sigma_p} g_i \frac{\partial \rho}{\partial x_i} \tag{2.12}$$

$$P_{\epsilon b} = C_\epsilon max(0, P_{kb}) \tag{2.13}$$

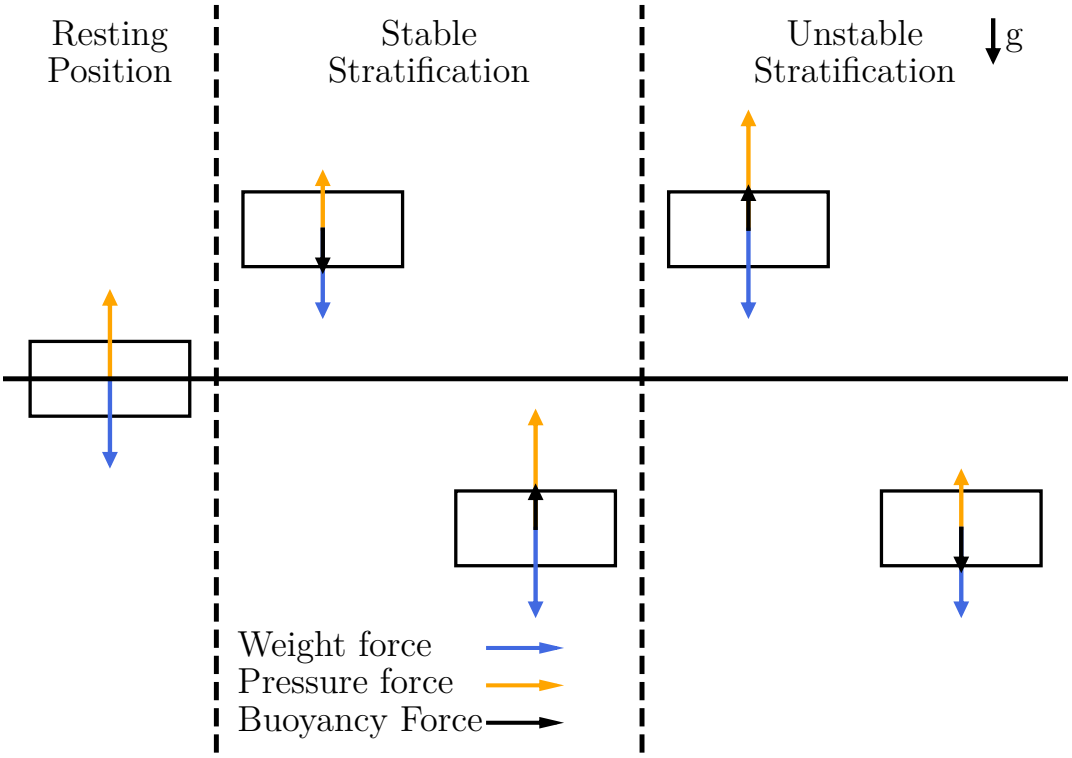

Figure 2.3: Illustration of the direct influence of buoyancy on turbulence

Velocity gradients are one of the primary sources of turbulence [Oertel, 2017] and as such also form the basis for the indirect influence of buoyancy on turbulence. As

described above, buoyancy increases the velocity gradient in the boundary layer, but also pushes this gradient closer to the wall surface. This has two effects on turbulence: The steeper gradients lead to an increased production of turbulence while the lower distance between the wall surface and the gradient leads to a stronger damping of the turbulent fluctuations. Additionally, the formation of a velocity maximum close to the wall surface leads to the development of an additional shear layer between the maximum and the bulk flow. This increases the production of turbulence. As can be seen, buoyancy indirectly influences turbulence in the boundary layer in multiple ways. However, the exact nature of this influence, especially the question whether it enhances or diminishes the turbulence in the boundary layer, is highly dependent on the exact flow conditions.

Wall condensation induces a wall normal flow in the boundary layer directed towards the wall surface. Such a flow is often called suction in boundary layer theory, as opposed to blowing, which describes a wall normal flow away from the wall surface. The suction effect results from the mass balance of the non-condensable gases at the phase interface. As stated in section 2.1, the phase interface can be assumed to be in equilibrium state. The mass balance of the non-condensable gases is given by equation 2.14 and the mass balance of the condensable gas is given by equation 2.15 in this case. The equation consists of a transport term due to the wall normal flow and one transport term due to mass diffusion. These terms must be either zero or of equal magnitude to satisfy the equation. As the non-condensable gases accumulate at the phase interface, creating a concentration gradient towards the bulk flow, a diffusive transport of non-condensable gases toward the bulk must be present. Hence, an equally large advective transport of non-condensable gases to the phase interface is necessary, to satisfy equation 2.14. This requires a wall normal velocity, the condensation induced suction effect.

$$\underbrace{\frac{\partial \rho Y_L u_n}{\partial x_n}}_{Wall\ normal\ flow} = \underbrace{\frac{\partial}{\partial x_n}(\rho D \frac{\partial Y_L}{\partial x_n})}_{Mass\ diffusion} \tag{2.14}$$

$$\underbrace{\frac{\partial \rho Y_S u_n}{\partial x_n}}_{Wall\ normal\ flow} = \underbrace{\frac{\partial}{\partial x_n}(\rho D \frac{\partial Y_S}{\partial x_n})}_{Mass\ diffusion} \tag{2.15}$$

The suction effect increases the transfer of momentum, energy, and vapor mass towards the wall surface, as can be seen from equations 2.4 to 2.7. Consequently, it also increases the wall shear, the sensible heat flux and the condensation mass flux. Lehmkuhl [Lehmkuhl, 2018] shows that suction also leads to a thinning of the boundary layers. Similar to buoyancy, this thinning of the boundary layers can lead to a decrease of turbulence. Lehmkuhl also shows that turbulence can be fully annihilated in the boundary layer at a sufficiently large wall normal velocity. In this case, the bulk flow directly transits into the viscous sublayer. This also applies for the energy, and species mass boundary layer. Thus, the suction effect also has a two fold effect on the boundary layers: It adds an additional advective transport towards the wall, but it also diminishes the turbulent transport of vapor mass, momentum, and energy to the wall surface.

3. Existing Boundary Layer Models

3.1. Boundary layer modeling approaches and examples

3.1.1. Different boundary layer modeling approaches

There are many approaches to model a boundary layer and integrate it into a CFD-code. Three of these approaches are discussed below. Namely, the use of an analytical expression, the use of a table and the use of a numerical subgrid solver. The discussion will focus on the advantages and disadvantages of the approaches for the boundary layer modeling itself as well as for the implementation into a CFD-code.

Probably the most widely used wall function for CFD-codes is of the analytical type: The well-known logarithmic law of the wall (or log-law) [Oertel, 2017]. Other examples of this type of wall function are the ones of Sucec [Sucec, 1999], Kader [Kader, 1981] and Popovac [Popovac et al., 2007]. The analytical wall function can be either an exact solution of the underlying boundary layer model or an empirical function based on measurement or simulation data. The case of an exact solution of the underlying model (like the log-law) is a strength and a weakness for this type of wall function at the same time. This is due to the fact that the possibility to find an exact solution is typically gained by introducing of rather limiting assumptions into the model. Nevertheless, if these assumptions are sufficiently satisfied, the models yield very accurate results. Some examples of such assumptions can be found later in this section (sections 3.1.2 to 3.1.5) where different boundary layer models are discussed.

From a computational point of view, there are typically no downsides to these analytical models if they prove to be numerically stable for the given application. However, they are the fastest type of wall function as they typically require only a few floating point operations per near wall grid cell to compute. Thus, analytical wall functions are usually the best at achieving the primary goal of any wall function, which is a speed up of the computation.

Another approach to model the near wall flow for CFD-codes is the use of tabulated boundary layer data. An example of this is the FIBULA model of Lehmkuhl [Lehmkuhl, 2018]. This type of boundary layer model is especially useful if measurement or more sophisticated computational data, like DNS results, shall be integrated into a CFD-code because it is very easy to add additional data points to the model. A tabular model does not require a full mathematical description of the underlying physical problem. Nevertheless, it does require a thorough understanding of the physics, since, for example, an appropriate scaling approach is necessary to achieve a sufficient range of applicability for the model. Nonetheless, the applicability of the tabular model is limited by the data used, and its accuracy is also highly dependent on the quality of said data.

For a tabular wall function, two computational tasks must be performed during the runtime of the CFD simulation. First, the table entries closest to the requested data points have to be found because the discrete table entries typically don't cover all possible data locations. Then, an interpolation between the table entries has to be performed to gain the desired result at the actual data points. This is a relatively simple and computationally inexpensive task for an univariate problem. However, the computational

cost can increase drastically for multivariate problems, depending on different factors like the size of the table, the exact number of input variables, and the definition of the distance between the data points and the table entries. Thus, tabular wall functions are best suited for univariate problems or multivariate problems with few input variables.

In addition, tabular wall functions can cause memory problems if one or multiple large tables are required [Lehmkuhl, 2018]. These large tables could block the memory of the computer for simulation data, thus slowing the simulation down or rendering it overall impossible. A workaround would be to dynamically load the required table from the hard disk during the run time of the simulation. However, this collection of data from the hard drive could again slow down the computation. Thus, tabular wall functions are limited in their resolution by the amount of memory they require.

A third possible approach is to numerically solve simplified one-dimensional boundary layer equations on a special near wall subgrid. While this does not fully remove the computational cost of a numeric solution of the boundary layer, it reduces them at least. An example of this approach is the UMIST-N wall function [Craft et al., 2004]. From a modeling point of view, such a subgrid based approach has the advantage of being relatively versatile, allowing the integration of many different effects, like buoyancy, into the model. Meanwhile it is only limited in its application range by the assumption of the one-dimensional nature of the boundary layer.

From the computational side the subgrid-based approach has two downsides. First, it is still slower than a comparable analytical wall function. Craft [Craft et al., 2004], for example, states that the UMIST-N wall function needed twice as long for a computation compared to a corresponding analytical wall function. The second issue is the integration of the approach into an existing CFD-code, especially in the case of a commercial code like ANSYS CFX used in the framework of this thesis. This is because the integration of an additional subgrid-based solver requires extensive modifications of the CFD-code and may only be possible with source code access, which is typically not available for commercial codes.

3.1.2. The logarithmic law of the wall

Probably the most widely known example of an analytical wall function is the logarithmic law of the wall [Oertel, 2017]. In the following, its derivation is described as an example of an analytical wall function as well as to introduce some important concepts of boundary layer modeling. As a first step, the assumptions introduced into equation 2.9 enabling to solve it analytically are described. Then the concept of non-dimensionalization and its use in boundary layer modeling is discussed. Next, the solutions for the viscous and the turbulent area of the flow are derived and finally the combination of both models via a blending function is explained.

To be able to solve equation 2.9 it has to be reduced from a partial differential equation to a differential equation in one variable. As it is the aim of a wall function to describe the velocity (temperature, species mass fraction, etc.) as a function of the wall distance, the remaining differential should be the one with respect to the wall distance. Thus, the pressure gradient is removed from the equation. Consequently, the gravity term is also

removed from the equation, as its retention would lead to an overprediction of buoyancy because it is not countered by a hydrostatic pressure gradient. Lastly, the wall normal velocity is also neglected because for many applications the momentum transport by this part of the flow is negligibly small or zero. Thus, equation 2.9 has been reduced to equation 3.1, which only accounts for viscous and turbulent momentum transport.

$$0 = \frac{\partial}{\partial x_n}(\mu\frac{\partial u_p}{\partial x_n} - \rho\overline{u''_p u''_n} + \mu\frac{\partial\overline{u''_p}}{x_n}) \tag{3.1}$$

Due to the turbulent fluctuations, equation 3.1 still cannot be solved. Thus, a turbulence model is required. For the log-law turbulence is modeled as an additional viscosity called eddy viscosity μ_T. The idea to model the momentum transport by the turbulent fluctuations as an additional viscosity was developed by Joseph Valentin Boussinesq in the form of equation 3.2, which is known today as the Boussinesq approximation [Oertel, 2017]. The rightmost term in the equation, which contains the Kronecker-Delta operator δ_{ij}, describes the turbulent pressure and is neglected in the following. Additionally, the rightmost term in equation 3.1, which describes the shear stresses due to turbulent fluctuations, is also neglected since they are not included in the Boussinesq approximation. Finally, equation 3.3 describes a simple model for the eddy viscosity based on Prandtl's mixing length theorem [Oertel, 2017], where κ is the von Kármán constant and Δx_n is the distance from the wall surface. Inserting equation 3.2 and equation 3.3 into equation 3.1 yields equation 3.4 for the momentum transfer near the wall.

$$-\rho\overline{u''_i u''_j} = \mu_T(\frac{\partial u_i}{\partial x_j} + \frac{\partial u_j}{\partial x_i}) - \frac{2}{3}\rho k\delta_{ij} \tag{3.2}$$

$$\mu_T = \rho\kappa^2\Delta x_n^2\frac{\partial u_p}{\partial x_n} \tag{3.3}$$

$$0 = \frac{\partial}{\partial x_n}(\mu\frac{\partial u_p}{\partial x_n} + \rho\kappa^2\Delta x_n^2\frac{\partial u_p}{\partial x_n}\frac{\partial u_p}{\partial x_n}) \tag{3.4}$$

As a last step to obtain a solvable equation, equation 3.4 is split into two parts. As already described in section 2.2 viscosity is the dominant influence on the boundary layer close to the wall, while further away from the wall surface turbulence is the dominant factor. Thus, it is assumed that turbulence can be neglected close to the wall and molecular viscosity can be neglected further away from the wall. Hence, equation 3.4 can be split into equation 3.5 for the viscous part of the boundary layer and equation 3.6 for the turbulent part of the boundary layer. How the solutions of the equations can again be combined to one single model of the boundary layer will be discussed later in this section.

$$0 = \frac{\partial}{\partial x_n}(\mu\frac{\partial u_p}{\partial x_n}) \tag{3.5}$$

$$0 = \frac{\partial}{\partial x_n}(\rho\kappa^2\Delta x_n^2\frac{\partial u_p}{\partial x_n}\frac{\partial u_p}{\partial x_n}) \tag{3.6}$$

As a last step before solving equation 3.5 and equation 3.6 they are non-dimensionalized. The benefit of this non-dimensionalization is that one finds one single scalable solution of the equations which is applicable for all flows that sufficiently fulfill the assumptions described above. For the non-dimensionalization of the equations a velocity and a length scale are needed. As the velocity scale the shear velocity u_τ is used, which is derived from the wall shear τ_W and the density ρ via equation 3.7. As a length scale the shear length L_τ is used, as given in equation 3.8. With these scales the non-dimensional velocity u^+, as given in equation 3.9, and the non-dimensional wall distance y^+, as given in equation 3.10, are defined and then introduced into equation 3.5 as well as equation 3.6. Thus, one finds the two differential equations 3.11 and 3.12 applicable for all boundary layer flows which satisfy the assumptions described above.

$$u_\tau = \sqrt{\frac{\tau_w}{\rho}} \tag{3.7}$$

$$L_\tau = \frac{\mu}{\rho u_\tau} \tag{3.8}$$

$$u^+ = \frac{u_p}{u_\tau} \tag{3.9}$$

$$y^+ = \frac{\Delta x_n}{L_\tau} \tag{3.10}$$

$$0 = \frac{\partial}{\partial y^+}\left(\frac{\partial u^+}{\partial y^+}\right) \tag{3.11}$$

$$0 = \frac{\partial}{\partial y^+}\left(\kappa^2 {y^+}^2 \frac{\partial u^+}{\partial y^+}\frac{\partial u^+}{\partial y^+}\right) \tag{3.12}$$

The first step in solving equation 3.11 and equation 3.12 is to integrate them twice. For equation 3.12 this is a straightforward process, yielding equation 3.13 with the integration constant C_1 after the first integration and equation 3.14 with the integration constant C_2 after the second integration. For equation 3.12 one finds equation 3.15 with the integration constant α after the first integration. To integrate equation 3.15 further, one needs to take its square root (see equation 3.16) and then separate the variables. The second integration then yields equation 3.17 with the additional integration constant C.

$$C_1 = \frac{\partial u^+}{\partial y^+} \tag{3.13}$$

$$u^+ = C_1\ y^+ + C_2 \tag{3.14}$$

$$\alpha = \kappa^2 {y^+}^2 \frac{\partial u^+}{\partial y^+}\frac{\partial u^+}{\partial y^+} \tag{3.15}$$

$$\sqrt{\alpha} = \kappa y^+ \frac{\partial u^+}{\partial y^+} \tag{3.16}$$

$$u^+ = \frac{\sqrt{\alpha}}{\kappa} ln(y^+) + C \tag{3.17}$$

As the second step of the solution of equation 3.11 and equation 3.12, appropriate values for the integration constants have to be selected via the choice of proper boundary conditions. The fact that the shear stress of the fluid is equal to the shear stress at the wall surface can be used to derive the constant C_1. Equation 3.18 describes this fact in a dimensional as well as a non-dimensional way and consequently the constant C_1 is 1. To derive the constant C_2 one can use the fact that the velocity is zero at the surface of the wall (no slip condition). Thus, equation 3.19 describes the dimensional and non-dimensional velocity at the wall surface. Accordingly, the constant C_2 is zero. Assuming that the shear force in the fluid is constant and equal to the wall shear τ_w throughout the whole boundary layer, the constant α, and consequently its square root, is also one. No such straight forward boundary condition can be found for the determination of the constant C. The constant C describes the build up of the non-dimensional velocity in the viscous sublayer and the buffer layer (see figure 2.2). Without a physical model for the buffer layer, no algebraic boundary condition can be deduced to determine C. Thus, a value of 5.5, determined empirically, is typically used for C [Oertel, 2017].

$$\tau_w = \mu \frac{\partial u}{\partial y}|_{y=0} \;\Leftrightarrow\; 1 = \frac{\partial u^+}{\partial y^+}|_{y^+=0} \tag{3.18}$$

$$u(y=0) = 0 \;\Leftrightarrow u^+(y^+=0) = 0 \tag{3.19}$$

Inserting the constants derived from the boundary conditions into equation 3.14 and equation 3.17 yields the solutions for the viscous sublayer (equation 3.20) and for the turbulent layer (equation 3.21). The solution for the second equation is the well known logarithmic law of the wall. Both solutions are depicted in figure 3.1 together with corresponding experimental data measured by Hundhausen [Hundhausen et al., 2017b] for comparison.

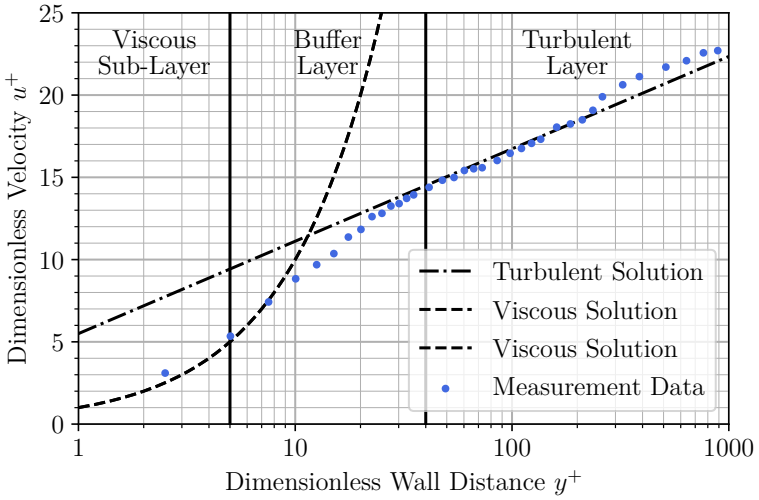

Figure 3.1: Log-law models of the viscous sublayer and the turbulent layer as well as experimental data measured by Hundhausen [Hundhausen et al., 2017b]

$$u^+ = y^+ \tag{3.20}$$

$$u^+ = \frac{1}{\kappa} ln(y^+) + C = \frac{1}{\kappa} ln(y^+) + 5.5 \tag{3.21}$$

As discussed above, the two models described in equation 3.20 and equation 3.21 must be combined to form a complete model of a boundary layer that can be used in a CFD-code. The simplest way to achieve such a transition is to selected a value of the non-dimensional wall distance y^+ where the transition takes place. For example, Cebeci [Cebeci, 1970] uses a y^+ value of 11.8 as the thickness of the viscous sublayer, while Han [Han et al., 1997] uses a value of 40. Another common approach is to combine both functions into a single one using a blending function. Three examples of possible blending functions are shown in equation 3.22 to equation 3.24, where the indices v and t describe the viscous sublayer and the turbulent layer, respectively. The first approach is to use the minimum of both functions (equation 3.22) [Popovac et al., 2007], the second approach is the bi-quadratic blending used, for example, in the automated wall treatment of ANSYS CFX (equation 3.23) and the third approach is an exponential blending developed by Kader [Kader, 1981] for his temperature and species wall function (equation 3.24), which can also be used for velocity wall functions with a Prandtl number Pr of 1 [Popovac et al., 2007]. The different approaches are illustrated in figure 3.2.

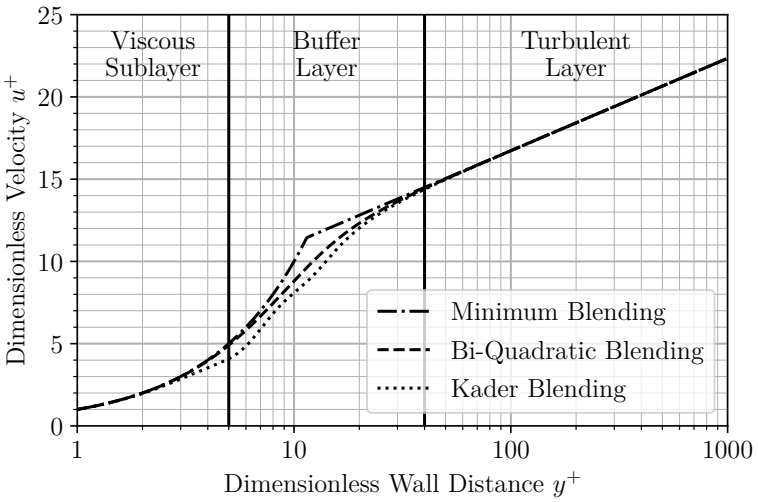

Figure 3.2: Combination of log-law models for the viscous sublayer and the turbulent layer via different blending functions

$$u^+ = min(u_v^+,\ u_t^+) \tag{3.22}$$

$$u^+ = \sqrt[4]{\frac{1}{\frac{1}{u_v^{+4}} + \frac{1}{u_t^{+4}}}} \tag{3.23}$$

$$u^+ = u_v^+ \, e^{-\Gamma} + \, u_t^+ \, e^{-\frac{1}{\Gamma}}, \qquad \Gamma = \frac{0.01(Pry^+)^4}{1 + 5Pr^3 y^+} \tag{3.24}$$

3.1.3. Kader's wall function

As described in section 2.2 flows with heat and mass transfer to the wall require dedicated wall functions for these fluxes. One of the probably most widely used approaches is the wall function of Kader [Kader, 1981], which is applicable to both heat and mass transfer. For example, Kader's wall function is used as temperature wall function in the automated wall treatment of ANSYS CFX [ANSYS, 2016b] and also is included in the wall condensation model of ANSYS CFX [Zschaeck et al., 2014]. In the following, Kader's derivation of his wall function and the resulting model are presented as a basic example of a wall function for heat and mass transfer.

Analogous to the log-law Kader, used a non-dimensional approach to derive his wall function to achieve a scalable result. Comparable to the non-dimensional velocity u^+ for the momentum equation, he derived a non-dimensional temperature T^+ for the energy equation and a non-dimensional mass fraction Y_s^+ for the species mass transfer. The definitions of these quantities are given in the equations 3.25 and 3.26 utilizing the heat flux density $\dot{q}''$ and the mass flux density $\dot{m}''$. A notable difference of equations 3.25 and 3.26 compared to the definition of the non-dimensional velocity in equation 3.7 is that the they include the wall surface values of the temperature and the steam mass fraction, respectively. The difference between the surface value and the local flow value is the driving momentum for the momentum, energy and mass transfer between the bulk flow and the wall surface. However, the wall surface velocity is typically zero and can therefore be neglected in equation 3.7. For a moving wall, for example due to a film running down its surface, the log-law would also have to include the wall surface velocity.

$$T^+ = \frac{\rho u_\tau c_p}{\dot{q}''}(T_w - T) \tag{3.25}$$

$$Y_s^+ = \frac{\rho u_\tau}{\dot{m}''}(Y_{s,w} - Y_s) \tag{3.26}$$

Similar to the log-law, Kader has split his wall function into two parts, one for the viscous sublayer and one for the turbulent part of the boundary layer. For the viscous sublayer the model derivation is nearly the same as for the log-law. Due to the fact that the thermal diffusivity and the mass diffusivity respectively are the important transfer parameters in the viscous sub-layer instead of the dynamic viscosity, Kader's solution for this region, shown in equation 3.27, also contains the Prandtl number Pr or the Schmidt number Sc as defined in equation 3.28. Except for the Prandtl and the Schmidt number, Kader's solutions for both the viscous sublayer and the turbulent layer are the same for the dimensionless temperature and the dimensionless species mass fraction. Therefore, only the solution for the dimensionless temperature is discussed below.

$$T_{visc}^+ = Pry^+ \, , \; Y_{visc}^+ = Scy^+ \tag{3.27}$$

$$Pr = \frac{\mu c_p}{\lambda} \, , \; Sc = \frac{\mu}{\rho D} \tag{3.28}$$

For the turbulent part of the boundary layer, Kader used similarity arguments to establish that the wall function for heat and mass transfer also obeys the logarithmic law. Consequently, the wall function given in equation 3.29 is strikingly similar to the one shown in equation 3.17. The only two differences are the determination of α and β, the latter one is a function of the Prandtl number. From experimental data Kader determines a value of 2.12 for the coefficient α. α can be seen as the quotient of the turbulent Prandtl number with a value of 0.85 and the von Karman constant κ with a value of 0.41. The function $\beta(Pr)$, as defined in equation 3.30, which describes the transport resistance of the viscous sublayer, is also extracted from experimental data by Kader.

$$T^+_{turb} = \alpha ln(y^+) + \beta(Pr) \tag{3.29}$$

$$\beta(Pr) = (3.85 Pr^{\frac{1}{3}} - 1.3)^2 + 2.12 ln(Pr) \tag{3.30}$$

Exemplary plots of Kader's wall function are shown in figure 3.3 for two different Prandtl numbers. The functions for the two parts of the boundary layer have been blended by Kader's blending approach already described in section 3.1.2 (see equation 3.24). As can be seen from the figure, a decrease of the Prandtl number leads to a decrease of the dimensionless temperature. In the viscous sublayer, the downward shift grows continuously with the wall distance, while it is constant in the turbulent layer. In terms of the wall heat flux this means that a decrease of the Prandtl number leads to an increase of the flux under otherwise constant boundary conditions, as can be deduced from equation 3.25.

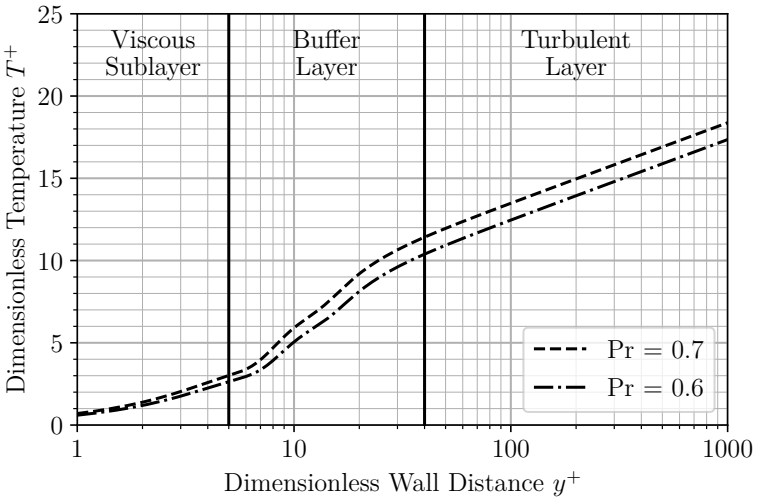

Figure 3.3: Kader's wall function for two different Prandtl numbers

3.1.4. Popovac's wall function

As discussed in section 2.2, wall condensation induces additional effects in the boundary layer, such as suction and buoyancy. These effects have been neglected in the derivation of the log-law and Kader's wall function. An approach to include these non-equilibrium effects, as Popovac calls them, into an algebraic wall function has been presented by Popovac [Popovac et al., 2007]. By changing one of the assumptions used to derive equation 3.4 and using a simplified turbulence model, Popvac found a solution of the equation that includes the non-equilibrium effects. This derivation and its result are presented below, and the applicability of the approach for flows with wall condensation is discussed.

The derivation of equation 3.4 assumes that all flow effects other then viscosity and turbulence are negligible in the boundary layer. To include the non-equilibrium effects in his wall function, Popovac instead assumes that the sum of all these effects is constant throughout the boundary layer and can thus be represented by a constant C_u. The definition of C_u is given in equation 3.31. In addition, Popovac changes the turbulence model given in equation 3.3 to the one in equation 3.32. The second turbulence model actually results from the first turbulence model when the wall normal velocity gradient of the log law is inserted into the equation. With these changes to equation 3.4, equation 3.33 is obtained as the basis for the derivation of Popovac's wall function.

$$C_u = \frac{\partial \rho u_p}{\partial t} + \frac{\partial \rho u_p u_p}{\partial x_p} + \frac{\partial u_n u_p}{\partial x_n} + \frac{\partial p}{\partial x_p} - g_p \rho \tag{3.31}$$

$$\mu_\tau = \rho \kappa u_\tau \Delta x_n \tag{3.32}$$

$$C_u = \frac{\partial}{\partial x_n}(\mu \frac{\partial u_p}{\partial x_n} + \rho \kappa u_\tau \Delta x_n \frac{\partial u_p}{\partial x_n}) \tag{3.33}$$

In the next step of the derivation equation 3.33 is again split into a viscous and a turbulent part and non-dimensionalized. Popovac provides a solution for the turbulent part only. This is sufficient because the influence of the non-equilibrium effects on the dimensionless velocity, temperature and mass fraction of the viscous sublayer is negligible, as can be seen from the experimental and simulation results presented in section 3.2.2. The resulting non-dimensional differential equation is presented in equation 3.34 and its solution is presented in equation 3.35. As can be seen, the resulting equation is nearly the same as the log-law, but has an additional term, linear in y^+ which describes the non-equilibrium effects.

$$\frac{C_u \mu}{\rho^2 u_\tau^3} = C_u^+ = \frac{\partial}{\partial x_n}(\kappa y^+ \frac{\partial u^+}{\partial y^+}) \tag{3.34}$$

$$u^+ = \frac{\alpha}{\kappa} ln(y^+) + C + \frac{C_u^+ y^+}{\kappa} \tag{3.35}$$

As final part of the solution process, the coefficients α and C must be determined from boundary conditions. In the case of Popovac's wall function, this is relatively

simple because in case C_u equals $0\,\mathrm{kg\,m^{-2}\,s^{-2}}$ the wall function should be the same as the log-law. Thus, α is 1 and C is 5.5. Additionally, Popovac rearranged equation 3.35 to the form given in equation 3.36. Through this rearrangement, the influence of the non-equilibrium effects no longer alter the log-law by an additional summand, but by multiplying it by a factor Ψ, which Popovac calls the non-equilibrium factor.

$$u^+ = (\frac{1}{\kappa} ln(y^+) + 5.5) \frac{1}{1 - \frac{C_u^+ y^+}{\kappa u^+}} = (\frac{1}{\kappa} ln(y^+) + 5.5)\Psi \tag{3.36}$$

Exemplary plots of Popovac's wall function are shown in figure 3.4 for three different values of C_u^+. For the plot, the standard solution for the viscous sublayer (equation 3.20) and Popovac's solution for the turbulent layer have been combined by a bi-quadratic blending. The plot shows that a C_u^+ of zero does indeed give the same result as the log-law. A C_u less then zero is associated with effects like suction or a buoyancy force in flow direction. It yields a u^+ smaller than the u^+ of the log-law in the turbulent layer and can indeed lead to a decrease of u^+. Thus, it would lead to an increase of the wall shear calculated by a CFD-code compared to the log-law. Meanwhile, a C_u larger than zero is associated with effects such as blowing (flow in wall normal direction away from the wall) or a buoyancy force opposing the flow direction. It gives a u^+ larger than the u^+ of the log-law. Thus, it would result ia a reduction of the wall shear calculated by a CFD-code compared to the log-law.

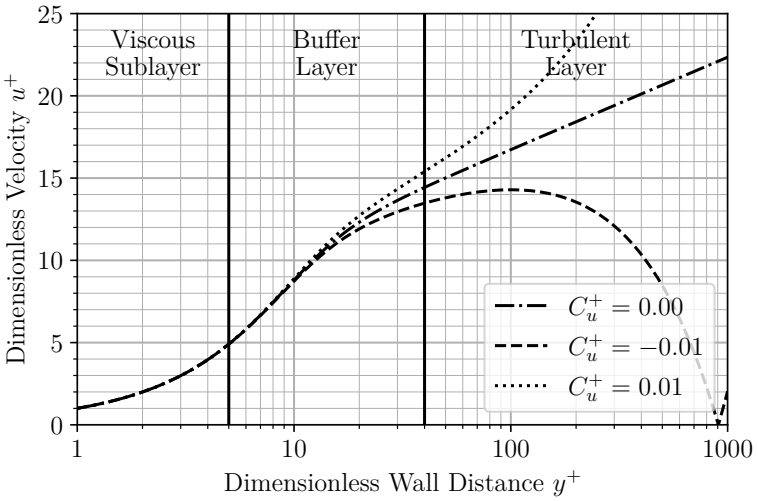

Figure 3.4: Popovac's wall function for different values of C_u^+

Aside from the velocity wall function, Popovac also derived a temperature wall function based on his non-equilibrium factor approach. Due to the similarity of heat and mass transfer, this wall function can also be used for mass transfer to the wall. Based on this similarity assumption, the author [Müller et al., 2016] used Popovac's temperature wall function in a wall condensation model. With this approach, he improved the prediction

of the condensation mass flux on coarse meshes for forced convection flow and concluded that further improvements would be possible if Popovac's approach would also be included in the velocity and temperature wall function in his simulations. But he also concluded that the approach would not yield equal successes in the mixed and natural convection flow regimes because the model does not capture the significant influence of buoyancy on turbulence.

3.1.5. FIBULA

With his FIUBULA approach, Lehmkuhl developed a dedicated wall function for flows with wall condensation [Lehmkuhl, 2018]. The acronym FIBULA stands for Fully-Integrated BoUndary LAyer. The FIBULA approach consists of two parts: A numerical solution of the one-dimensional boundary layer equations prior to the CFD simulation, which is stored in tabular form and an implementation into the CFD code that reads and interpolates data from this table during the runtime of the simulation.

To generate the data tables, Lehmkuhl numerically solves the non-dimensional form of the one-dimensional boundary layer equations for momentum, energy and species mass. To close the equations he uses a turbulence model of Cebeci [Cebeci, 1970], which is valid throughout the whole boundary layer, and the ideal gas equation to account for density changes due to changes in temperature and gas composition. The generated tables contain data of the non-dimensional velocity u^+, the non-dimensional temperature T^+ and the non-dimensional steam mass fraction Y_S^+ as a function of the non-dimensional wall distance y^+ and four additional non-dimensional parameters derived by Lehmkuhl. Lehmkuhl demonstrates that the generated data are in good agreement with fine mesh CFD simulations of corresponding flows.

Lehmkuhl implemented the FIBULA approach into the CFD-code ANSYS CFX using the USER-FORTRAN interface of the code. This implementation proved to be less successful than the a priori generation of the data tables. Primarily it suffered from slow computation times. This is likely the result of the fact that the 1.8 million data points in the data tables have to be searched for the closest data points to the flow situation in the cell for each near wall cell during each iteration. Additionally, the FIBULA approach is based on eight different parameters, but the interpolation library used in the implementation could only handle six variables. Thus, the approach was never tested with a full parameter set. Nevertheless, the FIBULA approach did yield an improvement of the CFD simulation result for wall shear and condensation rate on coarse meshes for separate effect tests, thus proving that a dedicated wall function can be used for flows with wall condensation to reduce the necessary near wall resolution.

3.2. The SETCOM test facility and data base

The 'Separate Effect Test for Condensation Modeling' or SETCOM for short, is an experimental facility specifically designed for the investigation of wall condensation and its influence on the boundary layers under containment like conditions [Belt, 2019]. Consequently, its data have been extensively used for the model development and

validation in the framework of this thesis. Thus, a brief introduction to the facility as well as its measurement results is given in the following. The facility was constructed and commissioned by Belt [Belt, 2019] and an extensive first set of experiments was provided by Hundhausen [Hundhausen et al., 2017b] [Hundhausen et al., 2017a]. The SETCOM facility has been constructed and instrumented with the aim of providing CFD grade data. Further unique features of SETCOM are are:

- Detailed flow boundary layer measurements using non-invasive optical measurement techniques
- High-resolution measurements of wall temperatures and heat fluxes
- A steady flow with precisely defined and reproducible boundary conditions
- The possibility to change the angle of inclination of the system to study the influence of gravity

The test section of the SETCOM facility is a 6 m long square flow channel with a side length of 0.44 m. The flow channel is integrated into a closed loop in which a steam air mixture is circulated. In the test section, condensation takes place on a 70 mm thick cooling plate, while the other three walls of the test section, like the rest of the facility, are heated to flow temperature to create an adiabatic boundary condition. The cooling plate is designed as a cross counter current flow heat exchanger with 25 mm wide boreholes for the coolant every 50 mm. Figure 3.5 shows a picture of the SETCOM facility where the cooling plate can be seen without its hoods in the background.

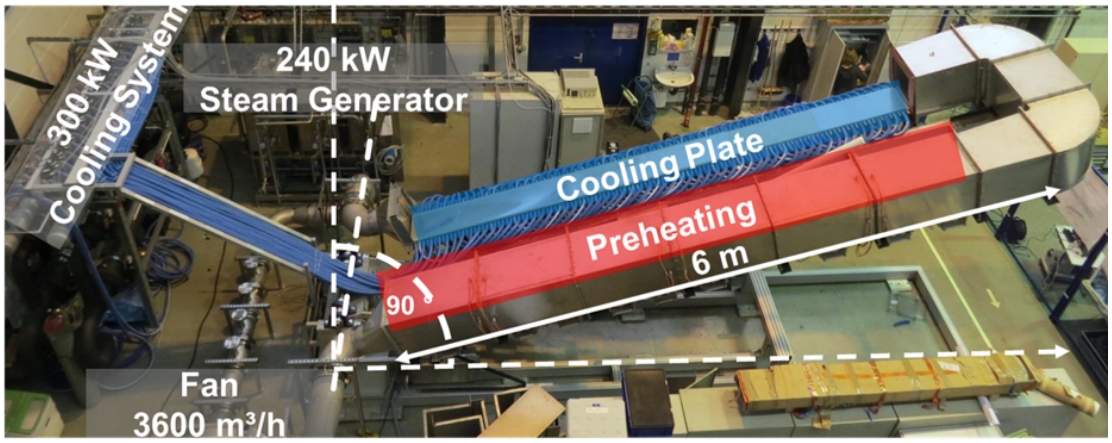

Figure 3.5: The SETCOM test facility

As mentioned above, SETCOM has been built to provide CFD grade data. This includes the necessary instrumentation to provide precise and high resolution measurements for wall condensation and boundary layer modeling. To provide a measure of the local

condensation mass flux, the total heat flux, as the sum of latent and sensible heat, is measured every 100 mm along the cooling plate. Each of these sensors consists of 3 PT-100 resistance thermometers positioned at a distance of 5 mm, 15 mm and 25 mm from the surface of the cooling plate. The heat flux was calculated from this data using Fourier's law of heat transmission. In addition, the condensate running down the cooling plate is collected and continuously weighted at the end of the cooling plate to measure the total condensation mass flux. A sketch of a part of the cooling plate with a heat flux sensor can be seen in figure 3.6.

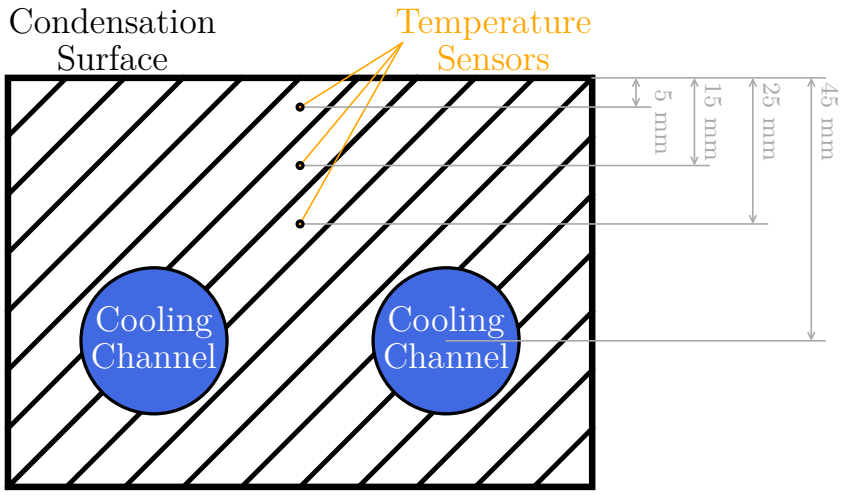

Figure 3.6: Slice of the SETCOM cooling plate with location of the heat flux sensors

Detailed velocity boundary layer data are measured via two non-invasive optical measurement systems in the SETCOM test section. Optical access is provided through one of the six hoods covering the cooling plate. Both measurement techniques are particle based. The first technique is the so called 'LASER Doppler Velocimetry' (LDV), which measures the velocity of the particles via the Doppler shift of a LASER beam reflected from the particle. It is especially useful as it provides a high spacial resolution and data down to very small distances from the wall surface due to its small measurement volume with a size of 1 mm in the wall normal direction [Allelein et al., 2019]. The other technique is the so called 'Particle Image Velocimetry ' (PIV), which measures the velocity from the displacement of particle groups between two images taken in rapid succession. While PIV does not provide the high spacial or near-wall resolution of the LDA, it does provide instantaneous velocity data over an area with the size of approx. 126 mm times 126 mm [Hundhausen et al., 2017b]. A sketch and a photo of the optical hood and the integration of the measurement systems are shown in figure 3.7.

The instrumentation used to measure the inlet boundary conditions at the test channel consists of a combined temperature and humidity sensor. The capacitive humidity sensor

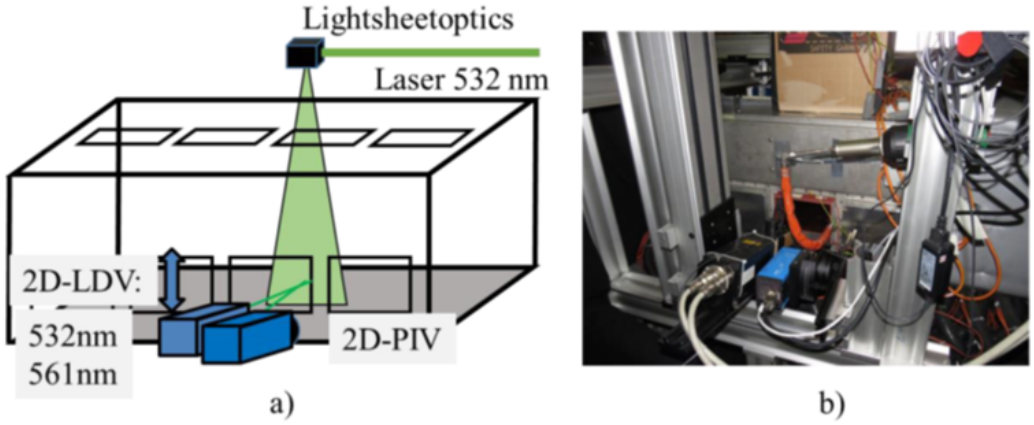

Figure 3.7: Sketch (a) a photo (b) of the optical hood and measurement system of the SETCOM facility [Hundhausen et al., 2017b]

is heated to prevent dew formation on the sensor at high humidity. The temperature of the gas-vapor mixture is measured with a PT1000 resistance thermometer. In addition to the humidity sensor, four other PT100s are installed in the duct. Two of these measurement points are used to validate the temperature in the center of the inlet flow, and the other two are used to ensure that the assumption of a homogeneous temperature profile across the channels cross section is correct. For this purpose, both thermometers are mounted in the duct at a distance of approximately 100 mm from the line of symmetry.

SETCOM was designed to be able to generate a wide variety of flows that are present in a containment under LOCA conditions [Belt, 2019]. These flows are generated by creating the appropriate boundary conditions for both the gas flow and the cooled wall. In the gas flow, the relevant boundary conditions are the pressure, the velocity, the gas temperature, the relative humidity of the gas, and the composition of the non-condensable gases. Combined, these control the two most important features of the condensing near wall flow, wall condensation itself and the flow regime ranging from forced to natural convection. While the pressure in the containment can range from ambient pressure up to 4.55 bar under LOCA conditions [Rosa et al., 2009] the SETCOM facility is limited to ambient pressure due to cost restrictions and safety concerns. A blower circulating the gas in the test loop can produce flow velocities from $0.5\,\mathrm{m\,s^{-1}}$ to $5\,\mathrm{m\,s^{-1}}$. Although SETCOM is very well insulated and its walls are heated, heat losses from the facility still limit the achievable gas temperatures to a range from ambient temperature to 90 °C. In this temperature range, the relative humidity in SETCOM can be varied between ambient humidity up to 100 %. Helium can be injected into the experimental loop to alter the composition of the non-condensable gases. However, all experiments used in this thesis have been performed with air the as non-condensable gas, and thus its composition is 79 vol% nitrogen and 21 vol% oxygen.

Regarding the cooled wall, two relevant parameters can be altered. The first parameter

is the volume flow of the coolant, which governs the heat transfer coefficient between the cooling plate and the coolant. The overall coolant volume flow can range from $20\,\mathrm{l\,min^{-1}}$ to $30\,\mathrm{l\,min^{-1}}$. The second parameter is the coolant temperature, which sets the lower limit for the cooling plate temperature. The design of SETCOM targeted a temperature range from 8 °C to 60 °C. However, due to the large and uncontrollable cooling capacity of SETCOM's ultimate heat sink, a temperature range of just 8 °C to 14 °C could be realized for the experiments used in this thesis. The overall operational area of the SETCOM facility is summarized in table 3.1.

Table 3.1: Operational area of SETCOM

Gas velocity	$0.5\,\mathrm{m\,s^{-1}}$ - $5\,\mathrm{m\,s^{-1}}$
Gas temperature	Ambient temperature - 90 °C
Gas relative humidity	Ambient humidity - 100 %
Gas dry composition	O_2 21 vol%, N_2 79 vol%
Coolant volume flow	$20\,\mathrm{l\,min^{-1}}$ - $30\,\mathrm{l\,min^{-1}}$
Coolant temperature	8 °C - 20 °C

The SETCOM operational area is also depicted in the flow map in figure 3.8, which was created before the first extensive SETCOM test series to plan the experiments. The flow map is based on about 1800 fine mesh CFD simulations using the modeling approach described in section 3.2.1. The flow map shows the forced (green) and the natural convection (white and red) flow regimes as a function of the Reynolds number Re_D (see equation 3.37) and the Grashof number Gr_L (see equation 3.38). To determine to which flow regime a specific data point belongs, the simulations used to create the flow map were always performed in pairs, one with and one without a buoyancy model. The quotient (B, equation 3.39) of the condensation mass fluxes of both simulations was used to determine whether buoyancy has an effect on the flow (natural convection $B < 1$ or $B > 1$) or not (forced convection $B = 1$). As shown by the separation of the natural convection regime, buoyancy can have different effects on condensation. When leaving the forced convection region, condensation is first impaired (white area) and then enhanced (red area) further away from the forced convection region. This trend is confirmed by the experimental results from the SETCOM facility. The data points shown in the flow map are the about 200 SETCOM experiments of the C (forced convection, blue) and D (natural convection, red and black) series which have been used for model development and validation in this thesis. A test matrix of the experiments used in this thesis can be found in appendix A.

$$Re_D = \frac{\rho u_{Bulk} D}{\mu} \tag{3.37}$$

$$Gr_L = \frac{\rho_{Bulk} - \rho_{Wall}}{\rho_{Bulk}} \frac{g L^3}{\nu_{Bulk}^2} \tag{3.38}$$

$$B = \frac{\dot{m}_{Cond,Buoyancy}}{\dot{m}_{Cond,noBuoyancy}} \tag{3.39}$$

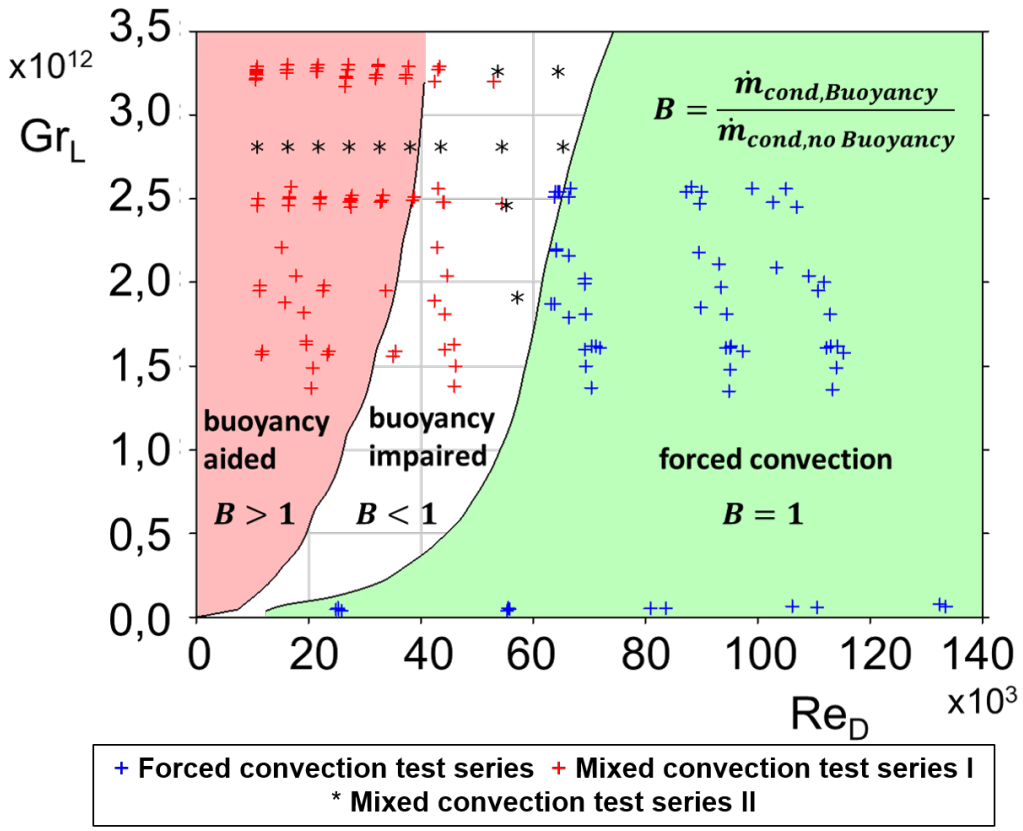

Figure 3.8: Flow map of the SETCOM facility with operation points of the experiments used in this work

3.2.1. Simulation Model of SETCOM

In order to gain a deeper understanding of the SETCOM measurement results and to generate additional data for model development and validation, fine mesh simulations of over 200 SETCOM experiments have been performed in the framework of this thesis. The setup used for these simulations is presented below. This setup, like any setup for a CFD calculation, essentially consists of four parts. First, the physical models that describe the physics involved in the simulation. Second, the numerical methods used to solve the equations contained in the physical model. Third, the geometry, which describes the boundaries of the simulation domain and the mesh used to resolve it. And fourth, the initial and boundary conditions necessary to calculate a given flow.

The physical model (see table 3.2) is based on the Reynolds Averaged Navier Stokes equations (RANS). Since the measurements in the SETCOM facility were performed under steady state conditions, a steady state version of the RANS equations is used. The equation system is closed with the ideal gas law as the equation of state and the $k-\omega\ SST$ turbulence model [ANSYS, 2016b]. In addition, further transport equations for the gas components and the total energy equation are solved. In contrast to the thermal energy equation, the total energy equation also includes the volume change energy. The energy equation was used in a 'non-unity Lewis number' formulation, i.e. the diffusion of enthalpy due to concentration gradients was also considered.

Table 3.2: Physical models used for the calculation of the SETCOM experiments

Conservation equations	Reynolds Averaged Navier Stokes equations (RANS), total energy equation, transport equation for each component of the gas mixture
Turbulence model	$k-\omega$ based SST-model with additional terms for turbulence production and dissipation due to buoyancy
Buoyancy model	Density based (no Boussinesq approximation)
Condensation model	ANSYS CFX internal wall condensation model
Equation of state	Ideal gas
Material Properties	Temperature dependent, ideal mixture

Buoyancy effects were calculated based on density differences and not estimated using the Boussinesq approximation. The production and dissipation of turbulence due to buoyancy was calculated using additional terms in the transport equations for the turbulent kinetic energy k and the eddy frequency ω.

The gas mixture was considered as an ideal mixture and its properties were averaged via the mass fraction. The transport properties (dynamic viscosity as well as thermal conductivity and diffusion coefficient) of the individual components were taken from the VDI Heat Atlas [VDI, 2013].

The applied numerical methods largely corresponded to the standard specifications of ANSYS CFX [ANSYS, 2016a] (see table 3.3). The 'High Resolution' method is used for the spatial discretization. Depending on the stability, the method locally blends between a first and second order scheme. A maximum normalized residual of 10^{-6} in the transport equations is used as the numerical convergence criterion. Additionally, physical quantities like the total wall heat flux are monitored to ensure that the simulation has reached a steady state.

Table 3.3: Numerical methods used for the calculation of the SETCOM experiments

Flow solver	ANSYS CFX v17.2 finite volume, fully coupled implicit solver
Spacial discretization	High resolution scheme
Temporal discretization	Steady state
Convergence criterion	Max normalized local residual $< 10^{-6}$

A two dimensional geometry was used to carry out most of the SETCOM simulations presented in this thesis, to be able to perform an extensive number of simulations in a reasonable amount of time. This approach is well founded by the geometry of SETCOM geometry and the large effort put into the creation of block profiles for the main gas inlet boundary conditions as described in section 3.2. Such a two dimensional approach is often used in similar work, for example by Lehmkuhl [Lehmkuhl, 2018] and by participants of the SARNET condensation benchmark [Ambrosini et al., 2014].

The geometry used for the fine mesh simulations includes not only the test section itself, but also other components of the SETCOM facility, as can be seen from the meshed geometry shown in figure 3.9. In the flow direction, the first additional component is the nozzle at the beginning of the test section. The nozzle is included in the geometry so that its influence on the development of the flow at the leading edge of the cooling plate can be taken into account. Additionally, the nozzle shapes the flow entering the test section to some extent and thus provides a better boundary condition than the block profile at the inlet boundary condition.

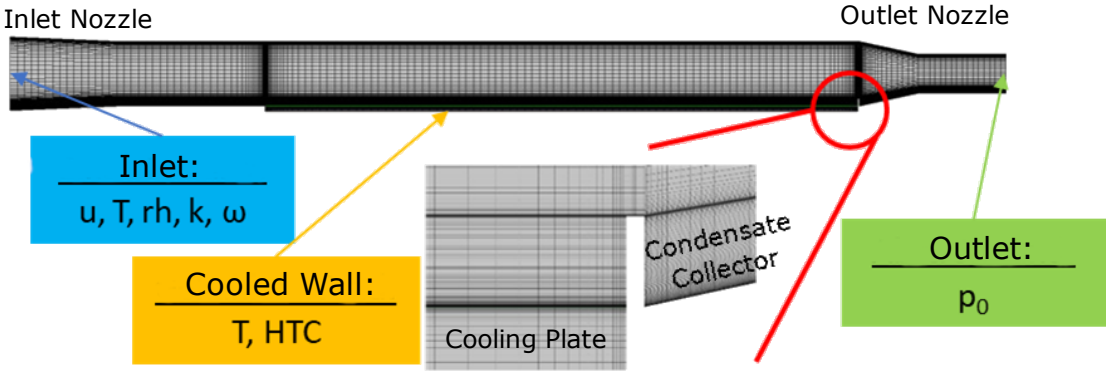

Figure 3.9: Geometry, mesh and boundary conditions for the SETCOM simulations

As the next additional component, the cooling plate is integrated in the geometry, since experience has show that the heat transfer between fluid and the structure, especially for condensing flows, can be better calculated if the structure is included in the mesh. As a third additional element, the condensate collector at the end of the cooling plate is included in the simulations in order to account for the influence of the flow detachment it causes at the end of the measurement section. Finally, the nozzle at the outlet of

the measurement section and a subsequent piece of piping are included in the geometry to account for the influence of the acceleration behind the measurement section and to create a buffer between the outlet of the measurement section and the outlet boundary condition.

The quality guidelines according to Mahaffay [Mahaffy et al., 2015] were applied during the generation of the mesh, which is also shown in figure 3.9. The boundary layer is resolved with a cell height of 0.1 mm and a growth rate of 1.1 for the following cells at all wall surfaces. This corresponds to a dimensionless wall distance y^+ between 0.5 and 2 for the different SETCOM experiments. The beginning and the end of the test section are resolved with a cell size of 1 mm in flow direction, since strong gradients of the wall fluxes occur at these locations, which have to be resolved accordingly. In order to keep the cell sizes in the remaining part of the measurement section constant for the following investigations with coarser boundary layer resolutions at the cooling plate, a split with a cell size of 1 mm was inserted into the grid at a distance of 5 mm from the surface of the cooling plate, which can be clearly seen in the zoom in figure 3.9.

The boundary conditions for the simulation of the SETCOM facility can be roughly divided into three sub-areas, as shown in figure 3.9. The inlet boundary condition, the outlet boundary condition and the wall boundary conditions. For the latter, the cooling plate plays a special role. All other walls can be assumed to be adiabatic in a good approximation, since they are heated to the temperature of the main flow. The cooling plate itself is resolved in the mesh, as already explained. Therefore, the boundary of the simulation domain is located at the transition between the cooling plate and the coolant. This transition is modeled in a simplified fashion with a coolant temperature and a heat transfer coefficient (HTC). This modeling approach was chosen because resolving the individual cooling channels in the computational grid would have required a too fine mesh resolution in the flow direction. Consequently, such an approach would yield a disproportionately long calculation time.

Since the difference between the coolant inlet and outlet temperature is less than one Kelvin for all SETCOM experiments, it is considered to be constant in the simulations. The secondary-side temperature was obtained by averaging the three temperatures measured in the collection chambers for the coolant at the inlet and outlet of the cooling plate. The Heat Transfer Coefficient (HTC) between the cooling plate and the coolant was determined by preliminary simulations of a section of the cold plate. At the coolant volume flow rate of $20\,\mathrm{l\,s^{-1}}$ used in all SETCOM experiments, the HTC is about $3400\,\mathrm{W\,m^{-2}\,K^{-1}}$. This means that the HTC is about one order of magnitude larger than the heat transfer coefficient between the gas in the test section and the cooling plate in the case of heavy condensation. Therefore, the heat transfer coefficient between the coolant and the cold plate only has a negligible effect on the overall heat transfer.

The inlet velocity is specified as constant across the whole inlet cross section because a flow conditioner installed just upstream of the test section generates a homogeneous block profile at this location [Hundhausen et al., 2017b]. The exact definition of this inflow velocity is difficult due to the relatively high inaccuracy of the three anemometers used to measure the average velocity at different locations of the SETCOM test loop, especially at flow velocities below $1.25\,\mathrm{m\,s^{-1}}$. At these low velocities the anemometers

either do not start at all or lag well behind the velocity that would be expected based on the frequency of the fan used to circulate the gas and LDA measurement data. Therefore, the expected velocity due to the fan frequency is used as a boundary condition for these flow velocities, after being plausibilized based on LDA and PIV data. For the flows above $1.25\,\mathrm{m\,s^{-1}}$, the mean value of the velocities measured by the three anemometers is used as the boundary condition, whereby the measurements of the anemometers were checked for plausibility beforehand.

In addition to the mean velocity boundary condition, boundary conditions for the turbulent kinetic energy and the turbulent vortex frequency used by the *SST* model must be specified at the inlet. Since no information on the turbulence could be derived from the anemometer measurements, only estimated values can be used here. Initial test calculations showed that the "High" setting in CFX for the turbulence boundary condition is particularly suitable for this purpose and is therefore used in this thesis. A turbulence intensity of 10 % and an eddy viscosity ratio of 100 [ANSYS, 2016b] are used to determine the boundary conditions for the turbulent kinetic energy and the turbulent vortex frequency from this information. LDA measurements performed as part of the flow homogenization development confirm that these assumption for the turbulence inlet condition are plausible.

In order to calculate water vapor and energy transport in the SETCOM facility, additional boundary conditions for temperature and relative humidity at the inlet are required. These were specified using a combined humidity and temperature sensor at the inlet of the test section. Preliminary calculations showed a strong sensitivity of the condensation rate to the inlet temperature. Therefore, it was experimentally investigated, whether the assumption of a block profile is permissible for this boundary condition [Hundhausen et al., 2017b]. The results of the measurements showed that the assumption was justified. Consequently, a block profile for the temperature can be used as a boundary condition for the simulations. A block profile is used as a boundary condition for relative humidity as well.

Finally, a pressure boundary condition must be selected for the outlet. A constant relative pressure of 0 Pa (relative to the reference pressure of 1 bar) is defined for all experiments.

3.2.2. Comparison of SETCOM measurement and fine mesh simulation data

In the following, the fine mesh simulation results of the SETCOM experiments are presented and compared with the measurement data. Two main experimental data sets are available for the comparison: The heat flux measurements along the cooling plate and the near wall velocity measurements. First, the results for the integral heat fluxes are presented to get a global comparison between experiment and simulation. Then, a the local heat flux data are presented for a selected set of experiments to substantiate and explain the results of the global comparison. Finally, the near wall velocities are compared for a selected set of experiments in a non-dimensional manner to investigate how well ANSYS CFX can reproduce the near wall flow in the wall condensation regime. The goal of the comparison is to determine how well ANSYS CFX is able to reproduce

the experimental results as a baseline for the validation of the new wall function approach and to determine if the simulation results are of high enough quality to be used as an additional data source for the model development and validation process.

A first impression of the quality of the fine mesh simulations and thus also of the best possible CFD result is provided by the comparison of the integral heat fluxes (as a measure of the condensation rate) of simulation and experiment. This comparison is shown in figure 3.10. The figure shows that a large part of the results show a deviation between calculation and experiment of less than 15 %. This result is in line with the empirical values from the SARNET condensation benchmark [Ambrosini et al., 2014] and represents a very good result considering the non-negligible uncertainty in the heat flux measurements, which are discussed in more detail later in this section. However, it is noticeable that in the area of the highest heat fluxes (>20 kW) a clear tendency of the simulations to overestimate the heat fluxes can be observed. Due to the comparatively small number of experiments in this area, the cause for this could not be conclusively determined within the scope of this thesis.

While most of the total heat fluxes are well predicted by ANSYS CFX, some of the simulations predict a too large heat flux, especially in the range from 12 kW to 20 kW experimental heat flux. Further analysis of the data shows that CFX is well able to calculate the condensation mass flux in the forced as well as in the natural convection regime, but is less accurate in the the transition region between these regimes (boarder of green and white area figure 3.8).

Examples for the accurate prediction of the heat fluxes in the forced and natural convection regime as well as the loss of accuracy in the transition region can be seen in figures 3.11 to 3.17, which compare the measured(dots) and calculated(line) local heat flux along the cooling plate for different velocities under otherwise constant boundary conditions. Thus, the figures show the change of the local heat flux during the transition from from natural (lower velocities) to forced (higher velocities) convection. The error bars are calculated via equation 3.40, from the thermal conductivity of the cooling plate, the largest distance Δs between two PT100, and the maximum temperature independent error T_{Err} of the PT100, which is specified by the supplier as 0.1 K. The plots show that CFX is well able to reproduce the heat fluxes at the lower (0.75 m s^{-1} to 1.75 m s^{-1}) and the higher velocities (4 m s^{-1} to 5 m s^{-1}), but loses some accuracy in the transition region in between.

$$\dot{q}''_{Err} = \pm\lambda \frac{2T_{Err}}{\Delta s} \tag{3.40}$$

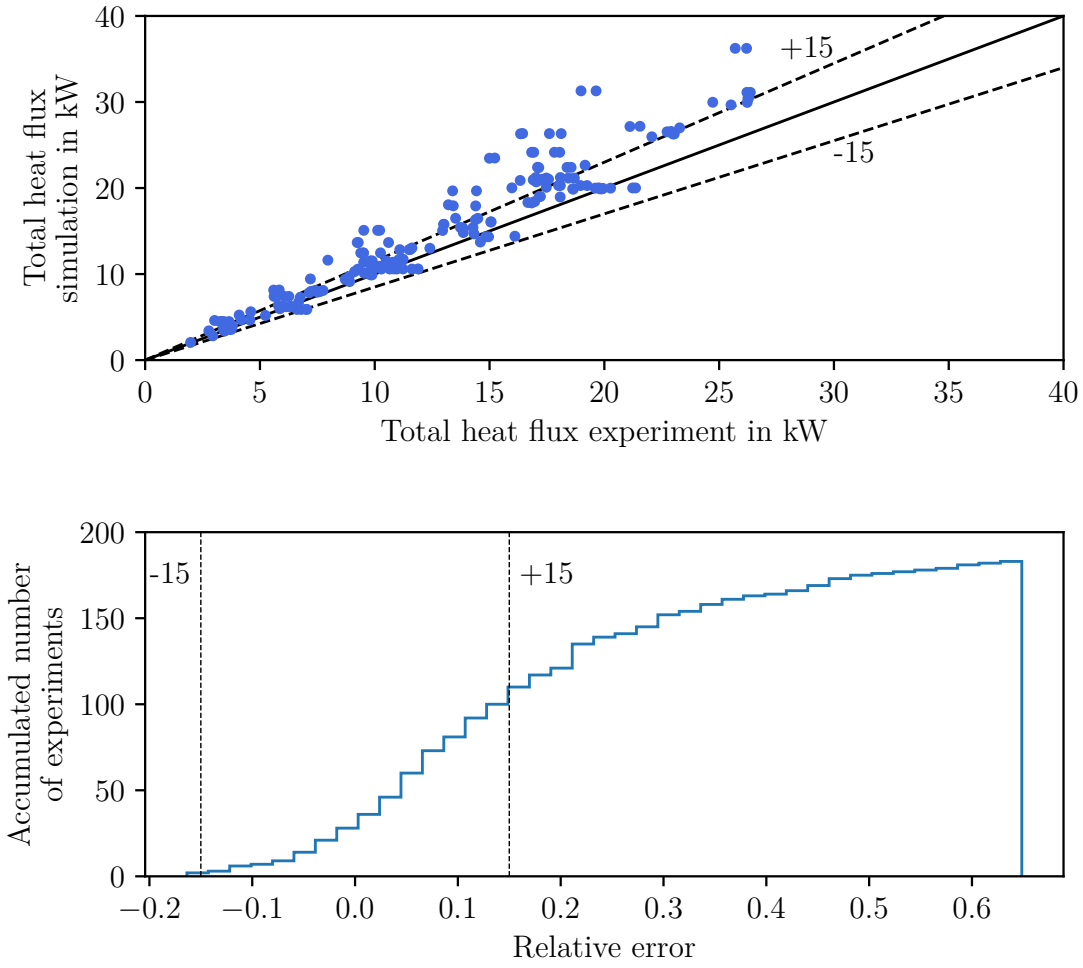

Figure 3.10: Comparison of experimental and simulated SETCOM total heat flux

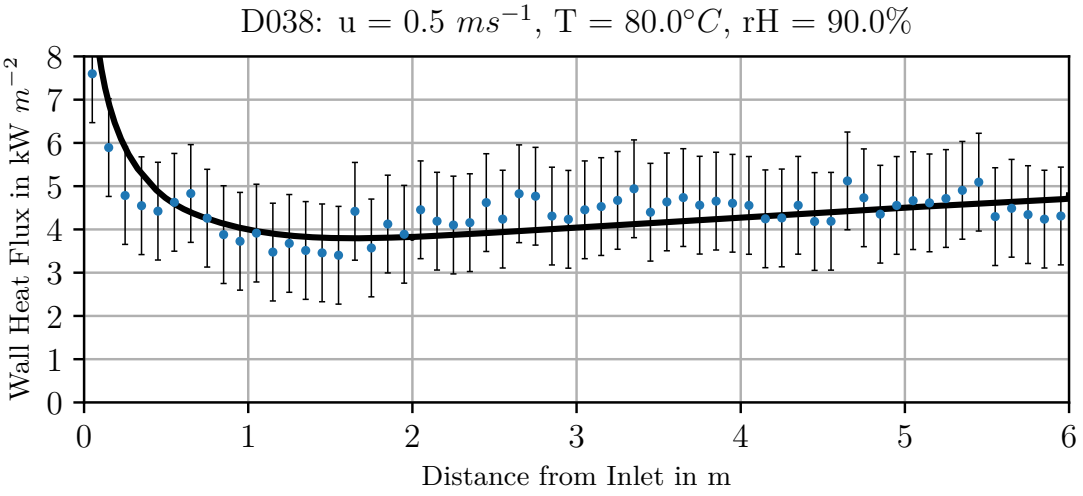

Figure 3.11: Comparison of experimental and simulated SETCOM local heat flux for experiment D038 in the mixed convection regime

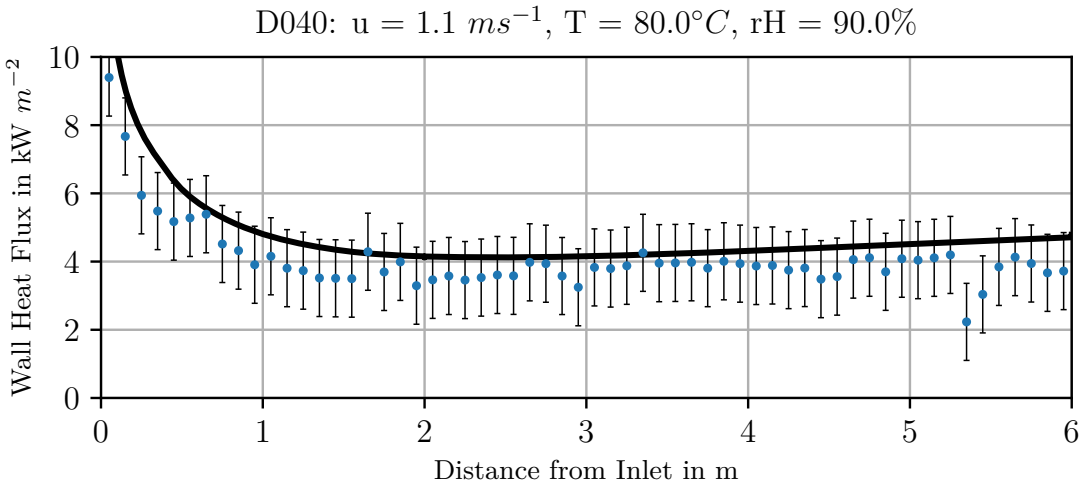

Figure 3.12: Comparison of experimental and simulated SETCOM local heat flux for experiment D040 in the mixed convection regime

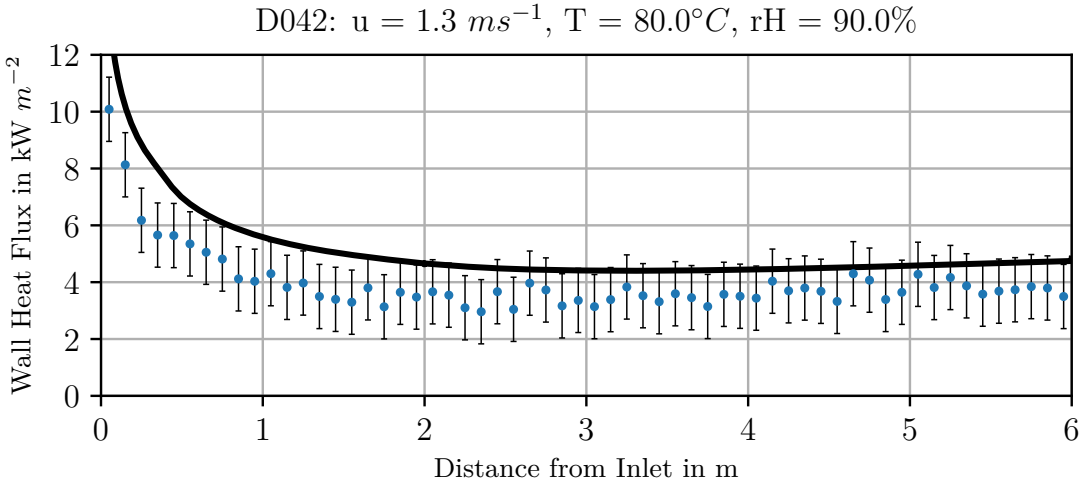

Figure 3.13: Comparison of experimental and simulated SETCOM local heat flux for experiment D042 in the mixed convection regime

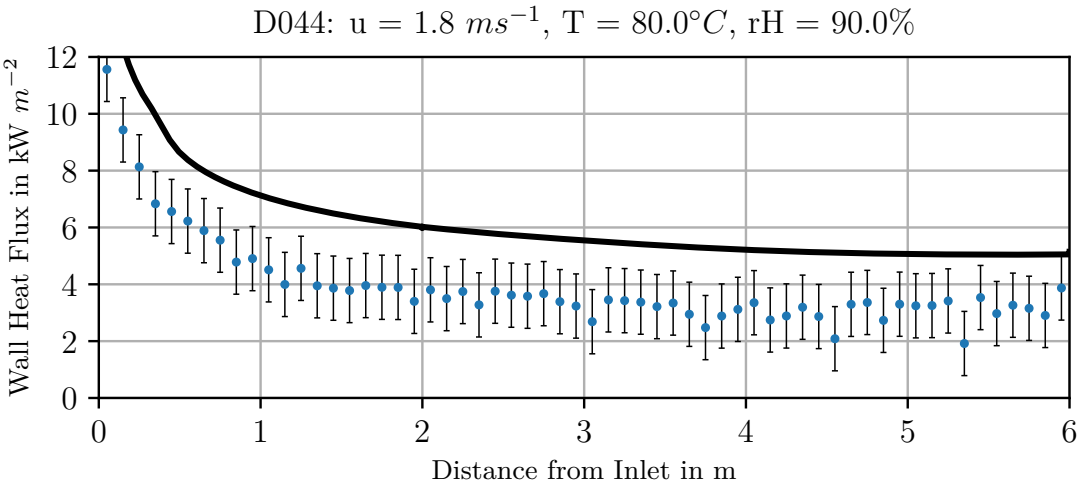

Figure 3.14: Comparison of experimental and simulated SETCOM local heat flux for experiment D044 in the mixed convection regime

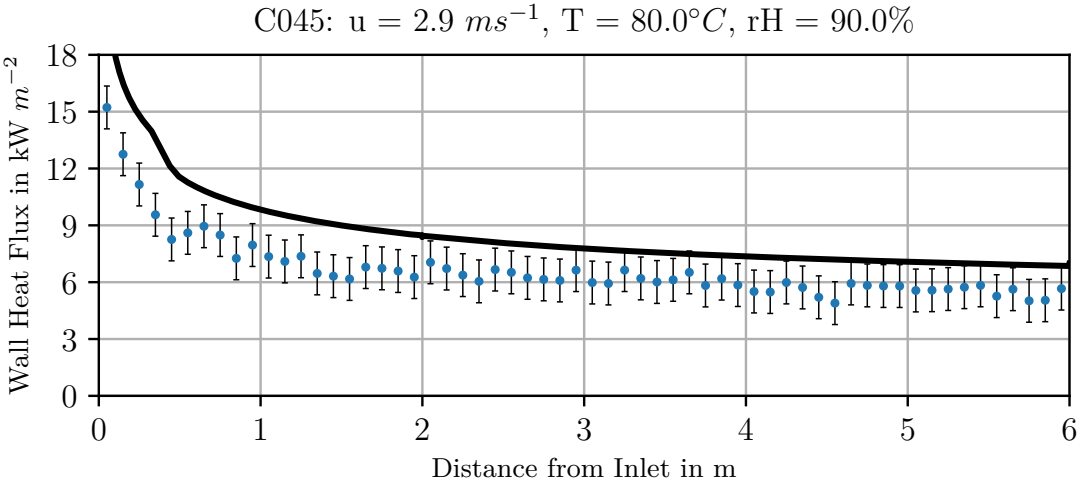

Figure 3.15: Comparison of experimental and simulated SETCOM local heat flux for experiment C045 in the forced convection regime

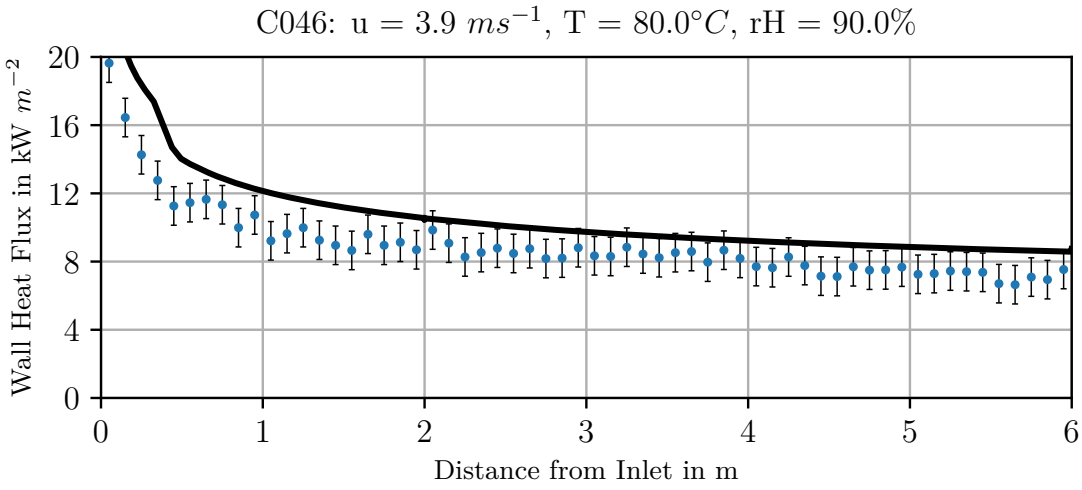

Figure 3.16: Comparison of experimental and simulated SETCOM local heat flux for experiment C046 in the forced convection regime

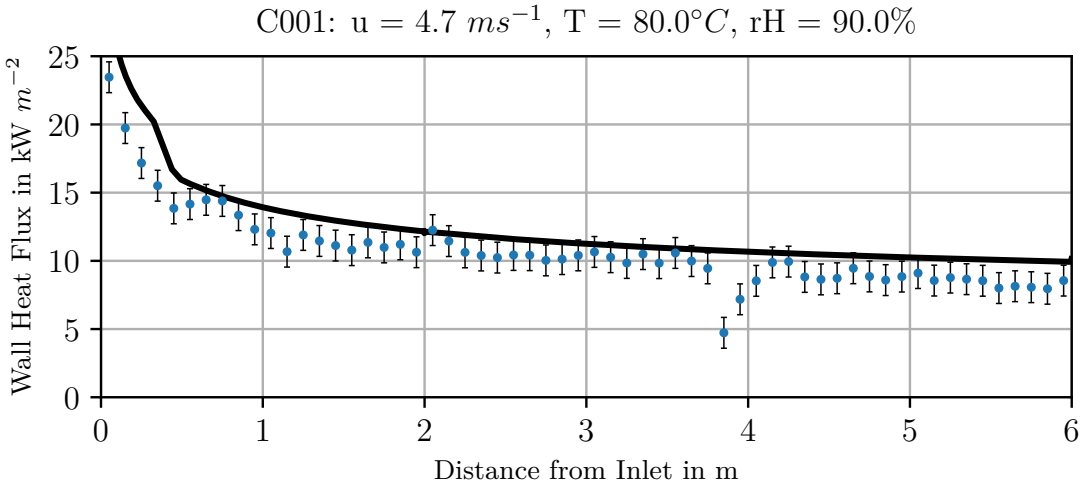

Figure 3.17: Comparison of experimental and simulated SETCOM local heat flux for experiment C001 in the forced convection regime

As discussed in the context of figure 3.8, the condensation rate decreases, compared to a non-buoyant flow, during the transition from a forced to a natural convection flow. The same behavior can be observed for the experimental data in figures 3.12 to 3.15. While buoyancy free experiments cannot be performed in reality, the experimental data show a nearly constant or even slightly decreasing heat flux in the velocity range from 1.25 m s^{-1}

to 2.25 m s^{-1}. This indicates the influence of buoyancy, as one would expect the heat flux to increase with velocity if no other effects were present. This increase is also clearly present in the ANSYS CFX results. Nevertheless, figure 3.8 indicates that ANSYS CFX can also compute the decrease of the condensation rate in the transition region. However, the data presented in figures 3.12 to 3.15 show that ANSYS CFX underestimates the magnitude of this effect.

Overall, the data presented in figures 3.10 to 3.17 show that ANSYS CFX is well able to reproduce the experimental heat flux data from the SETCOM facility. The only noteworthy exception is the transition region between the forced and the natural convection regime. Here, ANSYS CFX can predict the overall decrease in the heat flux due to buoyancy, but underestimates the magnitude of the effect. Nonetheless, the data confirm the modeling approach described in section 3.2.1 with respect to the heat flux.

The near wall velocity data recorded at the SETCOM facility are especially useful for the development and validation of near wall flow models. Even more so, as these are one of a kind data for flows with wall condensation. Figures 3.18 to 3.20 compare the non-dimensional velocity profiles measured in the facility with corresponding simulations. Again, plots with different bulk velocities with otherwise constant boundary conditions are shown to illustrate the influence of buoyancy. Each plot compares the result of two different experiments, performed under the same boundary conditions, with the simulation results. For the experiments two different error bars are given. The horizontal ones correspond to a measurement error in the wall distance of 1 mm. Meanwhile, the vertical error bars correspond to an error of 1 in the dimensionless velocity u^+ as it is difficult to quantify and combine the measurement errors for the dimensional velocity and the wall shear.

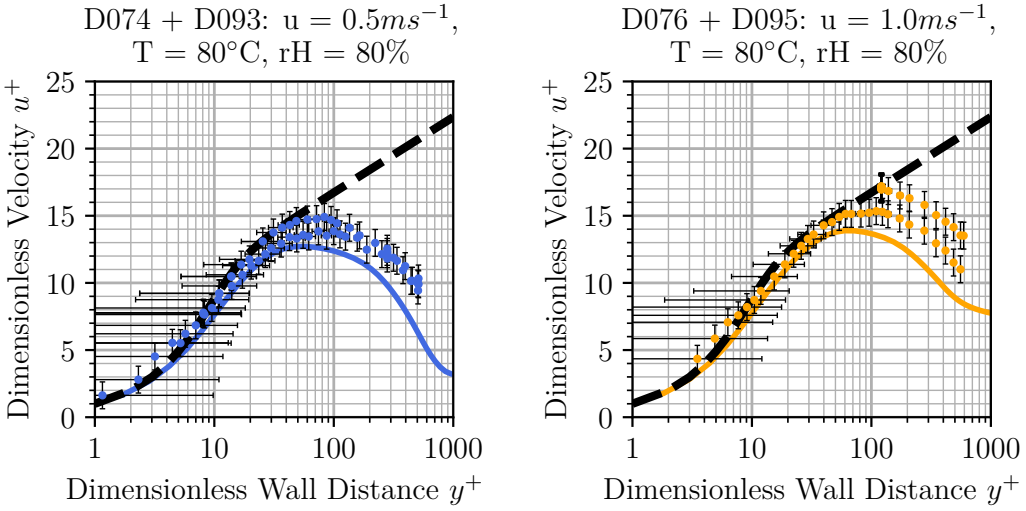

Figure 3.18: Comparison of experimental and simulated SETCOM dimensionless velocity profiles for the experiments D074, D093, D076 and D095

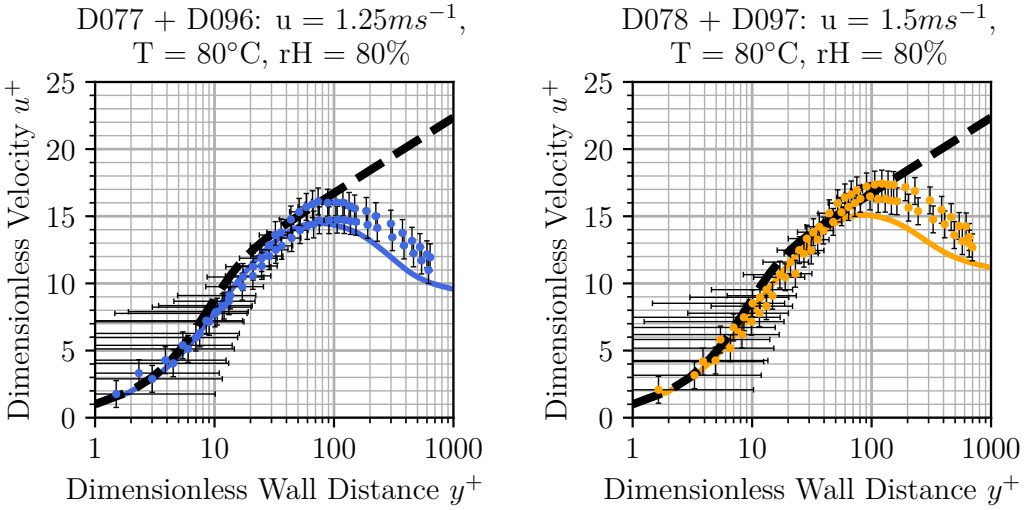

Figure 3.19: Comparison of experimental and simulated SETCOM dimensionless velocity profiles for the experiments D077, D096, D078 and D097

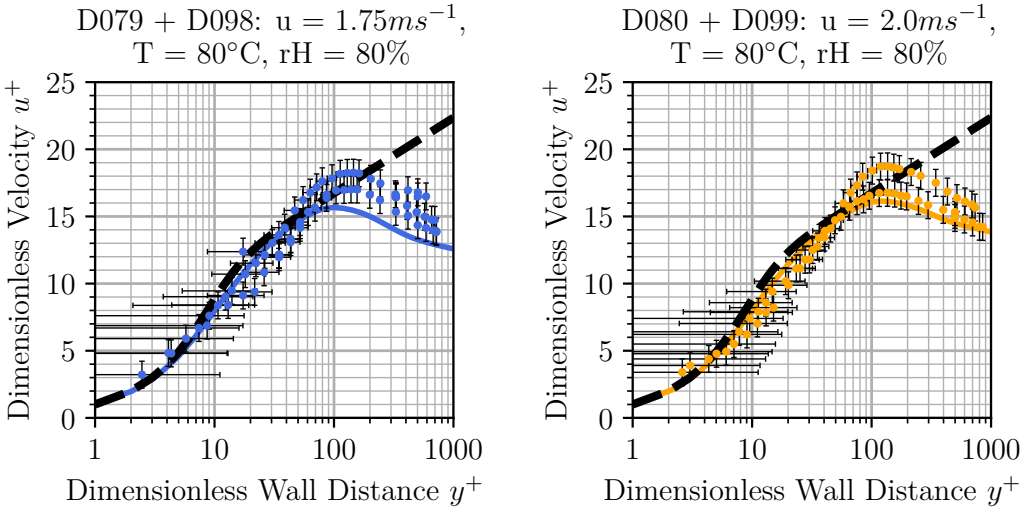

Figure 3.20: Comparison of experimental and simulated SETCOM dimensionless velocity profiles for the experiments D079, D098, D080 and D099

All of the flows presented in figures 3.18 to 3.20 show a least some influence of buoyancy by a distinct maximum of the non-dimensional velocity which is not predicted by the log-law. However, the shape and the magnitude of this peak varies with the bulk flow velocity and thus the buoyancy influence. For the lowest bulk flow velocity of $0.5\,\mathrm{m\,s^{-1}}$ the experimental data show the position of the peak at a dimensionless wall distance y^+ of about 70 to 80 and a magnitude between 13 and 15. After this peak the dimensionless

velocity u^+ drops to 10 at the maximum measurement distance of y^+ 500. At the bulk velocity of $2.0\,\mathrm{m\,s^{-1}}$ on the other hand the maximum is located at a y^+ of about 105 with a magnitude of 17 to 19. Afterwards, the dimensionless velocity drops to 14 at a wall distance of 800. Therefore, it becomes clear that the buoyancy induced by wall condensation leads to a wall jet like flow behavior with an increase in the magnitude of the jet with increasing buoyancy.

Comparing the experimental data with the simulation results in figures 3.18 to 3.20 it becomes immediately clear that ANSYS CFX is able to reproduce the results well. Qualitatively, the shape and magnitude of the simulated dimensionless velocity profiles are very similar to the measured ones. Quantitatively, the results are a bit more mixed. A very good agreement between experiment and simulation can, for example, be observed for the position and magnitude of the velocity maximum for bulk flow velocities of $1.25\,\mathrm{m\,s^{-1}}$ and $2.0\,\mathrm{m\,s^{-1}}$. Some deviation from these quantities can be seen for mean flow velocities of $1.5\,\mathrm{m\,s^{-1}}$ and $1.75\,\mathrm{m\,s^{-1}}$. However, these deviations are well within the range of the experimental data scatter. Consequently, it can be stated that the CFX fine mesh simulations are very well able to predict the non-dimensional near wall velocity in flows with wall condensation.

The comparison of the measured and calculated heat flux and velocity data shows that ANSYS CFX is well able to reproduce the experimental results within the bounds of the measurement errors in most cases. A notable exception regarding the heat fluxes is the transition between the forced and the natural convection regime. The most likely cause of this is an overprediction of the near wall turbulence by ANSYS CFX in this transition zone. However, because of the limited amount of experimental data available and the limited possibilities to influence the turbulence model of ANSYS CFX this remaining deviation could not be removed in the framework of this thesis. Nevertheless, due to the overall very good predictions by the ANSYS ANSYS CFX model presented in section 3.2.1 and the successful use of similar modeling approaches in a large number of benchmarks (e.g. [Ambrosini et al., 2014]) and application calculations (e.g. [Kelm et al., 2016], [Kelm et al., 2018]),the model is considered to be well suited for the calculation of near wall flows in the wall condensation regime. Consequently, the fine grid model can be used as a benchmark for the coarse grid simulations and also to complement the experimental database for the model development and validation.

4. Model Development and Implementation

This section describes the development of the comprehensive boundary layer model that has been created for this thesis. The development was done in three successive steps. In the first step, two additional dimensionless parameters were derived to describe the near wall flow. These parameters are necessary because the dimensionless wall distance y^+, which is in principle a Reynolds number, is not sufficient to describe all the phenomena in a boundary layer with wall condensation. In a second step, the actual model of the flow is developed as an extension of Popovac's concept of the non-equilibrium factor described in section 3.1.4. Since analytical functions are no longer sufficient to describe the complex interacting phenomena of near wall flows in the wall condensation regime, an empirical approach is used for the model. This empirical approach is based on the experimental data from the SETCOM facility, supplemented by validated fine mesh simulation data where no experimental data are available as of yet. In a third step, the model is transferred into a mathematical formulation that makes it fast to compute, easy to extend and easy to implement into a CFD code. For this step, an approximation process based on radial basis functions is used. A detailed description of the three steps and an in depth discussion of their necessity can be found in the following three sub-sections. The integration of the new model into the CFD code ANSYS CFX is described in appendix C.

4.1. New non-dimensional Parameters

For flows with wall condensation, the dimensionless wall distance y^+ is no longer sufficient to fully describe the behavior of the boundary layers, as already mentioned. This can be seen, for example, from the dimensionless velocity profiles measured at the SETCOM facility [Allelein et al., 2019]. It is obvious that the velocity profiles shown in figure 4.1 deviate from the logarithmic law of the wall with increasing condensation influence and that the group of resulting profiles cannot be described exclusively by the parameter y^+. Without further parameters, an unambiguous description of the flow and thus its modeling is not possible.

Based on the discussion of the influence of condensation on the boundary layers in section 2.2 and the equations 2.8 to 2.11 it can be seen that at least two additional parameters are necessary to fully describe the behavior of the boundary layer. As discussed in section 2.2, both the influence of buoyancy and wall normal convection must be included in the boundary layer model. The fact that these two phenomena are the relevant ones will again become apparent in the following, where the two new parameters are derived from the mathematical model of the boundary layer described in section 2.2.

An additional constraint for the derivation of these parameters is, that the quantities used should be available from SETCOM measurements. In this way, the data from the facility can be used to derive, verify and validate the model. In addition, the quantities used must be available locally at the cell level during the CFD simulation to ensure that the wall functions can be implemented into ANSYS CFX and other CFD codes.

The new parameters must be non-dimensional in order to obtain a scalable model.

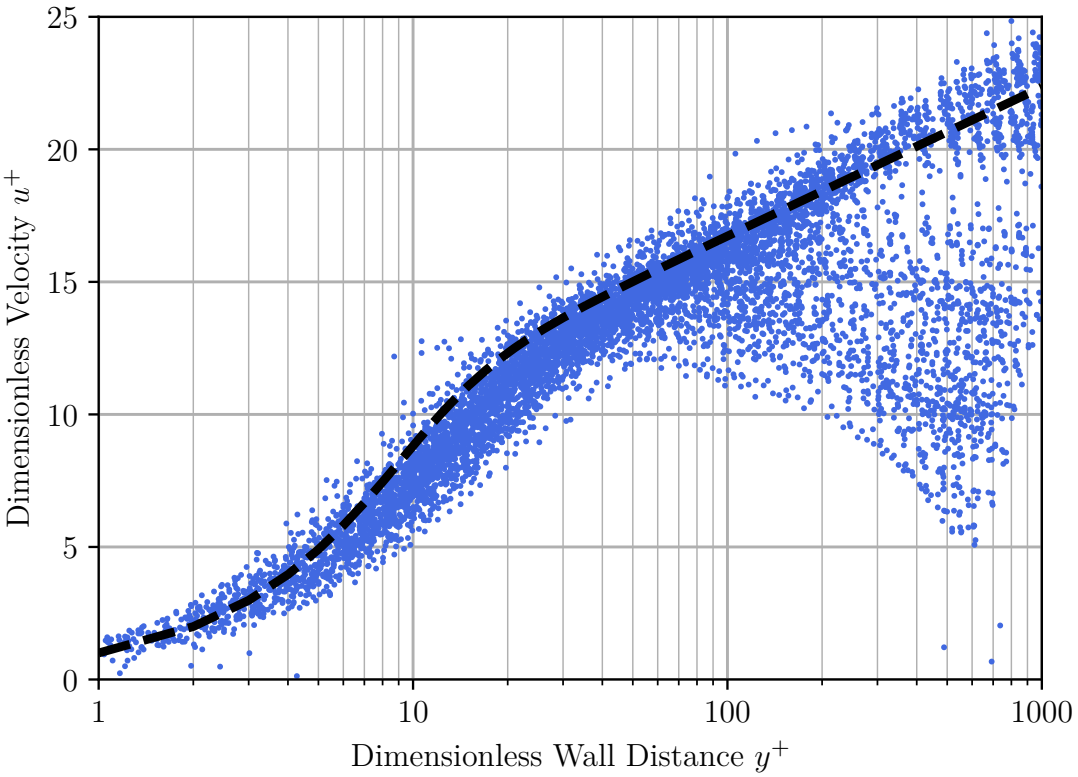

Figure 4.1: Dimensionless velocity profiles measured at the SETCOM facility as function of the dimensionless wall distance

Thus, the first step in finding the new parameters is to non-dimensionalize equations 2.9 to 2.11. This is done in the same way as described in section 3.1.2 for the logarithmic law of the wall and in section 3.1.3 for Kader's wall function. Additionally, eddy viscosity based models for the turbulent fluxes are introduced into the equation. This yields equations 4.1 to 4.3 as non-dimensional model of the condensing boundary layer.

$$\frac{\partial \frac{\rho u_n}{\rho_w u_\tau} u^+}{\partial y^+} = \frac{\partial}{\partial y^+}((1 + \frac{\mu_t}{\mu})\frac{\partial u^+}{\partial y^+}) + \frac{\mu(\rho g_p - \frac{\partial p}{\partial x_p})}{\rho_w^2 u_\tau^3} \tag{4.1}$$

$$\frac{\partial \frac{\rho u_n}{\rho_w u_\tau} \frac{c_p}{c_{p,w}} T^+}{\partial y^+} = \frac{\partial}{\partial y^+}((\frac{1}{Pr} + \frac{1}{Pr_t}\frac{\mu_t}{\mu}\frac{c_p}{c_{p,w}})\frac{\partial T^+}{\partial y^+}) \tag{4.2}$$

$$\frac{\partial \frac{\rho u_n}{\rho_w u_\tau} Y_s^+}{\partial y^+} = \frac{\partial}{\partial y^+}((\frac{1}{Sc} + \frac{1}{Sc_t}\frac{\mu_t}{\mu})\frac{\partial Y^+}{\partial y^+}) \tag{4.3}$$

However, the equations do not yet satisfy the above requirements. Thus, some additional modifications and assumptions have to be introduced. The first term requiring

modification is the wall normal convection ρu_n, which cannot be measured in the SETCOM facility. But the mass conservation equation for the boundary layer, as shown in equation 4.4, requires that the wall normal mass flow is constant. Thus, it must also be equal to the condensation mass flux density $\dot{m}''_{Cond}$ as the surface boundary condition for this equation. Consequently, the wall normal convection term can be replaced by the condensation mass flux density in equations 4.1 to 4.3 yielding equations 4.5 to 4.7.

$$\frac{\partial u_n}{\partial x_n} = 0 \tag{4.4}$$

$$\frac{\partial \frac{\dot{m}''_{Cond}}{\rho_w u_\tau} u^+}{\partial y^+} = \frac{\partial}{\partial y^+}((1 + \frac{\mu_t}{\mu})\frac{\partial u^+}{\partial y^+}) + \frac{\mu(\rho g_p - \frac{\partial p}{\partial x_p})}{\rho_w^2 u_\tau^3} \tag{4.5}$$

$$\frac{\partial \frac{\dot{m}''_{Cond}}{\rho_w u_\tau} \frac{c_p}{c_{p,w}} T^+}{\partial y^+} = \frac{\partial}{\partial y^+}((\frac{1}{Pr} + \frac{1}{Pr_t}\frac{\mu_t}{\mu}\frac{c_p}{c_{p,w}})\frac{\partial T^+}{\partial y^+}) \tag{4.6}$$

$$\frac{\partial \frac{\dot{m}''_{Cond}}{\rho_w u_\tau} Y_s^+}{\partial y^+} = \frac{\partial}{\partial y^+}((\frac{1}{Sc} + \frac{1}{Sc_t}\frac{\mu_t}{\mu})\frac{\partial Y^+}{\partial y^+}) \tag{4.7}$$

Even the local condensate mass flux density is not directly measured by SETCOM. It can be approximated from the total heat flux density $\dot{q}''_{\mathrm{Tot}}$ and the enthalpy of transformation at the wall surface $\Delta h_{t,w}$,assuming that the sensible heat flux $\dot{q}''_{\mathrm{Sen}}$ is small compared to the condensation heat flux $\dot{q}''_{\mathrm{Cond}}$ (see equation 4.8). Excluding the constant values from the partial differential for the wall normal convection yields equation 4.9 with the dimensionless heat flux $\dot{q}^+$ as the first of the two additional dimensionless parameters.

$$\dot{m}''_{Cond} = \frac{\dot{q}''_{Cond}}{\Delta h_{t,w}} \approx \frac{\dot{q}''_{Tot}}{\Delta h_{t,w}} \tag{4.8}$$

$$\underbrace{\frac{\dot{q}''_{Tot}}{\rho_w u_\tau \Delta h_{t,w}}}_{\dot{q}^+} \frac{\partial u^+}{\partial y^+} = \frac{\partial}{\partial y^+}((1 + \frac{\mu_t}{\mu})\frac{\partial u^+}{\partial y^+}) + \frac{\mu(\rho g_p - \frac{\partial p}{\partial x_p})}{\rho_w^2 u_\tau^3} \tag{4.9}$$

$$\underbrace{\frac{\dot{q}''_{Tot}}{\rho_w u_\tau \Delta h_{t,w}}}_{\dot{q}^+} \frac{\partial \frac{c_p}{c_{p,w}} T^+}{\partial y^+} = \frac{\partial}{\partial y^+}((\frac{1}{Pr} + \frac{1}{Pr_t}\frac{\mu_t}{\mu}\frac{c_p}{c_{p,w}})\frac{\partial T^+}{\partial y^+}) \tag{4.10}$$

$$\underbrace{\frac{\dot{q}''_{Tot}}{\rho_w u_\tau \Delta h_{t,w}}}_{\dot{q}^+} \frac{\partial Y_s^+}{\partial y^+} = \frac{\partial}{\partial y^+}((\frac{1}{Sc} + \frac{1}{Sc_t}\frac{\mu_t}{\mu})\frac{\partial Y^+}{\partial y^+}) \tag{4.11}$$

As can be seen from its derivation, the dimensionless heat flux $\dot{q}^+$ describes the wall normal convection induced by the wall condensation. Since this convection is directed towards the wall surface, a larger value of $\dot{q}^+$ also means a larger transport of momentum,

species-mass and energy towards the wall. Thus, an increase of $\dot{q}^+$ also increases the wall friction, the wall condensation mass flux, and the sensible heat transfer to the wall. The derivation also shows that $\dot{q}^+$ directly affects the transport equations for momentum, species-mass, and energy. This is not the case for the second new dimensional parameter, because its direct influence is limited to the momentum equation, as the following derivation will show. However, it can also have a great impact on the other two transport equations due to its influence on turbulence and the wall normal flow, as will be discussed in detail in section 5.1.

The second new dimensionless parameter is derived from the last term of equation 4.1. As can be seen from the equation, this term describes buoyancy, as defined by [Turner, 1973], as the difference between the local pressure gradient and the gravitational force on the fluid. More precisely, it describes the wall parallel part of the buoyancy force of the fluid, which acts as a momentum source or sink for the fluid. The wall normal buoyancy can also have a sizable influence on the flow as a source or sink of turbulence, but is only relevant for non vertical walls, which are not considered in this work due to a lack of experimental data.

Like the dimensionless heat flux, this term also contains two variables that cannot be determined directly from SETCOM experimental data: The local density and the local pressure gradient. The density can be approximated as the wall surface density ρ_w, which can be calculated from the wall temperature measurements assuming that the air is saturated with water at the wall surface. The local pressure gradient consists of a hydrostatic and a friction component. Since the friction pressure losses in the measurement section of the SETCOM facility are significantly smaller than the hydrostatic pressure gradient, the friction pressure loss can be neglected. The pressure gradient is therefore equal to the hydrostatic pressure gradient. Assuming that the condensation rate is small compared to the total mass flow, it can be calculated from the density at the inlet to the measuring section ρ_{In} and the acceleration due to gravity g_p. This results in equation equation 4.12 with the dimensionless gravity force FG^+.

$$\underbrace{\frac{\dot{q}''_{Tot}}{\rho_w u_\tau \Delta h_{t,w}}}_{\dot{q}^+} \frac{\partial u^+}{\partial y^+} = \frac{\partial}{\partial y^+}((1+\frac{\mu_t}{\mu})\frac{\partial u^+}{\partial y^+}) + \underbrace{\frac{\mu(\rho_w g_p - \rho_{In} g_p)}{\rho_w^2 u_\tau^3}}_{FG^+} \tag{4.12}$$

The definition of the two new parameters is also shown in equations 4.13 to 4.15. For the implementation in ANSYS CFX it is important to note that the assumption made for FG^+ regarding the pressure gradient is only valid in the SETCOM facility and can therefore only be used for the evaluation of the measurement results. For the transferability of the new wall function approach to other problems, the local pressure gradient must be used in the simulation. However, this is possible without limitations, since the pressure gradient is available locally on the cell level in CFX. It should be noted that for numerical reasons a part of the hydrostatic pressure gradient is subtracted from the pressure gradient based on a reference density ρ_{Ref} in CFX and therefore must be added to the pressure gradient when calculating FG^+ during the simulation.

$$\dot{q}^+ = \frac{\dot{q}''_{Tot}}{\rho_w u_\tau \Delta h_{t,w}} \tag{4.13}$$

$$FG^+_{Exp} = \frac{\mu(\rho_w g_p - \rho_{In} g_p)}{\rho_w^2 u_\tau^3} \tag{4.14}$$

$$FG^+_{Sim} = \frac{\mu(\rho_w g_p - (\frac{\partial p}{\partial x_p} + \rho_{Ref} g_p)}{\rho_w^2 u_\tau^3} \tag{4.15}$$

A first impression of the possibility to use the influence parameters derived from the differential equations to describe the influence of wall condensation on the boundary layers can be gained from figure 4.2. The figure shows the dimensionless velocity profile results of fine mesh simulations of four different SETCOM experiments. Simulation data are used to provided a clearer view on the results avoiding the influence of the stochastic error in the experimental results. The calculations have been specifically selected to show how the new dimensionless parameters allow to distinguish between the different profiles while the dimensionless wall distance y^+ would be insufficient in this regard. For the dimensionless gravity force FG^+ this possibility is very clear from the figure. This is because, the two curves with the larger FG^+ values have a distinct maximum while the other two curves are very similar to the standard wall function. Thus, an increase of the dimensionless gravity force FG^+ is associate with the behavior expected for an increase in buoyancy, which is the effect this factor aims to describe.

For the dimensionless heat flux $\dot{q}^+$ figure 4.2 shows a less pronounced influence on the dimensionless velocity profiles. Nevertheless, the figure shows that larger values of $\dot{q}^+$ lead to a decrease of the dimensionless velocity for both large and small values of the dimensionless gravity force FG^+. This is the expected behavior as larger values of the dimensionless heat flux $\dot{q}^+$ are associate with an increased flow in wall normal direction, also know as suction, which leads to a decrease in the dimensionless velocity as show by [Favre et al., 1966] and [Lehmkuhl, 2018], for example. Overall, the data shown in figure 4.2 are a first indication that the dimensionless parameters $\dot{q}^+$ and can be used in addition to y^+ to describe the influence of wall condensation on the boundary layers.

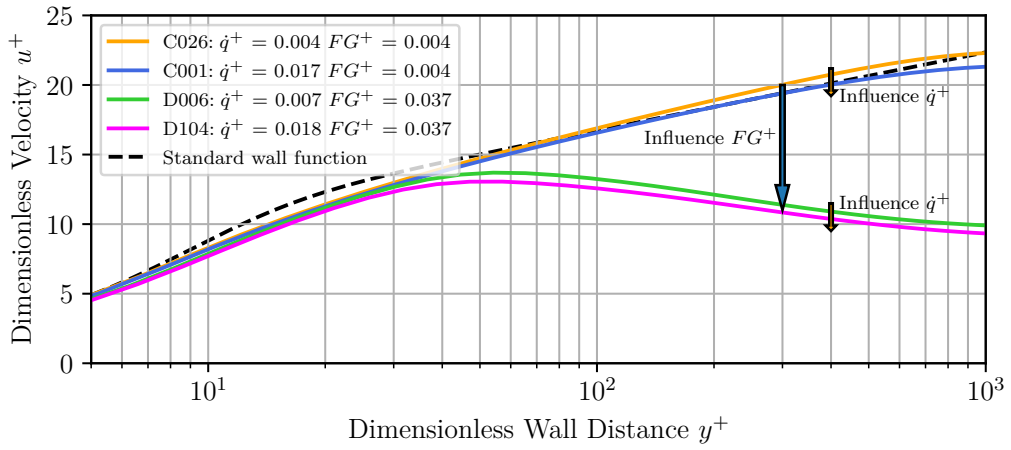

Figure 4.2: Dimensionless velocity profiles from fine mesh Simulations of four SETCOM experiments with different values for the dimensionless heat flux and gravity force

An overview of the influence of the newly derived dimensionless parameters on the dimensionless velocity of all SETCOM experiments is given in figure 4.3. Same as figure 4.1, the figure shows the dimensionless velocity profiles of all SETCOM experiments. Here, however, not only as a function of the dimensionless wall distance, but also of the dimensionless gravity force FG^+ and the dimensionless heat flux $\dot{q}^+$. While it is difficult to make out a specific profile in the large amount of data, the influences described in context of figure 4.2 can also be found for the whole set of experimental data presented in figure 4.3. Especially, the formation of the flow maximum with an increasing dimensionless gravity force FG^+ can well be seen from figure 4.3, while the impact of the dimensionless heat flux is more difficult to discern due to its less pronounced influence on the flow. Nevertheless, the data presented in figures 4.2 and 4.3 give a first indication that the newly derived influence factors can be used in combination with the dimensionless wall distance y^+ to fully describe the near wall flow in the wall condensation regime. Only such clear allocation of the behavior of the flow close to the wall on the basis of a sufficient number of influencing variables makes it possible to develop a model of this flow in the following. Further proof that the three selected influence factors suffice for this task is given in section 5.

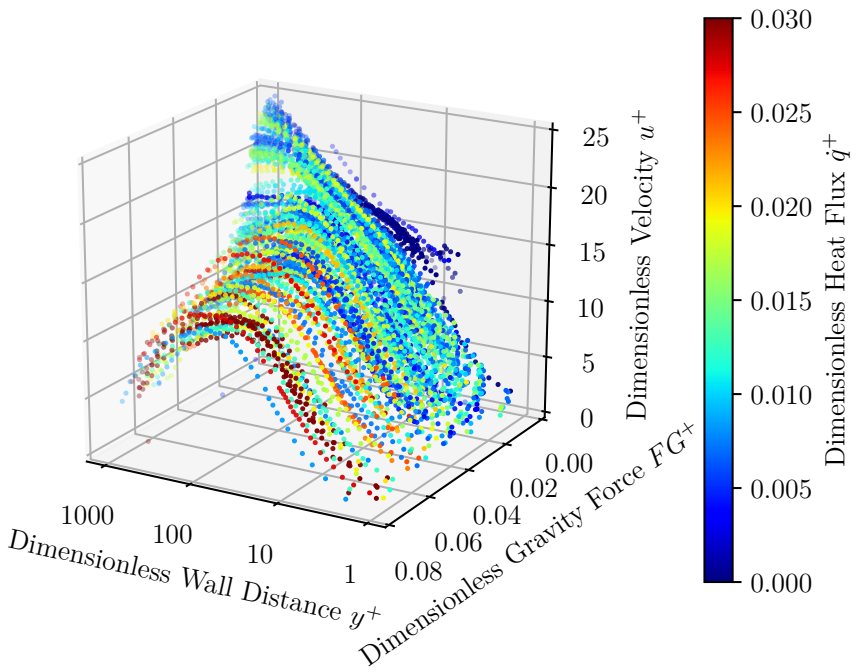

Figure 4.3: Dimensionless velocity profiles measured at the SETCOM facility as function of the dimensionless wall distance, gravity force and heat flux

4.2. Non-equilibrium Factors

The basis for the physical model of the boundary layers in the wall condensation regime is Popovac's concept of the non-equilibrium factor. This approach has several advantages. First, the log law and the corresponding models for heat- and mass-transfer are multiplied with the non-equilibrium factor. Thus, the these well known boundary layer models are retained in the overall model. Therefore, they can still be used for flow conditions where they are applicable and provide a fallback model when the limits of applicability of the new model are exceeded. Second, there are multiple possible ways to derive a physical model for the non-equilibrium factors (e.g. directly from first principles or empirically from measurement data) and also multiple ways to introduce them into a CFD code (e.g. as an analytical function or table). Third, the author [Müller et al., 2016] has already shown that Popovac's approach yields improved results in the forced convection flow regime. However, Popovac's original approach fails in mixed and natural convection flows for several reasons.

The first reason for the failure of Popovac's approach in these regimes is the influence of buoyancy and the wall normal mass transfer on the boundary layer, as discussed in sections 2.2, 3.1.4 and 4.1. In contrast to the forced convection flow, these influences play a much larger role in the wall normal transport processes in the natural and

mixed convection regime. Thus, Popovac's assumption of a constant non-equilibrium factor across the whole boundary layer is no longer applicable. As a consequence, the equations 4.1 to 4.3 describing the flow form a system of second order nonlinear partial differential equations. For such a system it is no longer possible to give a closed, analytical solution.

The second reason why Popovac's model is no longer applicable in buoyancy driven flows is the turbulence model used to solve the basic equations. Since the turbulence in the actual sense is a velocity fluctuation, a length and a time scale are needed for its description. From equation 3.3 it can be seen that the algebraic turbulence model used in the log-law uses the wall distance Δx_n as the length measure and the velocity gradient $\partial u_p / \partial x_n$ as the time measure. However, this time measure causes the modeled turbulence to become zero at the velocity maximum of a flow with buoyancy close to the wall. This behavior contradicts both the experimental observations [Allelein et al., 2019] and the results of simulations performed with a two-equation turbulence model. Other algebraic turbulence models for near-wall flow, such as that of Cebecci [Cebeci, 1970], typically use the same time and length scales and therefore cannot be used either, especially since this only slightly more complex model already leads to the fact that the boundary layer equations can no longer be solved analytically.

Since an algebraic modeling of the non-equilibrium factors for the mixed convection regime is not possible for these reasons, an empirical approach was used in this work. For the velocity wall function, measurement data from the SETCOM facility were used to derive the non-equilibrium factors. While the goal was to use experimental data for the other wall functions as well, the amount of available data is not sufficient as of yet. Hence, for the temperature, species and turbulence wall functions, data from validated fine mesh simulations were used as a supplement. The calculation of the non-equilibrium factors Ψ for the respective wall function was carried out on the basis of equation 4.16 to equation 4.18, whereby the index SWF stands for the respective standard wall function. The equations shown in table 4.1 have been used as standard wall functions. Thus, the definition of the non-equilibrium factors deviates slightly from that given in equation 3.36. However, this has the advantage that the transition area between the viscous sublayer and the turbulent layer of the boundary layer is also covered by the model.

$$\Psi_u = \frac{u^+}{u^+_{SWF}} \tag{4.16}$$

$$\Psi_T = \frac{T^+}{T^+_{SWF}} \tag{4.17}$$

$$\Psi_Y = \frac{Y^+_s}{Y^+_{s,SWF}} \tag{4.18}$$

Table 4.1: Overview of the new wall function approach

Property	Layer-wise formulation	Blending and non-equilibrium factor
Momentum (wall parallel)	sub-layer: $u_v^+ = y^+$ log-layer: $u_t^+ = \frac{1}{0.41} ln(y^+) + 5.5$	$u^+ = \Psi_u \sqrt[4]{\frac{1}{\frac{1}{{u_v^+}^4} + \frac{1}{{u_t^+}^4}}}$
Energy	sub-layer: $T_v^+ = Pr\ y^+$ log-layer: $T_t^+ = 2.12\ ln(y^+) + \beta(Pr)$ $\beta(Pr) = (3.85\ Pr^{\frac{1}{3}} - 1.3)^2 + 2.12\ ln(Pr)$	$T^+ = \Psi_T \sqrt[4]{\frac{1}{\frac{1}{{T_v^+}^4} + \frac{1}{{T_t^+}^4}}}$
Steam mass fraction	sub-layer: $Y_{s,v}^+ = Sc\ y^+$ log-layer: $Y_{s,t}^+ = 2.12\ ln(y^+) + \beta(Sc)$ $\beta(Sc) = (3.85\ Sc^{\frac{1}{3}} - 1.3)^2 + 2.12\ ln(Sc)$	$Y_s^+ = \Psi_Y \sqrt[4]{\frac{1}{\frac{1}{{Y_{s,v}^+}^4} + \frac{1}{{Y_{s,t}^+}^4}}}$
Turbulent kinetic energy	whole boundary layer: $\frac{\partial k}{\partial x_n} = 0$	
Turbulent eddy frequency	sub-layer: $\omega_v = \frac{6\mu}{\beta \Delta x_n^2}$ log-layer: $\omega_t = \frac{u_\tau^2}{a_1 \kappa \mu y^+}$	$\omega = \omega_t \sqrt{1 + (\frac{\omega_v}{\omega_t})^2}$

Figure 4.4 shows some examples that illustrate how the deviations from the standard wall function due to the influence of wall condensation can be represented in form of non-equilibrium factors. For this purpose figure 4.4 shows four dimensionless velocity profiles, the same as already presented in figure 4.2, and the corresponding non-equilibrium factors Ψ_u. As the figure shows the standard wall function has a constant non-equilibrium factor of one and the non-equilibrium factors resulting from the other non-dimensional velocity profiles vary around this value. This is because the non-equilibrium factors are calculated by dividing the actual non-dimensional profile of the given variable by the value of the standard wall function.

Figure 4.4 shows that the impact of the non-dimensional gravity force FG^+ and non-dimensional heat flux $\dot{q}^+$ have on the non-equilibrium factor increases with the wall distance. This is especially prominent for the two exemplary cases with a high FG^+. For these two cases, a strong decrease of the non-equilibrium factor above a y^+ of 30 can be observed, which is associated with the formation of the velocity maximum close to the wall surface. Meanwhile, the curves for the two cases with lower FG^+ stay close to a non-equilibrium factor of one even for high values of y^+. Similar to the observations made in context of figure 4.2 it can be observed again that the impact of $\dot{q}^+$ is comparatively small in the investigated parameter range.

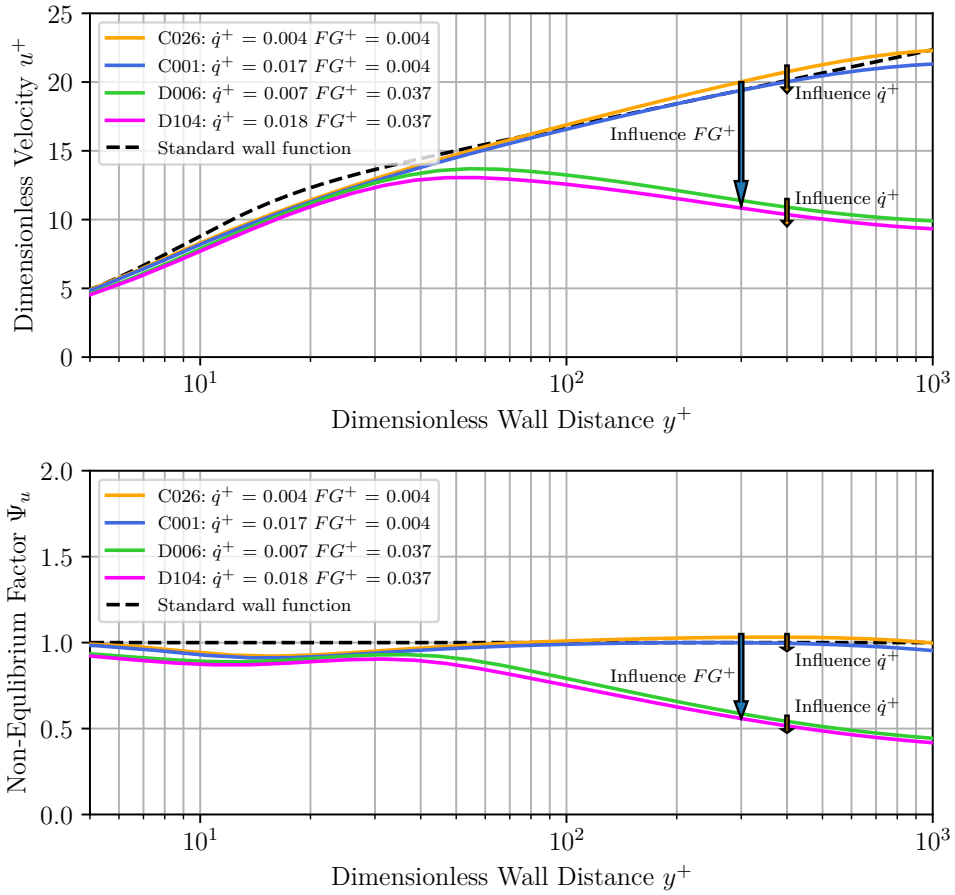

Figure 4.4: Dimensionless velocity profiles from fine mesh simulations of four SETCOM experiments with different values for the dimensionless heat flux and gravity force and the resulting non-equilibrium factors Ψ_u

The behavior of the non-equilibrium factors of the temperature and species wall functions show some important differences compared to those of the velocity wall function. For example, they increase with FG^+ and a decrease with $\dot{q}^+$, as can be exemplary seen for the non-equilibrium factor of the temperature wall function in figure 4.5. Meanwhile, the non-equilibrium factors for the velocity wall function exhibit a decrease with both of the new model parameters, as already discussed in context of figure 4.4. The reason for this are the different influences of buoyancy on the boundary layers as explained in section 2.2 and seen from equations 2.8 to 2.11. The velocity boundary layer is directly influenced by buoyancy, which acts as a momentum source or sink. Meanwhile, the influence of buoyancy on the temperature and steam mass boundary layer is mostly indirect via the buoyancy influence on turbulence and the wall normal flow. Thus, the observed difference between the non-equilibrium factors for the velocity on the one hand and the factors for temperature and steam mass on the other hand seems reasonable. A

detailed analysis of the behavior of the non-equilibrium factors and their influence on the flow is given in section 5.1.

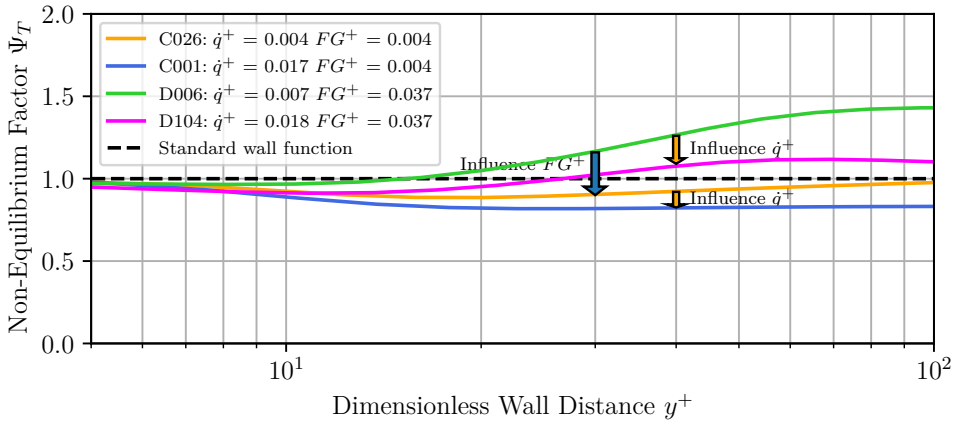

Figure 4.5: Non-equilibrium factors Ψ_T from fine mesh simulations of four SETCOM experiments with different values for the dimensionless heat flux $\dot{q}^+$ and gravity force FG^+

An overview of the input data used for the model as well as the resulting non-equilibrium factors is given in figure 4.6 for the velocity, in figure 4.7 for the temperature, and in figure 4.8 for the steam species wall function. The figures show the limits of the input data and thus also the limits of the applicability of the final model. For y^+ a lower limit of 5 was selected because the SETCOM data are too noisy below this limit. An upper limit of 100 was chosen for y^+ to cover a sufficiently large part of the boundary layer while certainly avoiding the wake area of the boundary layer that marks the transition to the main flow. For $\dot{q}^+$ a lower limit of 0 and an upper limit of 0.03 were chosen based on the data range provided by the SETCOM experiments. For FG^+ a data range of 0 to 0.08 is used for Ψ_u and 0 to 0.06 for Ψ_T and Ψ_Y. This results from the different maximum values obtained for FG^+ in the experimental and numerical input data for the model.

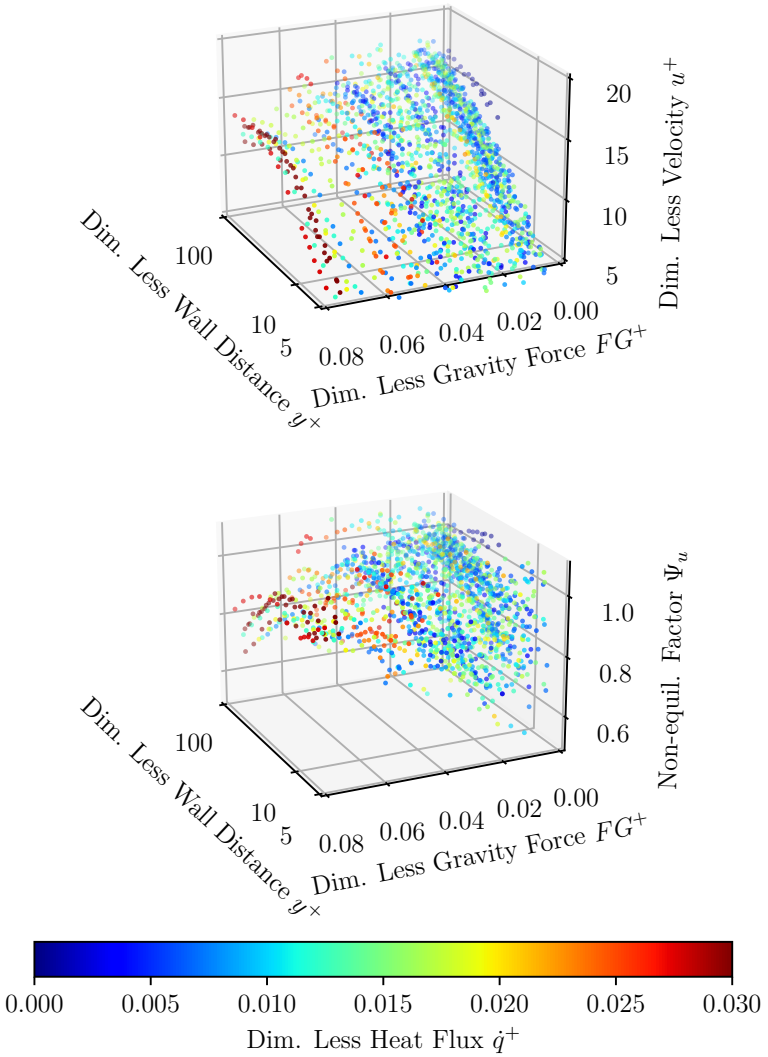

Figure 4.6: Model input data and the resulting non-equilibrium factors for the dimensionless velocity u^+

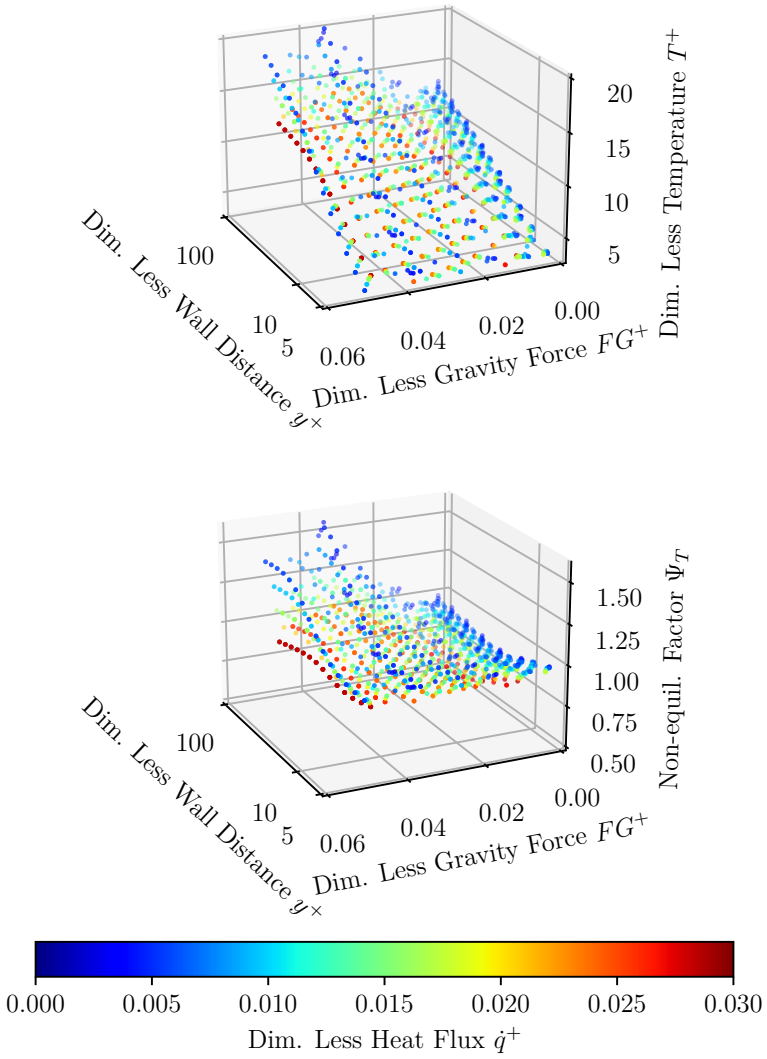

Figure 4.7: Model input data and the resulting non-equilibrium factors for the dimensionless temperature T^+

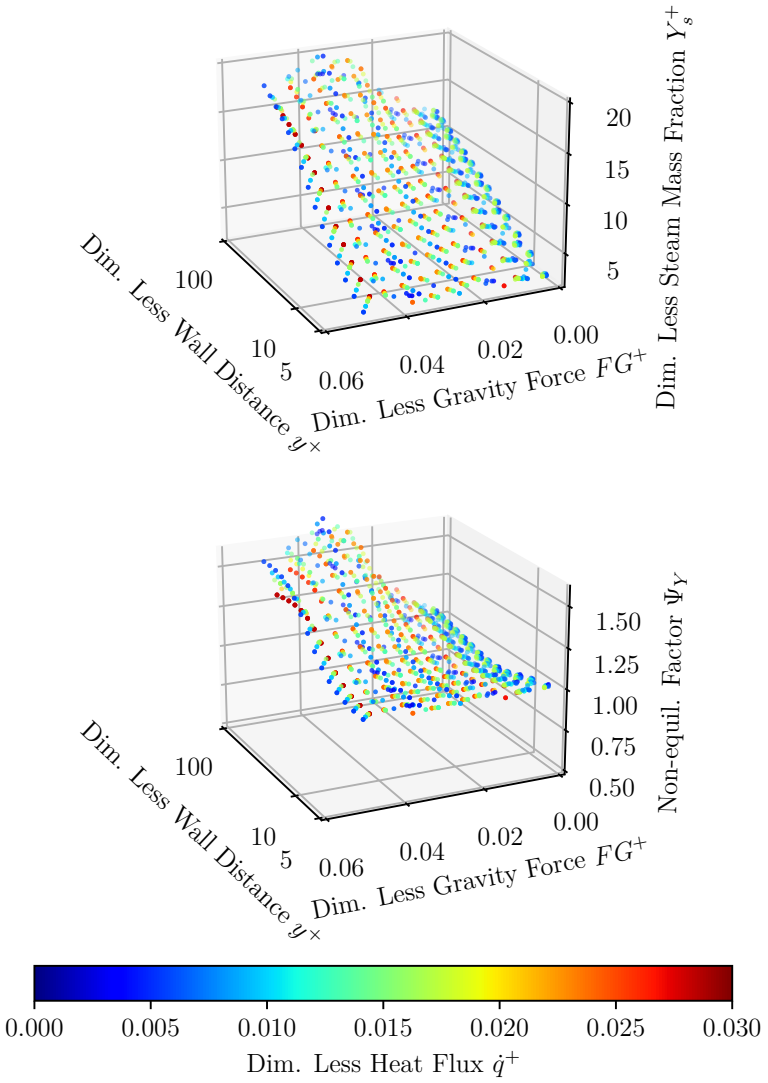

Figure 4.8: Model input data and the resulting non-equilibrium factors for the dimensionless steam mass fraction Y_s^+

One important trend for the non-equilibrium factors in the buffer layer can be seen

from figure 4.6 to figure 4.8. In the buffer layer, ranging from y^+ 5 to 30, it can be observed that most of the non-equilibrium factors are below one for all three boundary layers. Figure 4.9 shows this exemplary for all non-equilibrium factors of the temperature wall function located in the buffer layer. This behavior can be observed even for the non-equilibrium factors at small values of $\dot{q}^+$ and FG^+ and thus negligible influence of suction and buoyancy. This indicates a suboptimal performance of the models given in table 4.1 in this area of the flow, because under optimal conditions, non-equilibrium factors of 1 should be obtained. The poor performance of the models can be attributed to the fact that they are heavily influenced by the blending in this area which is a purely mathematical model with no physical background. However, the error introduced into the models by the blending is actually corrected by the introduction of the non-equilibrium factors. Thus, the small non-equilibrium factors in the buffer layer actually indicate a first improvement due to the model developed for this thesis.

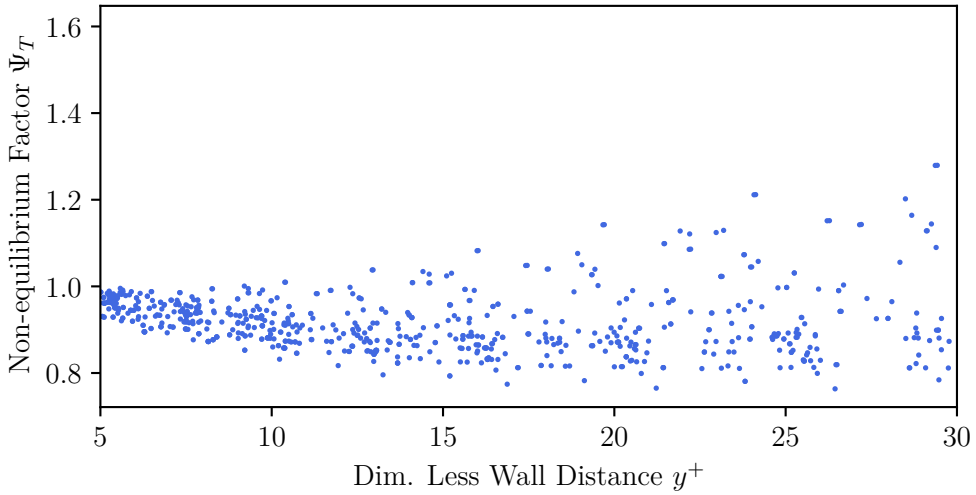

Figure 4.9: Non-equilibrium factors for the dimensionless temperature T^+ in the buffer layer

One important aspect of the boundary layer, namely turbulence, is not modeled via the non-equilibrium factors, as can be seen from table 4.1 and the preceding figures. Instead, a different approach was chosen for two reasons. First, no model covering the whole boundary layer could be found for the turbulent kinetic energy. Instead, a simple zero flux boundary condition is used. Second, while a model covering the whole boundary layer is available for the turbulent eddy frequency, the CFD code ANSYS CFX used for this work does not provide an interface to alter the turbulent eddy frequency at the wall surface. Additionally, it is important to have a coherent model for the turbulent kinetic energy and eddy frequency, because in two-equational turbulence models only their combination influences the flow in form of the eddy viscosity.

Consequently, a different modeling approach was chosen to describe and influence the eddy viscosity μ_t in the cell at the wall surface. To achieve this, the eddy viscosity ratio

μ_t^+, as described in equation 4.19, has been extracted from the fine mesh simulations as a function of y^+, $\dot{q}^+$, and FG^+. Four exemplary results of this process are shown in figure 4.10. The figures shows that the eddy viscosity ratio μ_t^+ decrease with increasing $\dot{q}^+$, and FG^+, similar to the dimensionless velocity. However, in contrast to the dimensionless viscosity, the eddy viscosity ratio is already well below its standard wall function for small values of FG^+ and $\dot{q}^+$, thus showing the huge influence the phenomena described by this factors have on turbulence. As can be seen in the figure, especially the dimensionless gravity force, and thus buoyancy, has a strong influence on turbulence. Therefore, a dedicated turbulence model is needed.

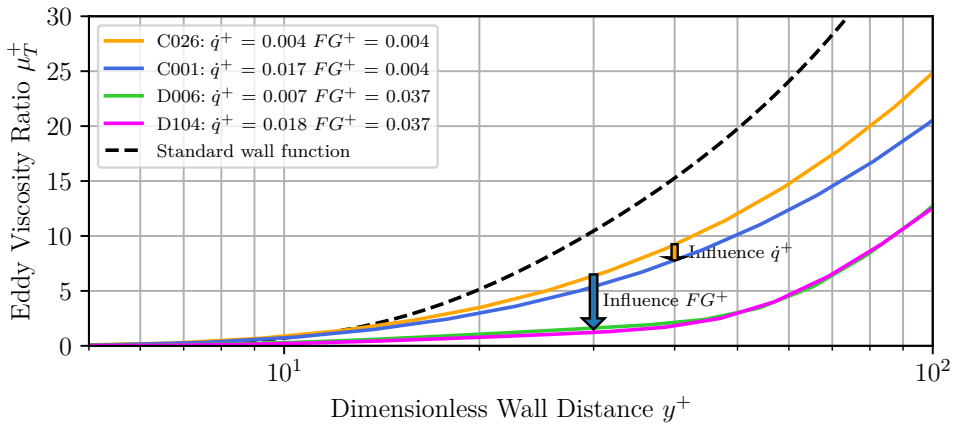

Figure 4.10: Dimensionless eddy viscosity μ_T^+ for the boundary layer model derived from fine mesh simulations of four SETCOM experiments with different values for the dimensionless heat flux $\dot{q}^+$ and gravity force FG^+

The resulting data field for the eddy viscosity ration μ_t^+ is visualized as an overview in figure 4.11. Figure 4.11 most importantly shows that the drop of the turbulence due to FG^+ is limited to the center of the application range of the new model and that the turbulence rises again for higher values of FG^+. This behavior of the turbulence will be discussed further in section 5.1.

$$\mu_t^+ = \frac{\mu_t}{\mu} \tag{4.19}$$

While there is an interface to directly transfer the results of the velocity, temperature and species wall function into ANSYS CFX, there is no such interface for the eddy viscosity. Hence, a different approach than described for the first three quantities in section 4.3 is needed for the eddy viscosity. As described above, the eddy viscosity is calculated from the combination of the turbulent kinetic energy and eddy frequency and ANSYS CFX only provides an interface for the turbulent kinetic energy. Therefore, a PID controller is used to regulate a source term for the turbulent kinetic energy in such a way that the modeled eddy viscosity ratio is achieved at the given turbulent eddy

frequency, similar to what Kelm [Kelm, 2010] did for the condensation mass flux in his condensation model by adjusting the steam partial pressure to the saturation pressure. However, this approach always led to instabilities in the simulations and consequently could not be used for the validation calculations presented in this work. Nevertheless, the model for the eddy viscosity ratio is available for the implementation of the new model in other CFD codes.

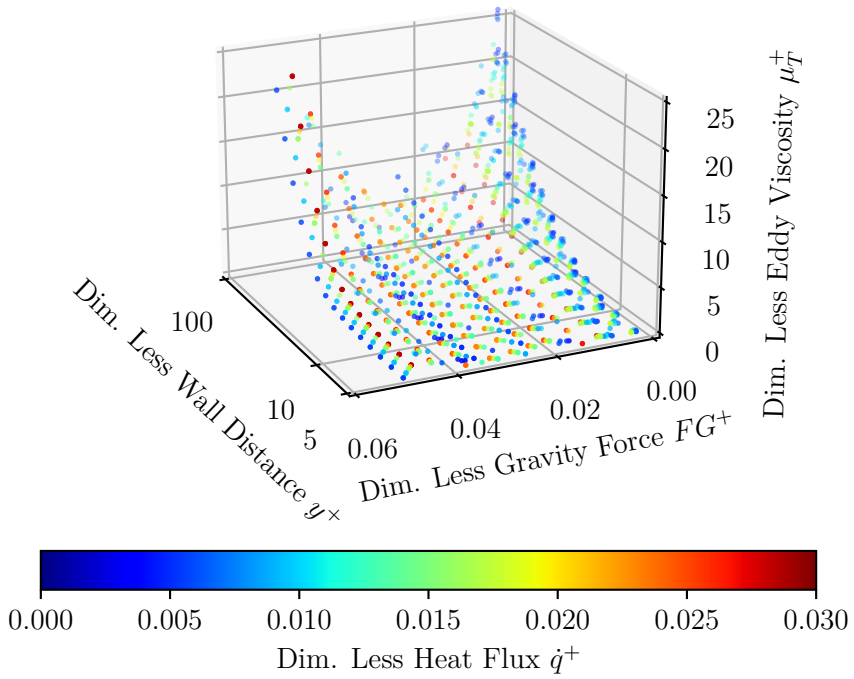

Figure 4.11: Dimensionless eddy viscosity μ_T^+ derived for the boundary layer model

4.3. Implementation via Radial Basis Functions

The integration of the non-equilibrium factors obtained from the measurement results and simulation data was performed using an approximation function based on so-called radial basis functions. The use of an approximation method is necessary because the non-equilibrium factors are only available at discrete data points. For the simulation, however, a continuous description of the flow behavior is necessary. The use of an approximation function has some advantages over other methods, such as the use of tabulated data with a local interpolation at the run time of the simulation. For example, it is computationally

more efficient, especially for multivariate problems, the approximation function only has a comparatively small memory requirement and is simple to parallelize.

The general description of an approximation function $P_f(\vec{x})$ for a linear approximation problem is shown in equation 4.20. The function results from a sum of n so-called base functions B_k which depend on the vector $\vec{x}$ and are multiplied by a constant coefficient c_k. The vector $\vec{x}$ describes the variables on which the function depends. In the case of the newly developed wall function approach, these are y^+, FG^+, and $\dot{q}^+$. The base function B_k is an arbitrary function that is suitable for modeling the approximation problem. In a simple and one-dimensional case this is for example the function x^{k-1}, which leads to an approximation polynomial. For the solution of the approximation problem with r data points x and data y, only the coefficients c_k have to be determined by solving the linear equation system described in equation equation 4.21. It should be noted that an exact solution of the problem is possible only for the case r equal to n. In all other cases the system of equations is underdetermined or overdetermined. In the underdetermined case there are infinitely many equivalent solutions for the problem and in the overdetermined case only an approximate solution can be calculated, for example, by means of the least squares method.

$$P_f(\vec{x}) = \sum_{k=1}^{n} c_k B_k(\vec{x}) \tag{4.20}$$

$$\begin{pmatrix} B_1(\vec{x}_1) & B_2(\vec{x}_1) & \cdots & B_n(\vec{x}_1) \\ B_1(\vec{x}_2) & B_2(\vec{x}_2) & \cdots & B_n(\vec{x}_2) \\ \vdots & \vdots & \ddots & \vdots \\ B_1(\vec{x}_r) & B_2(\vec{x}_r) & \cdots & B_n(\vec{x}_r) \end{pmatrix} \begin{pmatrix} c_1 \\ c_2 \\ \vdots \\ c_n \end{pmatrix} = \begin{pmatrix} y_1 \\ y_2 \\ \vdots \\ y_r \end{pmatrix} \tag{4.21}$$

Since the description of the boundary layers in the wall condensation regime is a multivariate problem, a simple approximation by means of a polynomial fit is not possible. From a mathematical point of view, this is a consequence of the so-called Mairhuber-Curtis theorem [Fasshauer, 2007]. As a consequence, for a well-defined multivariate approximation problem, the basis functions B_k (see equation equation 4.20) for the approximation must be dependent on the data locations. One possibility to meet the requirements of the Mairhuber-Curtis theorem is to use the distance from the approximation point $\vec{x}$ to the data locations $\vec{x}_k$ as input variable for the basis function B_k, as shown in equation equation 4.22. This leads to what is called approximation with radial basis functions (RBFs). The basis functions are called radial because they have a constant value for a given radius around the data locations. The RBF concept is used by the newly developed wall function approach.

$$P_f(\vec{x}) = \sum_{k=1}^{n} c_k B_k(||\vec{x} - \vec{x}_k||_2) \tag{4.22}$$

The approximation functions for the non-equilibrium factors were calculated with the Octave software package [Eaton et al., 2016]. The flow chart in figure 4.12 illustrates the procedure for this calculation. First, the experimental data must be read in and

the non-equilibrium factors must be calculated according to equations 4.16 to 4.18. The input variables of the functions y^+, FG^+, and $\dot{q}^+$ are then scaled using equation 4.23. This is necessary because the distances of the data points in the direction of the latter two variables are approximately 1000 times smaller than the distances in the direction of y^+. For a numerically stable and accurate approximation with RBFs, the distances of the data points in all directions should be within the same order of magnitude.

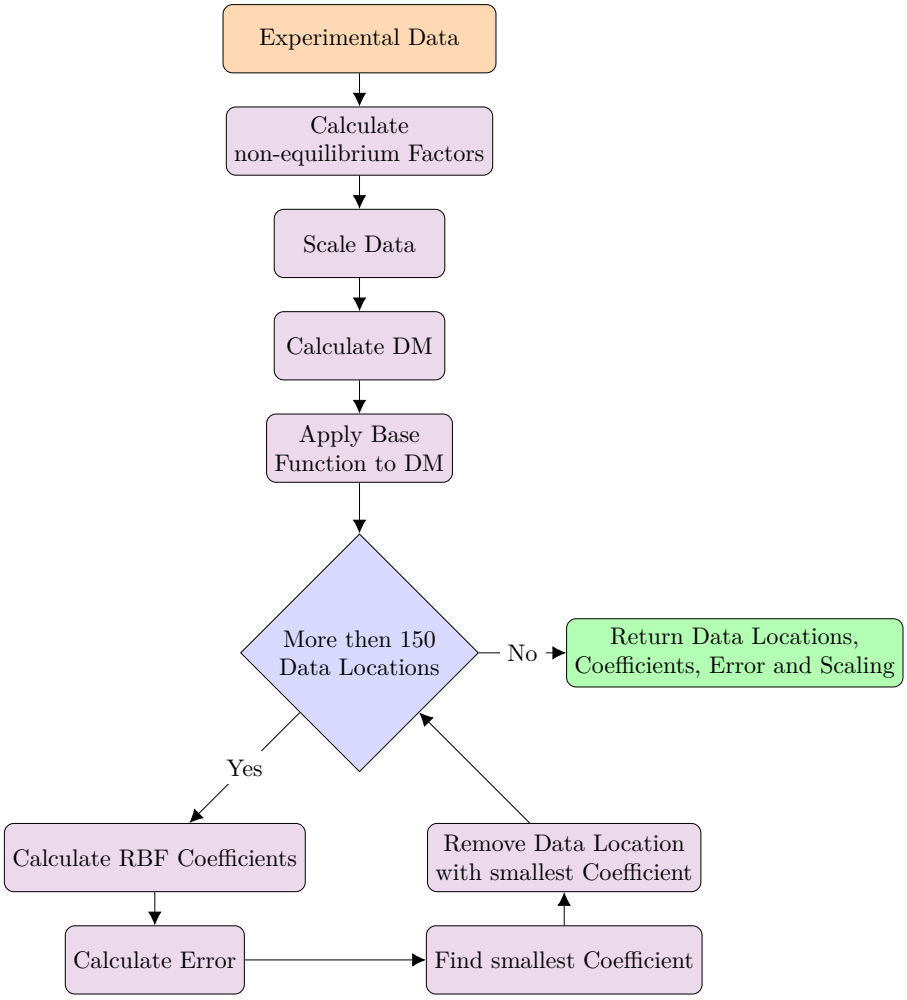

Figure 4.12: Flowchart of the calculation of the approximation function

$$\tilde{\Phi} = \frac{\Phi - \Phi_{Min}}{\Phi_{Max} - \Phi_{Min}} \tag{4.23}$$

In the next step, the so-called distance matrix DM is calculated from the scaled experimental data. This matrix contains the distance of all experimentally determined

data locations from each other according to the pattern shown in equation 4.24. The data set for the calculation of the newly developed wall function approach contains approx. 3400 data points, so that the distance matrix contains a total of approx. 11.4 million entries. The basis function is then applied to all entries of the distance matrix to obtain the collocation matrix CM, as shown in equation 4.25, which is used to calculate the RBF coefficients.

The basis function used for the new wall function approach is given in equation 4.26. As can be seen from the equation, the basis function limits the distance in which one data point $\vec{x}_k$ can influence the overall approximation function. This influences the quality of the approximation and also offers the possibility to let the approximation function return to the standard wall function outside of its applicability range. The range of the basis function is influenced by the scaling factor ϵ, which is set to $2/\sqrt{3}$ for the new wall function approach. Thus, the influence of one data location is limited to half of the diagonal of the unit cube formed by the scaled input data.

$$DM = \begin{pmatrix} ||x_1 - x_1||_2 & ||x_1 - x_2||_2 & \cdots & ||x_1 - x_n||_2 \\ ||x_2 - x_1||_2 & ||x_2 - x_2||_2 & \cdots & ||x_2 - x_n||_2 \\ \vdots & \vdots & \ddots & \vdots \\ ||x_n - x_1||_2 & ||x_n - x_2||_2 & \cdots & ||x_n - x_n||_2 \end{pmatrix} \tag{4.24}$$

$$CM = B(DM) \tag{4.25}$$

$$B(\vec{x}) = max(0, 1 - \epsilon||\vec{x} - \vec{x}_K||_2)^2 \tag{4.26}$$

In the next part of the calculation, the number of data locations used in the approximation function is reduced step by step. However, this does not explicitly mean that the number of data or data locations used for the approximation is reduced. There are two reasons for this procedure. First, the time to calculate the non-equilibrium factors Ψ using the approximation function scales linearly with the number of data locations in the function. Therefore, by reducing the number of data locations, the calculation can be significantly accelerated. Second, by reducing the number of data locations used in the function, a smoothing of the function is achieved, since not all experimentally determined non-equilibrium factors need to be exactly described by the function. This basically means that the function has an error compared to the data. It should be noted, however, that the experimental data themselves are afflicted with a stochastic error that can be partially compensated by the described approach to smooth the function. However, care was taken to ensure that the median relative error of the function with respect to to the input data does not exceed 5 %.

To reduce the number of data locations, a so-called "Knot Removal" algorithm is used [Fasshauer, 2007]. In the context of this thesis, the data locations used in the approximation function were reduced from approx. 3400 to 150. The general sequence of the "Knot Removal" algorithm is shown in the lower part of Figure figure 4.12. At the beginning of a run of the algorithm, the approximation problem is first solved by calculating the RBF coefficients. For this purpose, the inverse or pseudoinverse of the matrix CM must be formed in order to solve the linear equation system (see equation

equation 4.21). The so-called singular value decomposition of the matrix is used as a numerically efficient method, as for example described by Golub [Golub et al., 1965]. The solution of the approximation function at the data locations is then calculated by multiplying the matrix CM by the previously calculated coefficients. From this, the error Err in the current iteration step can be calculated on the basis of equation 4.27.

$$Err = \frac{|\Psi_{input} - CM\vec{c}|}{\Psi_{input}} \tag{4.27}$$

In the next step of the algorithm, the data location to be removed from the approximation function must be selected. The best solution is to remove the knot with the smallest coefficient c_k and thus removing the part of the approximation function that contributes the least to the approximation result. The corresponding data location is then deleted from the list of data locations used for the approximation function and the column corresponding to the data location is removed from the collocation matrix. This procedure is repeated until the number of data locations used in the approximation function is reduced to 150. When this goal is reached, the program outputs the results necessary for the implementation of the approximation function in CFX, i.e. the coefficients, the data locations used in the function and the scaling variables. The data locations, RBF coefficients and scales used for this thesis can be found in appendix B.

With this process, the goal of a median error of less than 5% has been achieved. A detailed breakdown of the error is given in table 4.2, which presents the 25%, 50%, 75% and 100% quantiles of the relative error between the input data and the approximation functions. For example, the table shows that 50 % of the non equilibrium factors of the temperature wall function are described by the corresponding approximation function with a relative error of 0.379 % or less and that 75 % of the data point are described by this function with an error 0.726 % or less.

Table 4.2: Distribution of the relative error of the RBF approximation

Non equilibrium factor	25% quantile	50% quantile	75% quantile	100% quantile
Velocity	2.04%	4.72%	8.73%	71.6%
Temperature	0.161%	0.379%	0.726%	6.47%
Species	0.241%	0.507%	0.898%	6.34%
Turbulence	0.657%	2.72%	11.4%	771.98%

Overall, table 4.2 shows that the approximation functions for the temperature and steam species non equilibrium factors exhibit very good results with 75% of the errors below 1% and a maximum error of less than 6.5%. Expectedly, the non-equilibrium factors for the velocity wall function show a larger error with all quantiles above 1%. This is because the experimental data used as input for the approximation are afflicted with a stochastic error (see e.g. figure 4.1). One goal was to smooth out this stochastic error through the approximation process, similar to a least squares approximation, therefore accepting larger errors between the input data and the approximation function. The data

for the turbulence wall function also show larger errors in the 75% and the 100% quantiles. This is due to the fact that the input data for the approximation of this function spans four orders of magnitude, while the data for the other functions stayed in the same order of magnitude. Thus, an absolute error of relatively minor magnitude in most of the input data area leads to a large relative error in a small part of this area where the data points of the smallest magnitude reside. This effect proved to be difficult to avoid in the approximation process. Nevertheless, the data in table 4.2 show that the approximation functions match well with most of the data points used in their generation.

5. Verification and Validation

In the following, the verification and first validation efforts for the new wall function approach are presented. As a first step, a qualitative assessment of the new wall function is performed regarding the expected behavior of the boundary layers. In a second step, coarse mesh simulations of the SETCOM experiment with the standard and the new wall function are compared with fine mesh best estimate simulations of these experiments. Finally, coarse mesh simulations of the TOSQAN ISP47 and THAI HM2 experiments utilizing the new wall function are compared to the experimental results as well as fine mesh best estimate simulations.

5.1. Qualitative analysis of the new wall function

As a first step of the validation of the new wall function approach, a qualitative analysis of the model results is presented in the following. As a basis for the analysis, the physically expected behavior of the near wall flow will be described, based on a brief but comprehensive summary of the data presented in sections 2 to 4. Then, a global overview of the results of the approximation functions is presented and assessed based on these expectations. Finally, the behavior of the model in some specific situations is evaluated.

As CFD codes typically use wall functions to calculate the wall fluxes, the first step in understanding how a wall function should behave is to understand how the non-dimensional velocity u^+, the non-dimensional temperature T^+ and the non-dimensional steam mass fraction Y_s^+ influence the wall fluxes and vice versa. This understanding can easily be gained by looking at the equations 3.9, 3.25 and 3.26. The equations immediately show, that the non-dimensional quantities are inversely proportional to their associated wall flux (or the square root of the wall flux in case of u^+). For example, an increase of T^+ above the value given by Kader's wall function would yield a decrease in the wall heat flux under otherwise constant boundary conditions. A qualitative depiction of this behavior is shown in figure 5.1. In summary, this means that any effect which increases a wall flux would decrease the corresponding non-dimensional quantity, and any effect which decrease the wall flux increase the corresponding non-dimensional quantity. The preceding statement is also true if the roles of the wall flux and non-dimensional quantities are switched. This also means that a non-equilibrium factor Ψ less than one leads to an increase of the associated wall flux and a non-equilibrium factor larger than one leads to a decrease of the associated wall flux.

The new wall function approach includes the influence of two condensation induced effects, buoyancy and suction. Consequently, the influence of these effects on the non-dimensional profiles has to be assessed for the qualitative analysis of the wall function. The suction effect is a wall normal flow directed towards the wall induced by condensation, as described in section 2. Consequently, more momentum, heat, and steam mass is transported towards the wall surface, and thus the wall fluxes increase. Therefore, the profiles of the non-dimensional velocity u^+, temperature T^+ and steam mass fraction Y_s^+ are decreased by the suction effect. A qualitative depiction of this effect is shown in figure 5.2 for the non-dimensional velocity. Experimentally, this behavior has been

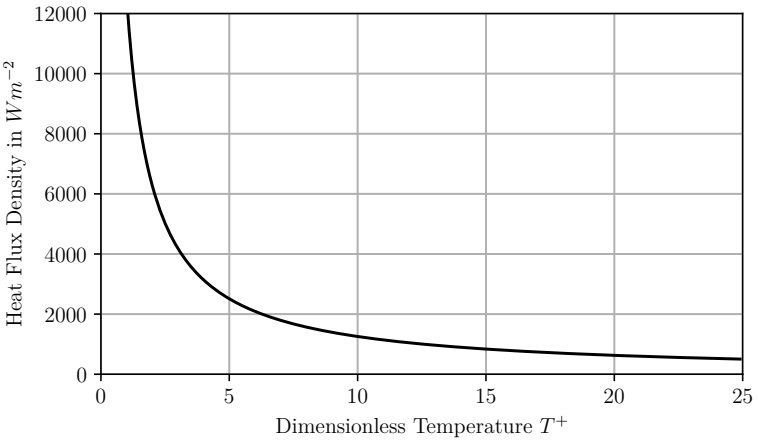

Figure 5.1: Qualitative depiction of the influence of the non-dimensional temperature T^+ on the wall heat flux density under otherwise constant boundary conditions

proven by Favre [Favre et al., 1966] for the non-dimensional velocity u^+ and theoretically as well as numerically it has been investigated by Lehmkuhl [Lehmkuhl et al., 2016].

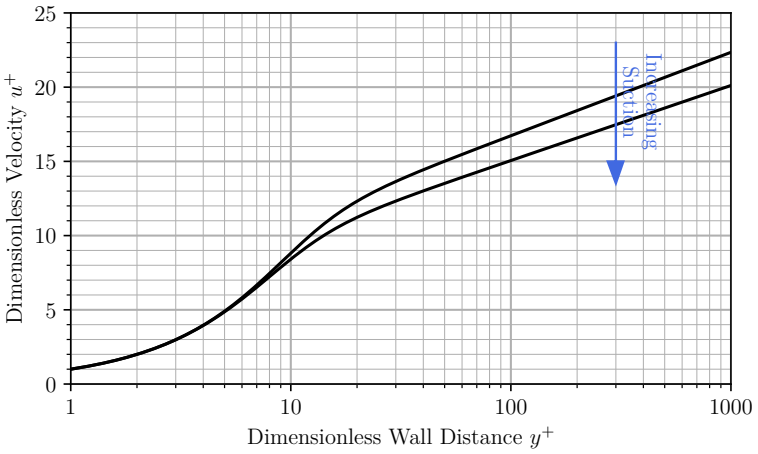

Figure 5.2: Qualitative depiction of the influence of the suction effect on the non-dimensional velocity u^+

The influence of buoyancy on the non-dimensional profiles is more complex than the influence of suction because it affects the profiles in four different ways. These four ways are:

- The direct influence of buoyancy on the momentum equation as a source term
- The increase of the suction effect by buoyancy
- The direct influence of buoyancy on turbulence

- The indirect influence of buoyancy on turbulence

However, the direct influence of buoyancy on turbulence requires the presence of a hydrostatic stratification of the fluid [Turner, 1973]. While such a stratification can form due to wall condensation, this formation is only possible for inclined or horizontal walls. As the scope of the model developed for this thesis is limited to vertical walls, the effect is not further discussed here.

As can be seen from equations 4.10 to 4.12 a direct influence of buoyancy is only present in the momentum equation. Therefore, only the non-dimensional velocity u^+ is directly influenced by buoyancy. Buoyancy acts as a source term in the momentum equation. Thus, it leads to an acceleration of the near wall flow and can lead to the formation of a velocity maximum near the wall surface [Hundhausen et al., 2017a] for the steam air flows investigated in this thesis. This has two effects on the non-dimensional velocity. First, the non-dimensional velocity profile and the non-equilibrium factor Ψ_u also show a distinct maximum because the non-dimensional velocity profile is a scaled version of the dimensional velocity profile. Second, the non-dimensional velocity profile is pushed below the log-law, indicating an increase in the wall shear. This has two reasons: First more momentum is present in the boundary layer because buoyancy acts as a momentum source, and second the velocity gradient close to the wall surface gets larger due to the higher near wall velocity. A qualitative depiction of the direct influence of buoyancy on the non-dimensional velocity u^+ is shown in figure 5.3.

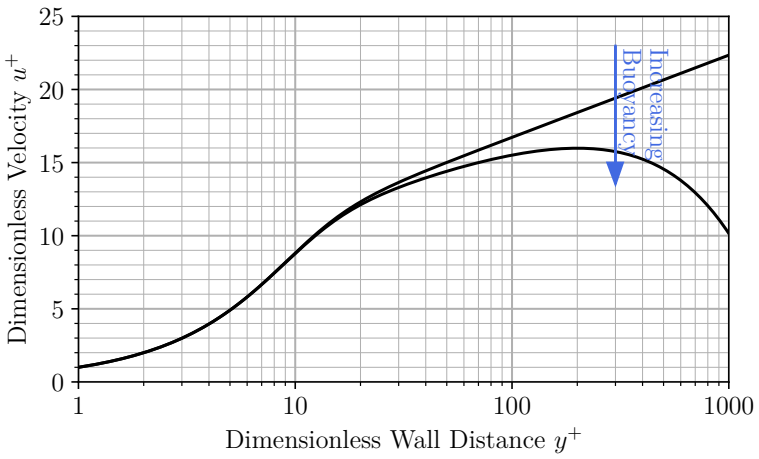

Figure 5.3: Qualitative depiction of the direct influence of buoyancy on the non-dimensional velocity u^+

The increase of suction due to buoyancy is a direct result of the increased near wall velocity. It can simply be explained by mass conservation. As the near wall flow accelerates along the wall, an increasing amount of mass is transported in the boundary layer. The only possible source for this mass is the bulk flow. Consequently, a velocity is induced from the bulk flow towards the wall. Via this velocity mass, momentum and energy experience an advective transport towards the wall surface, similar to the

suction effect directly induced by condensation. Therefore, the buoyancy induced suction increases the wall fluxes and hence reduces the corresponding non-dimensional profiles, as already discussed in the context of figure 5.2.

The change in the velocity profile due to buoyancy also effects turbulence in the boundary layer because it alters one of the two main effects that influence turbulence in the boundary layer. The first effect is the damping of turbulence close to the wall, as turbulent structures can't develop in its immediate vicinity. The second effect, which gets altered, is the production of turbulence due to the gradient of the mean flow velocity. The gradients change because of the acceleration of the flow close to the wall surface due to buoyancy. On the one hand, this increases turbulence production due to the steeper velocity gradient, and on the other hand, the gradient zone is "pushed" closer to the wall and hence to an area of increased turbulence dissipation. Additionally, a second gradient zone forms with the appearance of the velocity maximum close to the wall between said maximum and the mean flow. This increases the production of turbulence. Consequently, the influence of buoyancy on the flow varies with the intensity of the turbulence. As the data presented in figure 4.11 show, turbulence is at first damped with increasing buoyancy (increasing FG^+) and subsequently rises again with an further increase of buoyancy. Thus, with the onset of buoyancy, a decrease of the turbulent transport and therefore an increase of the non-dimensional profiles and the non-equilibrium factors is to be expected. When buoyancy is increased above a certain level, the turbulent transport rises again and the non-dimensional profiles and the non-equilibrium factors should decrease again. A qualitative depiction of this effect is shown in figure 5.4 for the non-dimensional temperature.

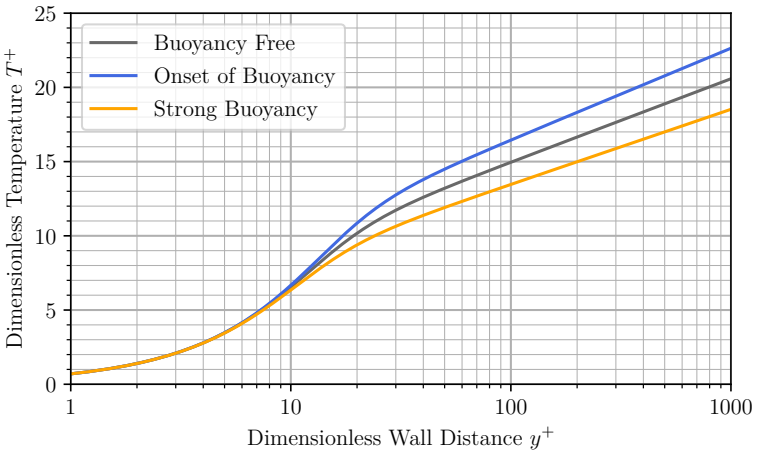

Figure 5.4: Qualitative depiction of the indirect influence of buoyancy on the non-dimensional temperature T^+ via turbulence

In order to illustrate the approximation functions of the newly developed wall function approach, figures 5.5 to 5.8 show a sectional plane for each of the three non-equilibrium factors and the eddy viscosity ratio. This format was chosen as the approximation function

cannot be completely represented graphically because it depends on three parameters. Therefore, the result of the approximation is a body in three-dimensional space or a four-dimensional hyperplane. The sectional planes were generated by treating $\dot{q}^+$as a linear function of FG^+.

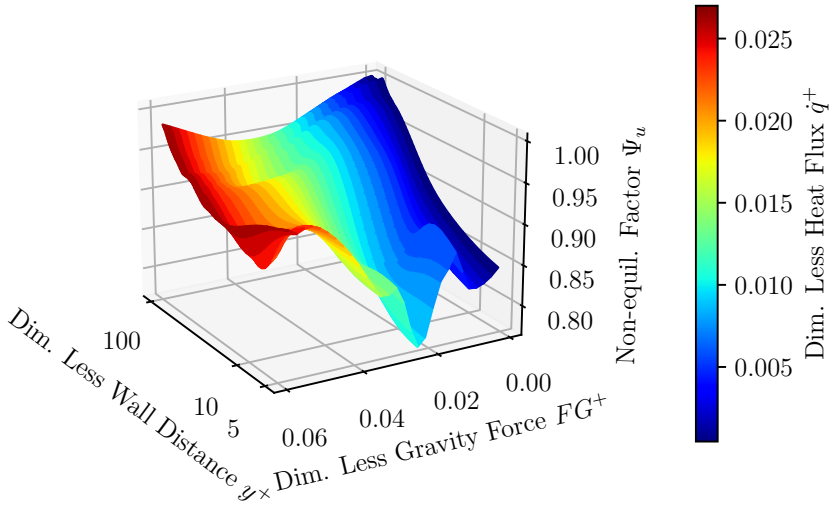

Figure 5.5: Surface plot of the non-equilibrium factors Ψ_u calculated via the radial basis functions

The approximation functions represent the input data very well, as can be seen when comparing figures 5.5 to 5.8 to figures 4.6 to 4.8 and 4.11. This is the expected result due to the approximation errors given in section 4.3. However, there is one noteworthy exception: For a y^+ above 60 and a FG^+ above 0.04, the non-equilibrium factors of the velocity wall function calculated by the approximation function starts to rise towards one, while the input data in figure 4.6 show a further drop of Ψ_u. One reasons for this is the knot removal algorithm used during the derivation of the approximation function, which tends to leave few centers in this area. The second reason are actual data points of about 1.0 for Ψ_u in the input data for this area, as can be seen in figure 4.6. However, as Ψ_u remains below one, the new model still yields a better result for the non-dimensional velocity than the log-law, even though the approximation function does not yield the intended result.

Otherwise, the input data are well reproduced by the approximation function for Ψ_u. At lower values of y^+ the approximation actually works a bit to well, as the scattering of the experimental input data leads to an oscillating behavior of the approximation function in this region. This issue could be addressed with an improved smoothing of the approximation function in future work.

Aside from the regions addressed above, the approximation function for Ψ_u yields qualitatively good results, as the expected trends described above are replicated well by

the approximation function. The plot in figure 5.5 shows that Ψ_u remains below one in the whole definition area. This results from the additional momentum released in the boundary layer due to buoyancy. Also, the formation of the distinct velocity peak can be observed above a FG^+ of 0.03. Consequently, the new model improves description of the velocity boundary layer under condensation influence, from a qualitative perspective, despite its shortcomings, which should be addressed in future work.

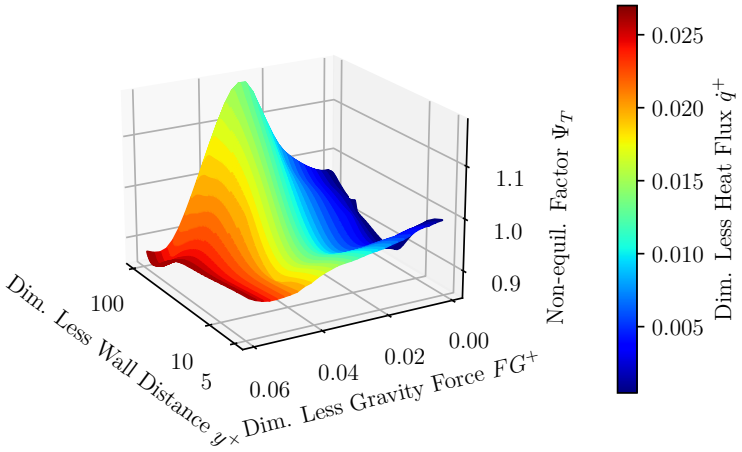

Figure 5.6: Surface plot of the non-equilibrium factors Ψ_T calculated via the radial basis functions

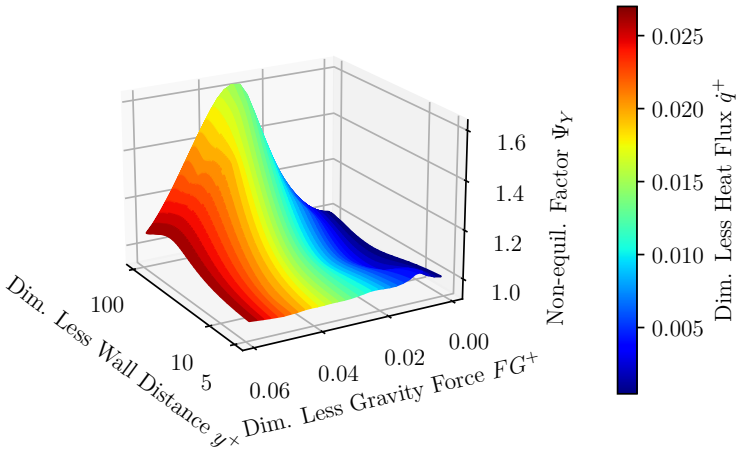

Figure 5.7: Surface plot of the non-equilibrium factor Ψ_Y calculated via the radial basis functions

As expected, the non-equilibrium factors for the temperature wall function Ψ_T, pre-

sented in figure 5.6, and the species wall function Ψ_y, presented in figure 5.7, show a behavior which differs notably from factor for the velocity wall function Ψ_u. This is because only the near wall velocity field is directly influenced by buoyancy. Nevertheless, the strong indirect influence of buoyancy on the temperature and the species boundary layer can be observed in the corresponding plots. An increase of the non-equilibrium factors with FG^+ as well as y^+ up to a maximum at an FG^+ of about 0.35 and and y^+ of 100 can be observed. This results from the damping of turbulence by buoyancy in this parameter area. For larger FG^+ the non-equilibrium factors start to drop towards one, as turbulence starts to grow again in this region of the parameter field. Overall, the plots show that the input data are well represented by the approximation functions for Ψ_T as well as Ψ_Y and that the functions properly depict the indirect influence of buoyancy on the boundary layer.

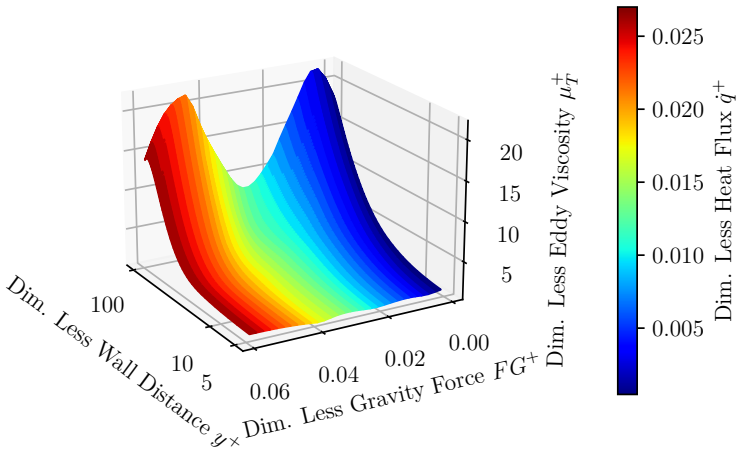

Figure 5.8: Surface plot of the dimensionless eddy viscosity μ_T^+ calculated via the radial basis functions

The large influence of the decay and subsequent regrowth of turbulence due to buoyancy on the condensing boundary layer has already been discussed in the preceding paragraphs. Figure 5.8 illustrates the integration of this effect in the new model approach via the eddy viscosity ratio μ_T^+. The plot of μ_T^+ appears like an inversion of the plots of Ψ_T and Ψ_Y with its two maxima at the minimum and maximum values of FG^+ and the minimum in between. This makes sense because a lower turbulent transport leads to lower wall fluxes and thus higher non-equilibrium factors. Thus, the behavior of turbulence in the boundary layer in the wall condensation regime is also well represented in the new model. However, it should be kept in mind that this part of the model could not be implemented into ANSYS CFX due to the lack of an appropriate interface.

Further insight into the influence of the dimensionless heat flux $\dot{q}^+$ on the new wall function is provided by the figures 5.9 to 5.11. The figures show the behavior of the new velocity, temperature, and steam species mass fraction wall functions for $\dot{q}^+$ values of

0.04, 0.014, and 0.03 at a constant FG^+ value of 0.037. As can be seen from figure 5.5, for example, the $\dot{q}^+$ values are close to the lower and upper bound as well as the center of the range of applicability of the model, while the FG^+ value is in the center of the range. Additionally, the results of the new wall function are compared to results of SETCOM fine mesh simulations.

The influence of $\dot{q}^+$ on the results of the new velocity wall function is relatively small, as figure 5.9 shows. Only at the largest value of $\dot{q}^+$ a noticeable difference in the curves can be observed. However, it can become much more influential at larger values as has been shown by Lehmkuhl [Lehmkuhl, 2018] who used a comparable value called v^+. Similar to figure 5.5, figure 5.9 shows the tendency of the new velocity wall function to return to the standard wall function above a y^+ of about 60 due to a lack of data centers in this region. Figure 5.9 also shows that below a y^+ of 60, the results of the new velocity wall function agree well with the fine mesh simulation data, where the inputs to the new wall function coincide with experimental data locations used as input for the new wall function (orange and blue curve). This is a good indicator for the validity of the new wall function and the included scaling approach.

Meanwhile, the green curve presents an extrapolation at the boundary of the new wall function where no input data points were located. As can be seen, there is a larger deviation between the results of the new wall function and the fine mesh simulation in this case. There are two reasons for this: First, there is some deviation between the non-dimensional velocity profiles of the experiments and the fine mesh simulations, as discussed in section 3.2.2, which can lead to this difference in results. Second, there is an uncertainty associated with the derivation of the values of FG^+ and $\dot{q}^+$ from the experimental data and consequently there can be a misalignment of these input data between the experiments and the simulations. Nevertheless, the new wall function will lead to an improvement of the prediction of the wall fluxes in all investigated cases, because the new wall function results are located close to the fine mesh simulation results or between the fine mesh simulation results and the standard wall function.

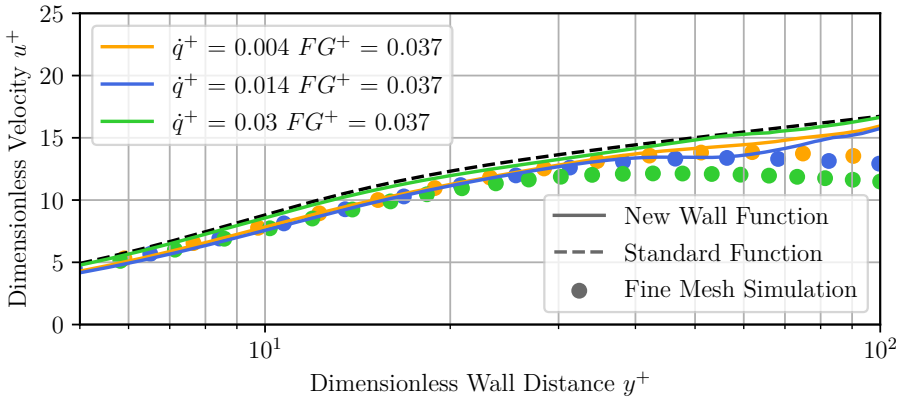

Figure 5.9: Influence of the dimensionless heat flux $\dot{q}^+$ on the dimensionless velocity u^+

A large influence of $\dot{q}^+$ can be observed for the new temperature wall function in figure 5.10. As discussed above, $\dot{q}^+$ actually describes the influence of the condensation induced flow towards the wall surface on the boundary layer. As this leads to an increased transport of heat towards the wall surface, an increase of $\dot{q}^+$ is expected to result in a decrease of T^+. This is exactly the behavior the new wall function exhibits in figure 5.10. Additionally, the plot also shows that the new temperature wall function agrees well with the data from the fine mesh simulations. Hence, the new temperature wall function represents its input data (orange and blue curve) well, can be used to extrapolate results (green curve), and shows the expected behavior. All three factors are a good qualitative indication for the validity of the new model approach.

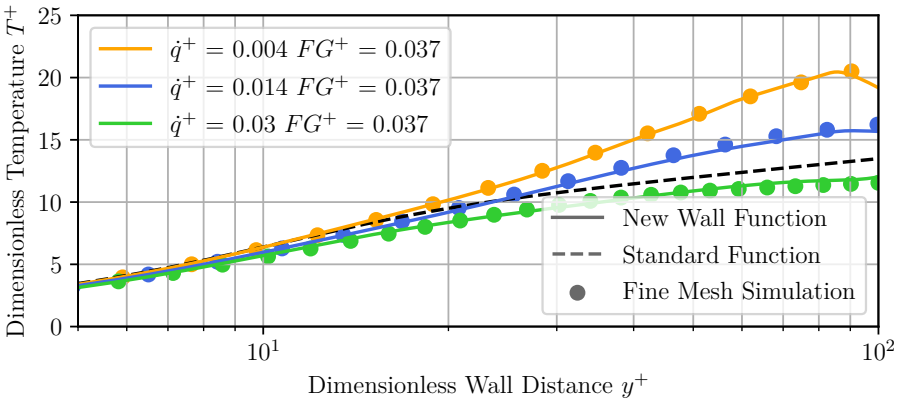

Figure 5.10: Influence of the dimensionless heat flux $\dot{q}^+$ on the dimensionless temperature T^+

The impact of $\dot{q}^+$ on the steam species wall function is not as large as for the temperature wall function, but still visible, as can be seen from figure 5.11. The results of the wall function for the small (orange) and medium (blue) $\dot{q}^+$ are are almost identical for y^+ values below 40 and show only a minor difference above this value. For the highest value (green) of $\dot{q}^+$ the results of the new wall function show a much larger impact of this parameter, as the behavior of the curve is noticeably different from the other two starting at a y^+ value of about 30. The curves again exhibit the expected behavior of a decreasing value of Y_s^+ with an increasing $\dot{q}^+$ due to the increased wall normal transport of steam. Also, it can be observed again that the new wall function results agree well with the fine mesh simulation results used as input for the derivation of the non-equilibrium factors (orange and blue) and that the extrapolation works well (green curve). Therefore, it can again be said that the depicted results qualitatively confirm the validity of the new wall function approach.

To depict the influence of $\dot{q}^+$ on the turbulence wall function, smaller values of FG^+, namely 0.005 to 0.008, are used than for the other wall functions as can be seen in figure 5.12. This is done because the suppression of turbulence by buoyancy is very strong for the initial FG^+ value of 0.037 and consequently the influence of $\dot{q}^+$ would be

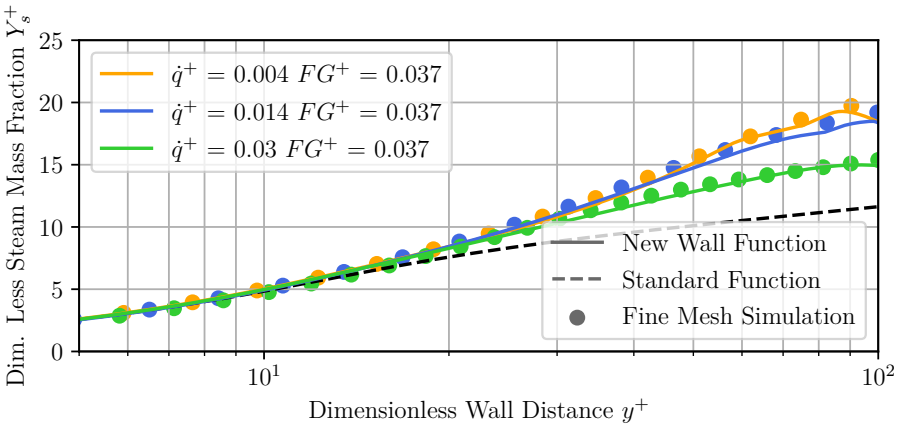

Figure 5.11: Influence of the dimensionless heat flux $\dot{q}^+$ on the dimensionless steam mass fraction Y_s^+

less pronounced. Nevertheless, one can observe that some damping of the turbulence due to buoyancy is already present at these low values of FG^+ by comparing the results with the standard wall function. Expectedly, figure 5.12 shows that turbulence is reduced with increasing $\dot{q}^+$. As described above, this happens because the velocity gradient is pushed closer to the wall surface, an area with higher damping, by the wall normal velocity characterized by $\dot{q}^+$. While this effect is small for the lower two $\dot{q}^+$ values, it becomes very strong for the largest value. While this is consistent with Favre's [Favre et al., 1966] and Lehmkuhl's [Lehmkuhl, 2018] observations on the influence of the suction effect on turbulence, this strong suppression is mostly due to a modeling error. This is because there were no experimental or simulation data available at the time this new wall function was derived at the upper bound of $\dot{q}^+$ for these low values of FG^+ and the model returns to its default value, which, in contrast to the other new wall functions, is zero for the new turbulence wall function. Overall, it can be said that the new turbulence wall function shows the expected behavior with respect to the influence of $\dot{q}^+$. However, this behavior is locally exaggerated due to the limited amount of input data.

Further insight into the influence of the dimensionless gravity force FG^+ on the new wall function is provided by the figures 5.13 to 5.15. The figures show the behavior of the new velocity, temperature, and steam species mass fraction wall functions for FG^+ values of 0.003, 0.037 and 0.06 at a constant $\dot{q}^+$ value of 0.007. As can be seen from figure 5.5, for example, the FG^+ values are close to the lower and upper bound as well as the center of the range of applicability of the model, while the $\dot{q}^+$ value is located at the lower bound of the range. Additionally, the results of the new wall function are compared to results of SETCOM fine mesh simulations.

The impact of FG^+ on the new velocity wall function is depicted in figure 5.13. The discrepancy between the wall function and the fine mesh simulation data at the lowest value of FG^+ (orange curve and dots) as well as the wavy nature of the wall function at this FG^+ illustrates one of the problems of using experimental input data for the wall

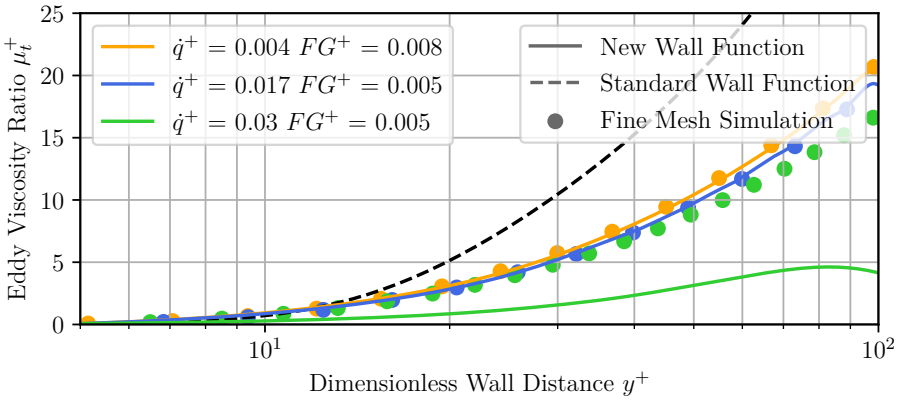

Figure 5.12: Influence of the dimensionless heat flux $\dot{q}^+$ on the eddy viscosity ratio μ_t^+

function development. Here, the scatter of the input data, of which plenty are available around this data point, has translated into the waviness of the wall function during its generation. This problem exists up to a y^+ of about 30, from where on the wall function is more stable and fits the fine mesh simulation data. In future work, the problem with the wavy wall function may be avoided by introducing an improved smoothing in the algorithm that generates the radial basis functions and by a more rigorous selection of the input data.

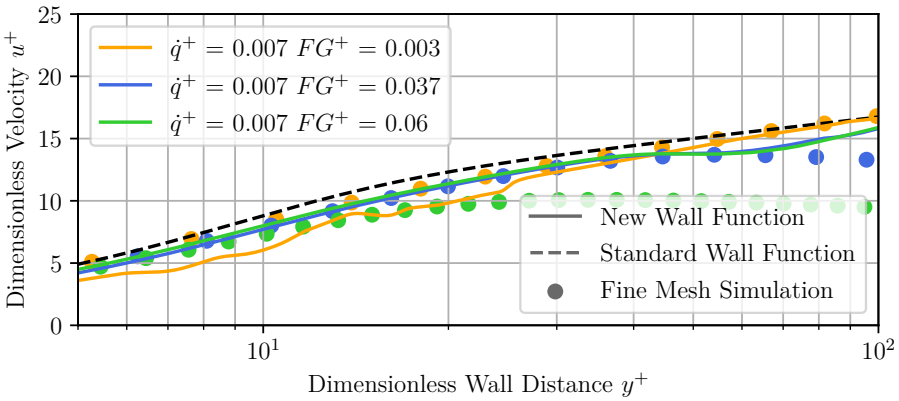

Figure 5.13: Influence of the dimensionless gravity force FG^+ on the dimensionless velocity u^+

For the medium value of FG^+, depicted by the blue curve in figure 5.13, a good agreement between the new velocity wall function and the fine mesh simulation data can be observed up to a y^+ of about 60. Below this point, the new wall function shows the expected behavior of running below the standard wall function due to the additional

momentum introduced into the boundary layer by buoyancy forces as discussed above. Beyond a y^+ of 60, the new wall function starts to trend towards the standard wall function, as observed before. For the highest value of FG^+, presented by the green data in figure 5.13, a large discrepancy between the new wall function and the fine mesh simulation can be observed. These new wall function results are an extrapolation at the boundary of the definition range of the new wall function. The reasons for the problem with this extrapolation are the same as already explained above in the context of figure 5.9. Overall, the new velocity wall function stays in between the standard wall function and the fine mesh simulation results and thus still yields a better result than the standard wall function.

The new temperature and steam species wall functions show a similar behavior with respect to the influence of FG^+, as can be seen from figures 5.14 and 5.15. At the lowest value of FG^+ (orange curve), both wall functions behave similarly to the standard wall function. For the medium value of FG^+ (blue curve) a strong increase of the wall functions can be observed, while values between the other curves can be observed for the largest value (green curve) of FG^+. As discussed above, this behavior results from the different influences that buoyancy has on the turbulent transport of energy and steam mass. This influence leads to a decrease of the turbulent transport in the center of the permissible data range of FG^+ (blue curves) and therefore to an increase of T^+ and Y_s^+. At the upper end of the data range the turbulent transport increases again and thus T^+ and Y_s^+ decrease. For both temperature and steam species, it can also be observed that the new wall function approach agrees well with the fine mesh simulation data used for its derivation (blue and orange curve) and the extrapolated result (green curve). Hence, the qualitative behavior of the temperature and steam species wall functions with respect to FG^+ is an additional indicator for the validity of the new wall function approach.

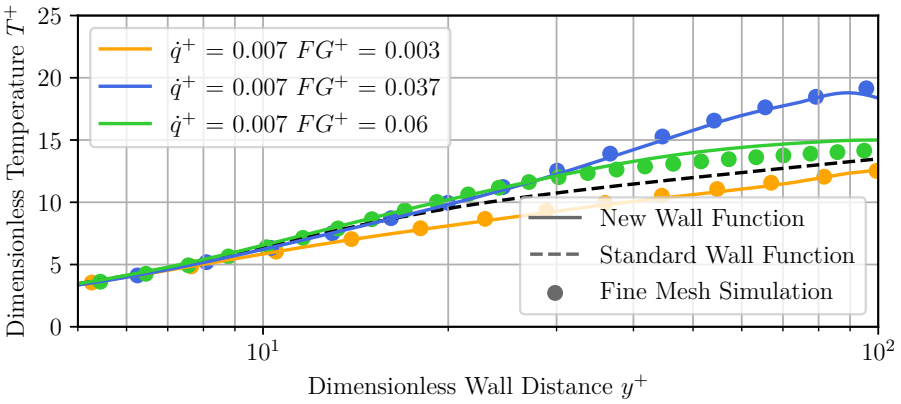

Figure 5.14: Influence of the dimensionless gravity force FG^+ on the dimensionless temperature T^+

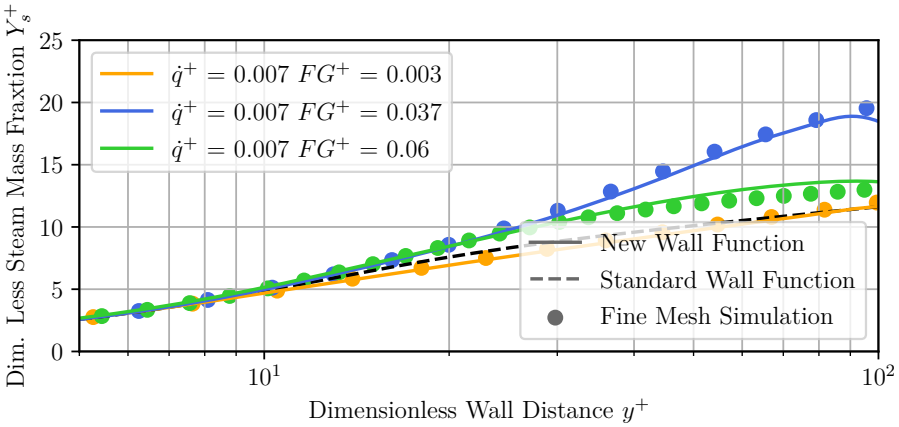

Figure 5.15: Influence of the dimensionless gravity force FG^+ on the dimensionless steam mass fraction Y_s^+

For the depiction of the influence of FG^+ on the eddy viscosity ratio, different values of $\dot{q}^+$ were chosen than for the other wall functions, ranging from 0.012 to 0.014, to get a more pronounced picture of this influence. Figure 5.16 shows that for small values of FG^+ (orange cure) the turbulence is already strongly damped compared to the standard wall function due to the influence of suction and buoyancy. This effect further increases for the medium value (blue curve) of FG^+, but partially recovers for the largest value (green curve). As already discussed in connection with figure 5.7, this is due to the indirect influence of buoyancy on turbulence, which reduces the turbulent fluctuations for FG^+ values in the middle of the application range of the new wall function, but also leads to subsequent regrowth of the fluctuations when FG^+ becomes even larger. However, the green data in figure 5.16 show that the regrowth of turbulence is smaller than expected and also smaller than observed in figure 5.7. The reason for this is that there were no experimental or simulation data available at the upper bound of FG^+ for these values of $\dot{q}^+$ at the time the new wall function was derived. Thus, the model returns to its default value, which, in contrast to the other new wall functions, is zero for the new turbulence wall function. Nevertheless, it can be observed that the new turbulence wall function qualitatively shows the expected behavior regarding the influence of FG^+ and also agrees well with its input data (orange and blue data), thus increasing the confidence in the validity of the modeling approach.

Overall, the qualitative investigation of the new wall function approach shows that all four new wall functions yield the expected behavior regarding the influence of buoyancy and the wall normal flow induced by wall condensation. However, the new velocity wall function still has some shortcomings. At some locations, the wall function showed erratic behavior due to the scattering of the experimental input data. In addition, the new velocity wall function showed the tendency to return to the standard wall function in the parameter area of a non-dimensional wall distance y^+ larger than 60 and non-dimensional gravity forceFG^+ larger than 0.03. This unphysical behavior could not be resolved in

the current work and requires further effort.

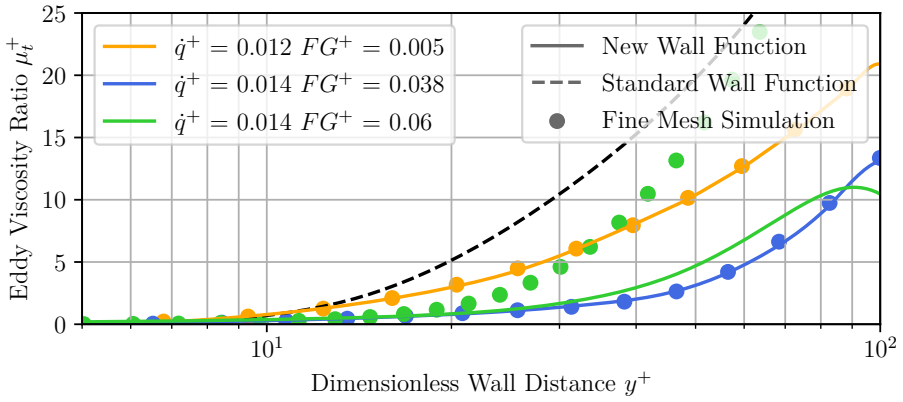

Figure 5.16: Influence of the dimensionless gravity force FG^+ on the eddy viscosity ratio μ_t^+

5.2. Comparison with SETCOM results

In the following, a first validation of the newly developed boundary layer model based on results from the SETCOM facility is discussed. The main goal of this validation step is to demonstrate that the new wall function approach, which has been derived from local measurements in and local simulation data of the SETCOM facility, is applicable along the whole length of the facility's measurement section. This would be a first proof of the scalability of the new wall function approach. To demonstrate this, it has to be shown that the new wall function improves the prediction of the global mass, energy and momentum fluxes to the cooling plate on a coarse mesh when compared to the standard wall function. In addition, the prediction of the local fluxes along the cooling plate, as well as the calculated non-dimensional profiles of the velocity, temperature, and species mass fraction should also improve if the new wall function approach is scalable. Thus, the behavior of these quantities is investigated below.

As has been shown in section 3.2, fine mesh CFD simulations using ANSYS CFX are well able to reproduce the experimental data. Thus, these simulations are used as the primary benchmark for the model as they offer additional variables not available from the experimental data, such as the wall shear along the entire condensation plate, and an enhanced resolution of the data for the comparison. In addition, this approach also shows a comparison between the best-estimate simulation with a fine mesh and the less well-posed simulations with the coarser meshes.

As a first step of this validation effort, the different meshes used for the simulations are introduced. The remaining simulation model is the same as that used in section 3.2. Then, a comparison of global variables between the fine mesh simulations of the SETCOM facility and the coarse mesh simulations with and without the new boundary layer model

is presented to offer an overview of the overall performance of the model. In particular, the total condensation mass flux, the total sensible heat flux, and the total wall shear are compared. Finally, a comparison of local variables is shown to investigate the performance of the new model along the whole length of the facility, offer additional insight into the effects observed in the global results, and to show the transferability of the empirical input data of the model, extracted at only one position of the cooling plate, to the whole length of the facility. In addition to the comparison of the local values of the aforementioned variables, this comparison also includes the non-dimensional velocity, temperature, and species mass fraction profiles.

As shown in figure 5.17, a two-part mesh was used to validate the wall function approach. This was done account for the fact that wall functions cannot represent a developing flow as it appears at the leading edge of the cooling plate. Accordingly, the same grid with a wall resolution of $\Delta y = 0.1\,\mathrm{mm}$ was used in all simulations for the first two meters of the test channel, which corresponds to a y^+ of 0.5 to 2 depending on the flow. For the remaining part of the test facility, three grids with different wall resolutions were created. One with a wall resolution corresponding to the front part of the duct as the reference grid, called the fine mesh in the following, one with a wall resolution of $\Delta y = 2.0\,\mathrm{mm}$ or a y^+ of 20 to 40, called the medium mesh in the following, and one with a wall resolution of $\Delta y = 8.0\,\mathrm{mm}$ or a y^+ of 70 to 120, called the coarse mesh in the following.

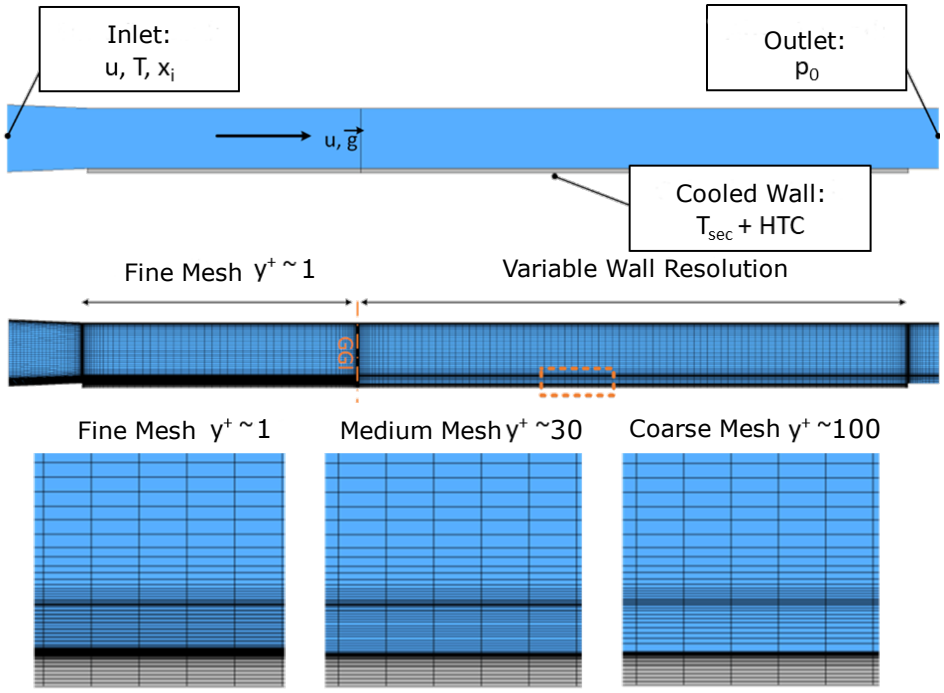

Figure 5.17: Geometry and mesh used for the validation of the new model with the SETCOM experiments

The two parts of the SETCOM mesh are connected by a so-called generalized-grid interface (GGI) [ANSYS, 2016a]. In principle, it would also have been possible to create a continuous grid, e.g. by a continuous coarsening along a part of the measurement section or by a step wise local coarsening introduced into the grid. However, tests with these approaches showed that they introduced a much stronger disturbance of the boundary layer than the GGI interface.

An overview of the overall performance of the model can be gained from the diagrams in figure 5.18. These figures compare the results of the coarse mesh simulations with and and without the new boundary layer model with the corresponding results of the fine mesh simulations. The variables under investigation are the condensation mass flux, the sensible heat flux, and the wall shear. These variables were chosen because they are directly influenced by the dimensionless variables modeled by the wall function, as can be seen from equations 3.7, 3.25 and 3.26. It should be noted that the evaluation of the fluxes includes only the part of the SETCOM mesh where the mesh has been coarsened for the simulations, which means 2 m downstream from the leading edge of the cooling plate up to the end of the cooling plate. It should also be noted that for some calculations the data points for the new and the standard model coincide on the coarse mesh due to the fact that y^+ became larger than 100 on the coarse mesh. Thus, the calculation went outside of the application range for the new model and fell back to the standard model as intended.

Regarding the condensation rate, figure 5.18 shows that the standard model still performs very well on the medium mesh, with little deviation from the fine mesh simulations. In fact, this is the only case where the standard model outperforms the new model, even though the latter also performs very well. However, this good performance of the standard model is rather a coincidence than an indication for a well developed model, as will be shown later in the discussion of the local results. Two indications for this can already be found in figure 5.18. The first of these indications is that the newly developed model also performs well on the coarse mesh, while the standard model overpredicts the condensation mass flux on this mesh by more than 10% in most cases. The second indication is, as already mentioned above, that this is the only case where the standard model outperforms the new model. Overall, the condensation data show that the new model performs well on both coarse grids, with an error of less than 10% in all cases, while the standard model yields good predictions only on the medium mesh.

For the sensible heat flux, figure 5.18 shows a completely different picture. For this variable, the worst performance of the standard model for the whole test series can be observed. This is especially true for the medium mesh, where most of the data points fall below the -10% error band using the standard model. Meanwhile, most of the results with the new model fall into the error band on this mesh, showing the large improvement potential the new model yields. On the coarse mesh, the standard model performs equally poorly, while the new model cannot fully maintain its good performance. The new model still improves the results for most of the simulations, especially at high sensible heat fluxes, but cannot bring all results back into the 10% error band. For the lower heat fluxes, the new model corrects the results in the right direction, but has a tendency to over-correct and thus only yields results as good as the standard model. Overall,

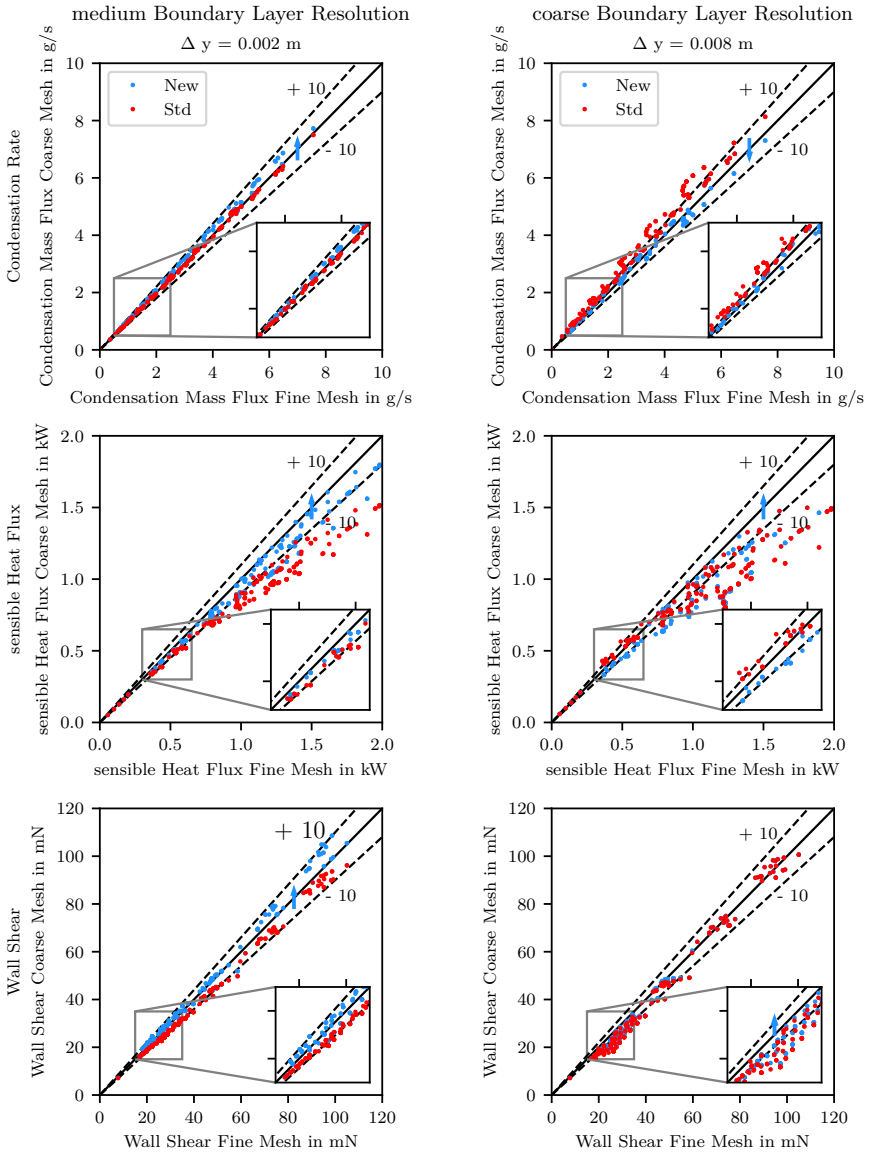

Figure 5.18: Comparison of the calculated total fluxes of the fine mesh and coarse mesh simulations of the SETCOM experiments

the latent heat flux results show the huge potential of the new model to improve the prediction of the wall fluxes on coarse meshes, especially on the medium mesh.

Regarding the wall shear, a significant improvement of the results with the new model can be observed up to a shear of 60 mN on the medium mesh. Above this value, the new model tends to overpredict the shear on the medium mesh. On the coarse mesh, it can be observed that the new model yields better results than the standard model for all simulations within the bounds of applicability of the new model. However, it can also be

observe that the improvement is relatively small in most cases. Overall, the wall shear results show that the new model yields better or at least similar results compared to the standard model.

The data presented in figures 5.19 and 5.20 are used to discuss the local behavior of the new wall function based on the SETCOM results. The subset of SETCOM experiments shown in the figures has been chosen to demonstrate the capabilities of the new model in both the forced (C021) and the mixed (D111) convection regime. Data for three additional SETCOM experiments can be found in appendix D.1 in support of the following discussion. Table 5.1 gives an overview of the boundary conditions of the two experiments presented below, C021 and D111.

Table 5.1: Overview of SETCOM experiments used for the validation

Experiment	Velocity	Temperature	Relative Humidity	Wall Temperature
C021	$3\,\mathrm{m\,s^{-1}}$	60 °C	87 %	7.5 °C
D111	$0.5\,\mathrm{m\,s^{-1}}$	70 °C	90 %	9.1 °C

The figures 5.19 and 5.20 show the local fluxes starting at the interface 2 m downstream of the leading edge of the cooling plate. Data are depicted for the fine mesh (black) as reference, the medium mesh (green) and the coarse mesh (blue). The results of the new wall function approach are represented as solid lines, while the standard model results are shown as dashed lines. Along with the fluxes, the corresponding non-dimensional profiles are also shown in the figures. The profiles were evaluated 4.5 m downstream of the leading edge of the cooling plate.

Regarding the non-dimensional profiles, it should be noted that only the first grid point of the wall surface is directly influenced by the wall functions, because they only serve as a boundary condition. The rest of the profile represents the flow solution obtained by CFX with this boundary condition. When interpreting the dimensionless profiles it should also be kept in mind that the fluxes are inversely proportional to the corresponding dimensionless variables as already explained in section 5.1.

The results of the simulations of the SETCOM experiment C021 show the influence of a wall condensation on a forced convection flow. Thus, the primary influence of the condensation on the boundary layers is the induced wall normal velocity (suction effect), while the influence of buoyancy is negligible. The following discussion of the C021 calculation results will show that the new model is well able to improve the prediction of the non-dimensional quantities as well as the local fluxes in cases where the standard model yields insufficient results.

The results of the simulations are depicted in figure 5.19 in the form of the wall fluxes and the dimensionless profiles. The results for the wall shear and the sensible heat flux are quite similar. In both cases the worst performing model is the standard model on the medium mesh and a significant improvement can be observed using the new model on this mesh. Meanwhile, the standard model performs well on the coarse mesh regarding both quantities. Thus, only a small improvement in the performance of the new model

can be observed regarding the sensible heat flux while the results of both models are ambiguous with respect to the wall shear calculation on the coarse mesh.

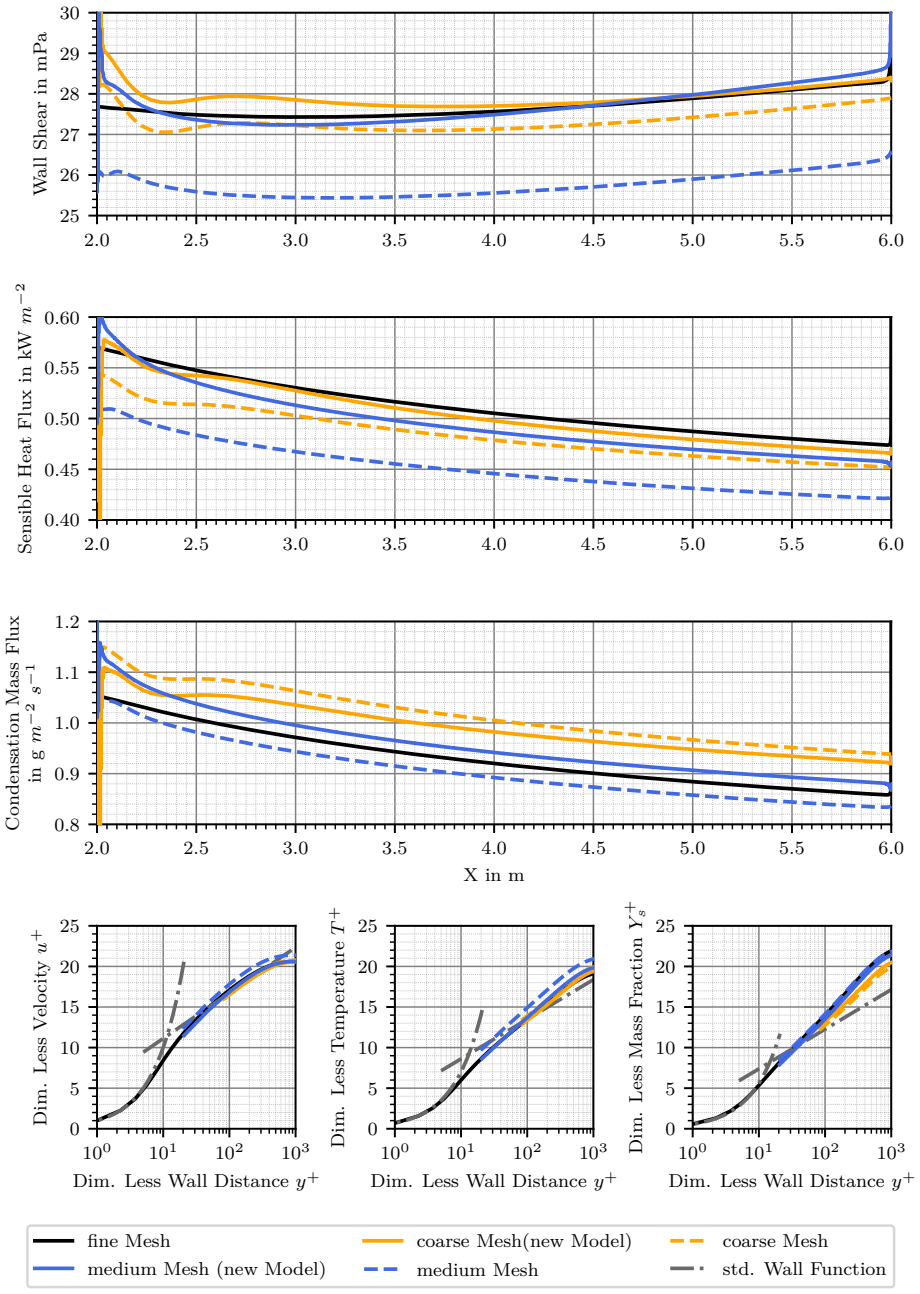

Figure 5.19: Local fluxes and dimensionless profiles for the simulations of the SETCOM experiment C021

The reason for the good results of both models on the coarse mesh can be deduced from

the non-dimensional velocity and temperature profiles shown in figure 5.19. In the case of the dimensionless velocity, the profile from the fine mesh solution actually coincides with the standard model in the turbulent layer. For the dimensionless temperature it can be observed that the intersection of the fine mesh solution and the standard model is close to the first grid point off the wall for the coarse mesh. Thus, the standard model actually yields good predictions of the non-dimensional quantities on the coarse mesh, and thus also yields good results for the wall fluxes under these specific conditions.

Meanwhile, there is a gap between the standard models for the non-dimensional velocity and temperature and the fine mesh solution in the buffer layer where the first grid point off the wall of the medium mesh is located. Consequently, this gap leads to an incorrect prediction of the non-dimensional velocity and temperature, and thus of the wall shear and the sensible heat flux. On the other hand, figure 5.19 shows that the new model significantly improves the prediction of the aforementioned non-dimensional quantities on the medium mesh and therefore the prediction of the wall fluxes. Hence, the medium mesh data of the simulations of the SETCOM C021 experiment indicated that the new model can greatly improve the prediction of the wall fluxes when there is a larger discrepancy between the actual non-dimensional profiles and the standard model.

Similar effects, but swapped for the meshes can be observed for the condensation mass flux. In this case, both medium mesh results are close to the fine mesh results because the fine mesh result of the dimensionless steam mass fraction and the respective standard model intersect close to the y^+ of the medium mesh. Meanwhile, the standard model on the coarse mesh shows the worst performance of all C021 condensation mass flux calculations because the standard model predicts a too low non-dimensional steam mass fraction. This is corrected by the new model, resulting in an improvement in the condensation mass flux prediction. While this improvement is not as significant as for the other two fluxes on the medium mesh, it is clearly present along the whole length of the cooling plate. This shows that the potential to improve the calculation of the wall fluxes is not limited to the medium mesh with its still comparatively fine near wall resolution, but is also present on the much coarser mesh with its 4 times larger near wall cells.

Overall, the previous discussion shows that the new model improves the prediction of the non-dimensional quantities and wall fluxes in cases where the standard model is insufficient. The results also show that this result is valid for different mesh resolutions. This is shown by the fact that the improvements occur on the medium mesh for both the wall shear and the wall heat flux, and on the coarse mesh for the condensation mass flux. This result is further substantiated by the data of the experiments C003, for forced convection flows, and D002, for mixed convection flows, presented in appendix D.1.

Table 5.2 offers further quantitative insight into the error sources of the medium mesh calculation of the experiment C021. To achieve this, the table compares the fine mesh and medium mesh results of the three most error-prone quantities used in the calculation of the wall fluxes (respectively two quantities in the case of wall shear) at 4.5 m downstream of the leading edge of the cooling plate. These quantities can be extracted from equations 3.7, 3.25 and 3.26. For the wall shear, these quantities are the non-dimensional velocity and the velocity at the first grid point off the wall; for the sensible heat flux, these quantities are the non-dimensional temperature, the temperature

difference between the wall and the first grid point off the wall, and the shear velocity; for the condensation mass flux, these quantities are the dimensionless steam mass fraction, the steam mass fraction difference between the walls surface and and the first grid point off the wall, and the shear velocity. The density at the wall surface was omitted because the surface temperature of the wall is relatively stable with respect to the mesh resolution, and thus the density only exhibits minor errors.

The errors are given in Table 5.2 in the form of the quotient of the medium mesh solution and the fine mesh solution, except for the non-dimensional quantities where the fine mesh solution is in the numerator and the coarse mesh solution is in the denominator. Additionally, the dimensionless and dimensional velocity used in the wall shear calculation are squared. In this way, the product of the singular errors equals total error in the wall flux calculation in the absence of other major sources of error. To demonstrate this, the product of the singular errors and the actual error in the fluxes extracted from the calculations are also presented in the table.

Table 5.2: Breakdown of the error in the calculation of the wall fluxes of SETCOM experiment C021 on the medium mesh at 4.5 m

Wall Shear

Wall Function	$(\frac{u^+_{fine}}{u^+_{coarse}})^2$	$(\frac{u_{coarse}}{u_{fine}})^2$	Cumulative error	Error from CFX result
Standard	0.9016	1.0294	0.9281	0.9279
New	1.0605	0.9433	1.0003	1.0004

Sensible Heat Flux

Wall Function	$\frac{T^+_{fine}}{T^+_{coarse}}$	$\frac{(T-T_W)_{coarse}}{(T-T_W)_{fine}}$	$\frac{u_{\tau,coarse}}{u_{\tau,fine}}$	Cumulative error	Error from CFX result
Standard	0.8884	1.0293	0.9633	0.8809	0.8835
New	1.0112	0.9534	1.0002	0.9643	0.9630

Condensation Mass Flux

Wall Function	$\frac{Y^+_{s,fine}}{Y^+_{s,coarse}}$	$\frac{(Y-Y_W)_{coarse}}{(Y-Y_W)_{fine}}$	$\frac{u_{\tau,coarse}}{u_{\tau,fine}}$	Cumulative error	Error from CFX result
Standard	0.9642	1.0429	0.9633	0.9687	0.9697
New	1.0364	0.9886	1.0002	1.0248	1.0243

The data in table 5.2 show that other factors besides the wall function play an important role in the prediction of the wall fluxes. For example, the very good prediction of the wall shear by the new model on the medium mesh is partly due to a cancellation of error effects. At the investigated location, the results exhibit an error of only +0.04 % in the wall shear calculation with the new model, but the error in the prediction of the dimensionless velocity would yield an error of +6.05 %. This is compensated by an error

of -5.67 % in the dimensional velocity. Similarly, the error of -9.84 % in the dimensionless velocity of the standard model is partially compensated by an error of +2.94 % in the dimensional velocity yielding an overall error of -7.21 % in the wall shear calculation.

As another example, the new model predicts the non-dimensional temperature with a high accuracy (+1.12 %), but the overall accuracy of the prediction of the sensible heat flux (-4.66 %) is limited by the prediction of the temperature difference between the wall surface and the first mesh point off the wall (-3.7 %). Overall, these data show that the new wall function can and does improve the calculation of the wall fluxes, but other parameters, which are not only influenced by the wall function but also, for example, by the upstream flow field and turbulence, also have a large influence on the prediction of the wall fluxes.

A further look at table 5.2 and figure 5.19 reveals another interesting difference between the medium and fine mesh calculation regarding the wall shear and the velocity at the first node off the wall. The graph for the wall shear shows a very good agreement between the fine mesh result and the medium mesh result using the new wall function along the whole cooling plate. Nevertheless, the data in the table show that the velocity is -2.77 % (keeping in mind that the velocity data in the table are squared) lower than the fine mesh solution; a result one would expect if a too large wall shear had been predicted.

An even more pronounced version of this effect can be observed for the sensible heat flux. Here, the flux into the wall from the medium mesh calculation is smaller than the flux from the fine mesh calculation when the new model is used. Nevertheless, the temperature difference between the wall surface and the the first mesh point in the flow is also smaller in the medium mesh result compared to the fine mesh result. This is the opposite of the expected behavior, as a smaller heat flux should preserve a larger temperature difference between the flow and the wall. A similar behavior can be observed for both calculations with the standard model. This does not seem to be a local effect induced by an incorrect calculation of the wall normal turbulent transport or flow, since both are in good agreement between the medium and the fine mesh results. Thus, it is likely to be either an effect of the averaging of flow variables at the GGI interface, or an effect of the overall coarsening of the near wall mesh and its resulting influence on the flow field. Regardless of the cause, this observation again points out that the new model can and does improve the prediction of the wall fluxes on coarse meshes compared to the standard model, but the prediction of the fluxes is also influenced by factors which cannot be influenced by the wall function, for example, the averaging at the interface.

Overall, the results from the simulations of the SETCOM experiment C021 show two important points: First, the new model improves the prediction of the dimensionless quantities of the boundary layer and the wall fluxes, when the flow deviates from the standard model. This is true for different mesh resolutions. Second, quantities resulting from the CFD calculation and not from the wall function, such as the local temperature or velocity, do impact the result of the wall flux calculation. This emphasizes the importance of obtaining the best possible results for the boundary layer over its entire length. This is because, errors steaming from upstream of a given location will affect the results of the wall flux calculation at that location. In particular, this means that it is important for a wall function to yield the best possible result for the entire length of a boundary layer.

Both findings are supported by the additional validation cases presented in appendix D.1.

The experiment D111 was chosen as an example of a test case for a mixed convection flow with condensation influence. The most striking feature of the results presented in figure 5.20 are the jumps of the fluxes in the coarse mesh solution of the new model between 3.30 m and 3.35 m plate length. These jumps have a magnitude of up to 30 % of the flux upstream of the jump. The jumps mark the location where the dimensionless parameters y^+, $\dot{q}^+$, and FG^+ reach the definition range of the new model. Upstream of the jumps, the new model yields the same results as the standard model, as intended during the model development. This is also shown by the results of the C063 simulation results presented in appendix D.1. Downstream of the jumps, the new model changes the results to a new stable level, thus proving that the transition between the two models does not contradict a stable simulation result.

The result of the transition between the standard model and the new model on the coarse mesh is different for each of the fluxes on the first glance. For the wall shear a small improvement of the result is visible, for the condensation mass flux a correction in the right direction takes place but the magnitude of the error remains the same and for the sensible heat flux a seemingly good result gets worse due to the transition. This is even more curious as the plots of the non-dimensional quantities u^+, T^+ and Y_s^+ in figure 5.20 show an improvement of the coarse mesh results by the new model for all three of them and consequently an improvement of all fluxes could be expected. However, the performance of the new model is again limited by the prediction of the other input data for the calculation of the wall fluxes from ANSYS CFX, as can be seen from table 5.3. In particular, in the case of the sensible heat flux, the error in the standard model for the non-dimensional temperature is compensated by the errors in the calculation of the shear velocity and the temperature difference between the wall surface and the first node in the flow. Notably, the error in the temperature difference is not corrected by the new model, and thus the standard model incidentally yields a better result for the sensible heat flux, although it performs worse than the new model with respect to the non-dimensional temperature.

While the new model yields improved results for the prediction of the non-dimensional quantities on the coarse mesh, it should also be noted that the non-dimensional temperature and the non-dimensional steam mass fraction are still afflicted with a relatively large error of 9.43 % and 6.35 %, respectively (compared to 20.96 % and 40.60 % for the standard model). The main reason for this remaining deviation are erroneous input data for the model. For the new model, the coarse mesh results y^+ deviates about +4 %, $\dot{q}^+$ deviates about -11.4 % and FG^+ deviates about +12.7 % from the fine mesh solution. The errors in these quantities are primarily caused by the results of the wall flux calculations, which highlights the iterative nature of the wall flux calculation via wall functions. It also highlights the importance of the correct calculation of the wall shear τ_w and consequently the shear velocity u_τ. The shear velocity affects not only the calculation of the fluxes from the results of the wall functions, but also the input data for the wall functions. As can be seen from the corresponding equations 3.10, 4.13 and 4.14, y^+ is affected by u_τ by a power of 1, $\dot{q}^+$ by a power of -1, and FG^+ by a power of 3. This emphasizes that the correct determination of the wall shear, while often considered

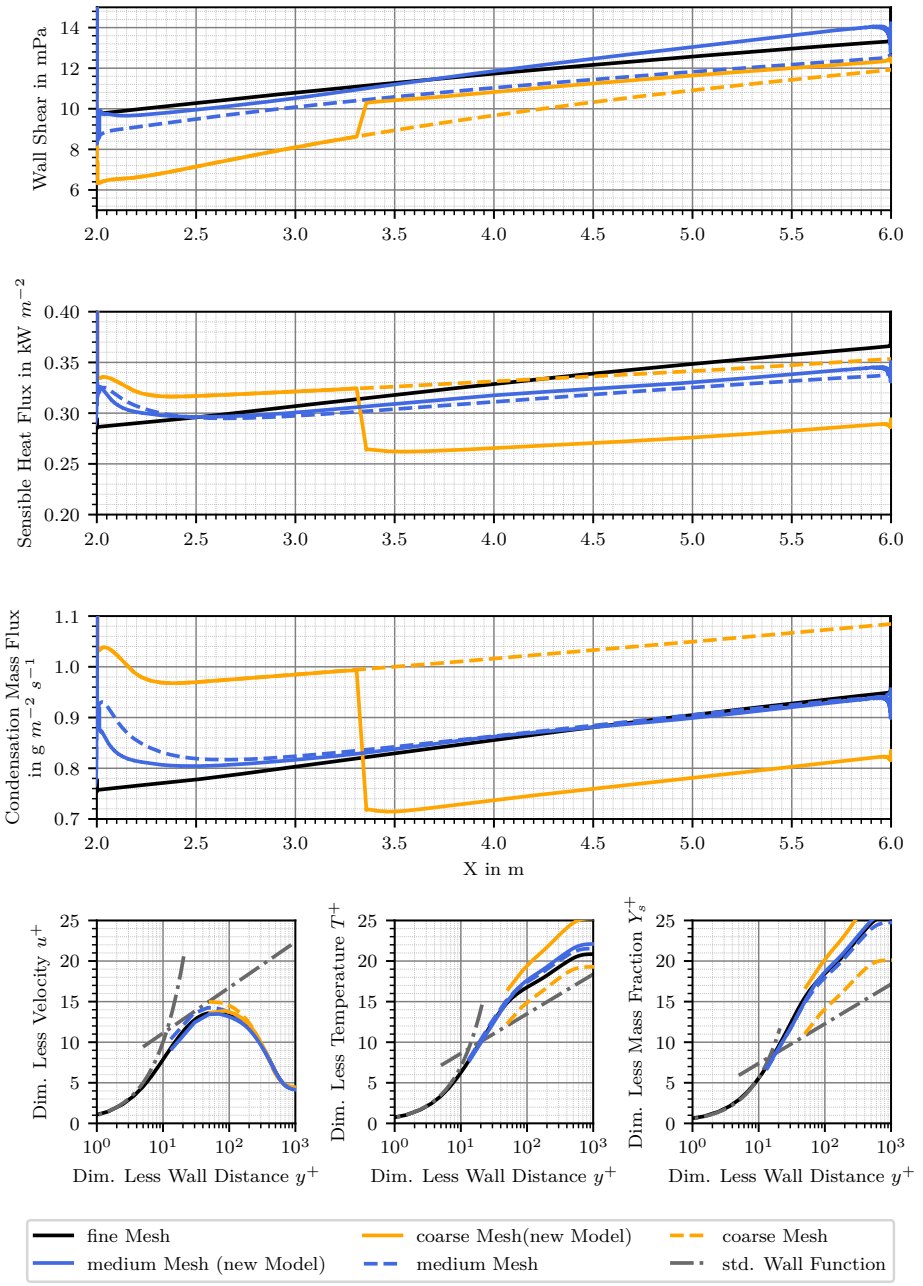

Figure 5.20: Local fluxes and dimensionless profiles for the simulations of the SETCOM experiment D111

of minor importance for the flow calculation, is actually of great importance for a correct prediction of a flow when using wall functions.

In conclusion, the results of the simulations of the experiment D111 show that the new

Table 5.3: Breakdown of the error in the calculation of the wall fluxes of SETCOM experiment D111 on the coarse mesh at 4.5 m

Wall Shear

Wall Function	$(\frac{u^+_{fine}}{u^+_{coarse}})^2$	$(\frac{u_{coarse}}{u_{fine}})^2$	Cumulative error	Error from CFX result
Standard	0.8221	1.0329	0.8491	0.8492
New	0.9984	0.9260	0.9245	0.9245

Sensible Heat Flux

Wall Function	$\frac{T^+_{fine}}{T^+_{coarse}}$	$\frac{(T-T_W)_{coarse}}{(T-T_W)_{fine}}$	$\frac{u_{\tau,coarse}}{u_{\tau,fine}}$	Cumulative error	Error from CFX result
Standard	1.2096	0.8961	0.9215	0.9988	0.9923
New	0.9057	0.9105	0.9615	0.7929	0.7980

Condensation Mass Flux

Wall Function	$\frac{Y^+_{s,fine}}{Y^+_{s,coarse}}$	$\frac{(Y-Y_W)_{coarse}}{(Y-Y_W)_{fine}}$	$\frac{u_{\tau,coarse}}{u_{\tau,fine}}$	Cumulative error	Error from CFX result
Standard	1.4060	0.9069	0.9215	1.1750	1.1725
New	0.9365	0.9556	0.9615	0.8605	0.8621

model also improves the prediction of the dimensionless velocity, temperature, and steam mass fraction for mixed convection flows. However, in contrast to the mixed convection experiment D002 presented in appendix D.1, this does not lead to an improvement in the prediction of the wall fluxes for the experiment D111 in all cases. This is because the new model is outside of its definition range upstream of about 3.4 m plate length. While the intended behavior of falling back to the standard model can be observed in this region, the results show that this fallback is a mixed blessing. On the one hand, it allows the model to continue to work even when it is outside of its application range. On the other hand, it becomes clear that the results obtained for the wall fluxes upstream of 3.4 m have a negative impact on the results for the fluxes downstream of this location. Consequently, the results of the experiment D111 highlight the importance to extend the application range of the new wall function approach beyond the range of the SETCOM experiments in future work.

Overall, the comparison of the standard and the new wall function with the fine mesh SETCOM simulation results shows that the new model generally yields better results, especially under containment typical flow conditions. The global investigation (see figure 5.18) showed that the new wall function leads to large improvements of the wall flux calculations where the standard wall function yields large errors, and yields similar results where the standard wall function already yields sufficient results.

The investigation of the local results of two exemplary SETCOM experiments confirmed

this finding and also provided insights into the main sources of the remaining error in the wall flux calculations when the new wall function is used. The first error source are incorrect input data, y^+, $\dot{q}^+$ and FG^+, for the wall functions. These three parameters are especially sensitive to the value of the wall shear and consequently the shear velocity, thus emphasizing the importance of the correct prediction of the wall shear and the iterative nature of the wall flux calculations via wall functions.

The second error source are errors in the data aside from the non-dimensional quantities influencing the wall flux calculation, such as the velocity at the first mesh node off the wall or the temperature difference between this node and the wall surface. These errors can result from many different sources, like an incorrect calculation of the near wall turbulence due to the missing implementation of the turbulent boundary condition or averaging at a GGI interface and are consequently difficult to avoid. However, the error can also be caused by the new model itself, due to the fall back to the standard model outside of its operating range. Thus, it is important to extend this range beyond the operating parameters of the SETCOM facility in future work, to ensure a broad applicability of the model. One way to do this is to use fine mesh simulations to create additional input data for the model beyond this operating range. Another option is to allow the new model to extrapolate results beyond its application range, rather than falling back to the standard model.

Nevertheless, the new model generally improves the wall flux calculation in the simulations of the SETCOM facility on the medium and the coarse mesh, both globally and locally. A fact that is worth mentioning because local data from the SETCOM experiments and simulations have been used for the model development, whereas the global improvement of the results by the new model is a strong argument for its general applicability beyond the scope of the SETCOM facility.

5.3. Integral tests

To further validate the new wall functions, two vessel experiments, which are closer to the conditions in a containment during a LOCA, were calculated using the new model. These are the TOSQAN ISP-47 experiment and the THAI HM2 experiment. These simulations were conducted with the following objectives:

- To show that the new model is functional on a purely technical level in these experiments
- To show that the new model can be scaled up and still provides physically reasonable results
- To show that the new model improves the coarse mesh simulation results of these experiments

The achievement of the first two goals is a necessary condition for the applicability of the new model to any problem other than the SETCOM test channel, for which its applicability has already been shown in section 5.2. The third goal is necessary to show that the new model is applicable for its intended purpose, the containment under LOCA

conditions. As the following description of the results will show, the first two goals are achieved with the simulations, while the third one is not. However, the reasons for this failure show that they can be overcome in the future and provide valuable insights into how this can be achieved.

5.3.1. TOSQAN ISP47

5.3.1.1. The TOSQAN vessel

The TOSQAN test facility, constructed and operated by the French Institut de Radioprotection et de Sûreté Nucléaire, is used to study the thermohydraulics of a pressurized water reactor containment atmosphere under severe accident conditions [Malet et al., 2010]. In particular, this includes the topics of wall condensation, heat and mass transfer between the sump and the atmosphere, steam condensation on spray droplets as well as the washout of aerosols from the atmosphere via spray.

The facility, as depicted in figure 5.21, consists of a large upper cylinder and a smaller bottom cylinder, which is also called the sump. The facility has a total internal volume of $7\,\mathrm{m}^3$, a total height of 4.8 m, a sump height of 0.87 m, the top cylinder has an internal diameter of 1.5 m and the sump has an internal diameter of 0.684 m. The vessel can be sealed from the environment, a maximum operating pressure of 7 bar can be achieved and the maximum possible wall temperature is 160 °C.

The temperature of the walls of the TOSQAN facility can be controlled by means of heated mineral oil pumped through them [Malet et al., 2010]. This is possible because the walls are made of a double shield of stainless steel, through which the oil can circulate. Furthermore, the wall is divided into two temperature zones: The hot zone at the top and bottom of the facility and the condensation zone in the center of the facility, as marked in figure 5.21. This allows wall condensation to occur only at the specified area of the facility and also allows for the creation of natural circulation loops within the facility.

An injection pipe for gases is located on the center axis of the vessel at a height of 2.1 m. The inner diameter of the pipe is 0.041 m. Gases that can be injected are air, helium and steam. Steam is provided by a boiler with a power of 100 kW. The boiler provides steam at a pressure of 8 bar with a maximum mass flow of $12\,\mathrm{g\,s^{-1}}$. Air and helium can be preheated prior to the injection. The exact injection temperature is measured by means of a thermocouple at the outlet of the injection pipe. The injection mass flow is measured by means of an ultrasonic flowmeter for steam and by two mass flowmeters for air and helium each.

For the ISP-47 experiment the TOSQAN facility was instrumented with 90 thermocouples, mostly located along the center axis of the vessel and near the walls [Malet et al., 2010]. The gas composition can be measured by mass spectrometry at 54 locations in the vessel. Additionally, the vessel has 14 optical accesses at 4 different heights, some of which have been used during several stages of the ISP-47 experiment for non-intrusive measurement techniques like LDV and PIV for velocity measurements and Raman spectrometry, for gas composition measurements.

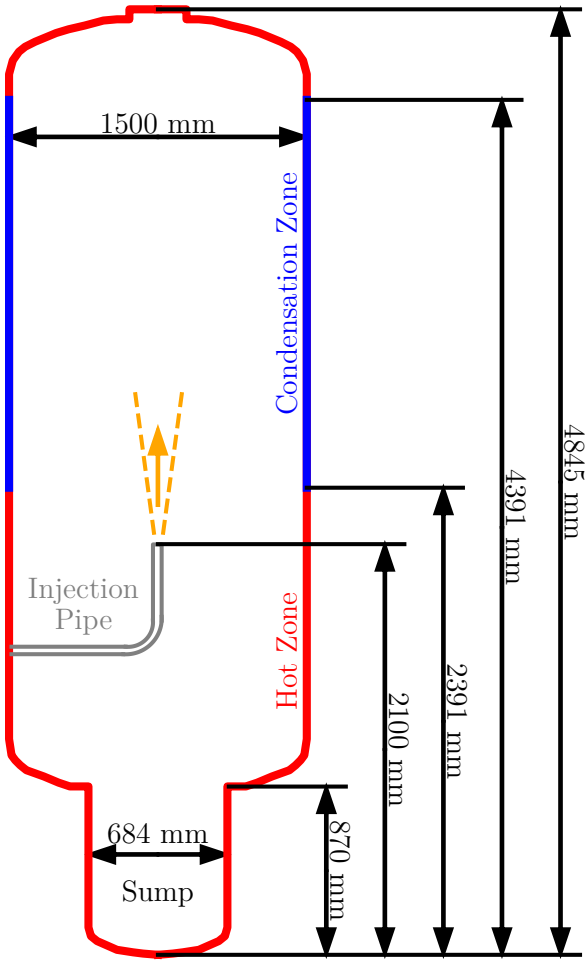

Figure 5.21: Drawing of the TOSQAN test facility [Malet et al., 2010]

5.3.1.2. The TOSQAN ISP47 experimental procedure and simulation setup

The TOSQAN experiment of the ISP-47 [Allelein et al., 2007] aims to investigate wall condensation under well-defined quasi-stationary boundary conditions. For this purpose, the experiment is divided into four steady states, which are linked by four transient phases (see figure 5.22). At the beginning, the atmosphere of the vessel is heated to 114 °C at ambient pressure by heating the lower part of the vessel (0 m to 2.391 m) and its lid (4.391 mto 4.8 m) to 123 °C using oil and cooling the vessel wall between them to 101 °C. Accordingly, two convection loops are formed in the vessel (see figure 5.23).

As soon as the temperature of the vessel atmosphere has reached a stable level, the vessel is closed and steam at a temperature of approx. 124 °C is fed into it through the

injection pipe. The steam mass flow decreases linearly from $1.4\,\mathrm{g\,s^{-1}}$ to $1.14\,\mathrm{g\,s^{-1}}$ during this phase. As soon as a constant pressure is reached due to the equilibrium between the steam mass fed into the vessel with the condensation on the cooled wall, the actual test sequence begins with the first transient. During this transient, $3.16\,\mathrm{g\,s^{-1}}$ air are injected into the vessel for 600 s while the steam mass flow is kept constant and the injection temperature rises to 125 °C.

During the second transient, the steam mass flow is increased to $12.27\,\mathrm{g\,s^{-1}}$ and the steam temperature is increased to 132 °C, resulting in an increase in equilibrium pressure. The temperature of the condensation wall also increases to 108 °C.

For the third transient, the steam mass flow is reduced to the level of $1.11\,\mathrm{g\,s^{-1}}$ and the steam temperature is reduced to 126 °C in order to observe whether the atmospheric conditions of the first steady state are restored. Additionally, the temperature of the condensation wall also drops to 101 °C during this transient.

The last transient of the experiment consists of two successive injections of non-condensable gases. First, as in the first transient, $3.16\,\mathrm{g\,s^{-1}}$ air are fed into the vessel for 600 s at a temperature of 126 °C. Finally, $1\,\mathrm{g\,s^{-1}}$ helium is injected into the vessel, also for 600 s at the same temperature, allowing the influence of a light gas on the flow in the vessel to be investigated. During this last injection the steam mass flow drops linearly from $1.11\,\mathrm{g\,s^{-1}}$ to $0.89\,\mathrm{g\,s^{-1}}$ The full test sequence of the TOSQAN ISP 47 experiment is presented in table 5.4 and figure 5.22.

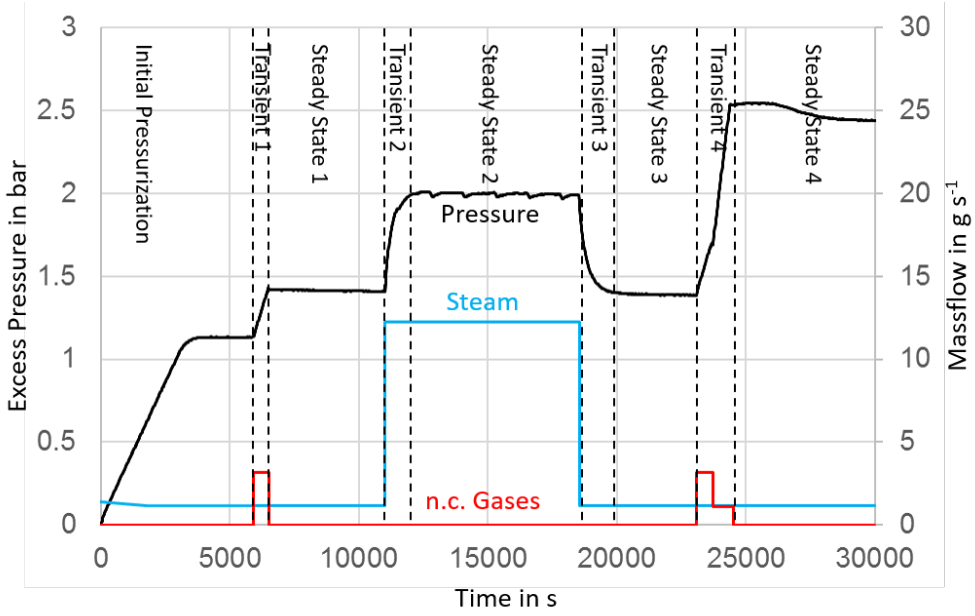

Figure 5.22: Test sequence of the ISP47 TOSQAN experiment [Malet et al., 2006]

The TOSQAN experiment of the ISP-47 was selected as the first experiment for the integral validation of the new wall function approach because of the comparatively simple geometry and experimental design, which led to the a-priori assumption that a stable and

Table 5.4: Test sequence of the ISP47 TOSQAN experiment [Malet et al., 2006]

Phase	Start time	Steam mass flow	Air mass flow	Helium mass flow	Injection temperature
Initial Phase	0 s	1.4 g s^{-1} - 1.14 g s^{-1} linear drop	0.0 g s^{-1}	0.0 g s^{-1}	124 °C
Transient 1	5957 s	1.14 g s^{-1}	3.16 g s^{-1}	0.0 g s^{-1}	125 °C
Steady State 1	6557 s	1.11 g s^{-1}1	0.0 g s^{-1}	0.0 g s^{-1}	126 °C
Transient 2	11 057 s	12.27 g s^{-1}	0.0 g s^{-1}	0.0 g s^{-1}	132 °C
Steady State 2	12 281 s	1.11 g s^{-1}	0.0 g s^{-1}	0.0 g s^{-1}	132 °C
Transient 3	18 564 s	1.11 g s^{-1}	0.0 g s^{-1}	0.0 g s^{-1}	131 °C
Steady State 3	20 196 s	1.11 g s^{-1}	0.0 g s^{-1}	0.0 g s^{-1}	126 °C
Transient 4.1	23 134 s	1.11 g s^{-1}	3.16 g s^{-1}	0.0 g s^{-1}	126 °C
Transient 4.2	23 734 s	1.11 g s^{-1} - 0.89 g s^{-1} linear drop	0.0 g s^{-1}	1.03 g s^{-1}	126 °C
Steady State 4	24 334 s	0.89 g s^{-1}	0.0 g s^{-1}	0.0 g s^{-1}	138 °C

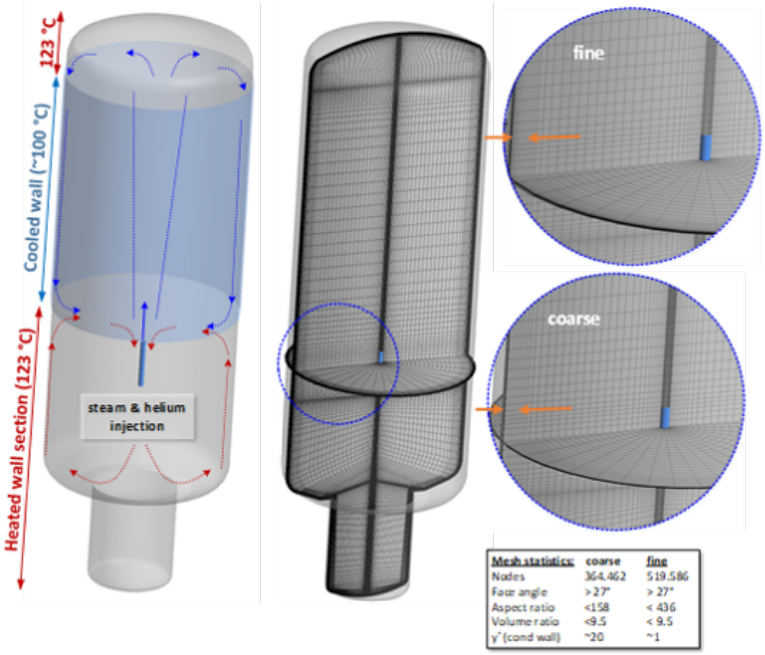

Figure 5.23: Facility configuration and numeric mesh for the simulation of the TOSQAN ISP47 experiment

thus easily calculable flow was present. In principle, this assumption was also supported by the available literature [Malet et al., 2006]. Furthermore, it was expected that due to the different feed rates and the resulting velocity of the steam jet at the wall, flows from the forced convection regime (steady state 2) as well as from the mixed convection regime

(e.g. steady state 1) would occur and thus a validation of the wall function approach over its entire permissible parameter range would be possible.

The model geometry and the block structured mesh used for the discretization of the TOSQAN vessel are shown in figure 5.23 (left and center). The straight part of the feed line and the trajectory of the plume are resolved in detail, allowing a consistent representation of the feed and entrainment of gas through the plume. Two different meshes are used to investigate the new wall function approach. A fine mesh, which resolves the boundary layers (y^+ approx. 1), and a coarse mesh, which has the same resolution in the bulk, but with a significantly lower boundary layer resolution (y^+ approx. 20). The use of an even coarser mesh proved to be impractical for the TOSQAN facility, as this would have meant that the resolution would have increased from the wall towards the volume.

The model approach used for the simulations is essentially the one described in section 3.2. However, two important changes are made for the simulations of the TOSQAN experiment. First, the transient solver of ANSYS CFX with a second-order Euler backward method is used for the temporal discretization of the simulations, since the transient parts of the experiment are also to be investigated with the simulations. As convergence criterion a maximum residual of 10^{-3} is chosen for all conservation equations and a minimum number of three iterations per time step is enforced. In addition, variables, such as the air mass in the vessel, are checked for consistency during the simulation. An adaptive time step control is used, which adapts the time step such that the root mean square of the CFL number in the vessel is one. This setting, which is necessary for the quality of the simulation, led to a time step size of < 0.01 s and thus to an unexpectedly high computation time for the entire transient of more than 30 000 s in total.

The second major change is the use of a thermal radiation model in the simulation. This is necessary because it has been shown, for example by Kelm [Kelm et al., 2016], that the temperature distribution in a vessel atmosphere containing steam is strongly influenced by radiation heat transport even at low temperatures. For the TOSQAN calculation the "Discrete Transfer" model with 100000 radiation histories, which is available in ANSYS CFX, was used for the calculations. An emissivity of 0.6 was used for the steel surface. To model the interaction of the radiation with the atmosphere, it was assumed to be gray. The emission coefficient was calculated as the mass average of the coefficients of air ($0\,\mathrm{m}^{-1}$) and water vapor ($1\,\mathrm{m}^{-1}$).

For the coarse mesh simulations three different boundary layer models were used. First, the standard wall function implemented into ANSYS CFX as a reference for the current state of the art. Second, the new wall function approach with deactivated non-equilibrium factors to show the coherent implementation of the model. Third, the fully active new wall function approach to show the influence of the new model on the flow simulation.

5.3.1.3. The TOSQAN ISP47 simulation results and discussion

The achievement of the above mentioned goals was verified by comparing the coarse mesh simulations with the experimental data as well as a fine mesh simulation, which was considered to be the best possible result. Figure 5.24 shows, for example, the time

history of the pressure as well as the condensation mass flux in the vessel. The focus here is on the initial pressure build-up as well as the first two steady states and the corresponding transients. The fine grid simulations (blue) show a very good agreement with the experimental results (red), but note that no reliable experimental data are available for the condensation rate, so that the steam injection into the vessel is shown here. Accordingly, the experimental data differ from the calculated condensation rates during the transient phases. Nevertheless, the results of the fine grid simulation presented in figure 5.24 show that the global behavior of the experiment can be well reproduced with CFD methods.

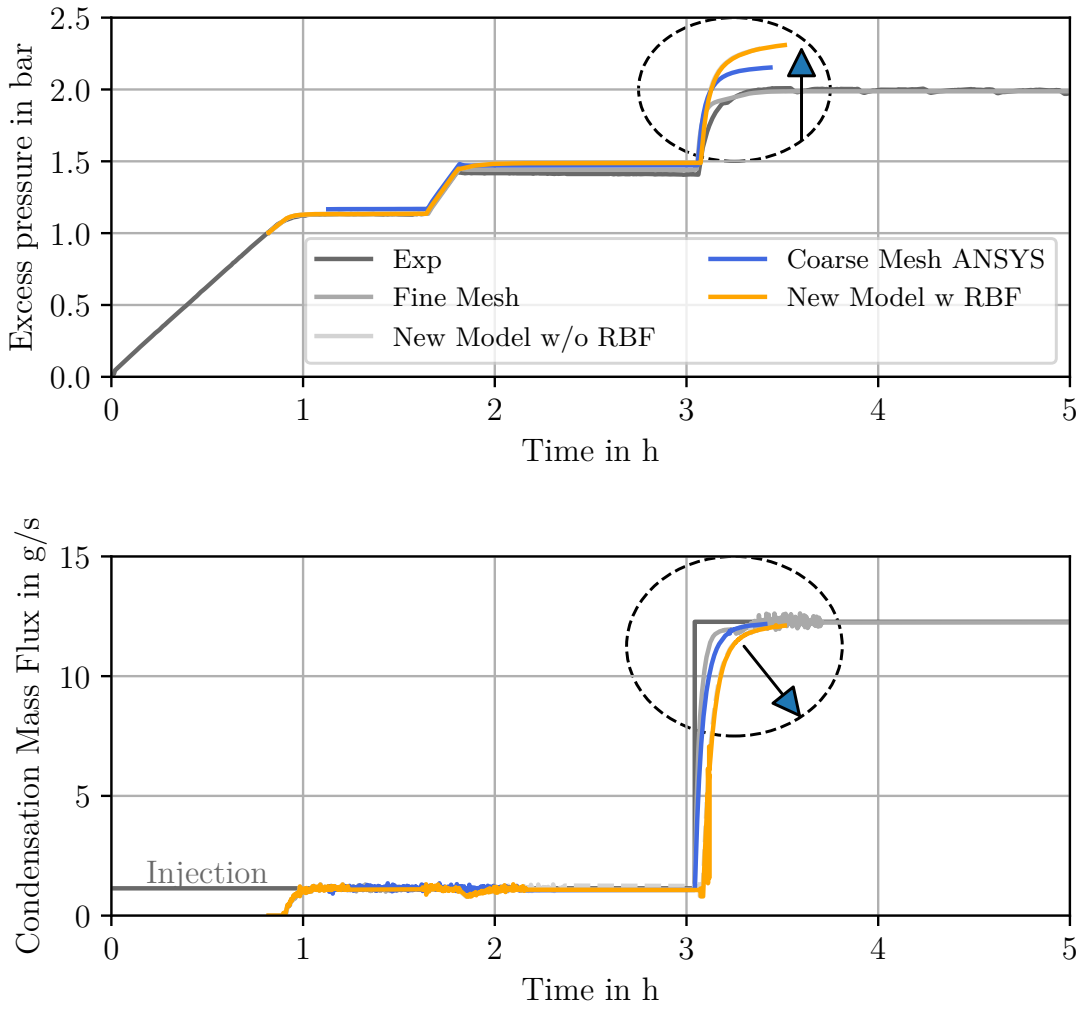

Figure 5.24: Measured and simulated time histories of the pressure and the condensation mass flux during the TOSQAN ISP47 experiment

All three coarse grid simulations correctly reflect the global behavior of the facility during the course of the experiment, as can be seen from figure 5.24. However, all three simulations also show considerable errors in the pressure curves compared to the experiment and the fine grid simulation. While this error is comparatively small during the initial pressure build-up and the first steady state, it is much larger during the second transient and the second steady state with up to 0.5 bar. It is also noticeable that the two calculations performed with the new wall function approach (w RBF, green and w/o RBF, orange) do not differ from each other. Hence, the non-equilibrium factors do not show a significant influence on the global simulation results of the experiment. The reason for this is that the flow at the vessel wall is outside the parameter range of the radial basis functions.

To identify why the boundary conditions are outside of the parameter range of the wall function approach, figure 5.25 shows these input variables at a single point in time during the second steady state and compares the results of the fine mesh simulation (reference) with those of the coarse mesh simulation. Here the fine mesh simulation shows that both FG^+ (bottom, right) and $\dot{q}^+$ (bottom, left) lie within the parameter range of the wall function approach resulting from the SETCOM experiments. The coarse mesh simulation show that the input data for the wall function significantly exceed the parameter range for the majority of the vessel surface, especially with regard to FG^+.

In order to show the reason for the deviation of the input parameters between the meshes, the wall shear stress (top, left) and the shear velocity (top, right) are also shown in figure 5.25. The data show that the wall shear stress in the area of the cooled wall is approximately one third of the fine mesh value on the coarse mesh. This error translates to a factor of 0.6 in u_τ, 1.8 in $\dot{q}^+$ and a factor of 5 in FG^+. This again emphasizes the importance of a correct prediction of the wall shear stress for the overall results of the new wall function approach.

As already discussed in section 5.2, there are multiple sources of error that lead to an erroneous calculation of the wall shear and the other wall fluxes. One important source of error is that it is not possible to integrate the new turbulence wall function into ANSYS CFX. Hence, the effective viscosity, described by equation 5.1, is not calculated correctly by the existing approach. This heavily influences the calculation of the wall shear, as can be seen in figure 5.25 top left.

$$\mu_{eff} = \mu + \mu_t \tag{5.1}$$

Another important point that has limited the ability of ANSYS CFX to converge towards the correct solution is the application range of the new model. Even though the fine mesh solution is located within the application range the coarse mesh solution fails to converge towards this solution, as can be seen from figure 5.25. An improved prediction of the non-dimensional quantities and thus the wall fluxes by the wall function would potentially increased the accuracy of the simulation results on the coarse mesh even for the incorrect input data. Also, this improved prediction could help the CFD-code to converge towards the correct solution improving the simulation results even further. Thus, it would have been helpful for the solution in multiple ways if the new model

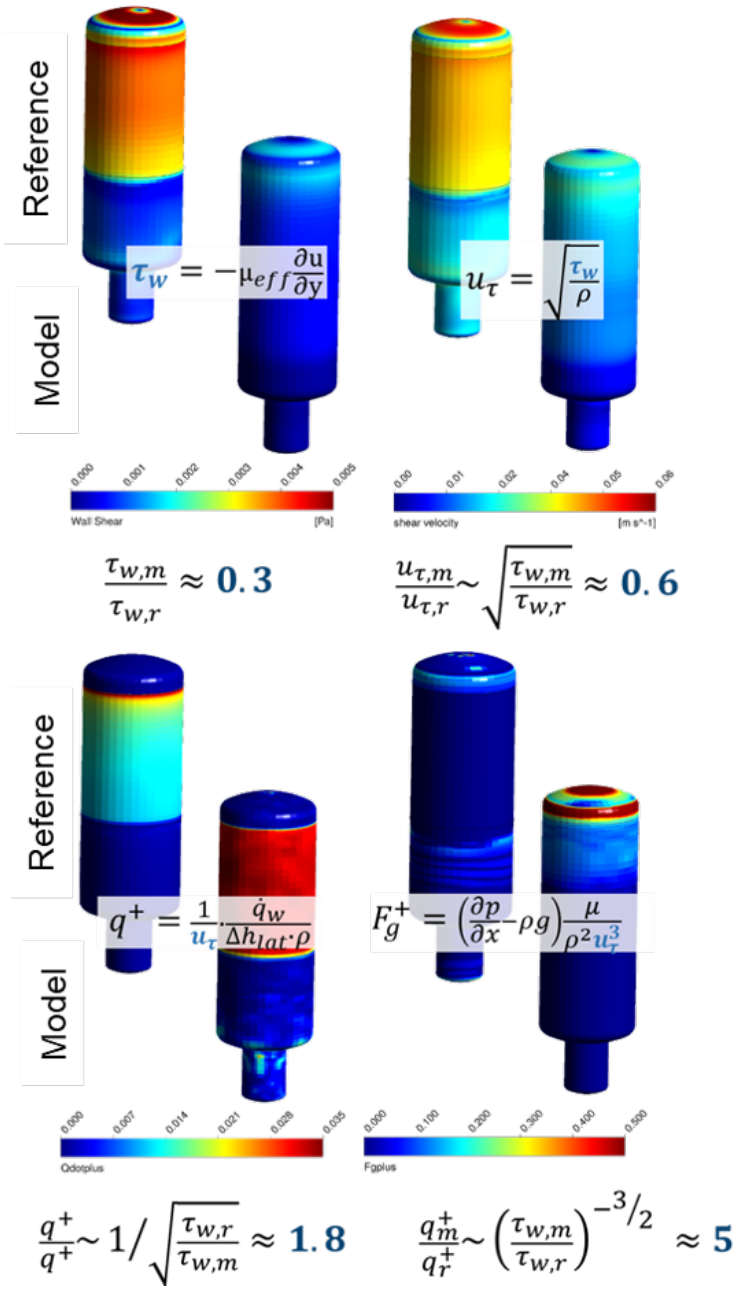

Figure 5.25: Comparison of the wall shear and its propagation into the input parameters of the new model between the fine mesh (Reference) and the coarse mesh simulation (Model)

would have been active for the input parameters currently achieved on the coarse mesh. Therefore, an expansion of the application range of the new model beyond its current

application range is an important task in the future model development process. One way to do this is to use fine mesh simulations to create additional input data for the model beyond this operating range. Another option is to allow the new model to extrapolate results beyond its application range, rather than falling back to the standard model.

Overall, figure 5.25 shows that under the ideal conditions of the fine mesh simulation, the TOSQAN ISP47 experiment is well within the parameter range of the new wall function approach. However, under the non-ideal conditions of the coarse mesh simulation conditions outside the parameter range of the model are present and consequently the new wall function approach cannot improve the calculation result.

In addition to the comparison of the global variables, a comparison of the results based on local measurement values has also been carried out. For this purpose, figure 5.26 shows the near wall velocity profiles in 4 m vessel height in the second stationary state. The simulation results are averaged over at least 20,000 time steps. This averaging is necessary because the flow in the TOSQAN vessel is highly transient, contrary to the assumptions made prior to the simulations. This is especially true for the steam jet, which is subject to strong directional fluctuations in all experimental phases caused by the interaction with the convection loops. These fluctuations also repeatedly caused the jet to impinge on the wall, so that the velocity profile there is clearly influenced by the jet. Accordingly, only a temporal averaging of the data leads to a meaningful result. No statement can be made about a possible averaging of the experimental velocity results obtained by means of LDA on the basis of the available test documentation [Malet et al., 2006]. However, it is likely that a temporal averaging was performed in the measurements.

The velocity profiles also show a good agreement between the experiment (dark gray dots) and the fine mesh simulation (gray curve) for the local level, both with regard to the maximum of the velocity profile near the wall and its shape. This observation again shows that the TOSQAN experiment of the ISP-47 can be well reproduced with CFD methods with a sufficiently good mesh resolution. For all the coarse mesh simulations performed, the velocity profiles, as well as the pressure curves, show a clear deviation from the experimental result and the fine mesh simulation, both with regard to the shape and the maximum of the velocity profile.

In contrast to the global view based on the pressure curves, the local velocity profiles show differences between all three coarse mesh simulations. From a local point of view, there are therefore not only differences between the simulations with the new wall function approach and the standard wall function approach (blue curve), but also between the simulations with (orange) and without (light gray) use of the radial basis functions and thus the non-equilibrium factors. This shows that the radial basis functions are at least locally and temporarily active during the simulation of the TOSQAN experiment and that they can influence local quantities during the simulation of the experiment. However, the global results as well as the explanations in connection with figure 5.25 show that the effect of the non-equilibrium factors is locally limited and overall so small that they cannot influence the global behavior of the experiment.

In conclusion, it can be seen that the expectations of the experiment were not fulfilled, especially with regard to the simple flow. Instead, a highly transient total flow is formed by the interaction of the jet with the flow detached from the wall, even in the stationary

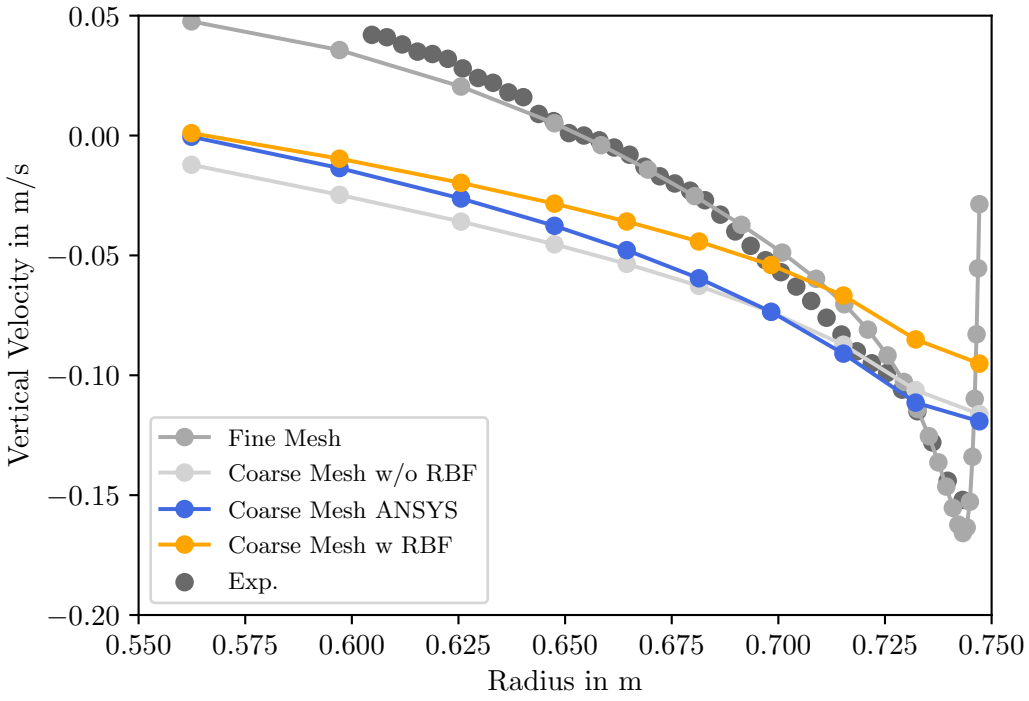

Figure 5.26: Near wall velocity profiles during the second steady state of the TOSQAN ISP47 experiment in 4 m vessel height

states. Contrary to expectations, the flow close to the wall is not driven by the momentum of the steam jet during the second steady state, but remains buoyant during the entire experimental transient. Additionally, the boundary conditions of the flow on the coarse grid were outside the parameter range necessary for the application of the non-equilibrium factors. This is one main reason for the lack of improvement in the calculation results with the new wall function and highlights the importance to extend the parameter range of the new model in future work. As already explained in section 5.2 there are two ways to achieve this: The first way is to use fine mesh simulations to create additional input data for the model beyond this operating range. The second way is to allow the new model to extrapolate results beyond its application range, rather than falling back to the standard model.

Nevertheless, two of the three goals for the integral validation using the TOSQAN-ISP47 experiment were achieved. Thus, it was shown that the model developed on the basis of a flow channel is technically also functional in a vessel experiment. Additionally, it was demonstrated that the model provides results comparable to the standard wall function approach outside of its parameter range. Thus, it is shown that the new wall function approach has been implemented consistently and can be used for containment applications in principle once the turbulent boundary condition can be addressed and the models application range is extended.

5.3.2. THAI HM2

5.3.2.1. The THAI vessel

The THAI test facility, constructed and operated by the German company Becker Technologies GmbH, is used to study a multitude of phenomena present in a pressurized water reactor containment atmosphere under severe accident conditions [Gupta et al., 2010]. These include thermal hydraulics, hydrogen transport and combustion, aerosol transport and deposition, and iodine transport and chemistry.

The facility, as depicted in figure 5.27, consists of a large upper and a smaller bottom cylinder, which is also called the sump. The facility has a total internal volume of 60 m^3, a total height of 9.2 m, a sump height of 1.24 m, the top cylinder has an internal diameter of 3.156 m and the sump has an internal diameter of 1.368 m. The vessel can be sealed from the environment. A maximum operating pressure of 14 bar and a maximum operating temperature of 180 °C can be achieved.

The internal volume of the THAI test facility can be further subdivided by the use of optional internal structures. These structures, which were used for the HM2 test, are an inner cylinder and four condensate trays [Gupta et al., 2010]. The ends of the inner cylinder, both of which are open, are located at a height of 2.155 m for the lower end and 6.245 m for the top end. The cylinder has an inside diameter of 1.38 m and an outside diameter of 1.4 m. The condensate trays are located between the inner cylinder and the vessel walls at a height of 4.02 m. Each tray blocks the entire radius of the gap for 60° of the vessel's circumference, thus the trays block 67 % of the flow area in total (see figure 5.29). With these structures, the THAI vessel is subdivided into five volumes (as can be seen from figure 5.27): The dome, the upper annulus, the lower annulus, the inner cylinder, and the sump.

The wall temperature of the THAI facility can be controlled by pumping heated mineral oil through the walls. However, the walls were not heated for the HM2 test [Gupta et al., 2010].

The THAI test facility can be equipped with several different gas injection devices. For the HM2 test, two were present(as can be seen from figure 5.27): First, a gas release pipe used to inject hydrogen or helium with an inner diameter of 28.5 mm at a height of 4.8 m and a distance from the center axis of 1.15 m. Second, a vertical steam injection nozzle with a diameter of 138 mm at a height of 1.8 m directly at the center axis of the vessel. Steam is supplied to the vessel by a steam generator with a power of 110 kW supplying saturated steam at a pressure of 6 bar. The steam mass flow is measured by a rotameter-type transducer and its injection temperature is measured by a thermocouple at the steam release site.

For the HM2 test, the THAI facility was instrumented with 242 thermocouples in the gas and on the surface of the vessel wall and the inner cylinder. Hydrogen concentrations were measured at 15 locations by a heat conductivity measurement after the gas has been extracted from the vessel and dried. Flow velocities were measured by three vane wheel transducers at the top of the inner cylinder.

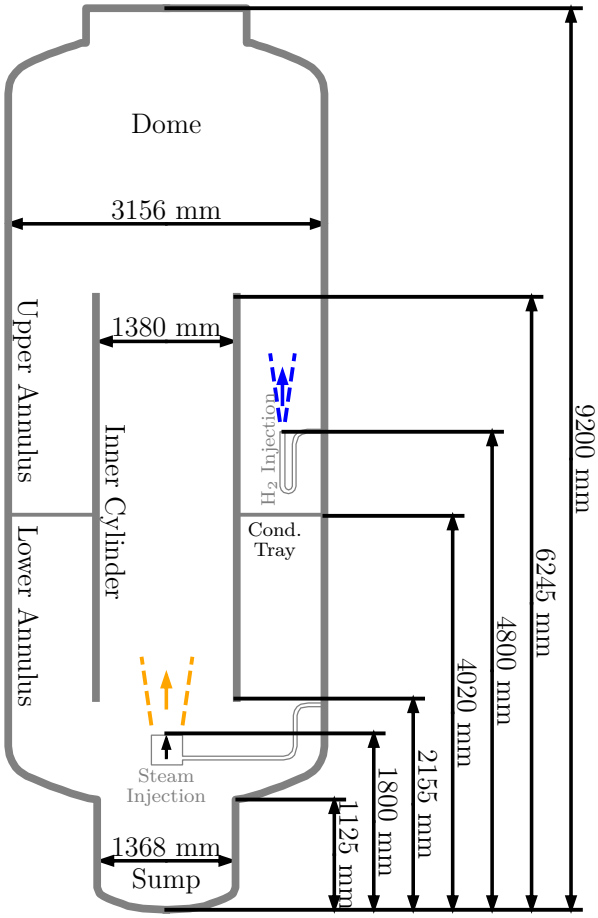

Figure 5.27: Drawing of the THAI test facility configured for the HM2 test [Gupta et al., 2010]

5.3.2.2. The THAI HM2 experimental procedure and simulation setup

The THAI experiment HM2 [Gupta et al., 2010] [Schwarz et al., 2011] was conducted within the OECD/NEA-THAI project [OECDNEA, 2010] and is the successor of the ISP-47 THAI experiment TH13 [Allelein et al., 2007]. In the framework of the ISP-47, clear evaluation uncertainties were determined for the computational programs of the last experimental phase "stratification resolution by deep steam injection" of the THAI experiment. Here it could not be clarified beyond doubt whether the observed deviations between simulation and experiment are due to model deficits or incorrectly specified boundary conditions [Royl et al., 2006] [Kelm et al., 2018]. To address these and other remaining questions from ISP-47, the Hydrogen Mixing (HM) test series of

the OECD/NEA-THAI project was carried out. The experiments essentially simplified the experimental design of the erosion phase, i.e. instead of an eccentric horizontal, a central vertical steam injection was realized, as can be seen in figure 5.27. Furthermore, the instrumentation was refined and possible differences in the use of helium instead of hydrogen were investigated.

Within the scope of this thesis, the experiment was considered as an application-oriented validation case and was simulated with the new model approach to demonstrate its applicability to complex three-dimensional mixture transients with dynamically changing boundary conditions. The experiment is divided into three phases. Prior to the first phase, the vessel is purged with nitrogen to minimize the risk of a hydrogen combustion. In phase 0, a stable hydrogen stratification is built up in the upper vessel dome based on ambient conditions (1 bar, 20 °C). The total hydrogen mass injected is 1.203 kg This phase was well depicted by the model and is not discussed further in the following because no condensation occurs.

In phases 1 and 2, steam ($24\,\mathrm{g\,s^{-1}}$) is fed into the inner cylinder from below through the central nozzle (see figure 5.28 and figure 5.27). During both phases the steam has a temperature of about 110 °C. Due to its buoyancy, the jet turns into a plume flow after a short distance. In the first phase, the steam plume stagnates inside the inner cylinder since its density is greater than that of the hydrogen stratification. The steam fed into the system condenses on the inner cylinder, introducing a local circulation or a mixing process within the inner cylinder. After a short period of time, the layer within the inner cylinder has mixed to such an extent that the steam/H_2/N_2 mixture can spread radially from the upper opening of the inner cylinder. Since the gas mixture is heavier than the H2 stratification above it, but lighter than the gas in the annular space, there is still no global circulation. Instead, the condensation of steam on the cold vessel wall induces local circulation and mixing in the annulus (see figure 5.28 top).

As soon as the gas in the annular space is mixed to such an extent that its density is the same inside and outside the lower opening of the inner cylinder, phase 2 begins and a global circulation between the inner cylinder and the annular space is established, which erodes the hydrogen layer (see figure 5.28 bottom).

It is to be expected that it is difficult for computational programs to find the exact time for the transition between both phases. However, for the purpose of validation, the phenomenology, i.e. the separation of the two phases, as well as the temporal development of the measured variables (gradients) should be reproduced consistently in the model.

The simulation was carried out in the same way as the simulation of the ISP 47 TOSQAN experiment. The test facility was meshed with a block structured hexahedron mesh without using symmetries. This was based on previous experience in the simulation of the ISP 47 THAI experiment [Kelm et al., 2018]. Figure 5.29 shows the meshes used. A fine calculation mesh with very good resolution of the boundary layer ($y^+ <2$, > 30 cells in the boundary layer) was used as a reference. To test the new model, a mesh with a coarser boundary layer resolution of $20 < y^+ < 80$ is used.

A coarser grid could not be used because the dimensionless wall distance changes continuously due to the dynamic transient as well as the changing boundary conditions, and model errors due to a too low boundary layer resolution with only one cell should be

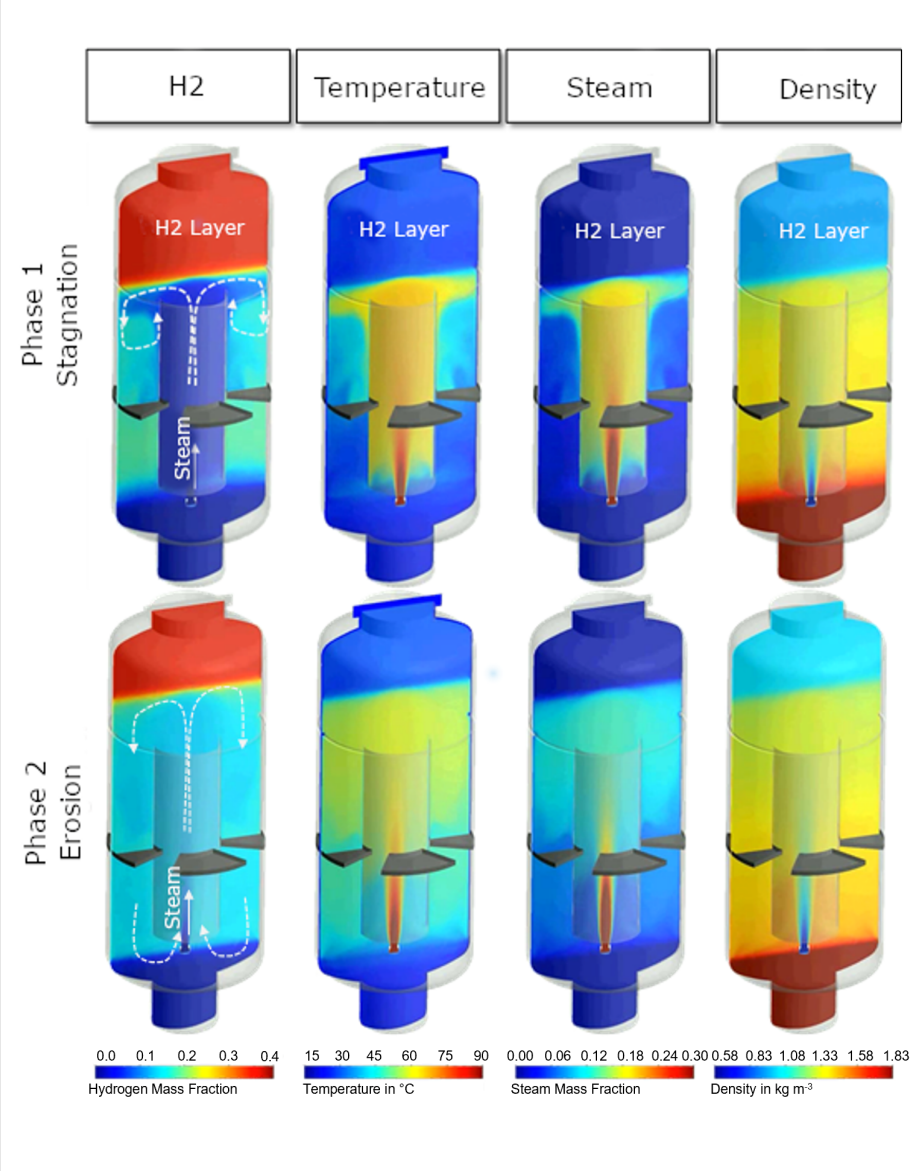

Figure 5.28: Exemplary distributions of the hydrogen mass fraction, temperature, steam mass fraction, and density during phase 1 (top) and phase 2 (bottom) of the THAI HM2 experiment

avoided. The mesh was refined near the wall, along the trajectory of the steam plume and in the area of the hydrogen stratification (see figure 5.29 right) to resolve the gradients in the flow.

A calculation model analogous to the TOSQAN experiment (see section 5.3.1) is used. Sensitivity studies showed a clear influence of the modeling of the vapor injection (jet-plume transition, as well as entrainment of surrounding fluid), the volume condensation

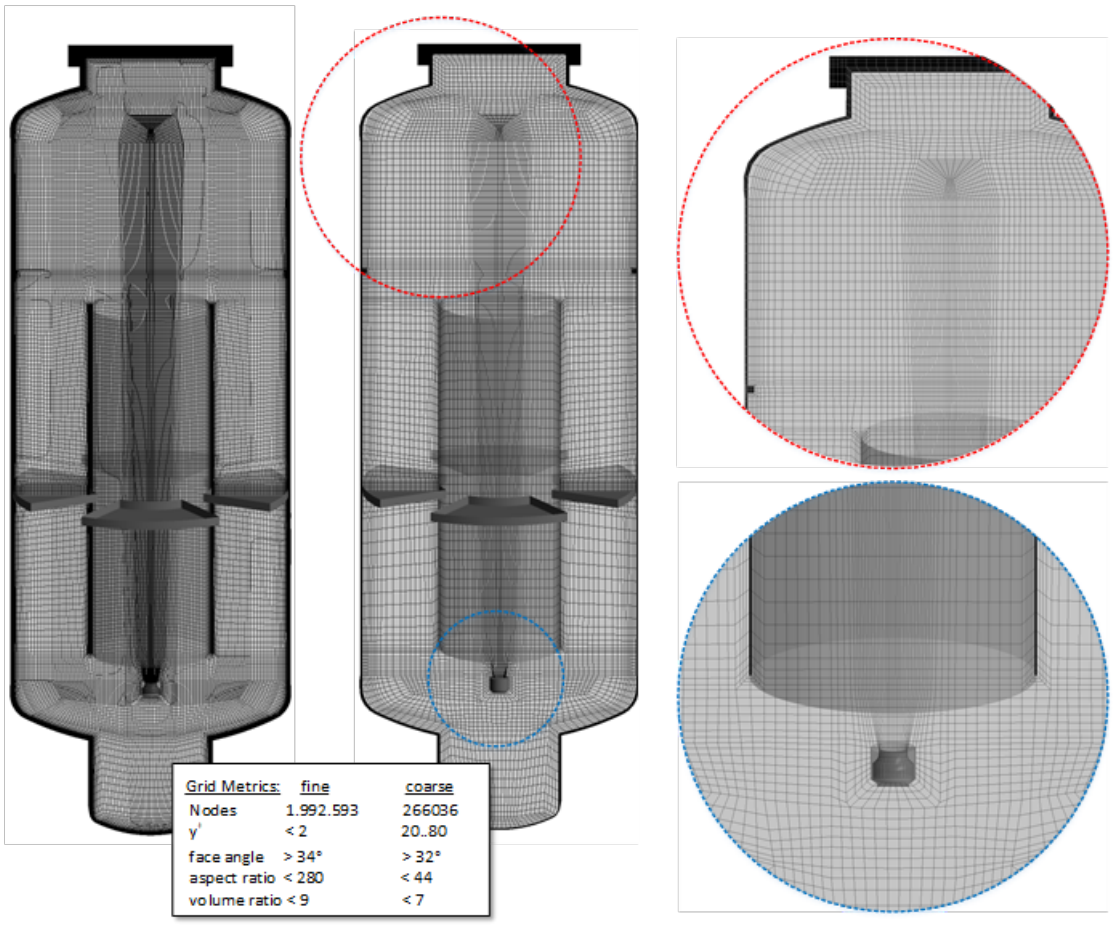

Figure 5.29: THAI-HM2 - Fine reference Mesh (left), mesh with coarse boundary layer resolution (center) and details of the nozzle as well as dome area (right)

(local density change of the gas mixture) and heat radiation (gas temperature and relative humidity) on the transient. An optimal modeling could not be identified due to opposing effects. Thus, some assumptions regarding these effects have been introduced in the model in order to obtain reasonable calculation results in a reasonable time frame. This is justified because the focus of the investigation does not lie on these effects but on the behavior of the near wall flow.

Therefore, a simplified block profile was assumed for the velocity at the steam nozzle, the absorption coefficient for steam was set as gray with a value of $1.0\,\mathrm{m}^{-1}$, and volume condensation was not considered. These model simplifications lead to a model error, which can be recognized as a deviation between reference simulation and the experiment. In the following, the results obtained on the coarse grid are therefore primarily compared with the reference calculation; the experimental values are only used as a guide.

5.3.2.3. The THAI HM2 simulation results and discussion

For an integral evaluation of the different simulations, the development of the vessel pressure (see figure 5.30) can be used. It is mainly based on the global energy and water/steam balance and is thus influenced by the wall heat transfer and the condensation rate. The temporal development of the pressure curve is therefore a measure for the integral condensation rate.

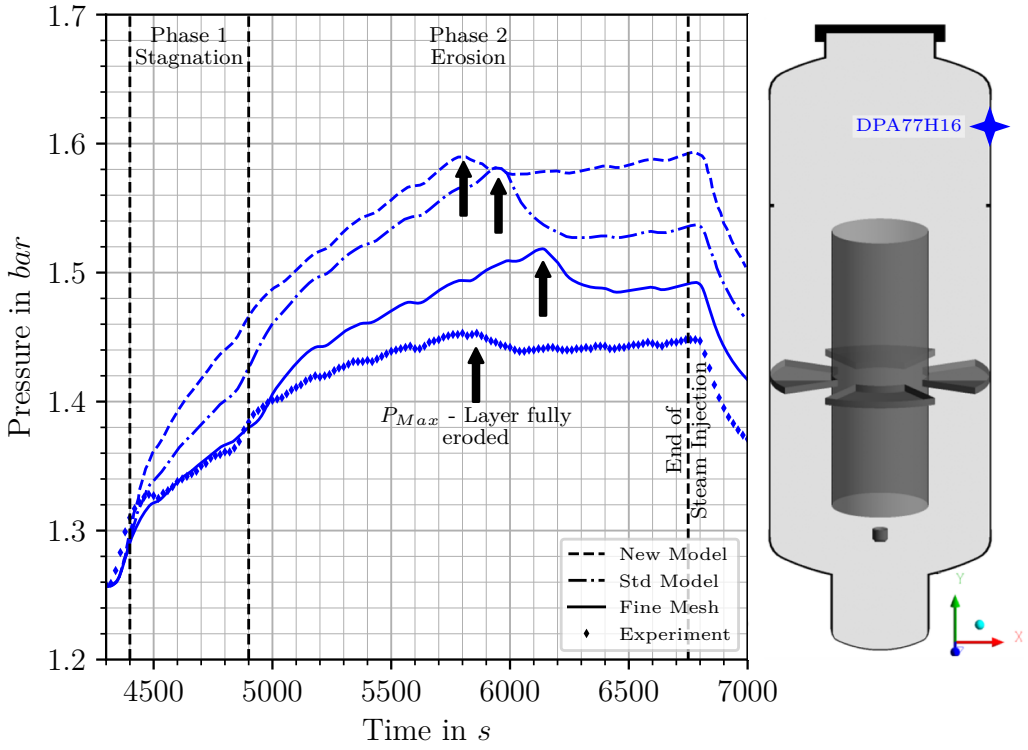

Figure 5.30: THAI-HM2 Pressure during the steam injection

The reference simulation reproduces the stagnation phase (1), i.e. the condensation on the inner cylinder, well, but deviates increasingly in the erosion phase due to the model simplifications mentioned above and underestimates the condensation rate. The ANSYS wall condensation model with standard wall functions ('Std Model') underestimates the condensation rate even in the stagnation phase. This trend continues in the erosion phase, i.e. the deviation from the reference simulation increases continuously. The new model ('New Model') shows the clearest deviation from the reference simulation in the stagnation phase and calculates too little condensation on the inner cylinder. In the mixing phase, the pressure curves of the reference simulation and the new model are almost parallel, indicating a consistent representation of the wall condensation on the vessel wall. The maximum vessel pressure is reached shortly before the full dissolution of the stratification. After this point, the entire wall surface of the vessel is available

for wall condensation and consequently the pressure drops. The different mixing times already make it clear that wall condensation is not the only parameter influencing the mixing transient.

There are no direct measurements available to evaluate the local condensation rates. However, an indirect evaluation based on the increase of the structure temperature, which is mainly due to latent heat, is possible. Figure 5.31 depicts the temperature development of the inner cylinder. Data of further sensors can be found in figure D.4 in appendix D.2.

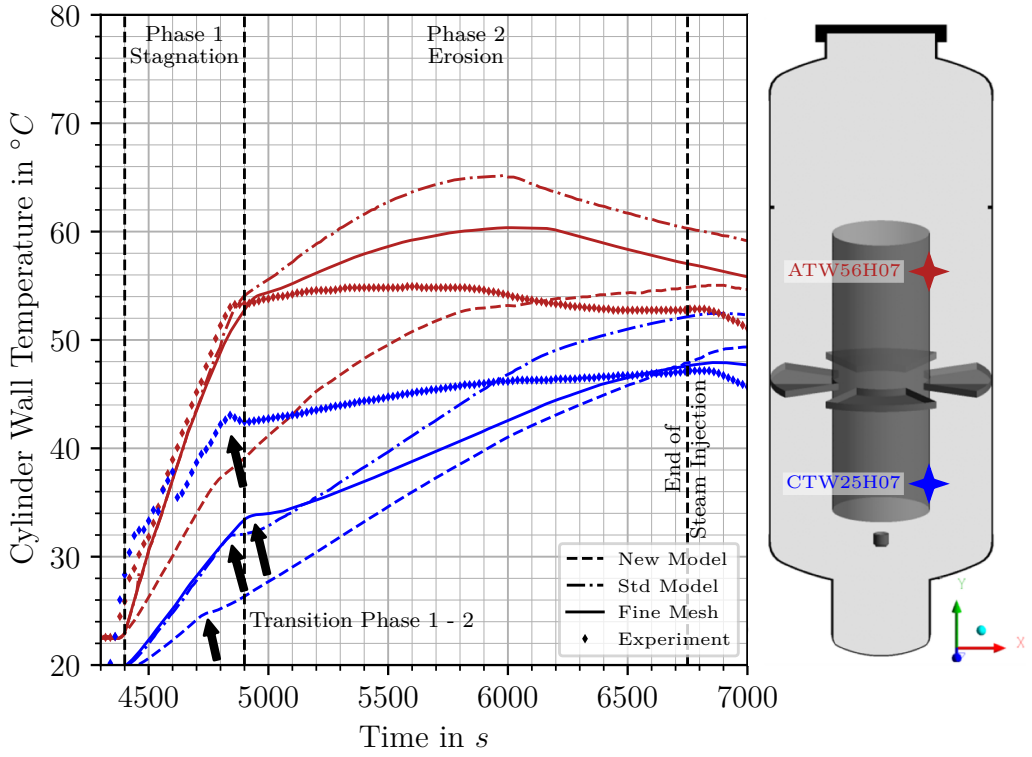

Figure 5.31: THAI-HM2 Development of the cylinder wall temperature

The reference simulation reflects the almost uniform heating rate of the upper part of the inner cylinder and thus also the local condensation rate very well (see sensor ATW56H07), but underestimates the rate somewhat in the lower part (see sensor CTW25H07). The standard model ('Std Model') shows a heating rate comparable to the reference simulation. The new model ('New Model') shows a visibly lower heating rate and temperature at the end of the stagnation phase. The change of the heating rate (arrow mark) indicates the transition from stagnation to global circulation. Again, the two coarse grid simulations show visible deviations from the reference simulation. While the experiment shows quasi-constant wall temperatures of the inner cylinder in the mixing phase and thus no wall condensation, all simulations show a further increase of the wall temperature, i.e. further condensation. This heating is the lowest for the reference simulation, thus this

simulation is the closest to the experiment.

Shortly after the start of the steam injection, the stratification within the inner cylinder has already mixed to such an extent that steam can flow to the vessel wall and condense there. This is demonstrated by the increase of the vessel wall temperatures in the lower part of the vessel (see figure 5.32). Data of further sensors can be found in figure D.5 in appendix D.2.

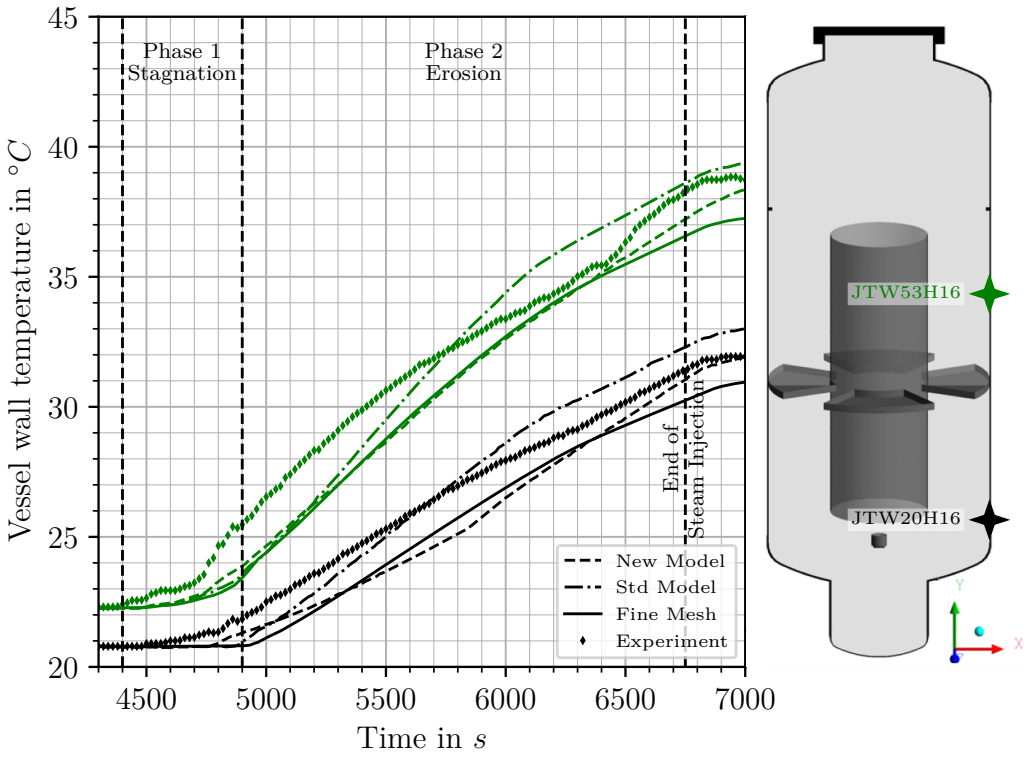

Figure 5.32: THAI-HM2 Development of the lower vessel wall temperature

The increasing propagation of the vapor-rich gas mixture is shown by the successive temperature increase of the temperature measurement points JTW53H16 and JTW20H16 at the lower vessel wall. Note that the condensation on the vessel wall in the first phase is visibly underestimated by all simulations, which is balanced out in the mixing phase. Here, the new model ('New') shows the highest heating rate respectively wall condensation rate of all models.

The wall temperatures in the vessel dome increase as soon as the stratification has been locally eroded and steam can condense on the wall (see for example sensor JTW64H16 in figure 5.33). Correspondingly, the temperature at the upper manhole cover rises last after complete stratification dissolution, as shown by sensor DTW92M00. This measurement point shows that the temperature rise much higher than in the simulations and thus the condensation rate at the upper vessel wall is also underestimated in all simulations.

However, if only the gradients of the two coarse grid simulations are compared with the reference calculation, an improved prediction of the condensation rate for the new model can be determined, i.e. the curves exhibit a parallel shift. Data of further sensors can be found in figure D.6 in appendix D.2.

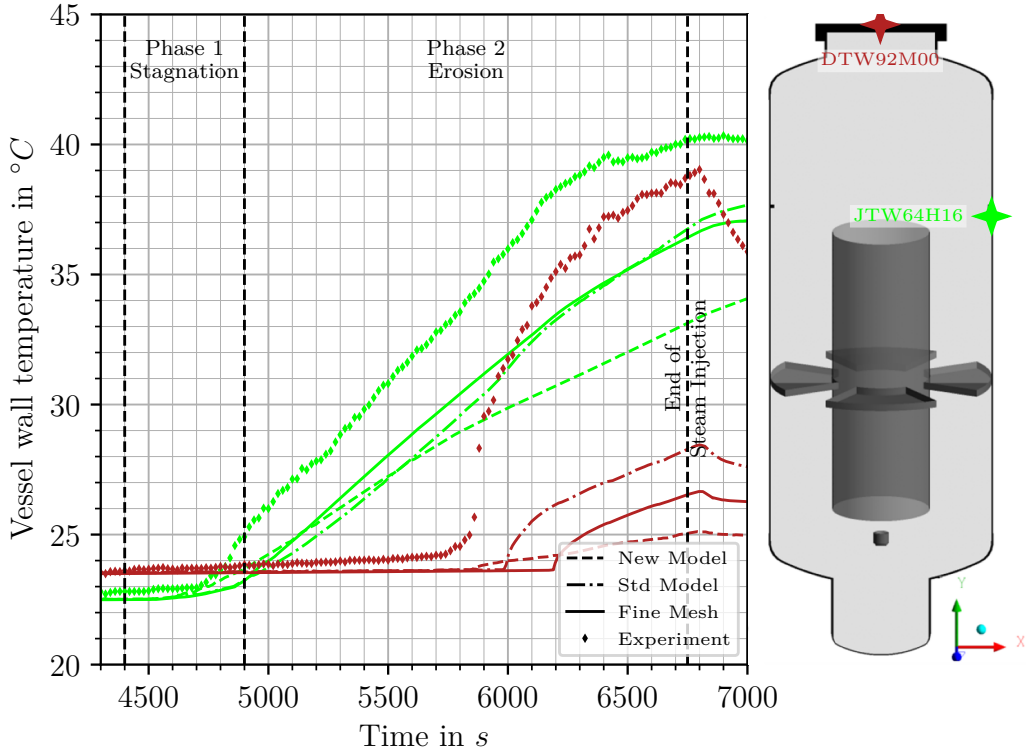

Figure 5.33: THAI-HM2 Development of the upper vessel wall temperature

The previously discussed deviations in the condensation rate lead to a local deviation of the mixture density and thus affect the buoyancy superimposed mixing process. This process is illustrated by the time evolution of the hydrogen concentration in the vessel in figure 5.34. By means of the sensor ACH31H10 in the lower part of the annular space the transition between phase 1 and 2 can be traced. The increase of the hydrogen concentration at this position indicates an almost complete homogenization of the mixture density inside and outside the inner cylinder and is very well represented in the reference simulation. Similar to the wall condensation rate, both coarse grid simulations with the standard ('Std') and also with the new ('New') condensation model overestimate the mixture, resulting in a shorter stagnation phase.

In the second phase, however, the best result for the coarse grid simulation with the new model can be observed at the sensor location DCH87M00, whereas the reference simulation visibly underestimates the mixing time. In the equilibrium state after the stratification resolution, all simulations show a lower mean hydrogen concentration than

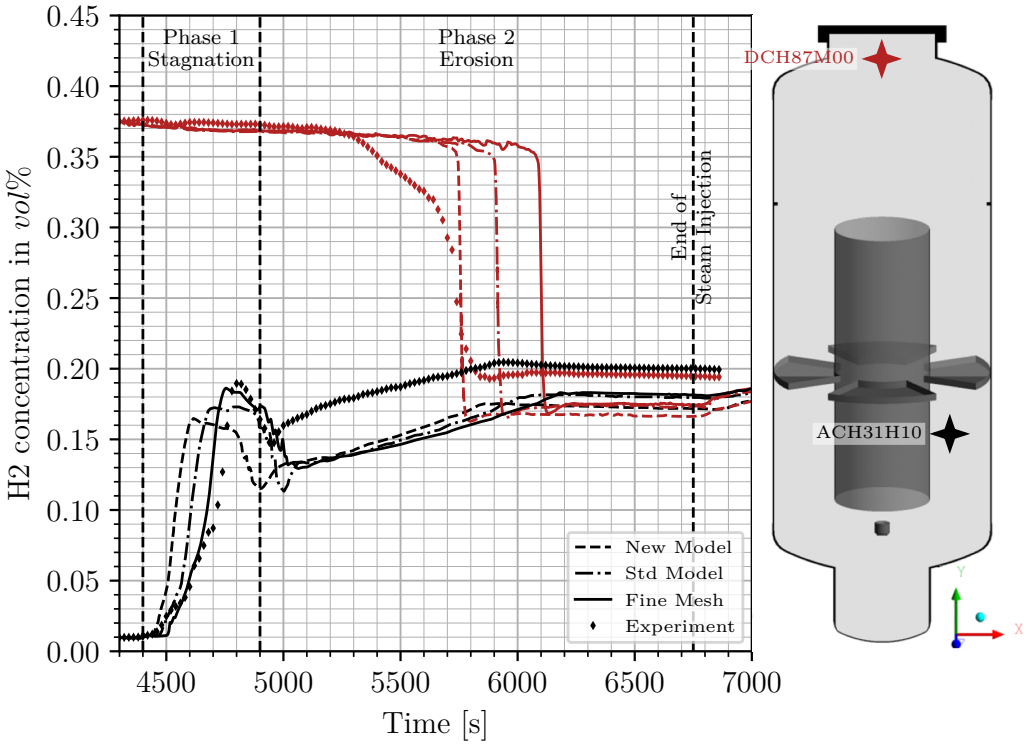

Figure 5.34: THAI-HM2 Development of the hydrogen distribution during the mixture transient

the experiment. This can be explained by the higher saturation pressure or steam mass fraction due to the overestimated vessel pressure. Data of further sensors can be found in figure D.7 in appendix D.2.

From the previous observation it is evident that model errors in both coarse grid simulations accumulate or balance out during the transients, which prevents a differentiated evaluation of the wall condensation modeling. In summary, however, it can be stated that the new model also exceeds its definition range in the HM2 experiment, which can be traced back to an inconsistent calculation of the wall shear stress (or turbulent boundary conditions, see figure 5.25). Thus, the model falls back to the original wall model and prevents an evaluation of the actual model improvement by means of the new wall function approach.

Another important point to avoid this fallback in future work is the extension of the application range of the new model, as already discussed in sections 5.2 and 5.3.1. An extended application range will allow the model to improve the prediction of the wall fluxes in many situations, even if the input data do not perfectly match the input data of an experiment or fine mesh simulation. This is similar to the situation presented in section 5.2 where the local validation results for the SETCOM facility showed an improvement of the wall flux calculation by the new model even so there were differences

between the model input data between the fine and the coarse mesh calculations. As a consequence this improved prediction of the wall fluxes will in turn lead to an improved prediction of the input data and thus help the CFD code to converge to a better solution. Thus, an extension of the application range of the model beyond the operating range of the SETCOM facility is of very high importance for future work as it is one of the main reasons that did not allow to show model improvements due to the new model in the application-oriented validation calculations of this thesis. As already explained in sections 5.2 and 5.3.1 there are two ways to achieve this: The first way is to use fine mesh simulations to create additional input data for the model beyond this operating range. The second way is to allow the new model to extrapolate results beyond its application range, rather than falling back to the standard model.

Nevertheless, the basic applicability of the new approach to an application-oriented three-dimensional dynamic mixture transient is shown. The small difference to the previous modeling or reference calculation also confirms the consistent implementation of the new approach. Thus, the new wall model provides a solid basis for the further improvement of wall function modeling. In addition to the further improvement of the implementation in ANSYS CFX and the extension of the application range of the new model, the transfer of the model into the open source CFD package, like Open Foam, should be carried out in future work. The direct source code access would allow for a better integration into the solver and thus a better evaluation of the model approach.

6. Summary and Conclusion

6.1. Summary

There is an increasing demand for the application of CFD to investigate the behavior of the containment of a nuclear reactor under loss of coolant accident conditions. However, the large geometric and temporal scale as well as the multitude of physical phenomena involved, make such calculations computationally expensive up to the point where the cost becomes prohibitive. One way to reduce this computational cost is to reduce the required near-wall grid resolution by using suitable subgrid models, so-called wall functions.

In the containment, the near-wall flow, also known as the boundary layer, can be subjected to a variety of effects which are not covered by the standard wall functions due to the heat and mass transfer induced by wall condensation. The two most prominent of these effects are buoyancy and the wall normal velocity, also known as the suction effect. The interaction between the different boundary layers is also not covered by most wall functions available in the literature.

The new wall function approach presented in this thesis incorporates the momentum, heat, and mass transfer as well as turbulence effects present in a boundary layer in the wall condensation regime. It was also specifically designed to include buoyancy effects and the condensation induced wall normal flow. The development of the new wall function approach was done in three steps. First, a covering set of non-dimensional parameters has been derived from the boundary layer conservation equations that allow the integration of buoyancy and suction into the new wall functions. Then, a set of non-equilibrium factors was derived from experimental as well as validated fine mesh simulation data. This allows the additional effects to be incorporated into the standard wall functions. While the goal was to use experimental data for all required wall functions a sufficient amount of experimental data is only available for the velocity wall function as of yet. Finally, the model data are combined into multivariate algebraic functions utilizing the concept of radial basis functions which allows for an easy and computationally fast integration of the new wall functions into different CFD codes. In addition, the new wall function has been implemented into the CFD code ANSYS CFX for its verification and first validation. However, due to the lack of an appropriate interface, the turbulence wall function could not be included in the implementation.

The qualitative investigation of the new wall function approach shows that all four new wall functions yield the expected behavior regarding the influence of buoyancy and the wall normal flow induced by wall condensation. However, the new velocity wall function still presented some flaws. In some locations, the wall function showed erratic behavior due to the scatter of the experimental input data. In addition, the new velocity wall function showed the tendency to return to the standard wall function in the parameter area of a non-dimensional wall distance y^+ larger than 60 and a non-dimensional gravity forceFG^+ larger than 0.03. While this behavior is not physical and should be addressed in future work, the exhibited behavior is still an improvement compared to the standard wall function approach.

The comparison of the standard and the new wall function with the fine-mesh SETCOM

simulation results shows that the new model generally yields better results, especially under containment like flow-conditions. The global investigation showed that the new wall function leads to significant improvements of the wall flux calculations where the standard wall function yields large errors, and yields similar results if the standard wall function already yields sufficient results. The detailed discussion of the local results of two characteristic SETCOM experiments confirms this finding. There remain two main sources error in the wall flux calculations when the new wall function is used. The first error source are incorrect input data, y^+, $\dot{q}^+$ and FG^+, for the wall functions. These three parameters are especially sensitive to the value of the wall shear and consequently the shear velocity, thus emphasizing the importance of the correct prediction of the wall shear and the iterative nature of the wall flux calculations via wall functions. The second source of error are errors in the data other than the non-dimensional quantities that influence the wall flux calculation, like the velocity at the first mesh node off the wall or the temperature difference between this node and the wall surface. These errors have many different sources, such as an incorrect calculation of the near wall turbulence, and are consequently difficult to avoid. Nevertheless, the new model generally improves the wall flux calculation in the simulations of the SETCOM facility on the medium and the coarse mesh, both globally and locally.

The simulations of the two integral tests TOSQAN ISP47 and THAI HM2 do not show the anticipated improvements using the new wall function approach. This is due to the fact that the new model is active only locally and for a short time duration, because the boundary conditions of the flow on the coarse grid are mostly outside the parameter range necessary for the application of the non-equilibrium factors. Thus, the the model falls back to the original wall model and prevents an evaluation of the actual model improvement by means of the new wall function. Nevertheless, the basic applicability of the new approach to an application-oriented three-dimensional dynamic mixture transient is demonstrated. Thus, it is shown that the model developed on the basis of a flow channel can be transferred to vessel applications. Additionally, it is shown that the model provides comparable results to the standard wall function approach outside of its parameter range. Thus, it is shown that the new wall function approach has been implemented consistently and can, in principle, be used for containment applications.

The results of the first validation show that the newly developed wall function approach has the potential to enable computationally affordable CFD calculations of a full containment under LOCA conditions with an accurate prediction of the near-wall momentum, heat and mass transfer, even though some work remains to be done.

6.2. Outlook

The new wall function approach presented in this thesis shows promising results in its qualitative assessment as well as in the coarse mesh simulations of the SETCOM facility. However, the application-oriented simulations of the TOSQAN ISP47 and THAI HM2 experiments do not provide sufficient evidence of model improvements due to the new wall function approach. The reason for this is the limited application range of the model, due to which the model was only active locally and for a limited time duration. This leaves

room for future improvements upon which a more detailed evaluation can be founded. Thus, one of the primary goals of the future development should be to extend the range of application range of the new model. This can be done, for example, by incorporating the results of additional SETCOM experiments currently underway. In addition, application range of the new model could be further extended by the use of simulation data to cover parameters beyond the operational range of the SETCOM facility to enable the model to be used for the target application.

An additional option to extend the application range of the new model in future work is to allow the model to provide extrapolated results beyond its application range, rather than falling back to the standard wall function. This would require using a different basis function for the RBF interpolation, since the current basis function was deliberately chosen to allow for the fallback to the standard model. The advantage of such an extrapolation approach is that the application range of the new model can be extended without the need for additional data. The disadvantage, however, is that the exact application range is not known exactly based on the input data, as is the case for the fallback option. Therefore, it becomes a necessary step in the validation process to specify the additional application range of the model, or at least to ensure that the intended application for the model falls into the extended application range created by the extrapolation. Thus, both approaches have their advantages and disadvantages. The currently used fallback option has a well known application range based on its input data, but its improvements in the modeling of the near-wall flow are limited to this application range. Meanwhile, using the new model to extrapolate results beyond the range of the input data can immediately expand the application range of the model. However, the physical and mathematical limits of this extended application range are no longer known and thus need to be identified in the validation process.

Another important aspect regarding the extension of the applicability range of the new wall function is the issue of inclined walls, which could not be covered in this work due to the lack of available experimental data. Thus, the new wall function is currently valid only for flows along vertical walls. However, the available experimental data (see [Allelein et al., 2019]) show a strong influence of the wall inclination on the velocity boundary layer. As discussed in this thesis, this is primarily due to the direct influence of buoyancy on turbulence, which is much stronger for flows along inclined walls than for flows along vertical walls. The addition of inclined wall effects to the model is of great relevance for the target application since, for example, the containment shell of a KONVOI type reactor is a sphere.

While the approximation functions for the non-equilibrium factors of the temperature and the steam species mass as well as the eddy viscosity ratio showed good agreement with the input data, some potential for improvement could be identified for the approximation function for the velocity non-equilibrium factors. First, the new velocity wall function showed an erratic behavior at some locations due to the scattering of the input data. Approaches to avoid this behavior would be a more rigorous selection of the experimental data points and a smoothing of the function, for example, via a least squares approach as presented by Fasshauer [Fasshauer, 2007]. Second, the new wall function shows a tendency to return to the standard wall function in a parameter area of FG^+ larger than 0.03

and y^+ larger than 60. To avoid this behavior more data centers of the approximation function should be positioned in this area. This could be achieved, for example, by simply increasing the number of data centers used for the approximation function or by introducing additional constraints on the relative position of the data centers.

In this thesis, the new wall function approach has been implemented into the commercial CFD code ANSYS CFX. A reliable and computationally inexpensive implementation of the wall function has been created. However, there are some limitations of the implementation which could not be overcome because ANSYS CFX as a commercial code offers only limited interfaces and no access to the source code. Especially, the implementation of the new turbulence wall function was not possible due to the missing interface. Therefore, it is recommended to implement the new wall function into an open source CFD code such as OpenFOAM, which offers more possibilities for the implementation due to the full access to the source code. Since the new wall function approach was specifically designed for a simple implementation, this should be a straightforward task and additional results obtained with another CFD code should yield further prove of the capabilities and validity of the approach.

7. References

[Allelein et al., 2007] H.-J. Allelein, K. Fischer, J. Vendel, J. Malet, E. Studer, S. Schwarz, M. Houkema, H. Paillère, and A. Bentaib. *International Standard Problem ISP-47 on Containment Thermal-hydraulics. Final Report.* Tech. rep. NEA/CSNI(2007)10. NEA; Committee on the Safety of Nuclear Installations, 2007.

[Allelein et al., 2019] H.-J. Allelein, A. Hundhausen, H. Müller, and S. Kelm. *Experimente und CFD-Modellentwicklung zu Wandkondensationsvorgängen im Sicherheitseinschluss (Projektnummer 1501489).* Research rep. 2019.

[Ambrosini et al., 2014] W. Ambrosini, N. Forgione, F. Merli, F. Oriolo, S. Paci, I. Kljenak, P. Kostka, L. Vyskocil, J. R. Travis, J. Lehmkuhl, S. Kelm, Y.-S. Chin, and M. Bucci. "Lesson learned from the SARNET wall condensation benchmarks". In: *Annals of Nuclear Energy* 74 (Dec. 2014), pp. 153–164. DOI: 10.1016/j.anucene.2014.07.014.

[ANSYS, 2016a] ANSYS. *CFX-Solver Modeling Guide. Release 17.2.* Canonsburg, PA, USA: SAS, INC, 2016.

[ANSYS, 2016b] ANSYS. *CFX-Solver Theory Guide. Release 17.2.* Canonsburg, PA, USA: SAS, INC, 2016.

[Arya, 1975] S. P. S. Arya. "Buoyancy effects in a horizontal flat-plate boundary layer". In: *Journal of Fluid Mechanics* 68.02 (Mar. 1975), pp. 321–344. DOI: 10.1017/s0022112075000833.

[Belt, 2019] A. D. Belt. "Konzeptionierung, Aufbau und Inbetriebnahme eines großmaßstäblichen Versuchsstands zur Untersuchung von Wandkondensation". PhD thesis. RWTH Aachen University, 2019.

[Bucci, 2009] M. Bucci. "Experimental and computational analysis of condensation phenomena for the thermal-hydraulic analysis of LWRs containments." PhD thesis. University of Pisa, Italy, 2009.

[Cebeci, 1970] T. Cebeci. "Behavior of turbulent flow near a porous wall with pressure gradient". In: *AIAA Journal* 8.12 (Dec. 1970), pp. 2152–2156. DOI: 10.2514/3.6079.

[Craft et al., 2004] T. J. Craft, S. E. Gant, H. Iacovides, and B. E. Launder. "A NEW WALL FUNCTION STRATEGY FOR COMPLEX TURBULENT FLOWS". In: *Numerical Heat Transfer, Part B: Fundamentals* 45.4 (Apr. 2004), pp. 301–318. DOI: 10.1080/10407790490277931.

[Dupont, 2017] J. Dupont. “Thin liquid film dynamics in a condensing and re-evaporating environment”. en. PhD thesis. ETH Zürich, 2017. DOI: 10.3929/ETHZ-A-010882077.

[Eaton et al., 2016] J. W. Eaton, D. Bateman, S. Hauberg, and R. Wehbring. *GNU Octave version 4.2.0 manual: a high-level interactive language for numerical computations*. 2016.

[Fasshauer, 2007] G. Fasshauer. *Meshfree approximation methods with MATLAB*. Singapore Hackensack, N.J: World Scientific, 2007. ISBN: 9789812706331.

[Favre et al., 1966] A. Favre, R. Dumas, E. Verollet, and M. Coantic. “Couche limite turbulente sur paroi poreuse avec aspiration”. In: *Journal de Mécanique* 5.1 (1966), pp. 3–28.

[Golub et al., 1965] G. Golub and W. Kahan. “Calculating the Singular Values and Pseudo-Inverse of a Matrix”. In: *Journal of the Society for Industrial and Applied Mathematics Series B Numerical Analysis* 2.2 (Jan. 1965), pp. 205–224. DOI: 10.1137/0702016.

[Götz et al., 2017] L. Götz, S. Kelm, and H.-J. Allelein. “Coupling Approach for the CFD Code CFX and the Lumped Parameter Code COCOSYS and First Results”. In: *Proceedings of the 8th European Review Meeting on Severe Accident Research*. ERMSAR 2017 (May 16–18, 2017). Severe Accident Research NETwork of Excellence (SARNET). Warsaw, Poland, 2017.

[Grotjans et al., 1998] H. Grotjans and F. Menter. “Wall Functions for General Application CFD Codes”. In: *Proceedings of the Fourth European Computational Fluid Dynamics Conference*. ECCOMAS 98. 1998, pp. 1112–1117.

[Gupta et al., 2010] S. Gupta, T. Kanzleiter, K. Fischer, G. Langer, and G. Poss. “Interaction of a Stratified Light Gas Layer with a Buoyant Jet in Containment: Hydrogen/Helium Material Scaling”. In: *Proceedings of the ICAPP ‘10* (June 13–17, 2010). San Diego, CA, USA, 2010.

[Han et al., 1997] Z. Han and R. D. Reitz. “A temperature wall function formulation for variable-density turbulent flows with application to engine convective heat transfer modeling”. In: *International Journal of Heat and Mass Transfer* 40.3 (Feb. 1997), pp. 613–625. DOI: 10.1016/0017-9310(96)00117-2.

[Hundhausen et al., 2017a] A. Hundhausen, H. Müller, S. Kelm, C. Druska, E.-A. Reinecke, and H.-J. Allelein. "CFD-GRADE MEASUREMENTS IN A CONDENSING BOUNDARYLAYER - RESULTS OF THE SETCOM FACILITY". In: *Proceedings of the 7th International Topical Meeting on Nuclear Reactor Thermal Hydraulics*. NURETH-17 (Sept. 3–8, 2016). Xi'an, Shaanxi, China, 2017.

[Hundhausen et al., 2017b] A. Hundhausen, H. Müller, S. Kelm, E. Reinecke, and H.-J. Allelein. "Towards CFD-Grade Measurements in a Condensing Boundary Layer - First Results of the New SETCOM Facility". In: *Proceedings of the 8th European Review Meeting on Severe Accident Research*. ERMSAR 2017 (May 16–18, 2017). Severe Accident Research NETwork of Excellence (SARNET). Warsaw, Poland, 2017.

[Kader, 1981] B. A. Kader. "Temperature and concentration profiles in fully turbulent boundary layers". In: *International Journal of Heat and Mass Transfer* 24.9 (Sept. 1981), pp. 1541–1544. DOI: 10.1016/0017-9310(81)90220-9.

[Kelm et al., 2016] S. Kelm, H. Müller, and H.-J. Allelein. "Importance of thermal radiation heat transfer modeling in containment typical flows". In: *Proceedings of the 6th Computational Fluid Dynamics for Nuclear Reactor Safety Applications Workshop*. CFD4NRS6 (Sept. 13–15, 2016). OECD NEA. Cambridge, MA, USA, 2016.

[Kelm et al., 2018] S. Kelm, H. Müller, and H.-J. Allelein. "A Review of the CFD Modeling Progress Triggered by ISP-47 on Containment Thermal Hydraulics". In: *Nuclear Science and Engineering* 193.1-2 (Sept. 2018), pp. 63–80. DOI: 10.1080/00295639.2018.1503858.

[Kelm, 2010] S. Kelm. "Kombination eines Gebäudekondensators mit H2-Rekombinatorelementen in Leichtwasserreaktoren". PhD thesis. Aachen: RWTH Aachen University, 2010.

[Kim et al., 2008] W. S. Kim, S. He, and J. D. Jackson. "Assessment by comparison with DNS data of turbulence models used in simulations of mixed convection". In: *International Journal of Heat and Mass Transfer* 51.5-6 (Mar. 2008), pp. 1293–1312. DOI: 10.1016/j.ijheatmasstransfer.2007.12.002.

[Lehmkuhl et al., 2016] J. Lehmkuhl, S. Kelm, M. Bucci, and H.-J. Allelein. "Improvement of wall condensation modeling with suction wall functions for containment application". In: *Nuclear En-*

gineering and Design 299 (Apr. 2016), pp. 105–111. DOI: 10.1016/j.nucengdes.2015.08.002.

[Lehmkuhl, 2018] J. Lehmkuhl. "Modellierung einer numerischen Wandfunktion für einphasige CFD-Simulationen in einem LWR- Sicherheitsbehälter". de. PhD thesis. RWTH Aachen University, 2018. DOI: 10.18154/RWTH-2018-231515.

[Mahaffy et al., 2015] J. Mahaffy, B. Chung, F. Dubois, F. Ducros, E. Graffard, M. Heitsch, M. Henriksson, E. Komen, F. Moretti, T. Morii, P. Mühlbauer, U. Rohde, M. Scheuerer, B. L. Smith, C. Song, T. Watanabe, and G. Zigh. *Best Practice Guidelines for the Use of CFD in Nuclear Reactor Safety Applications – Revision*. Tech. rep. NEA/CSNI/R(2014)11. OECD/NEA, Feb. 12, 2015.

[Malet et al., 2006] J. Malet, E. Porcheron, P. Cornet, P. Brun, O. Norvez, B. Menet, and L. Thause. *ISP-47 – STEP 1: TOSQAN – Mistra, Phase A: TOSQAN experimental results of the air-steam phase*. Tech. rep. DPEAJSERAC/LPMAC /02-45. Institut de Radioprotection et de Sûreté Nucléaire (IRSN), 2006.

[Malet et al., 2010] J. Malet, E. Porcheron, and J. Vendel. "OECD International Standard Problem ISP-47 on containment thermal-hydraulics—Conclusions of the TOSQAN part". In: *Nuclear Engineering and Design* 240.10 (Oct. 2010), pp. 3209–3220. DOI: 10.1016/j.nucengdes.2010.05.061.

[Müller et al., 2016] H. Müller, J. Lehmkuhl, S. Kelm, A. Hundhausen, A. Belt, and H.-J. Allelein. "DEVELOPMENT OF A WALL CONDENSATION MODEL FOR COARSE MESH CONTAINMENT SCALE APPLICATIONS". In: *Proceedings of the 6th Computational Fluid Dynamics for Nuclear Reactor Safety Applications Workshop*. CFD4NRS6 (Sept. 13–15, 2016). OECD NEA. Boston, MA, USA, 2016.

[OECDNEA, 2010] OECD/NEA. *OECD/NEA THAI Project - Hydrogen and Fission Product Issues Relevant for Containment Safety Assessment under Severe Accident Conditions*. Tech. rep. NEA/CSNI/R(2010)3. OECD/NEA, June 2010.

[Oertel, 2017] H. Oertel. *Prandtl - Führer durch die Strömungslehre : Grundlagen und Phänomene*. 14th ed. Wiesbaden, Germany: Springer Vieweg, 2017. ISBN: 9783658086268.

[Perrot, 1998] P. Perrot. *A to Z of thermodynamics*. Oxford New York: Oxford University Press, 1998. ISBN: 9780198565529.

[Popovac et al., 2007] M. Popovac and K. Hanjalic. "Compound Wall Treatment for RANS Computation of Complex Turbulent Flows and Heat Transfer". In: *Flow, Turbulence and Combustion* 78.2 (Jan. 2007), pp. 177–202. DOI: 10.1007/s10494-006-9067-x.

[Prandtl, 2010] L. Prandtl. *Vier Abhandlungen zur Hydrodynamik und Aerodynamik*. Göttingen: Universitätsverlag Göttingen c/o SUB Göttingen, 2010. ISBN: 9783941875753.

[Rosa et al., 2009] J. C. de la Rosa, A. Escrivá, L. E. Herranz, T. Cicero, and J. L. Muñoz-Cobo. "Review on condensation on the containment structures". In: *Progress in Nuclear Energy* 51.1 (Jan. 2009), pp. 32–66. DOI: 10.1016/j.pnucene.2008.01.003.

[Royl et al., 2006] P. Royl, U. J. Lee, J. R. Travis, and W. Breitung. "BENCHMARKING OF THE 3D CFD CODE GASFLOW II WITH CONTAINMENT THERMAL HYDRAULIC TESTS FROM HDR AND THAI". In: *Proceedings OECD/NEA and IAEA Workshop on Experiments and CFD Codes Application to Nuclear Reactor Safety*. CFD4NRS (Sept. 5–7, 2006). München, Germany, 2006.

[Schlichting et al., 2006] H. Schlichting and K. Gersten. *Grenzschicht-Theorie*. Springer-Verlag GmbH, Feb. 21, 2006. ISBN: 3540230041.

[Schwarz et al., 2011] S. Schwarz, K. Fischer, A. Bentaib, J. Burkhardt, J.-J. Lee, J. Duspiva, D. Visser, J. Kyttälä, P. Royl, J. Kim, P. Kostka, and R. Liang. "Benchmark on Hydrogen Distribution in a Containment Based on the OECD-NEA THAI HM-2 Experiment". In: *Nuclear Technology* 175.3 (Sept. 2011), pp. 594–603. DOI: 10.13182/nt11-a12508.

[Sucec, 1999] J. Sucec. "Prediction of Heat Transfer in Turbulent, Transpired Boundary Layers". In: *Journal of Heat Transfer* 121.1 (Feb. 1999), pp. 186–190. DOI: 10.1115/1.2825940.

[Turner, 1973] J. Turner. *Buoyancy effects in fluids*. Cambridge England: University Press, 1973. ISBN: 9780521086233.

[VDI, 2013] VDI. *VDI-Wärmeatlas*. 11th ed. Berlin, Heidelberg: Imprint Springer Vieweg, 2013. ISBN: 9783642199806.

[Wilcox, 1993] D. Wilcox. *Turbulence modeling for CFD*. La Cãnada, CA: DCW Industries, Inc, 1993. ISBN: 0963605100.

[Zschaeck et al., 2014] G. Zschaeck, T. Frank, and A. D. Burns. “CFD modelling and validation of wall condensation in the presence of non-condensable gases”. In: *Nuclear Engineering and Design* 279 (Nov. 2014), pp. 137–146. DOI: 10.1016/j.nucengdes.2014.03.007.

A. Boundary Conditions of the SETCOM Experiments used in this Thesis

Table A.1: Boundary conditions of the SETCOM experiments used in this thesis

Experiment	Angle in °	Velocity in ms^{-1}	Gas Temperature in °C	Relative Humidity in %	Coolant Temperature in °C
C001	90	4.7	80.0	90.0	08.4
C002	90	4.1	80.0	90.0	08.4
C003	90	3.0	80.0	90.0	07.9
C004	90	4.8	79.0	70.0	08.1
C005	90	4.1	80.0	70.0	08.1
C006	90	3.0	79.0	70.0	07.7
C007	90	4.9	78.0	50.0	07.7
C008	90	4.1	79.0	59.0	07.8
C009	90	3.0	78.0	50.0	07.6
C010	90	4.9	71.0	90.0	08.1
C011	90	4.1	72.0	90.0	07.8
C012	90	3.0	70.0	90.0	07.6
C013	90	5.0	70.0	70.0	07.8
C014	90	4.2	70.0	73.0	07.6
C015	90	3.1	70.0	70.0	07.4
C016	90	5.0	70.0	50.0	07.6
C017	90	4.2	70.0	50.0	07.4
C018	90	3.1	70.0	50.0	07.3
C019	90	4.8	60.0	90.0	07.6
C020	90	4.0	60.0	90.0	07.5
C021	90	3.0	60.0	87.0	07.5
C022	90	4.7	60.0	70.0	07.5
C023	90	4.0	60.0	70.0	07.4
C024	90	2.9	60.0	70.0	07.5
C025	90	4.7	60.0	50.0	07.3
C026	90	4.0	60.0	50.0	07.3
C027	90	2.9	60.0	50.0	07.5
C028	90	3.0	80.0	50.0	07.9
C029	90	2.9	80.0	70.0	07.8
C030	90	2.9	80.0	90.0	08.0
C031	90	2.9	80.0	50.0	07.6
C032	90	2.9	80.0	70.0	07.7
C033	90	2.9	80.0	90.0	08.0
C034	90	3.9	80.0	90.0	08.1
C035	90	4.6	80.0	90.0	08.3
C036	90	4.3	80.0	90.0	08.2

Table A.1: Boundary conditions of the SETCOM experiments used in this thesis

Experiment	Angle in °	Velocity in ms^{-1}	Gas Temperature in °C	Relative Humidity in %	Coolant Temperature in °C
C037	90	4.6	80.0	90.0	08.2
C038	90	4.6	70.0	90.0	07.8
C039	90	3.0	60.0	90.0	07.4
C040	90	4.0	60.0	90.0	07.5
C041	90	4.7	60.0	90.0	07.5
C042	90	2.9	80.0	90.0	07.9
C043	90	2.9	80.0	90.0	07.5
C044	90	3.9	80.0	90.0	07.8
C045	90	2.9	80.0	90.0	11.5
C046	90	3.9	80.0	90.0	12.6
C047	90	4.7	80.0	90.0	13.4
C048	90	3.0	70.0	90.0	10.2
C049	90	4.0	70.0	90.0	10.6
C050	90	4.7	70.0	90.0	11.0
C051	90	3.0	60.0	90.0	09.3
C052	90	4.0	60.0	90.0	09.7
C053	90	4.7	60.0	90.0	10.1
C054	90	1.0	23.0	43.0	23.1
C055	90	2.1	24.0	38.0	22.6
C056	90	3.1	24.0	39.0	22.6
C057	90	4.1	25.0	38.0	22.6
C058	90	5.0	29.0	33.0	22.6
C059	90	1.0	24.0	57.0	23.6
C060	90	2.0	24.0	55.0	23.6
C061	90	3.0	28.0	51.0	26.7
C062	90	4.0	31.0	47.0	27.0
C063	90	4.9	28.0	42.0	24.5
C064	90	4.8	80.0	90.0	13.2
C065	90	4.0	80.0	90.0	13.3
C066	90	3.0	80.0	90.0	12.2
C067	90	4.8	70.0	90.0	11.9
C068	90	4.1	70.0	90.0	11.4
C069	90	3.0	70.0	90.0	10.9
C070	90	4.8	60.0	90.0	10.6
C071	90	4.1	60.0	90.0	10.4
C072	90	3.1	60.0	90.0	09.9
C073	90	4.8	80.0	90.0	13.8
C074	90	4.1	80.0	90.0	12.9
C075	90	3.0	80.0	90.0	12.1

Table A.1: Boundary conditions of the SETCOM experiments used in this thesis

Experiment	Angle in °	Velocity in ms^{-1}	Gas Temperature in °C	Relative Humidity in %	Coolant Temperature in °C
C076	90	4.8	70.0	90.0	11.9
C077	90	4.1	70.0	90.0	11.4
C078	90	3.0	70.0	90.0	10.8
C079	90	4.8	60.0	90.0	10.6
C080	90	4.1	60.0	90.0	10.2
C081	90	3.1	60.0	90.0	09.4
C082	90	4.8	80.0	90.0	13.6
C083	90	4.0	80.0	90.0	13.4
C084	90	3.0	80.0	90.0	12.0
D001	90	1.9	80.0	90.0	07.7
D002	90	0.8	80.0	90.0	07.6
D003	90	2.0	80.0	70.0	07.5
D004	90	0.7	80.0	70.0	07.6
D005	90	2.0	80.0	50.0	07.3
D006	90	0.7	80.0	49.0	07.3
D007	90	1.9	70.0	90.0	07.4
D008	90	0.8	70.0	90.0	07.3
D009	90	2.0	70.0	70.0	07.2
D010	90	0.8	70.0	70.0	07.5
D011	90	2.0	70.0	49.0	07.2
D012	90	0.9	70.0	50.0	07.0
D013	90	1.9	60.0	90.0	07.5
D014	90	0.8	60.0	90.0	07.2
D015	90	2.0	60.0	70.0	07.4
D016	90	0.9	60.0	70.0	07.4
D017	90	2.0	60.0	50.0	07.3
D018	90	1.0	60.0	50.0	07.3
D019	90	0.0	90.0	90.0	11.9
D020	90	0.0	90.0	90.0	11.7
D021	90	0.6	90.0	90.0	11.7
D022	90	0.6	90.0	90.0	11.5
D023	90	1.0	90.0	90.0	11.4
D024	90	1.3	90.0	90.0	11.4
D025	90	1.6	90.0	90.0	11.4
D026	90	1.9	90.0	90.0	11.6
D027	90	0.2	90.0	90.0	11.7
D028	90	0.5	90.0	90.0	11.5
D029	90	0.8	90.0	90.0	11.5
D030	90	0.9	90.0	90.0	12.3

Table A.1: Boundary conditions of the SETCOM experiments used in this thesis

Experiment	Angle in °	Velocity in ms^{-1}	Gas Temperature in °C	Relative Humidity in %	Coolant Temperature in °C
D031	90	1.2	90.0	90.0	11.5
D032	90	1.6	90.0	90.0	11.6
D033	90	1.9	90.0	90.0	11.8
D034	90	0.0	90.0	90.0	12.5
D035	90	0.0	80.0	90.0	10.2
D036	90	0.0	80.0	90.0	10.2
D037	90	0.0	80.0	90.0	10.2
D038	90	0.5	80.0	90.0	10.0
D039	90	0.7	80.0	90.0	09.9
D040	90	1.1	80.0	90.0	09.8
D041	90	1.0	80.0	90.0	09.7
D042	90	1.3	80.0	90.0	09.7
D043	90	1.6	80.0	90.0	10.0
D044	90	1.8	80.0	90.0	10.1
D045	90	0.0	70.0	90.0	09.0
D046	90	0.8	70.0	90.0	08.8
D047	90	1.4	70.0	90.0	08.9
D048	90	0.0	60.0	90.0	08.3
D049	90	0.9	60.0	90.0	08.3
D050	90	1.4	60.0	90.0	08.3
D051	90	0.0	70.0	90.0	09.2
D052	90	0.8	70.0	90.0	09.0
D053	90	1.4	70.0	90.0	09.0
D054	90	0.0	60.0	90.0	08.6
D055	90	0.8	60.0	90.0	08.4
D056	90	1.4	60.0	90.0	08.4
D057	90	0.0	80.0	90.0	10.2
D058	90	0.0	80.0	90.0	10.0
D059	90	0.8	80.0	90.0	10.0
D060	90	1.1	80.0	90.0	10.2
D061	90	1.4	80.0	90.0	10.1
D062	90	1.7	80.0	90.0	10.1
D063	90	1.8	80.0	90.0	10.3
D064	90	0.0	90.0	90.0	11.7
D065	90	0.0	90.0	90.0	11.2
D066	90	0.8	90.0	90.0	11.4
D067	90	1.0	90.0	89.0	11.4
D068	90	1.3	90.0	90.0	11.5
D069	90	1.7	90.0	90.0	11.5

Table A.1: Boundary conditions of the SETCOM experiments used in this thesis

Experiment	Angle in °	Velocity in ms^{-1}	Gas Temperature in °C	Relative Humidity in %	Coolant Temperature in °C
D070	90	1.9	90.0	90.0	12.0
D071	90	2.5	90.0	90.0	12.2
D072	90	3.0	90.0	90.0	13.0
D073	90	0.0	90.0	90.0	11.6
D073	90	0.0	90.0	90.0	11.7
D073	90	0.0	90.0	90.0	11.9
D074	90	0.0	80.0	90.0	10.4
D075	90	0.0	80.0	90.0	10.4
D076	90	0.8	80.0	90.0	10.2
D077	90	1.1	80.0	90.0	10.3
D078	90	1.4	80.0	90.0	10.3
D079	90	1.7	80.0	90.0	10.2
D080	90	2.0	80.0	90.0	10.6
D081	90	2.5	80.0	90.0	11.0
D082	90	3.0	80.0	90.0	11.5
D083	90	0.0	90.0	90.0	12.0
D084	90	0.0	90.0	90.0	12.0
D085	90	0.8	90.0	90.0	11.8
D086	90	1.0	90.0	90.0	11.9
D087	90	1.3	90.0	90.0	12.0
D088	90	1.6	90.0	90.0	12.0
D089	90	1.8	90.0	90.0	12.1
D090	90	2.5	90.0	90.0	12.6
D091	90	3.0	90.0	90.0	13.8
D092	90	0.1	80.0	90.0	11.0
D093	90	0.0	80.0	90.0	10.8
D094	90	0.0	80.0	90.0	10.6
D095	90	0.5	80.0	90.0	10.9
D096	90	1.0	80.0	90.0	10.6
D097	90	1.4	80.0	90.0	10.7
D098	90	1.7	80.0	90.0	10.6
D099	90	1.9	80.0	90.0	10.7
D100	90	2.5	80.0	90.0	11.1
D101	90	3.0	80.0	90.0	11.9
D102	90	0.0	85.0	90.0	10.4
D103	90	0.0	85.0	90.0	10.3
D104	90	0.8	85.0	90.0	10.2
D105	90	1.1	85.0	90.0	10.0
D106	90	1.4	85.0	90.0	10.3

Table A.1: Boundary conditions of the SETCOM experiments used in this thesis

Experiment	Angle in °	Velocity in ms^{-1}	Gas Temperature in °C	Relative Humidity in %	Coolant Temperature in °C
D107	90	1.6	85.0	90.0	10.7
D108	90	1.9	85.0	90.0	10.7
D109	90	2.5	85.0	84.0	11.4
D110	90	3.0	85.0	90.0	12.2
D111	90	0.0	70.0	90.0	09.1
D112	90	0.8	70.0	90.0	09.0
D113	90	1.4	70.0	90.0	09.0
D114	90	0.0	60.0	90.0	08.5
D115	90	0.9	60.0	90.0	08.6
D116	90	1.4	60.0	90.0	08.8
D117	90	0.0	85.0	90.0	11.0
D118	90	0.0	85.0	90.0	11.3
D119	90	0.7	23.0	09.0	18.6
D120	90	1.0	85.0	90.0	11.2
D121	90	1.3	85.0	90.0	11.2
D122	90	1.6	85.0	90.0	12.7
D123	90	1.8	85.0	90.0	11.6
D124	90	2.5	85.0	90.0	11.8
D125	90	3.0	85.0	90.0	13.0
D126	90	0.0	70.0	90.0	09.8
D127	90	0.8	70.0	90.0	09.5
D128	90	1.4	70.0	90.0	09.5
D129	90	0.2	60.0	90.0	09.0
D130	90	0.9	60.0	90.0	09.1
D131	90	1.4	60.0	90.0	09.1

B. Data Centers, RBF Coefficients and Scales of the New Wall Function Approach

Table B.1: Data centers and RBF coefficients of the new velocity wall function

y^+	FG^+	$\dot{q}^+$	$RBF\ Coefficient$
19.86578673172	0.00460652225885712	0.015291602671278	3.01597
10.436797392196	0.005785760586431801	0.016574400422730003	4.75734
18.48466802968	0.0120055712742612	0.010529400165518	8.73451
14.37699533124	0.0120055712742612	0.010529400165518	9.02577
12.323102040412	0.0120055712742612	0.010529400165518	6.81752
10.269303652264	0.0120055712742612	0.010529400165518	5.79534
8.215410361436	0.0120055712742612	0.010529400165518	6.73208
6.161564521948	0.0120055712742612	0.010529400165518	8.00837
10.081396345864	0.0061524667578591605	0.009736005341519999	4.92985
7.561075363372	0.0061524667578591605	0.009736005341519999	3.72284
10.306695308184	0.0107877702833956	0.007268410554016001	3.74381
6.184037476572	0.0107877702833956	0.007268410554016001	4.60613
8.297472708832	0.00430111745135308	0.011016400494788001	2.99015
10.667695612635999	0.009687155087598	0.009414468155605999	6.62154
8.534122031679999	0.009687155087598	0.009414468155605999	6.06709
8.764479306844	0.00346385986851128	0.008171755858066	4.78569
5.9145603676852	0.0115580146648856	0.008116053515958	4.77709
17.4411181604	0.00533891019608608	0.006201720186588001	-3.89226
9.9663458269	0.00533891019608608	0.006201720186588001	-4.92685
24.948394661799995	0.00349795239816252	0.00682854540754	5.02867
16.632167716079998	0.00349795239816252	0.00682854540754	9.33098
13.8602027873	0.00349795239816252	0.00682854540754	3.90614
11.088199897448	0.00349795239816252	0.00682854540754	17.3412
8.316121085452	0.00349795239816252	0.00682854540754	9.07621
5.544080234528001	0.00349795239816252	0.00682854540754	33.8178
14.396602224928	0.0054193726016003195	0.007001216345448	5.09954
7.198300378804	0.0054193726016003195	0.007001216345448	3.02935
8.068852152712001	0.0093100651682368	0.0059538099897600005	-7.04981
10.274997813064001	0.0112001711542508	0.007725504858522	-3.13231
6.1649810184280005	0.0112001711542508	0.007725504858522	-8.40253
18.42516404932	0.0122942674051572	0.010685000011066	-7.16651
14.330701803935998	0.0122942674051572	0.010685000011066	-8.1025
12.283499152048	0.0122942674051572	0.010685000011066	-6.19568
10.236201597480001	0.0122942674051572	0.010685000011066	-5.00931
8.188979965056	0.0122942674051572	0.010685000011066	-6.34417

Table B.1: Data centers and RBF coefficients of the new velocity wall function

y^+	FG^+	$\dot{q}^+$	$RBF\ Coefficient$
6.141739352096001	0.0122942674051572	0.010685000011066	-6.51835
31.324526120279995	0.00397228324548412	0.014454992693102	3.78435
19.93383195328	0.00397228324548412	0.014454992693102	5.83282
5.6953702908768005	0.00397228324548412	0.014454992693102	5.53996
8.543052373868	0.00397228324548412	0.014454992693102	6.09126
18.63935939808	0.00440350368938832	0.006256031550800001	4.33049
10.926599613944	0.00440350368938832	0.006256031550800001	4.71376
5.7846499870868	0.00440350368938832	0.006256031550800001	6.02472
7.540282186184	0.011097497772214401	0.00990529367409	2.64187
5.6552103237812	0.011097497772214401	0.00990529367409	3.92179
14.290804717263999	0.0081178743180152	0.015988798728514	2.73184
9.527202655736	0.0081178743180152	0.015988798728514	3.63865
22.264357066039995	0.0038800324146249596	0.014189790111976	4.15438
16.32724540524	0.0038800324146249596	0.014189790111976	8.83192
13.358604162427998	0.0038800324146249596	0.014189790111976	7.55914
10.390000880688	0.0038800324146249596	0.014189790111976	11.9502
7.421454540556001	0.0038800324146249596	0.014189790111976	11.353
8.291256583292	0.00531661385242844	0.009477631197338	-5.14775
9.839802593388	0.0098002277388656	0.006141465553184	2.94245
7.8718436792999995	0.0098002277388656	0.006141465553184	7.68823
19.139496521679998	0.005304980640057121	0.006661248702412001	2.99052
16.747094861559997	0.005304980640057121	0.006661248702412001	4.11757
11.96219663864	0.005304980640057121	0.006661248702412001	6.14637
9.569738036912	0.005304980640057121	0.006661248702412001	8.61158
7.177307905988	0.005304980640057121	0.006661248702412001	5.38882
9.963432314624	0.0030919307805222797	0.006341734757074001	3.90133
11.249999476580001	0.0043529508238868	0.015936004794734	3.36487
8.437492122904	0.0043529508238868	0.015936004794734	5.26349
9.556166953672001	0.00707745847402836	0.016293296435202	6.80745
8.361645901048	0.00707745847402836	0.016293296435202	7.24407
5.972613286068	0.00707745847402836	0.016293296435202	7.89252
28.219500236039995	0.0111758027173956	0.019277386605998002	-3.11208
17.76777318496	0.0111758027173956	0.019277386605998002	-12.0341
20.268743510999997	0.0040881574909252	0.014814402413548	-6.54628
9.458739862384	0.0040881574909252	0.014814402413548	-3.08581
6.756243695364	0.0040881574909252	0.014814402413548	-6.65711
5.4049899176932	0.0040881574909252	0.014814402413548	3.63529
17.324292961319998	0.0100518279690712	0.009692189537795999	3.04435
11.20990309428	0.0100518279690712	0.009692189537795999	-3.26465

Table B.1: Data centers and RBF coefficients of the new velocity wall function

y^+	FG^+	$\dot{q}^+$	$RBF\ Coefficient$
8.152622748348	0.0100518279690712	0.009692189537795999	5.79182
7.133538789972	0.0100518279690712	0.009692189537795999	11.7243
6.114473812132	0.0100518279690712	0.009692189537795999	8.86625
5.09539004356136	0.0100518279690712	0.009692189537795999	9.84602
24.68968995612	0.00330011018136328	0.006820673737174	-5.09093
16.4598244492	0.00330011018136328	0.006820673737174	-7.8684
10.973196829824	0.00330011018136328	0.006820673737174	-14.0138
6.858264076364001	0.00330011018136328	0.006820673737174	-5.42764
5.4866100186004	0.00330011018136328	0.006820673737174	-25.3926
18.92511136756	0.004330219883903081	0.006541751055892	-5.8005
11.355104194679999	0.004330219883903081	0.006541751055892	-7.98023
10.093401534884	0.004330219883903081	0.006541751055892	-3.59846
7.5700436666319995	0.004330219883903081	0.006541751055892	-3.58099
5.046700033782001	0.004330219883903081	0.006541751055892	-10.2931
10.74079914704	0.00499996386498708	0.016484397830232003	-2.59423
9.398220423348	0.00499996386498708	0.016484397830232003	-4.82066
14.392103837895998	0.00711332043157864	0.016173198139136	-3.12744
10.794096492127998	0.00711332043157864	0.016173198139136	-3.47315
9.59475438336	0.00711332043157864	0.016173198139136	-7.76069
8.395402784324	0.00711332043157864	0.016173198139136	-9.61366
5.996718566788	0.00711332043157864	0.016173198139136	-7.44433
28.264009592959997	0.011197222107752399	0.019448793018546004	3.0708
17.795864378239997	0.011197222107752399	0.019448793018546004	11.3747
6.280904642048	0.011197222107752399	0.019448793018546004	4.84425
5.234079681281201	0.011197222107752399	0.019448793018546004	-5.5203
31.25809424428	0.0035437712679692395	0.014205501839574001	-3.82754
21.312293380279996	0.0035437712679692395	0.014205501839574001	-5.11319
17.04992931344	0.0035437712679692395	0.014205501839574001	-4.49132
15.629046388479999	0.0035437712679692395	0.014205501839574001	-6.46613
12.787403912043999	0.0035437712679692395	0.014205501839574001	-6.33762
11.366596909228	0.0035437712679692395	0.014205501839574001	-3.38026
9.94575194534	0.0035437712679692395	0.014205501839574001	-9.378
8.524925961988	0.0035437712679692395	0.014205501839574001	-4.56203
7.104109468904	0.0035437712679692395	0.014205501839574001	-8.3939
5.6832901287396	0.0035437712679692395	0.014205501839574001	-5.04582
9.554449215163999	0.00610054801818996	0.010709405350514	-3.27448
10.621098396756	0.0090947071673668	0.009428757292174	-5.59995
8.496891710316	0.0090947071673668	0.009428757292174	-7.50347
5.3105598530396	0.0090947071673668	0.009428757292174	-5.67491

Table B.1: Data centers and RBF coefficients of the new velocity wall function

y^+	FG^+	$\dot{q}^+$	$RBF\ Coefficient$
9.359414717496	0.0035200081617110797	0.007195352601342	-4.77844
8.022349839512	0.0035200081617110797	0.007195352601342	-5.23484
15.924573333999998	0.00465660172478916	0.006912731183382	-6.57002
13.474603708192	0.00465660172478916	0.006912731183382	-5.86276
12.2497043077	0.00465660172478916	0.006912731183382	-2.8675
9.79974417216	0.00465660172478916	0.006912731183382	-4.87672
7.349812507424	0.00465660172478916	0.006912731183382	-6.17406
10.773796808876	0.00966115691452	0.0066182864533060005	-3.71763
7.835524423663999	0.00966115691452	0.0066182864533060005	-3.74795
47.79536074767999	0.0489794745674116	0.010996610672904	7.27388
8.511506723036	0.0489794745674116	0.010996610672904	-23.3857
11.50319982682	0.0498634124520636	0.024626392105066	-4.66543
7.540244225112	0.0331000232708296	0.012136485445542	-4.58577
6.032193188572	0.0331000232708296	0.012136485445542	-4.40231
8.272646167744	0.020452882149467597	0.0056771634541260005	3.38884
6.618122334892	0.020452882149467597	0.0056771634541260005	3.88184
7.242183378036	0.024660938683224	0.003555195060644	5.43962
6.645767485576	0.0687110014427984	0.012025207213861999	-3.91296
5.5381402757868	0.0687110014427984	0.012025207213861999	3.98883
9.154833010219999	0.0204687914792616	0.005716521805956	-3.44111
7.490315925164	0.0204687914792616	0.005716521805956	-2.72445
5.8257997891348	0.0204687914792616	0.005716521805956	-2.90155
7.372959271076001	0.0238123893565528	0.0035789997505459997	-6.05781
11.047695433624	0.049532265572888	0.024693791306754	4.60299
7.508299983024	0.032744275135338397	0.012112491076836	4.1592
6.0066358968480005	0.032744275135338397	0.012112491076836	4.89384
6.846932696372	0.009055283072072401	0.010039586267322001	5.60351
8.15266070942	0.018164965312116796	0.012160005617238	4.00648
7.24681462882	0.018164965312116796	0.012160005617238	-4.37434
48.61085947692	0.0488224766446152	0.011026200566328	-7.35326
8.614590014052	0.0488224766446152	0.011026200566328	23.4659
6.1237363137	0.021352496544453196	0.00469307820584	8.81751
5.3582702773560005	0.021352496544453196	0.00469307820584	-7.60806
17.092635519439998	0.010051517543124	0.009860371410676	-6.06602
7.97656878668	0.010051517543124	0.009860371410676	-13.3637
6.837062817652	0.010051517543124	0.009860371410676	-14.6317
5.6975502054364	0.010051517543124	0.009860371410676	-17.3385

Table B.2: Scales of the new velocity wall function

	y^+	FG^+	$\dot{q}^+$
Min	5.00602	4.57132e-05	0.000369666
Max	99.9087	0.0776522	0.0319828

Table B.3: Data centers and RBF coefficients of the new temperature wall function

y^+	FG^+	$\dot{q}^+$	$RBF\ Coefficient$
5.2108467084273995	0.0036384216559753	0.01747218284726	0.215682
66.37554158216	0.0036384216559753	0.01747218284726	0.741353
5.263319055882399	0.0034059320721676	0.01316248334135	0.169732
10.496673192345998	0.0034059320721676	0.01316248334135	-0.180652
31.71949027914	0.009509748648544	0.012265152009886	0.156138
18.23151015106	0.0030688795541095	0.008558341729897999	0.136477
23.21768844156	0.0030688795541095	0.008558341729897999	0.266824
6.786130656519999	0.0045722250934063	0.011984630720695999	0.325922
9.319631341004	0.0045722250934063	0.011984630720695999	-0.340141
5.428287749518399	0.0027148668565791997	0.008441137437386	0.110679
10.821285027936	0.0027148668565791997	0.008441137437386	-0.127871
18.587211437199997	0.0027148668565791997	0.008441137437386	-0.2082
23.67031286972	0.0027148668565791997	0.008441137437386	-0.231072
5.419333038463799	0.002628357024907	0.00612952413658	0.145192
10.482300847878	0.0025624438259505998	0.005399719726094	-0.208085
7.2713159443399995	0.007465386300448	0.005383918476888	0.177226
9.64147123169	0.007465386300448	0.005383918476888	-0.184856
5.2551902325218	0.0024862670854624	0.004000256690288	0.0900298
7.239296183514	0.007222161231039999	0.003992791091195999	0.182777
9.598828846385999	0.007222161231039999	0.003992791091195999	-0.208167
30.669283893080003	0.007222161231039999	0.003992791091195999	0.135311
6.109880522526	0.006335452843813	0.009064234299947998	0.118117
11.126559699931999	0.006335452843813	0.009064234299947998	-0.126562
5.4602220736864	0.009605031672058	0.012807530590535998	0.135011
20.880046549059998	0.00977363990032	0.016934098389396	0.583514
7.401825185916	0.009221614375143999	0.008733895573207999	0.0967846
9.815391788492	0.009221614375143999	0.008733895573207999	-0.117052
9.949432411932	0.009609502721128	0.012808793567825999	-0.144526
5.4172085135682	0.010455127135234001	0.017059077008782002	0.162244
35.66125289039999	0.0036404087888952997	0.017473979081628	0.333165

Table B.3: Data centers and RBF coefficients of the new temperature wall function

y^+	FG^+	$\dot{q}^+$	$RBF\ Coefficient$
66.40829230105999	0.0036404087888952997	0.017473979081628	0.765602
9.872140715328	0.010459300114366	0.01705946993505	-0.145116
25.452521555599997	0.005300454662431	0.017416275052556	0.343873
31.7117060503	0.005300454662431	0.017416275052556	0.432586
20.49168947364	0.009632205714738998	0.016906565484474	-0.555603
24.83728268838	0.0051671776574866	0.017334321859516	-0.299435
30.944769650319998	0.0051671776574866	0.017334321859516	-0.422745
35.34504232618	0.0033634670416672	0.017358542957322	-0.393757
65.81801992390001	0.0033634670416672	0.017358542957322	-0.824142
6.510322138572	0.017434186341888997	0.0002061085248105498	0.169191
12.611619689287998	0.017434186341888997	0.0002061085248105498	-0.204069
41.37297826656	0.017434186341888997	0.0002061085248105498	0.129613
6.534510205747999	0.0042719047273744	0.000218564430643576	0.125541
13.544939234242	0.0042719047273744	0.000218564430643576	-0.14302
6.47979277278	0.00098056331617279	0.00020931893168986	0.129524
46.29166159724	0.00098056331617279	0.00020931893168986	1.14028
56.66699441514	0.00098056331617279	0.00020931893168986	1.25597
14.348565932351999	0.000640777	0.000205038	-0.191872
45.822899133680004	0.000640777	0.000205038	-1.08771
56.34727145498	0.000640777	0.000205038	-1.33756
10.808877726601999	0.0031108825762059997	0.017432834088136	-0.139986
14.337202856838	0.0031108825762059997	0.017432834088136	-0.114545
69.02284389510001	0.0031108825762059997	0.017432834088136	-0.746416
20.99775927786	0.019369653805968997	0.015283499336014	0.749373
5.079434970954059	0.034575492979747	0.013080389817499998	0.285141
8.72226772123	0.034575492979747	0.013080389817499998	-0.301576
6.030804149065999	0.019156881548559997	0.011778091834537999	0.119184
10.356633016922	0.019156881548559997	0.011778091834537999	-0.118664
12.612493041792	0.044062264253118995	0.011337060164869999	-0.160731
23.89719466152	0.044062264253118995	0.011337060164869999	0.100584
52.65441430736001	0.044062264253118995	0.011337060164869999	0.160357
5.8472994978288	0.041242125213055	0.006770050085744	0.227891
9.641309851336	0.041242125213055	0.006770050085744	-0.24528
74.105850398	0.041242125213055	0.006770050085744	-0.200865
5.510385732783	0.018076825128216997	0.006271061791545999	0.106103
12.047158675806	0.018076825128216997	0.006271061791545999	-0.13908
43.94452674274	0.030562428369483995	0.005107887773618001	-0.122265
94.26187689412	0.030562428369483995	0.005107887773618001	0.310572
39.8073040439	0.037059905912977	0.0029943036986516	0.185293

Table B.3: Data centers and RBF coefficients of the new temperature wall function

y^+	FG^+	$\dot{q}^+$	$RBF\ Coefficient$
58.487364808260004	0.037059905912977	0.0029943036986516	0.202085
70.71439479387999	0.037059905912977	0.0029943036986516	0.201934
85.38671686108	0.037059905912977	0.0029943036986516	0.385174
6.272257637536	0.046702915512184	0.028262976614534	0.0965145
9.227274313706	0.03250147267282	0.023047441730074	-0.168842
82.27957546886	0.042816232555633	0.025870420502520003	0.110741
11.170531099916	0.037778453176849	0.024063913919228002	-0.121721
60.923353787079996	0.032472112783927	0.023026616637870003	0.14145
5.6406063883141995	0.027765141357999998	0.022660886480848002	0.131762
9.687996238452	0.027765141357999998	0.022660886480848002	-0.145643
5.936610233621	0.023673535319073995	0.023615276319658	0.129565
10.196951903119999	0.023673535319073995	0.023615276319658	-0.147226
10.742398513716	0.019975928059861	0.025071573333514	-0.193299
8.154218368112	0.046691886924477996	0.0282712	-0.144913
5.8818149583645996	0.047815461555769	0.015983441350132	0.0977678
10.075764750228	0.042933125649651994	0.014720351795484	-0.098698
5.6665126816122	0.022778779043521	0.014467924734455998	0.171295
9.73098986335	0.022778779043521	0.014467924734455998	-0.203842
78.7911017931	0.022778779043521	0.014467924734455998	-0.125324
95.26347931474	0.022778779043521	0.014467924734455998	-0.262763
20.459793121319997	0.019202833997335	0.015295567785673998	-0.719525
35.786749848039996	0.050305984922727996	0.005740218403478	0.120974
83.61808311086	0.04899318555913	0.009601617103761999	-0.0951246
5.095837670134619	0.025743581360160993	0.008706923991525999	0.117245
11.141121903639998	0.025743581360160993	0.008706923991525999	-0.131531
11.70951300339	0.035152208631454004	0.004985799968918	-0.0879357
9.713589264004	0.047807165275828	0.015988998450208	-0.163143
61.7607279651	0.047807165275828	0.015988998450208	-0.0983191
29.3916261375	0.042933125649651994	0.014720351795484	0.121621
90.652083164	0.026744152463704	0.013487517563472	0.183602
6.284133332998	0.046697401218331	0.028267186538833998	0.0958253
79.69369262006	0.046697401218331	0.028267186538833998	-0.184964
38.034778179259995	0.042816033842341	0.025866603504488002	0.195783
6.773068340808	0.037778453176849	0.024063913919228002	-0.147342
5.6135533452066	0.010098734846032	0.028017538027844	0.176092
10.228240705872	0.010098734846032	0.028017538027844	-0.121124
16.87335207772	0.010098734846032	0.028017538027844	-0.233114
6.101460265231999	0.042934814712633995	0.014714261438329998	0.111339
6.682410553707999	0.013562953343790998	0.016322227991634002	0.104782

Table B.3: Data centers and RBF coefficients of the new temperature wall function

y^+	FG^+	$\dot{q}^+$	$RBF\ Coefficient$
11.477058842896	0.013562953343790998	0.016322227991634002	-0.156927
13.051656449835999	0.046693675344106	0.028269880890386	-0.180147
5.101119649121039	0.037777111862127996	0.024060966972218	0.123268
5.369201655437999	0.032500081679776	0.023046599745214	0.15196
5.0574499354694	0.014145878785873	0.026949452166772	0.12157
96.6739436087	0.014145878785873	0.026949452166772	-0.137215
5.6135533452066	0.010098734846032	0.028017538027844	0.176092
7.711143859723999	0.010098734846032	0.028017538027844	-0.139558
73.05184682714	0.010098734846032	0.028017538027844	-0.206955
96.41269729446	0.046691886924477996	0.0282712	-0.146701
5.101119649121039	0.037777111862127996	0.024060966972218	0.123268
6.25020548681	0.019972748647189	0.025073734427988	0.147587
5.0574499354694	0.014145878785873	0.026949452166772	0.12157
9.213537997692	0.014145878785873	0.026949452166772	-0.19924
44.94470521906	0.046691886924477996	0.0282712	-0.198907
6.303973623577999	0.042909727159519	0.019280120804814	0.12646
10.396028809221999	0.042909727159519	0.019280120804814	-0.220329
6.597420064922	0.037359615235636	0.01808837543397	0.112047
5.245902318501	0.031873190921839	0.017230477060116	0.13088
11.471799741947999	0.031873190921839	0.017230477060116	-0.172063
5.5273515544694	0.027233235553638997	0.017223432453454	0.138164
92.93219770678	0.027233235553638997	0.017223432453454	0.274228
5.804531805426399	0.023263142692770997	0.018243974236098	0.130598
9.968892984032	0.023263142692770997	0.018243974236098	-0.139825
12.991148310048	0.009975930031576	0.021551431096988	-0.157309
47.29734599152	0.04899318555913	0.009601617103761999	-0.137788
57.275588208959995	0.04899318555913	0.009601617103761999	-0.141433
83.61808311086	0.04899318555913	0.009601617103761999	-0.0951246
10.380802098174	0.0503191	0.005732724738224	-0.146772
80.7423801322	0.024461334165207994	0.005711534785914	-0.0978728
24.77386970222	0.042909727159519	0.019280120804814	0.14095
10.894190976095999	0.037360906872034	0.018092669556755998	-0.145692
27.3729477682	0.031875625159666	0.017233564337936002	0.128351
9.498488238046	0.027234874938297994	0.017223769247398	-0.149169
5.5002861705112	0.009968577639771999	0.021550925906072	0.1282
29.425610941459997	0.050305984922727996	0.005740218403478	0.200237
52.58036920376	0.050305984922727996	0.005740218403478	0.157615
92.59178008946	0.050305984922727996	0.005740218403478	0.193094
55.14717119893999	0.024461334165207994	0.005711534785914	-0.0593015

Table B.3: Data centers and RBF coefficients of the new temperature wall function

y^+	FG^+	$\dot{q}^+$	$RBF\ Coefficient$
66.78136570766	0.024461334165207994	0.005711534785914	-0.103753
80.7423801322	0.024461334165207994	0.005711534785914	-0.0978728
97.4955594698	0.024461334165207994	0.005711534785914	-0.0823827

Table B.4: Scales of the new temperature wall function

	y^+	FG^+	$\dot{q}^+$
Min	5.00658	0.000640777	0.000205038
Max	99.9362	0.0503191	0.0282712

Table B.5: Data centers and RBF coefficients of the new steam species wall function

y^+	FG^+	$\dot{q}^+$	$RBF\ Coefficient$
6.83162760035	0.004993537997421999	0.0174244272258	-0.653278
9.383602306228	0.004993537997421999	0.0174244272258	-0.161171
16.120851950080002	0.004993537997421999	0.0174244272258	0.532877
5.3237195434636	0.0030688809454719997	0.0085583270587	0.201038
29.2009683389	0.0030688809454719997	0.0085583270587	0.512978
23.34080380296	0.0029229030921519997	0.010904630024299998	1.51608
29.356039292600002	0.0029229030921519997	0.010904630024299998	0.244018
68.10376550278	0.0029229030921519997	0.010904630024299998	0.311766
16.26311888008	0.008829046109079999	0.010724102404499999	0.849324
20.45335419168	0.008829046109079999	0.010724102404499999	0.44185
25.4816365656	0.008829046109079999	0.010724102404499999	0.580797
31.515651290000005	0.008829046109079999	0.010724102404499999	0.664144
38.756374114660005	0.008829046109079999	0.010724102404499999	0.52435
57.87192789718001	0.008829046109079999	0.010724102404499999	0.449318
29.770130903520002	0.0027148736140552	0.008441143350299999	-0.443327
5.2730099189344	0.00722213802352	0.00399277546535	0.351616
12.430277065563999	0.00722213802352	0.00399277546535	-0.314851
6.723628031556	0.00529229832589	0.0174123701445	0.319918
20.20571488886	0.00529229832589	0.0174123701445	0.162771
7.692902110107999	0.0034634914265439997	0.0174741468881	-0.12154

Table B.5: Data centers and RBF coefficients of the new steam species wall function

y^+	FG^+	$\dot{q}^+$	$RBF\ Coefficient$
10.567528728764	0.0034634914265439997	0.0174741468881	0.0932737
14.017093949398001	0.0034634914265439997	0.0174741468881	0.267682
22.756181565280002	0.003640416392818	0.017473969949799998	0.396513
54.24459540528001	0.003640416392818	0.017473969949799998	0.864147
98.52024544754	0.003640416392818	0.017473969949799998	0.342501
5.297371708027599	0.0034634914265439997	0.0174741468881	0.193969
18.15659687376	0.0034634914265439997	0.0174741468881	0.389923
66.03160024502	0.003236693093092	0.0109255340206	0.882036
97.95867045252	0.003236693093092	0.0109255340206	0.959034
6.733852281592	0.005300460992835999	0.017416262787099998	0.340729
12.267751324732	0.005300460992835999	0.017416262787099998	-0.238783
20.23653939036	0.005300460992835999	0.017416262787099998	0.185047
25.45251926726	0.005300460992835999	0.017416262787099998	0.515785
31.711695119540003	0.005300460992835999	0.017416262787099998	0.463926
39.222630266580005	0.005300460992835999	0.017416262787099998	0.401777
48.2358093498	0.005300460992835999	0.017416262787099998	0.380294
9.026578703162	0.0051671854201779995	0.017334315077299996	0.117236
11.971930954952	0.0051671854201779995	0.017334315077299996	0.234933
15.5063536571	0.0051671854201779995	0.017334315077299996	-0.531364
19.74761537426	0.0051671854201779995	0.017334315077299996	-0.425206
24.83726221732	0.0051671854201779995	0.017334315077299996	-0.518646
30.9446866776	0.0051671854201779995	0.017334315077299996	-0.44097
38.273709843480006	0.0051671854201779995	0.017334315077299996	-0.389617
47.06846176684	0.0051671854201779995	0.017334315077299996	-0.32011
7.504958011115999	0.003363471163666	0.017358555624399998	0.145162
10.308621885088	0.003363471163666	0.017358555624399998	-0.084254
13.6730071525	0.003363471163666	0.017358555624399998	-0.3028
17.71025809204	0.003363471163666	0.017358555624399998	-0.441728
22.55501612626	0.003363471163666	0.017358555624399998	-0.39792
53.76278473568	0.003363471163666	0.017358555624399998	-0.950408
97.64378631412	0.003363471163666	0.017358555624399998	-0.394135
16.028473290199997	0.00869098618666	0.010676708216999998	-0.455389
20.15819773424	0.00869098618666	0.010676708216999998	-0.260552
25.11382912924	0.00869098618666	0.010676708216999998	-0.185114
31.060586803240003	0.00869098618666	0.010676708216999998	-0.20947
38.19669601204	0.00869098618666	0.010676708216999998	-0.163893
57.03606226112	0.00869098618666	0.010676708216999998	-0.207037
22.62501145582	0.003001962432502	0.0108245022513	-0.888506
66.01282101026001	0.003001962432502	0.0108245022513	-0.885117

Table B.5: Data centers and RBF coefficients of the new steam species wall function

y^+	FG^+	$\dot{q}^+$	$RBF\ Coefficient$
97.93050160038	0.003001962432502	0.0108245022513	-0.91287
23.49151190414	0.0027453504499011998	0.0108427268962	-0.742882
68.54280124876	0.0027453504499011998	0.0108427268962	-0.300114
25.128435200720002	0.00869660071948	0.010678806199699999	-0.175472
31.07870212566	0.00869660071948	0.010678806199699999	-0.203169
38.21898449774	0.00869660071948	0.010678806199699999	-0.154049
57.069257878120006	0.00869660071948	0.010678806199699999	-0.185126
29.545538843360003	0.0027453504499011998	0.0108427268962	-0.269988
16.03786290758	0.00869660071948	0.010678806199699999	-0.409751
20.169958467119997	0.00869660071948	0.010678806199699999	-0.237289
25.128435200720002	0.00869660071948	0.010678806199699999	-0.175472
31.07870212566	0.00869660071948	0.010678806199699999	-0.203169
38.21898449774	0.00869660071948	0.010678806199699999	-0.154049
14.211838407644	0.00233164	0.0067546433054	-0.175906
25.969991513980002	0.019369683647919998	0.015283499072699998	0.739702
6.03080705138	0.01915690725028	0.0117780985807	0.273394
13.188085579364	0.01915690725028	0.0117780985807	-0.253209
12.612492549508	0.0440622550279	0.0113370672295	-0.344504
29.25436585996	0.0440622550279	0.0113370672295	0.329311
54.276747731460006	0.01742484786904	0.0056122790868	0.175405
74.80681417666001	0.0379618491754	0.00474698255217	-0.224025
6.160023361667999	0.030562422780699997	0.00510789371344	0.167362
12.772666143763999	0.030562422780699997	0.00510789371344	-0.261064
94.26181685416	0.030562422780699997	0.00510789371344	0.418989
58.48737463636	0.037059876877239994	0.0029943	0.396628
85.38673153766001	0.037059876877239994	0.0029943	0.374341
24.65430694534	0.04670290897678	0.028262985007499998	-6.51741
44.77464463214	0.04670290897678	0.028262985007499998	0.709811
79.54269058712	0.04670290897678	0.028262985007499998	1.62074
79.69368322216	0.04669739041888	0.0282671809729	-0.821337
31.16273445898	0.04281592471678	0.025864687458599996	0.220317
99.16860326986	0.04281592471678	0.025864687458599996	0.15886
85.88845957746	0.03777844110328	0.0240639105488	-1.5195
9.227269919082001	0.03250145207692	0.0230474505691	-0.254211
11.750430829404	0.03250145207692	0.0230474505691	0.957818
14.77823150936	0.03250145207692	0.0230474505691	0.983662
28.0035550114	0.03250145207692	0.0230474505691	1.73853
61.7061165053	0.03250145207692	0.0230474505691	0.233919
24.701065343	0.04669739041888	0.0282671809729	-1.50556

Table B.5: Data centers and RBF coefficients of the new steam species wall function

y^+	FG^+	$\dot{q}^+$	$RBF\ Coefficient$
5.1073599963196	0.03777844110328	0.0240639105488	0.160782
85.88845957746	0.03777844110328	0.0240639105488	-1.5195
9.110421347242	0.032472131738859995	0.023026597126599997	0.924831
11.60155322939	0.032472131738859995	0.023026597126599997	-1.91594
14.59091338486	0.032472131738859995	0.023026597126599997	-2.09434
27.64845675412	0.032472131738859995	0.023026597126599997	-1.72558
24.74782374066	0.04669187186098	0.028271199999999996	3.17996
44.9447010358	0.04669187186098	0.028271199999999996	-0.331718
81.46585494686	0.03695214502954	0.013842134403999999	-0.192882
98.36953734636	0.03695214502954	0.013842134403999999	0.170873
86.1029981079	0.031297734630279996	0.0132197160184	0.23364
25.30446681544	0.0192028312495	0.015295581430899999	-0.740068
35.71480199588	0.0503191	0.0057327235153	0.211203
71.21466903878	0.031297734630279996	0.0132197160184	0.155839
24.701065343	0.04669739041888	0.0282671809729	-1.50556
79.69368322216	0.04669739041888	0.0282671809729	-0.821337
85.88845957746	0.03777844110328	0.0240639105488	-1.5195
9.221683570964	0.03250006044058	0.023046616431399998	-0.259648
95.03242939166	0.02776998449584	0.022660966768099998	0.191739
11.940271820796	0.01414931982436	0.026948080669499996	-0.170519
78.79104697362	0.022778808781239997	0.0144679398942	-0.203976
8.761175003016	0.0377770974544	0.0240609784284	-0.162315
85.78318204926	0.0377770974544	0.0240609784284	2.30441
9.221683570964	0.03250006044058	0.023046616431399998	-0.259648
11.743307998441999	0.03250006044058	0.023046616431399998	0.910456
95.03242939166	0.02776998449584	0.022660966768099998	0.191739
5.057449911937	0.014145864727239998	0.0269494456221	0.154885
24.74782374066	0.04669187186098	0.028271199999999996	3.17996
44.9447010358	0.04669187186098	0.028271199999999996	-0.331718
8.392836436784	0.0428160206917	0.025866608502999995	-0.141486
85.78318204926	0.0377770974544	0.0240609784284	2.30441
14.76922127046	0.03250006044058	0.023046616431399998	0.940528
24.74782374066	0.04669187186098	0.028271199999999996	3.17996
60.23630942916	0.031873200250599996	0.0172304775721	0.168262
92.93219012638001	0.02723324475574	0.017223425317	0.253202
85.02755496172	0.01967248452052	0.0193733773234	-0.162354
12.991140725934	0.009975898415619999	0.021551437242599995	-0.193689
6.0991426000899995	0.047217574485279995	0.020975578906799998	0.247695
7.898800295666	0.047217574485279995	0.020975578906799998	-0.321449

Table B.5: Data centers and RBF coefficients of the new steam species wall function

y^+	FG^+	$\dot{q}^+$	$RBF\ Coefficient$
63.95877107492	0.047217574485279995	0.020975578906799998	-0.187823
36.99264356114	0.04290969221362	0.019280130839299997	0.285408
5.2527131702544	0.031875599623599996	0.0172335866308	0.204606
11.486715363494	0.031875599623599996	0.0172335866308	-0.235056
66.70357437772	0.0232656895504	0.0182426152019	-0.20703
5.500286081840399	0.009968604321699999	0.0215509317046	0.14922
83.54655622042	0.048998773025559994	0.0095981934478	-0.153695
92.59169794058	0.05030595143596	0.005740205477699999	0.220139
71.70160131786001	0.03515501465254	0.004990803529569999	0.17589
55.147136809200006	0.02446134510376	0.0057115414731	-0.154253
66.78134696612	0.02446134510376	0.0057115414731	-0.162893
80.74228534088	0.02446134510376	0.0057115414731	-0.223188
97.49554417306001	0.02446134510376	0.0057115414731	-0.0865937

Table B.6: Scales of the new steam species wall function

	y^+	FG^+	$\dot{q}^+$
Min	5.00658	0.00233164	0.0029943
Max	99.8512	0.0503191	0.0282712

Table B.7: Data centers and RBF coefficients of the new turbulence wall function

y^+	FG^+	$\dot{q}^+$	$RBF\ Coefficient$
98.46322994152	0.003636183607296	0.017477382092349995	12.1048
39.79714210172	0.004991668301208	0.017401840462270002	-1.78792
88.8885401794	0.004991668301208	0.017401840462270002	-2.57236
48.4651668226	0.00977638697064	0.01701830288761	-1.67667
71.89854103496	0.00977638697064	0.01701830288761	-1.66665
87.23682022756	0.00977638697064	0.01701830288761	-2.77736
44.49558246484	0.0033778442032619998	0.012760679298639999	1.57949
54.720312506240006	0.0033778442032619998	0.012760679298639999	2.40999
66.98989382548001	0.0033778442032619998	0.012760679298639999	1.35828
99.38173628776	0.0033778442032619998	0.012760679298639999	8.09182

Table B.7: Data centers and RBF coefficients of the new turbulence wall function

y^+	FG^+	$\dot{q}^+$	$RBF\ Coefficient$
39.47467968396	0.004896398309465999	0.01307664854665	-0.588198
48.54530877484	0.004896398309465999	0.01307664854665	-2.55001
59.42993106128	0.004896398309465999	0.01307664854665	-2.36307
72.49155358936	0.004896398309465999	0.01307664854665	-1.9795
88.16546273088	0.004896398309465999	0.01307664854665	-3.17532
7.482249175852	0.0094741117431	0.012082803975909998	-1.95085
85.93692912988	0.0094741117431	0.012082803975909998	-2.54571
44.267661026199995	0.0031864901769839997	0.008128744042000001	-1.37607
54.43915256032	0.0031864901769839997	0.008128744042000001	-3.29158
66.64498029344	0.0031864901769839997	0.008128744042000001	-1.89416
81.29191673492001	0.0031864901769839997	0.008128744042000001	-1.85024
98.86820257252	0.0031864901769839997	0.008128744042000001	1.84674
39.2057399648	0.004677861550332	0.00877581013486	-2.68448
59.023632204120005	0.004677861550332	0.00877581013486	-2.38523
71.9952608142	0.004677861550332	0.00877581013486	-2.23821
87.561366715	0.004677861550332	0.00877581013486	-4.24187
69.94463097952	0.009057780574919998	0.00819436119772	-1.44764
84.86524366216001	0.009057780574919998	0.00819436119772	-2.97056
36.58038055064	0.0029314681097724	0.011006962049049999	2.11688
68.1151019918	0.0029314681097724	0.011006962049049999	1.64524
83.08544815544	0.0029314681097724	0.011006962049049999	3.13558
37.09685090952	0.0027142023367908	0.00843315079561	2.42569
45.88215191512	0.0027142023367908	0.00843315079561	1.11723
56.42451312184	0.0027142023367908	0.00843315079561	3.99078
69.07538446208001	0.0027142023367908	0.00843315079561	2.84491
84.25641112427999	0.0027142023367908	0.00843315079561	2.97136
38.379690528000005	0.004422562438721999	0.0061501290497710005	-1.72159
47.19738934408	0.004422562438721999	0.0061501290497710005	-2.91264
57.778684761639994	0.004422562438721999	0.0061501290497710005	-3.28134
70.4762582088	0.004422562438721999	0.0061501290497710005	-3.20564
85.71327056104	0.004422562438721999	0.0061501290497710005	-3.882
70.95890980060001	0.0077399757181799995	0.005988557643649	-2.84303
86.09560261688	0.0077399757181799995	0.005988557643649	-3.69743
44.48847768184	0.0026373994230402	0.00687553826875	2.44413
54.70998688828001	0.0026373994230402	0.00687553826875	2.37898
66.97568425948	0.0026373994230402	0.00687553826875	2.33159
81.69461583536001	0.0026373994230402	0.00687553826875	3.07767
99.35729583424	0.0026373994230402	0.00687553826875	6.00848
69.10863484652	0.00765214005096	0.00659061913591	2.26488

Table B.7: Data centers and RBF coefficients of the new turbulence wall function

y^+	FG^+	$\dot{q}^+$	$RBF\ Coefficient$
99.20392725188	0.0025625065864973997	0.005399132994226	2.03599
87.3591172256	0.0037117816477620002	0.0054427187804079995	-2.4034
81.93892564012	0.008285204491199998	0.006919355304819999	1.82073
99.22590471396	0.008285204491199998	0.006919355304819999	-1.68946
7.6276414551639995	0.00248886	0.00400851068466562	-3.46431
22.90319962344	0.00248886	0.00400851068466562	1.50863
35.884964390600004	0.00248886	0.00400851068466562	2.72433
44.38209539772	0.00248886	0.00400851068466562	2.2047
54.578595768	0.00248886	0.00400851068466562	3.29081
66.81445305060001	0.00248886	0.00400851068466562	4.59066
81.49757652016	0.00248886	0.00400851068466562	6.31513
99.11715416884	0.00248886	0.00400851068466562	15.238
98.24970752976	0.00777456129324	0.00399997	1.89973
36.73147560244	0.003076684349274	0.017386833308079996	3.00451
45.4318981338	0.003076684349274	0.017386833308079996	3.15873
55.87223465664	0.003076684349274	0.017386833308079996	4.01982
68.40080899884	0.003076684349274	0.017386833308079996	4.43573
83.43500347904	0.003076684349274	0.017386833308079996	6.10063
47.22306129332	0.005183314663295999	0.017346244135029998	-1.48459
57.81146149388	0.005183314663295999	0.017346244135029998	-2.8058
70.51756068064	0.005183314663295999	0.017346244135029998	-2.60745
85.76489865084001	0.005183314663295999	0.017346244135029998	-2.51042
47.65389533444	0.019348136011139997	0.015321916339419999	2.24139
70.32023717412	0.019348136011139997	0.015321916339419999	3.01117
82.6841700116	0.03834006921834	0.01422278080405	-2.33174
99.8408	0.03834006921834	0.01422278080405	2.22909
7.9793661058400005	0.0191086005459	0.01157814927241	-1.38256
67.02058648804001	0.03779848339926	0.010422574311249998	1.74227
97.84539801184	0.03779848339926	0.010422574311249998	4.98073
99.40958703712	0.018733241365859996	0.008255184735969999	-3.99361
65.5114358484	0.03733681769316	0.00708436173532	1.91746
79.20718394184	0.03733681769316	0.00708436173532	4.04406
95.64196797744	0.03733681769316	0.00708436173532	9.67931
37.84105324616	0.01732562195334	0.00952751680204	2.31724
99.72248168044001	0.01732562195334	0.00952751680204	3.02795
64.46580125168	0.03691652874786	0.00812067438445	-3.90136
77.94281675916001	0.03691652874786	0.00812067438445	-1.97271
94.1152922064	0.03691652874786	0.00812067438445	-4.76035
99.10029215052	0.016862427106079998	0.0075741538158099996	1.73584

Table B.7: Data centers and RBF coefficients of the new turbulence wall function

y^+	FG^+	$\dot{q}^+$	$RBF\ Coefficient$
76.48823085296	0.03680314742832	0.006234711105159999	-3.94296
92.35880038792	0.03680314742832	0.006234711105159999	-3.74333
45.23419570552	0.01647717348324	0.005455107511387	2.43275
66.74814174260001	0.01647717348324	0.005455107511387	1.61477
97.72821645756	0.01647717348324	0.005455107511387	1.75683
74.87118224216	0.0368488867389	0.004487977120417	1.9759
90.4061218282	0.0368488867389	0.004487977120417	4.9601
54.55936548868001	0.04640844762486	0.028088499999999995	4.21892
66.07053490528	0.04640844762486	0.028088499999999995	3.66051
79.8839382052	0.04640844762486	0.028088499999999995	4.66605
96.46006005728	0.04640844762486	0.028088499999999995	16.783
38.05419673616	0.04270824084084	0.025655052610869998	-1.96344
56.1549102896	0.04270824084084	0.025655052610869998	-2.97895
68.00265695952001	0.04270824084084	0.025655052610869998	-2.89203
82.21989612515999	0.04270824084084	0.025655052610869998	-6.34464
85.93853954736001	0.0377013829356	0.023913283272159996	-2.54957
28.01542254848	0.0324445104507	0.02293191655996	1.33608
74.75646367932	0.0324445104507	0.02293191655996	1.6155
90.3857547836	0.0324445104507	0.02293191655996	2.03222
64.9425795562	0.02772904388592	0.02255119734331	-3.09201
78.6443903978	0.02772904388592	0.02255119734331	-2.47709
83.4562230976	0.02286970312788	0.0237740033917	-4.31362
48.60650463908	0.01994418624036	0.02494102040461	2.675
71.72736312988	0.01994418624036	0.02494102040461	1.95673
86.86102457208	0.01994418624036	0.02494102040461	2.33392
51.641573206240004	0.0474636	0.015962791680069997	3.70903
62.53661584108001	0.0474636	0.015962791680069997	3.26155
75.6106480568	0.0474636	0.015962791680069997	4.28885
91.29952460784	0.0474636	0.015962791680069997	12.1364
44.1497216284	0.04279787549766	0.01477932220117	-1.54235
53.56753778188	0.04279787549766	0.01477932220117	-1.95542
78.43039433384	0.04279787549766	0.01477932220117	-3.63252
82.49357236632	0.03689111801976001	0.013892430703629999	1.79864
99.6106050308	0.03689111801976001	0.013892430703629999	1.8991
27.014216528120002	0.03127791066984	0.01325764976107	1.3796
72.08089713196	0.03127791066984	0.01325764976107	-1.42745
87.1502366054	0.03127791066984	0.01325764976107	-3.10291
52.7825066256	0.04694688521214	0.02088622223824	2.33413
63.91844876936	0.04694688521214	0.02088622223824	2.68691

Table B.7: Data centers and RBF coefficients of the new turbulence wall function

y^+	FG^+	$\dot{q}^+$	$RBF\ Coefficient$
77.28159828796	0.04694688521214	0.02088622223824	2.50022
93.31728297984	0.04694688521214	0.02088622223824	10.5022
44.89392396504	0.0427976955987	0.019248394906479997	-1.80936
54.47069779684	0.0427976955987	0.019248394906479997	-1.56458
65.96273166456001	0.0427976955987	0.019248394906479997	-2.34268
79.753210198	0.0427976955987	0.019248394906479997	-6.29406
96.30176549204	0.0427976955987	0.019248394906479997	-2.15507
8.534079143348	0.03728775025182	0.01807908948322	-1.93943
21.05860849576	0.03728775025182	0.01807908948322	1.71683
88.07774234344001	0.031824218836620004	0.017227102265649996	2.02928
76.65561954044	0.027192810060899998	0.01722556059973	-2.39908
92.68164172744	0.027192810060899998	0.01722556059973	-2.45112
45.053828947759996	0.02322612794238	0.0182553211687	2.41662
80.51029587448001	0.02322612794238	0.0182553211687	-1.969
97.34237937544	0.02322612794238	0.0182553211687	-2.07936
70.03168825388	0.0196363791198	0.019381628565909997	2.84227
84.80717390244	0.0196363791198	0.019381628565909997	2.46591
8.999792932476	0.01394428607592	0.02075327764117	-1.86497
94.40734615292	0.01394428607592	0.02075327764117	3.95544
48.16070318844	0.009952418102999998	0.021550246656219997	0.0958013
58.74559836272	0.009952418102999998	0.021550246656219997	0.715491
71.44752941012	0.009952418102999998	0.021550246656219997	0.933766
86.689846667	0.009952418102999998	0.021550246656219997	2.45686

Table B.8: Scales of the new turbulence wall function

	y^+	FG^+	$\dot{q}^+$
Min	5.11036	0.00248886	0.00399997
Max	99.8408	0.0474636	0.0280885

C. Integration of the New Wall Function into ANSYS CFX

In the following, the implementation of the new wall function approach in the CFD solver ANSYS CFX is explained. First, the basic structure of the near-wall grid in ANSYS CFX is described and the different interfaces provided by ANSYS CFX that can be used to implement a wall function are explained. Finally, the structure and function of the "CFX USER FORTRAN" code used for the implementation is explained.

The topology of a near-wall grid in ANSYS CFX is shown in a simplified two-dimensional way in figure C.1 [ANSYS, 2016a]. It is immediately obvious that it is actually not a single grid but two overlapping grids. The grid consisting of the solid lines and the vertices (filled circles) is the grid generated by the user for the simulation. At runtime, ANSYS CFX generates a second grid around the vertices. This creates a control volume (dashed lines) for each vertex. For each of these control volumes, the relevant conservation equations are solved iteratively at runtime and the results of the respective iteration step, such as pressure and temperature, are stored at the vertices. However, only scalar quantities can be calculated and stored at the vertices, since the simultaneous storage of vectorial quantities at the vertices can lead to so-called "checkerboarding". This is a numerical problem that occurs when scalar and vectorial quantities are calculated at the same location on a grid. Therefore, so-called Integration Points (IP) are created at the boundaries of the control volumes. At these points, vectorial quantities, such as velocity, are calculated and stored. This was particularly relevant for the implementation of the new wall function approach because the different interfaces used access either the IPs or the vertices, so that different information are available depending on the interface. This problem was further complicated by the fact that the vertices and IPs of ANSYS CFX close to the wall were grouped into so-called Boundary Element Groups (BELGs) and, as can be seen in figure C.1, these groups each contain twice as many vertices as IPs.

Two different interfaces, provided by ANSYS CFX, are used to integrate the individual components of the new wall function approach. These are the so-called "Wall Function Transfer Coefficients" (WFTC) for the velocity and temperature wall functions and source terms for mass and energy at the wall surface. The WFTCs are the most sensible choice for the implementation of the wall functions, since they are intended for the integration of user-defined wall functions in ANSYS CFX. However, the WFTCs are only available for the energy and momentum conservation equation, so that another interface has to be used as substitute for the condensation mass flux.

The definition of the WFTCs according to the CFX User's Manual [ANS16] is given in equations C.1 and C.2. Equations C.3 and C.4 shows how CFX calculates the respective wall flux from the WFTCs.

$$WFTC_u = \frac{u_\tau}{u^+} \tag{C.1}$$

$$WFTC_T = \frac{u_\tau}{T^+} \tag{C.2}$$

$$\tau_w = \rho_w WFTC_u u_p \tag{C.3}$$

$$\dot{q}'' = \rho_w c_{p,w} WFTC_T (T - T_w) \tag{C.4}$$

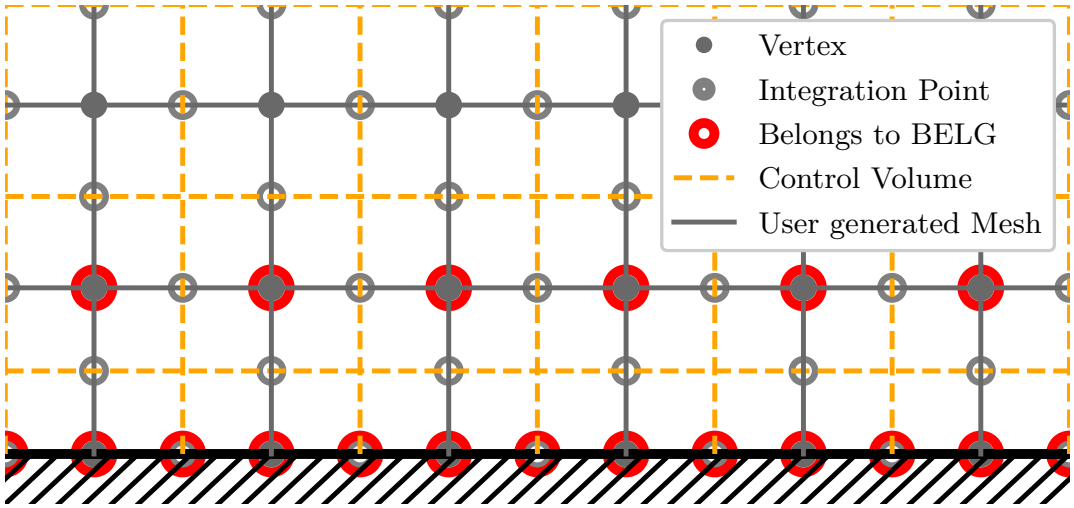

Figure C.1: Depiction of the near wall grid in ANSYS CFX

The biggest advantage of WFTCs over wall sources is that WFTCs are calculated at the vertices of a BELG, while sources are calculated at the integration points. Therefore, the WFTCs offer access not only to the data at the wall surface, but also the data at the first node in the flow. Only in this way it is possible to access important data for the wall functions such as velocity, temperature and the water vapor mass fraction at this node and thus implement the wall functions consistently in ANSYS CFX. Therefore, the interface for the WTFC of the momentum equation shown in figure C.2 is also used to execute the Fortran subroutines used to read in the data and calculate all wall functions.

There is also a special feature regarding the interface for the WTFC of the energy equation, also shown in figure C.2. This interface is intended for the transfer of sensible heat only. However, within the implementation of the new wall function approach, it is used for the total heat flow consisting of sensible and latent heat. This is because, according to the model assumptions described in section 2, the latent heat of condensation is transferred directly into the wall. However, this cannot be easily achieved by an energy source at the solid side of the interface because the integration points, at which the source terms are calculated, are sorted differently in the memory of ANSYS CFX at the fluid side of the interface than at the solid side of the interface. This makes it difficult to transfer the required information. However, for the interface of the WTFC of the energy equation, ANSYS CFX already has an internal function for the transfer of heat from the fluid to the solid domain. Thus, the heat transfer between the domains can be easily realized through this interface by calculating the WTFC using equation C.5. It should

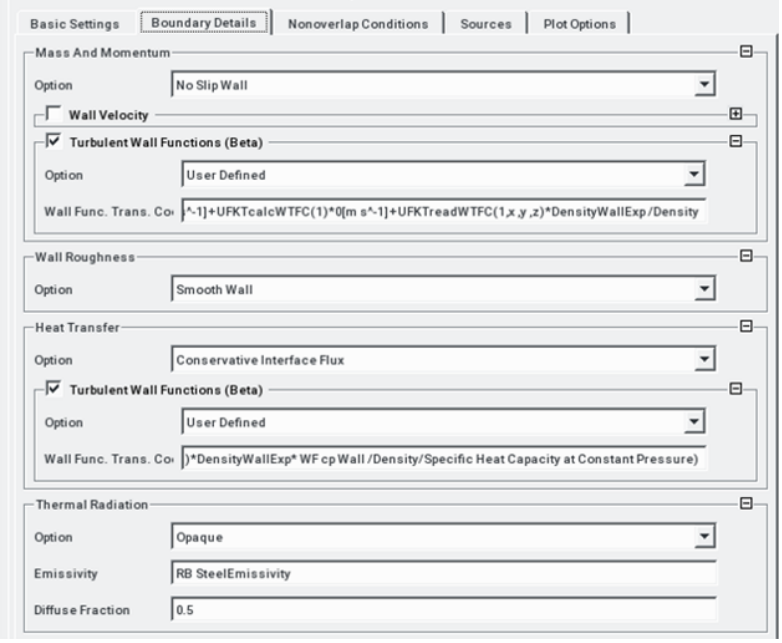

Figure C.2: CFX pre processor dialog as direct interface for user defined wall functions in ANSYS CFX

be noted, however, that at the fluid side of the wall an additional wall source for the latent heat is required to satisfy the energy conservation equation.

$$WFTC_T = \frac{\rho_w c_{p,w}(T - T_w)}{\dot{q}''_{Sen} + \dot{q}''_{Cond}} \tag{C.5}$$

The wall sources serve as the second interface for the new wall function approach. The corresponding pre-processor interface is depicted in figure C.3. The sources are used to extract the condensate mass flow from the fluid and to supply the latent heat to the flow, which is then transferred directly to the wall via the temperature WFTC. Unlike the WFTCs, the sources are calculated and used at the integration points of a BELG. Accordingly, when implementing the subroutine for data output described below, care had to be taken to ensure that the fluxes calculated at the vertices are correctly transferred to the corresponding integration points. The exact procedure for this is described in connection with the subroutine for data output.

During the runtime of a simulation ANSYS CFX uses its so-called 'Memory Management System' or MMS [ANSYS, 2016a] to manage the memory of the computer allocated to it. The MMS consists of five Fortran stacks, one for each data type (e.g. integer or character), in which all simulation data are stored. These stacks can also be accessed by the user via the 'CFX USER FORTRAN' interface to store information in the computer's memory. Similar to the operation system of a computer, certain areas of the MMS stacks can be allocated as files, and these files can be organized in different folders to allow the user to locate data in the five large arrays.

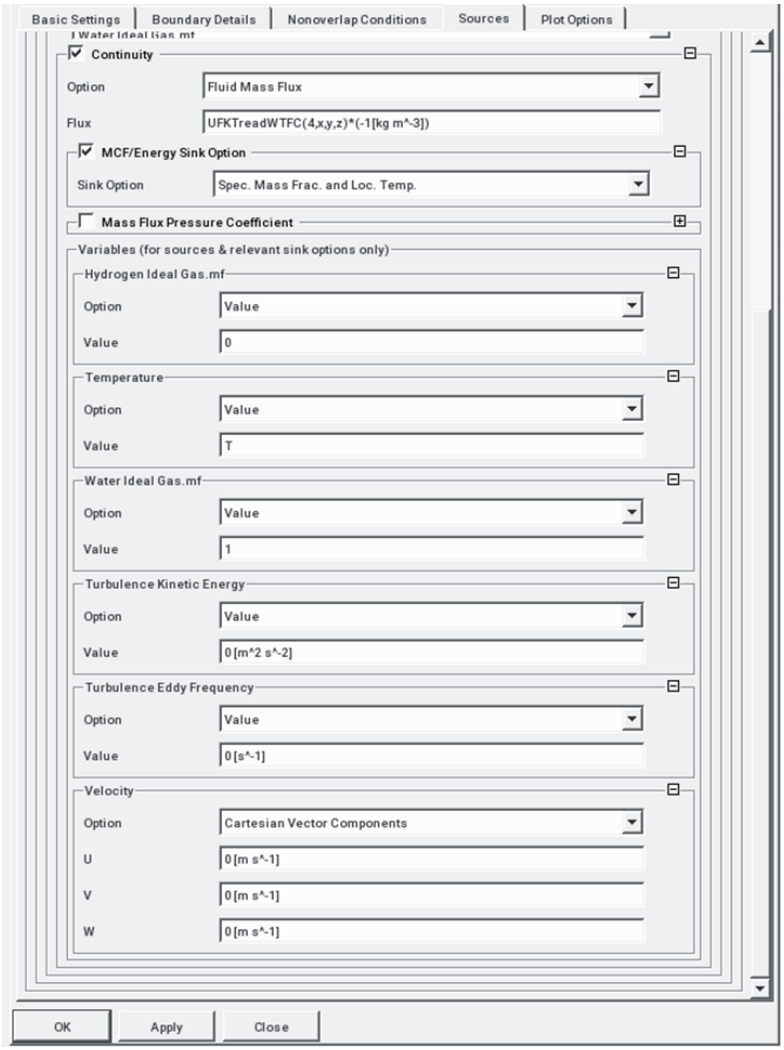

Figure C.3: CFX pre-processor interface for the mass source at the wall surface as connecting point for the condensation mass flux

The implementation of the new wall function approach in ANSYS CFX is based on a total of ten 'USER FORTRAN' subroutines, which are listed in table C.1 together with their respective tasks. Of the ten subroutines, four are called directly by ANSYS CFX, while the remaining six are each used by one or more of the directly called subroutines. The four subroutines called directly by ANSYS CFX are used to read data into the MMS stack before simulation run time, read simulation data into the MMS stack at run time, perform the calculation of the wall functions, and return the results of the calculation to ANSYS CFX in a suitable format.

The subroutine "rbfdata" reads the data required for the RBF approximation into the MMS stack. The subroutine is integrated into CFX as a so-called junction box routine,

Table C.1: USER FORTRAN subroutine of the new wall function approach

Subroutine	Called by	Task
dataInput	CFX $WFTC_u$	Transfers data from the simulation into the USER area of the MMS stack
calcWallNormal	dataInput	Calculates wall distance
calcWFTC	CFX $WFTC_u$	Calculates the WFTC
exchangeData	calcWFTX	Swaps data between wall and fluid vertices and calculates additional data
Swapinfo_f_w	exchangeData	Swaps data from fluid to wall vertices
Swapinfo_w_f	exchangeData	Swaps data from wall to fluid vertices
writeResults	calcWFTC	Writes calculation results to text file
readWFTC	CFX	transfers calculation results to CFX
calcDist	calcWFTC	Calculates the non equilibrium factors
rbfData	calcDist	Contains input data for the calculation of the non equilibrium factors

which is executed once at the start of the simulation and writes the values required for the RBF approximation, i.e. data locations, coefficients and scaling factors, into the random access memory. The data locations are written into the memory in scaled form to save computing time during the simulation.

The subroutine "dataInput" is used to read simulation data into the user area of the MMS stack and is called by ANSYS CFX through the interface for the WFTC of the velocity wall function. This interface is used because it accesses the vertices and therefore has access to the data at the first node off the wall. Before actually reading the data, the system checks if the folder /USER exists in the MMS stack and, if not, creates it together with the subfolder DATACONTAINER, where the data for the wall function calculation is stored. In addition, the integer file NLOCALE is created to count the calling BELGs and the character file CLOCALE to store the names of these BELGs. A subfolder is then created for each BELG, in which the corresponding data are stored.

The data to be read are passed as arguments to the subroutine "dataInput" in ANSYS CFX. It is important to hand over the input data to the subroutine in the correct sequence. A list of the arguments in this order as well as their mathematical description can be found in table C.2. To ensure that the data fields in the MMS stack can be addressed with a meaningful name, the names of the variables required for the wall function calculation are also stored in the Fortran variable "VarNames". The first time the subroutine is called on a BELG, a data field of length NLOC is created in the corresponding directory for each variable listed in "VarNames". The data are written into the data fields each time the subroutine is called. It is important to note that the name rows in table C.2

represent these "VarNames" but the final calculation of the described variables is carried out by the FORTRAN subroutines and thus only some of the data need to be read in from ANSYS CFX as described by the equation rows. For example, only the quotient of the density ρ_w and the dynamic viscosity μ_w at the wall surface are read in for the determination of y^+. This is later on multiplied with the distance of the first mesh point from the wall Δx_n, that is calculated by another FORTRAN subroutine, and the shear velocity u_τ which is an input variable itself.

Table C.2: Input data for the calculation of the wall functions

Name	y^+	u_τ	Pr	Sc	FG^+
Equation	$\frac{\rho_w}{\mu_w}$	$\sqrt{\frac{\tau_w}{\rho_w}}$	$\frac{\mu_w c_{p,w}}{\lambda_w}$	$\frac{\mu_w}{\rho_w D}$	$\frac{\mu_w}{\rho_w^2}$

Name	$\dot{q}^+$	Density	Velocity u	Velocity v	Velocity w
Equation	$\frac{\dot{q}''_{Tot}}{\rho_w \Delta h_{Cond}}$	ρ_w	u	v	w

Name	Temperature	T_{Wall}	Y_{Flow}	c_p	Latent Heat
Equation	T	T_w	Y_{H2O}	$c_{p,w}$	Δh_{cond}

Name	myTmy	Y_{Wall}	pdx	pdy	pdz
Equation	$\frac{\mu_T}{\mu_w}$	$Y_{H2O,Wall}$	$\frac{\partial p}{\partial x}$	$\frac{\partial p}{\partial y}$	$\frac{\partial p}{\partial z}$

Name	g_x	g_y	g_z	$Density_{Ref}$	Eddy Frequency
Equation	g_x	g_y	g_z	ρ_{Ref}	ω

Name	kinematic Viscosity
Equation	$\frac{\mu_w}{\rho_w}$

If less than the specified number of arguments are passed to the subroutine "dataInput", an error occurs when it is called for the first time during the simulation, because not all information are available to calculate the wall functions. If more than the required number of variables are passed as arguments, the subroutine will create additional data fields named "ARGn", where n corresponds to an ascending number starting with one. It is important that the necessary arguments are first passed to the subroutine in the correct order.

The first time the subroutine "dataInput" is called, the subroutine "calcWallNormal" is also called. This subroutine is used to calculate the distance between the wall node (vertex) and the first node off the wall for all nodes of the BELG, since this information

is not made available to the user by ANSYS CFX. A major challenge here is that the sequence in which the data is stored on the vertices of a BELG is not subject to any obvious order. As a result, it is not possible to find the node of a cell in the flow that belongs to a wall node. Experiments regarding this problem showed, however, that the storage structure is divided into eight blocks, each corresponding to one corner of the hexahedron described by the vertices (see figure C.1). Furthermore, it was shown that the vertices belonging to a cell always take the same position in these blocks and that the blocks always follow each other in the order of wall nodes and associated flow nodes. This memory structure makes it possible to calculate the wall distance by means of a simple loop using the Euclidean norm.

The actual calculation of the wall functions of the new wall function approach is performed by the subroutine "calcWFTC". This subroutine is also called from ANSYS CFX by the interface for the WFTC of the momentum equation. When this subroutine is called for the first time, data areas are created in the folder of the calling BELG for all quantities necessary for the calculation of the wall functions. Then, the current iteration step is read from the MMS stack and, when the subroutine is called for the first time, a data field is created to store the iteration step. This allows to check whether the calculation of the wall functions has already been performed in the current iteration step, so that a further calculation with a possibly different result can be avoided. The check is done by comparing the iteration step read from the MMS stack with the stored value. If they do not match, the wall functions are calculated and the stored value is overwritten with the current one. If the values match, the subroutine is terminated.

The calculation of the WFTCs is under-relaxed with PT1 elements because the potentially strong fluctuations of the heat flows between two iteration steps in condensing flows can lead to numerical instabilities. The under-relaxation avoids excessive changes between two iteration steps and thus increases the numerical stability of the calculation. The number of iteration steps is used as the time measure for the PT1 element, therefore the PT1 element can be described by equation C.6 if four iteration steps are used as thr time constant. Here $WFTC_n$ and $WFTC_{n-1}$ stand for the WFTCs stored in the n-th and (n-1)-th iteration step in the MMS stack and $WFTC_{calc}$ for the WFTC currently calculated by the subroutine "calcWFTC".

$$WFTC_n = \frac{1}{5}(WFTC_{calc} - 4WFTX_{n-1}) \tag{C.6}$$

In addition to the WFTC, additional variables are calculated in the subroutine "calcWFTC". These are:

- the condensation mass flux and the latent heat flux, since these are required as explicit quantities for the wall sources described above
- the sensible and the total heat flux, since a new WFTC with the total heat flux is required for the previously described procedure of transferring the latent heat flux into the solid domain

The subroutine "calcWFTC" accesses three additional subroutines to perform its calculations. These are the subroutines "calcDist", "exchangeData" and "writeResults".

The subroutine "calcDist" is used to calculate the non-equilibrium factors during the simulation. The calculation process is presented in figure C.4. The subroutine is called directly before the calculation of the WFTCs. In the subroutine "calcDist" itself, the input variables for the approximation function (y^+, FG^+, $\dot{q}^+$) and the scaling variables are read from the MMS as a first step of calculating the non-equilibrium factors. Then all non-equilibrium factors are calculated via a loop, each following the same pattern. First, the data locations and coefficients relevant for the respective factor are read from the MMS stack. Then the input variables are scaled. Then the distance matrix (equation 4.24) is calculated and the basis function equation 4.26 is applied to it. The resulting matrix is then multiplied by the RBF coefficients, to finally gain the non-equilibrium factors.

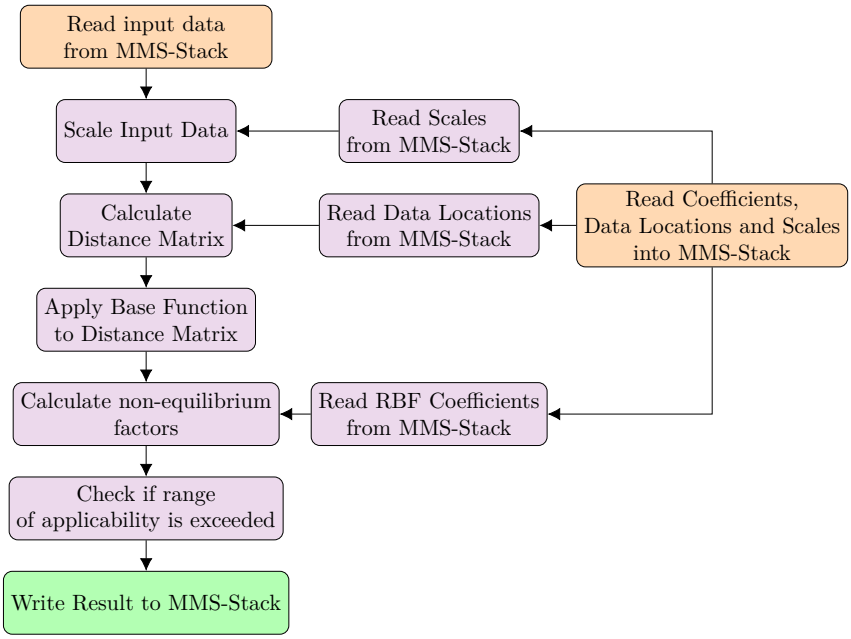

Figure C.4: Flowchart of the calculation of the non-equilibrium factors during simulation run time with the subroutine "calcDist"

After the calculation of the non-equilibrium factors, a final check is performed to determine whether and at how many positions in the BELG the input variables of the model exceed the definition range, in order to be able to output corresponding information to the user. To increase the numerical stability of the simulation, the non-equilibrium factors are also under-relaxed by a PT1-element. Finally, the factors are written into the MMS stack and are thus available for the calculation of the WFTCs.

The subroutine "exchangeData" serves two purposes. First, it exchanges information between the vertices located on the wall surface and the vertices of a BELG located in the flow. This is necessary because not all information is available at all vertices. For example, a value for the ANSYS CFX variable T.Boundcon, which describes the actual wall surface temperature, only exists at the wall vertices. However, this information is required at all

vertices for the calculation of the sensible heat flux from T^+ (see equation 3.25). To be able to perform this exchange, the subroutine "exchangeData" accesses the subroutines "swapinfo_f_w" and "swapinfo_w_f", which perform the exchange of the information. Here f and w stand for fluid and wall, whereby the first of these letters in the name of the subroutine indicates the origin of the information and the second its destination.

The second purpose of the subroutine "exchangeData" is to calculate quantities that cannot be read into the MMS stack via the subroutine "dataInput" and, if necessary, to add this missing information to other variables. For example, u_τ is not included in the formula for y^+ in table C.2, since u_τ is calculated in the subroutine "exchangeData" and therefore y^+ can only be completely calculated there. The reason for this is that the attempt to read u_τ via the subroutine "dataInput" results in a wall shear stress of 0 throughout the simulation. The fact that the subroutine "dataInput" continues to read a value for u_τ therefore only serves the purpose to create a suitable data field. This value is no longer used for the calculation of the wall functions.

The subroutine "writeResults" is used to write the calculation results of the subroutine "calcWFTC" into a text file, which is stored together with the simulation results of ANSYS CFX. This is necessary because the calculation results of the wall function approach exist only on the BELGs and therefore cannot be output as variables in ANSYS CFX. Accordingly, they cannot be saved in the .res file to which ANSYS CFX writes the simulation results. Therefore, the subroutine "writeResults" outputs a result file for each BELG every 20 iteration steps for steady state calculations and every 20 time steps for transient calculations.

The third subroutine called directly from ANSYS CFX is the subroutine "readWFTC", which transfers the calculation results of the new wall function approach to ANSYS CFX. For this purpose, the subroutine is passed the location coordinates x, y and z as well as an integer parameter that specifies which variable is to be passed to ANSYS CFX (see table C.3). Since the three interfaces used to connect the wall function approach to CFX require data on different parts of the grid (IP, vertex, etc.), the subroutine "readWFTC" must output the data in a form suitable for each interface. This is simple for the interfaces for user-defined wall functions, since these require the data on the vertices of the BELGs on which they were calculated. Thus, the subroutine only has to read and output the data from the MMS stack here.

Table C.3: Association of calculation results with the output parameters of the subroutine "readWFTC"

Calculation result	Parameter
WFTC velocity	1
WFTC temperature	2
WFTC species	3
Condensation Mass Flux	4
Latent Heat Flux	6

The data output at the wall sources and sinks is somewhat more complex. Here the calculation results have to be transferred from the vertices to the corresponding IPs of a BELG. The division of the vertices into eight blocks in the MMS stack, as described above, is helpful in solving this task, since each block corresponds to one corner of a cell. For example, the first block could contain all vertices of a BELG, which are located on the wall surface at the back left corner of the cell. A similar structure is found in the IPs of a BELG. However, there are only four blocks, because the BELG only contains IPs on the wall surface. Otherwise, the structure of the data storage corresponds exactly to the one used at the vertices. Therefore, the subroutine "readWFTC" only returns the first, third, fifth, and seventh block of the data on the integration points.

D. Additional Validation Results

D.1. Additional SETCOM validation cases

In addition to the two local SETCOM results presented in section 5.2, this appendix presents the local results of three additional SETCOM experiments to further substantiate the findings discussed in that section and offer additional insights in the operation of the model. These three experiments are:

- C063 showing the new model's capability to operate in a flow without condensation
- C003 as an additional validation case for forced convection flows
- D002 as an additional validation case for mixed convection flows

The boundary conditions of the three experiments are presented in table D.1.

Table D.1: Overview of SETCOM experiments used as additional validation cases

Experiment	Velocity	Temperature	Relative Humidity	Wall Temperature
C063	$4.9\,\mathrm{m\,s^{-1}}$	28 °C	42 %	24.5 °C
C003	$3\,\mathrm{m\,s^{-1}}$	80 °C	90 %	7.9 °C
D002	$1\,\mathrm{m\,s^{-1}}$	80 °C	90 %	7.6 °C

The figures D.1 to D.3 show the local fluxes starting at the interface 2 m downstream of the leading edge of the SETCOM cooling plate. Data are depicted for the fine mesh (black) as reference, the medium mesh (green) and the coarse mesh (blue). The results of the new wall function approach are represented as solid lines, while the standard model results are shown as dashed lines.

Along with the fluxes the corresponding non-dimensional profiles are also shown in the figures. The profiles have been evaluated 4.5 m downstream of the leading edge of the cooling plate. Regarding the non-dimensional profiles, it should be noted that only the first grid point off the wall surface is directly influenced by the wall functions because they only serve as a boundary condition. Meanwhile, the rest of the profile represents the flow solution obtained by ANSYS CFX with this boundary condition. When interpreting the dimensionless profiles it should also be kept in mind that the fluxes are inversely proportional to the corresponding dimensionless variables as already explained in section 5.1.

The experiment C063 differs substantially from the other experiments for which local results are presented, because no condensation took place during the experiment, as can be seen from the boundary conditions in table 5.1. Consequently, the experiment is outside of the application range of the new model. Nevertheless, the results offer some valuable insights. The first relevant insight to be gained from the results shown in figure D.1 is the fact that the fallback to the standard model implemented into the new model works perfectly, as the results from both models are identical (thus no dashed lines can be seen).

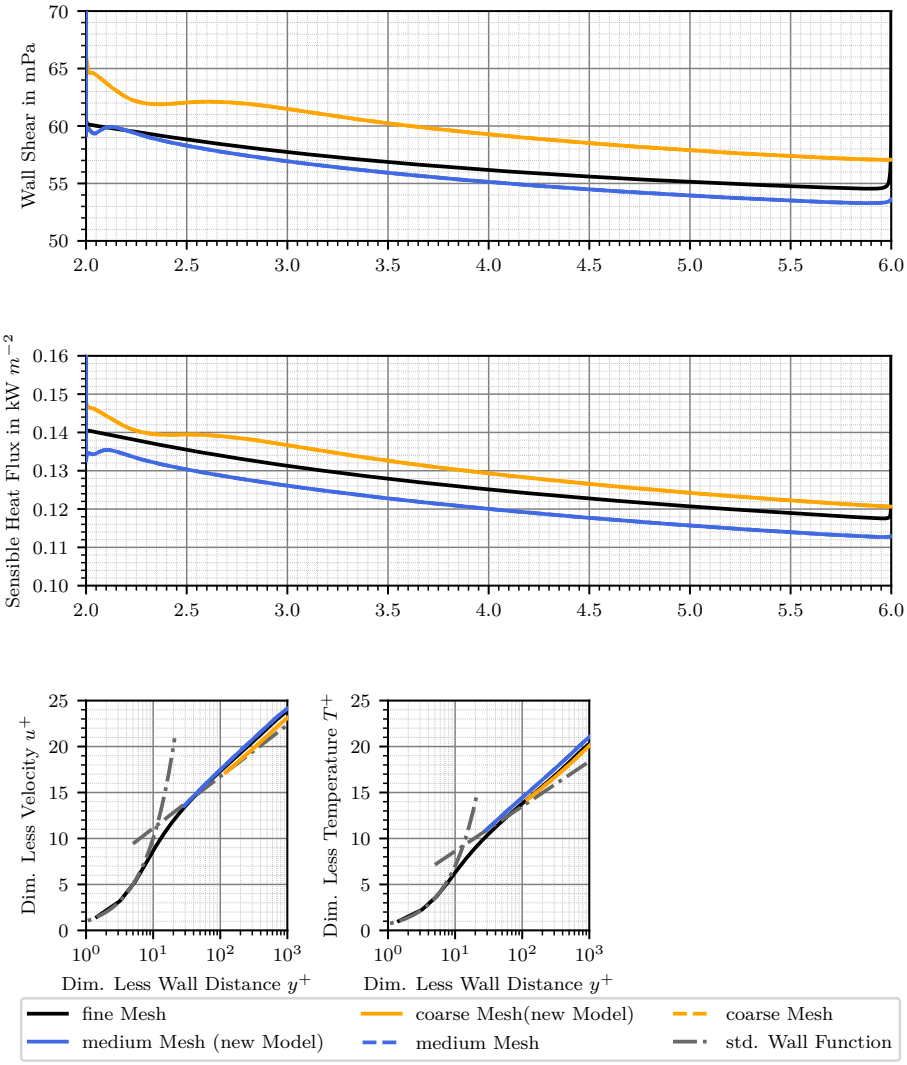

Figure D.1: Local fluxes and dimensionless profiles for the simulations of the SETCOM experiment C063

Figure D.1 also shows that the ANSYS CFX fine mesh results deviate slightly from the standard model and how these deviations influence the wall fluxes. For both the dimensionless velocity u^+ and the dimensionless temperature T^+, ANSYS CFX predicts a slope larger than the slope of the standard model in the turbulent layer. This leads to deviations in the calculation of the wall shear on the coarse mesh, since the u^+ predicted by the wall function is too small, and the calculation of the sensible heat flux on the medium mesh, since the T^+ predicted by the wall function is too large. The calculation of the wall shear on the medium mesh and the heat flux on the coarse mesh are not directly affected, since the first grid point off the wall surface incidentally lies close to the

intersection point between the standard model and the fine mesh solution in this cases. Thus, the standard model incidentally yields correct results in these cases. Nevertheless, the results for the sensible heat flux show a similar magnitude of error on the medium and the coarse mesh. However, on the coarse mesh this is not due to the wall function but due to the error in the calculation of the wall shear and consequently the shear velocity u_τ, which also influences the calculation of the heat flux (seeequation 3.25). This result shows the importance of the correct calculation of the wall shear for the overall calculation of the wall fluxes.

There are several possible reasons for the difference between the fine mesh solution and the standard model in the given simulation. The most likely reason is the calibration of the k-ω SST turbulence model used for the simulations. Similar to most two-equation models the SST model contains a set of coefficients that must be determined from experimental or DNS data, for example. Thus, the quality of the prediction of different turbulent flow phenomena by a two-equational model always depends on the calibration cases used. While the original k-ω model by Wilcox [Wilcox, 1993] used the log-law as a calibration case, it was not used to calibrate the SST model [Grotjans et al., 1998]. Thus, some deviations from the log-law are understandable. However, it should also be noted that the log-law also contains two empirical constants, κ and β, and while 0.41 and 5.5 are the most commonly used values for these constants, a variety of different values have been reported in the literature. Thus, the standard models themselves may be a source for the deviation.

Overall, the results depicted in figure D.1 show that the standard wall functions are well integrated into ANSYS CFX and yield reasonable results when applied to coarse meshes. Remaining errors can be attributed to model inconsistencies between the log-law and the SST turbulence model. The data also show that the integration of the new model into ANSYS CFX works correctly and that its fallback to the standard model outside of its application range works as intended. However, the results also stress the necessity of a correct prediction of the wall shear for an accurate prediction of the sensible heat flux and the condensation mass flux. This is due to the fact that it represents the momentum transfer and thus the convective transport in the scaling approach in the form of the shear velocity u_τ.

The experiment C003 was chosen as a test case because it has a strong condensation influence while remaining a forced convection flow. Thus, it illustrates the impact of a strong suction effect on the flow while buoyancy is still insignificant. The two most prominent differences between the simulations of the experiments C003 shown in figure D.2 and C021 shown in figure 5.19 are the large error the new model medium mesh results for the wall shear exhibit for the first 1.5 m of the examined part of the cooling plate and the deterioration of the coarse mesh results for the wall shear and the sensible heat flux.

The large discrepancy between the fine mesh and the coarse mesh is due to the corresponding non-equilibrium factors. Thus, this is either the consequence of faulty experimental input data, an error in the generation of the approximation function, or a model error in the fine mesh calculation. Since the approximation function yields only a small error compared to the experimental data for most of the data points, as shown in section 4.3, and the new model medium mesh solution behaves differently compared

to all other calculations, the faulty experimental data are the most likely cause of the error. Nevertheless, it can also be observed that the new model is able to recover from such an error, as the new model medium mesh calculation actually yields the best result downstream of 2.5 m plate length.

While the standard model coarse mesh results for the wall shear and sensible heat flux of the C003 simulations show the same trend of getting worse compared to the C021 simulations, the reasons for this behavior are diametrically different. The plot of the non-dimensional velocity in figure D.2 shows that the fine mesh solution is still in very good agreement with the standard model. Accordingly, both the standard model and the new model give good results for the non-dimensional velocity. This observation is also supported by the data shown in table D.2. Table D.2 also shows that the reason for the worse performance of the standard model on the coarse mesh is not due to the wall function but due to the incorrect prediction of the near wall velocity by ANSYS CFX. In this case, even the slightly better prediction of the wall shear by the new model on the coarse mesh is due to a cancellation of errors effect and not due to an improvement of the near wall flow model.

Table D.2: Breakdown of the error in the calculation of the wall fluxes of SETCOM experiment C003 on the coarse mesh at 4.5 m

Wall Shear

Wall Function	$(\frac{u^+_{fine}}{u^+_{coarse}})^2$	$(\frac{u_{coarse}}{u_{fine}})^2$	Cumulative error	Error from CFX result
Standard	1.0110	0.9080	0.9180	0.9181
New	1.0510	0.8968	0.9425	0.9426

Sensible Heat Flux

Wall Function	$\frac{T^+_{fine}}{T^+_{coarse}}$	$\frac{(T-T_W)_{coarse}}{(T-T_W)_{fine}}$	$\frac{u_{\tau,coarse}}{u_{\tau,fine}}$	Cumulative of error	Error from CFX result
Standard	0.8562	0.9655	0.9582	0.7921	0.7857
New	0.9854	0.9199	0.9709	0.8801	0.8768

Condensation Mass Flux

Wall Function	$\frac{Y^+_{s,fine}}{Y^+_{s,coarse}}$	$\frac{(Y-Y_W)_{coarse}}{(Y-Y_W)_{fine}}$	$\frac{u_{\tau,coarse}}{u_{\tau,fine}}$	Cumulative error	Error from CFX result
Standard	1.1393	1.0230	0.9582	1.1168	1.1142
New	1.0353	1.0503	0.9709	1.0557	1.0546

In stark contrast to the wall shear calculation, it is immediately clear that the better prediction of the sensible heat flux by the new model on the medium as well as on the coarse mesh by the new model is due to the model improvements, if one looks at the plot of the dimensionless velocity in figure D.2. The fine mesh result shows that the

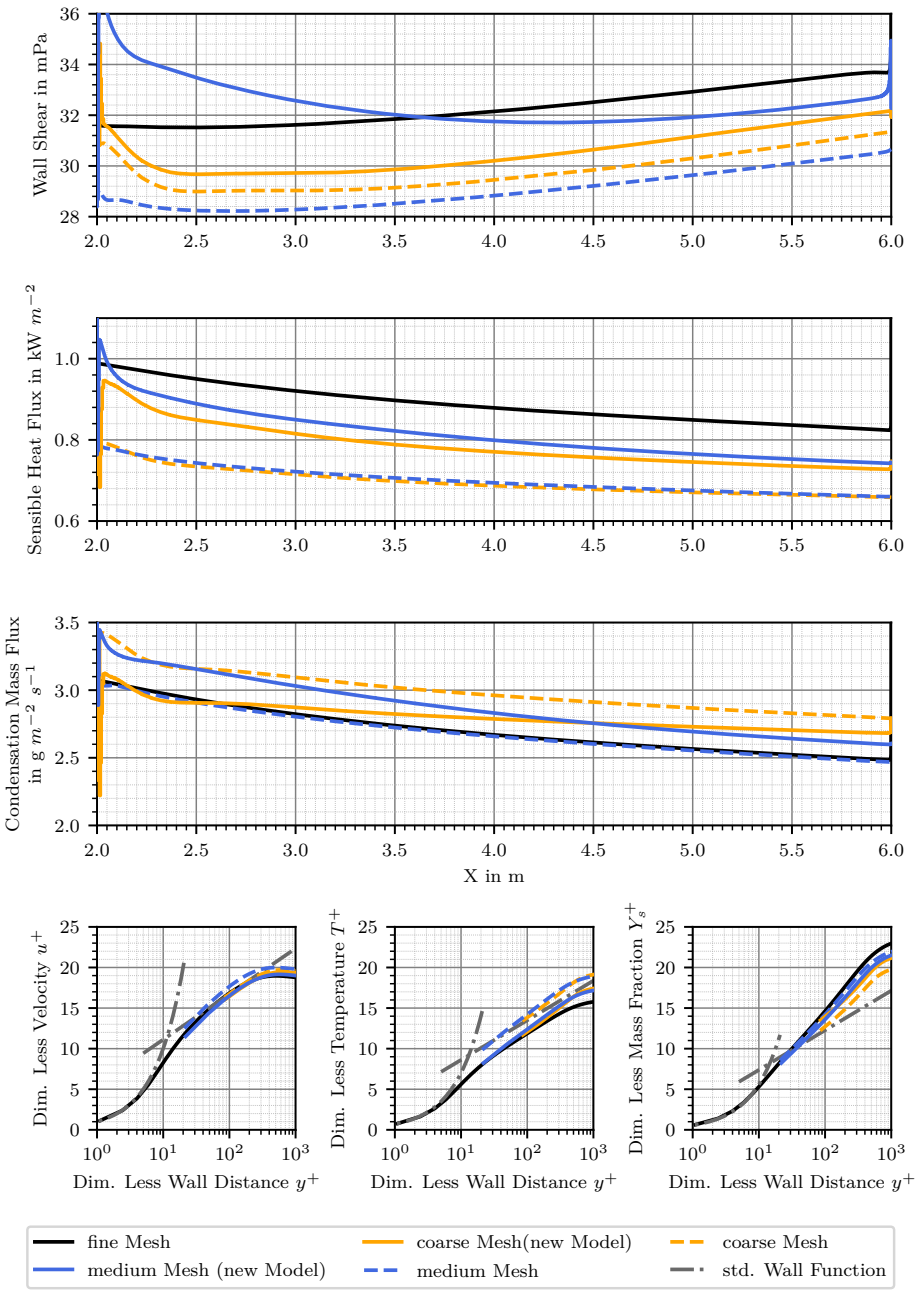

Figure D.2: Local fluxes and dimensionless profiles for the simulations of the SETCOM experiment C003

dimensionless temperature in the turbulent layer has been pushed down even further than in the experiment C021 by the suction effect. In fact, it has been pushed so low that it no longer intersects with the standard model.

Figure D.2 and table D.2 show that the new model yields very accurate (less than 2 % error) results for the dimensionless temperature on both meshes while the standard model leads to errors of more than 14 % for this quantity. Nevertheless, the new model results for the sensible heat flux still show an error of about 14 % (compared to about 26 % for the standard model) due to errors in the prediction of the shear velocity and especially the temperature difference between the wall surface and the first node in the flow.

The wall condensation results of the C003 simulations are relatively similar to those of the C021 simulations. Again, the fine mesh solution and the standard model intersect close to the y^+ of the medium mesh, and thus both models yield good results for the condensation mass flux. The slightly better performance of the standard model is due to a cancellation of errors effect and not due to a better performance of the wall function, as both models yield an error of about 2.5 %. On the coarse mes,h the new model yields a better result due to its better prediction of the non-dimensional steam mass fraction (3.5 % compared to 13.5 % error), as already seen for the simulations of the experiment C021. But again, the improvement of the prediction of the condensation mass flux is limited by the ANSYS CFX prediction of the steam mass fraction difference between the wall surface and the first mesh node in the flow. Nonetheless, the wall condensation data show that the new wall function is well able to improve CFX's prediction of the wall fluxes when the actual flow behavior differs from the standard model.

Overall, the results for the experiment C003 again emphasize that the capability of the new model is limited by the correct prediction of the rest of the flow field by ANSYS CFX. But more importantly, the sensible heat flux data show the huge potential of the new model to improve the calculation of wall fluxes on coarse meshes, since the error in the prediction of the flux is at least halved by the model on the coarse as well as the medium mesh.

The experiment D002 combines a highly buoyant flow with a high condensation rate and thus a high suction effect. It is therefore the most challenging for the new wall function. The D002 experiment is also one of the most important test cases for the new model, since it most closely resembles the flow type further away from the break and the long-term situation in a containment under severe accident conditions. The simulation results for the experiment are presented in table D.3 and figure D.3.

The strong buoyancy in experiment D002 leads to a continuous increase of the fluxes along the cooling plate, for example the wall shear increases by 39 % in the observation area, as shown in the flux plots in figure D.3. While both wall functions are well able to mimic this gradient on both meshes for the wall shear and the condensation mass flux this is not the case for the sensible heat flux. This leads to two interesting observations. First, the observed error seems to be present only in buoyant flows, as it can be found only in the simulations of the experiments D002 and D111, but not in the results of the less buoyant flows.

Second, the erroneous prediction of the gradient seems to be independent of the wall function result. For example, the medium mesh result with the new wall function and the coarse mesh result with the standard wall function are very similar, but the former simulation yields the best wall function result for the D002 experiment (error less than

2 %), while the latter yields the worst wall function result for the experiment (error about 9 %), as can be seen from figure D.3. Additionally, the plot of the dimensionless temperature in figure D.3 shows a characteristic bend in the turbulent layer that is not adequately represented by any of the coarse mesh solutions. This is especially interesting with respect to the medium mesh results, since their first mesh node of the wall ($y^+ \approx 20$) is a significant distance away from the bend ($y^+ \approx 60$), and the wall function results are close to the fine mesh solution at this location. The latter two observations make it unlikely, but not impossible, that the wall function is the cause of the observed error. The fact that the observed effect does not influence the other two fluxes also makes it unlikely that the error is caused by local transport phenomena such as turbulence or the wall normal velocity. Potentially, the erroneous behavior results from a higher sensitivity of the energy equation to the overall coarser mesh near the condensation plate or to the averaging at the GGI interface, but an exact cause could not be determined.

Table D.3: Breakdown of the error in the calculation of the wall fluxes of SETCOM experiment D002 on the coarse mesh at 4.5 m

Wall Shear

Wall Function	$(\frac{u^+_{fine}}{u^+_{coarse}})^2$	$(\frac{u_{coarse}}{u_{fine}})^2$	Cumulative error	Error from CFX result
Standard	0.9124	0.9604	0.8763	0.8763
New	1.1048	0.8230	0.9093	0.9092

Sensible Heat Flux

Wall Function	$\frac{T^+_{fine}}{T^+_{coarse}}$	$\frac{(T-T_W)_{coarse}}{(T-T_W)_{fine}}$	$\frac{u_{\tau,coarse}}{u_{\tau,fine}}$	Cumulative error	Error from CFX result
Standard	1.0924	0.8904	0.9361	0.9105	0.9003
New	0.9222	0.8798	0.9535	0.7735	0.7776

Condensation Mass Flux

Wall Function	$\frac{Y^+_{s,fine}}{Y^+_{s,coarse}}$	$\frac{(Y-Y_W)_{coarse}}{(Y-Y_W)_{fine}}$	$\frac{u_{\tau,coarse}}{u_{\tau,fine}}$	Cumulative error	Error from CFX result
Standard	1.4602	0.9056	0.9361	1.2379	1.2334
New	0.9862	0.9950	0.9535	0.9356	0.9368

While three of the four remaining fluxes yield rather unimpressive results, the wall shear results on both meshes and the condensation mass flux results on the medium mesh show some slight improvements by the new model, the coarse mesh results for the condensation mass flux show one of the largest improvements of the flux prediction by the new model. While the error of the standard model is so large that its curve is outside the range of the condensation mass flux plot in figure D.3 the new model result agrees relatively well with the fine mesh result. Quantitatively, the new model

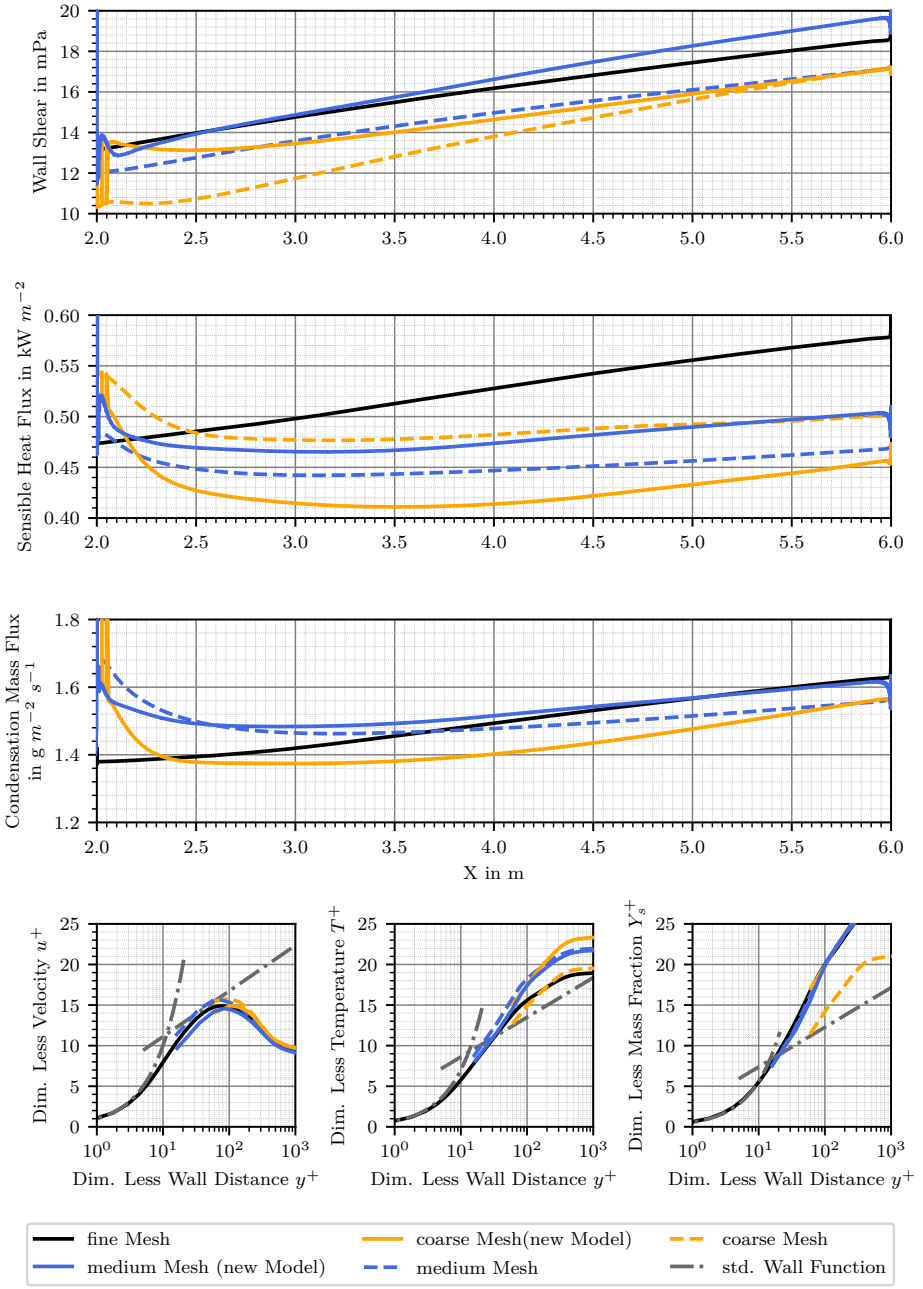

Figure D.3: Local fluxes and dimensionless profiles for the simulations of the SETCOM experiment D002

reduces the error at 4.5 m plate length from +23.4 % with the standard model to -6.3 % with the new model, as can be seen in table D.3. The difference in the wall function results is even larger with an error of -46.0 % for the standard wall function compared to

+1.4 % for the new model. Thus, the standard model would yield an even worse result without compensation of errors effect present in the current calculation. This result again illustrates the large potential to improve the calculation of the wall fluxes with the new model.

D.2. Additional THAI HM2 validation results

The following figures D.4 to D.7 contain plots of experimental and simulation results of the THAI HM2 test for the cylinder wall temperature, the lower vessel wall temperature, the upper vessel wall temperature and the hydrogen distribution, respectively.

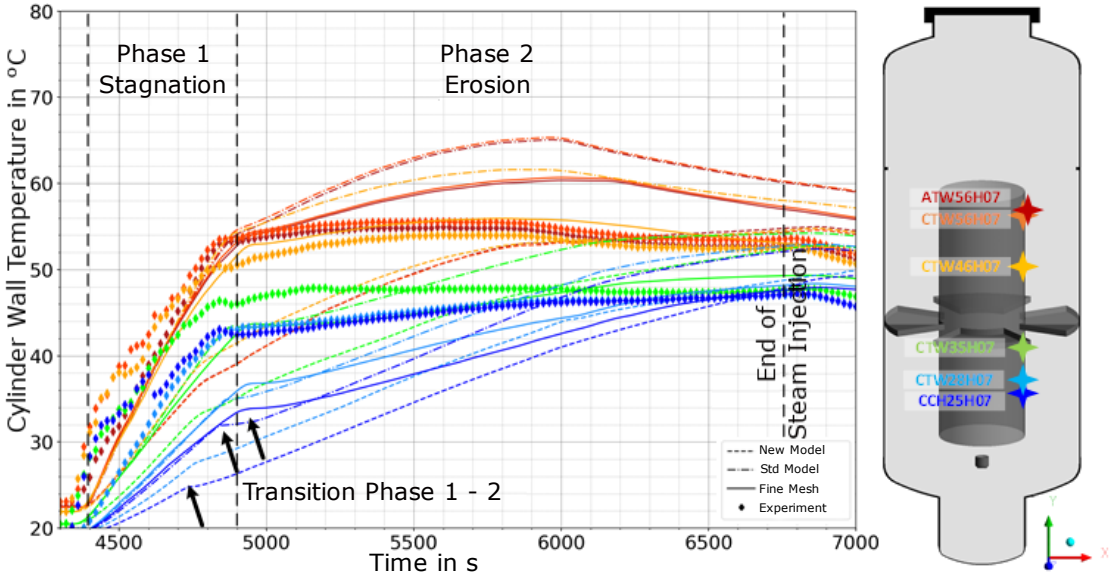

Figure D.4: THAI-HM2 Development of the cylinder wall temperature

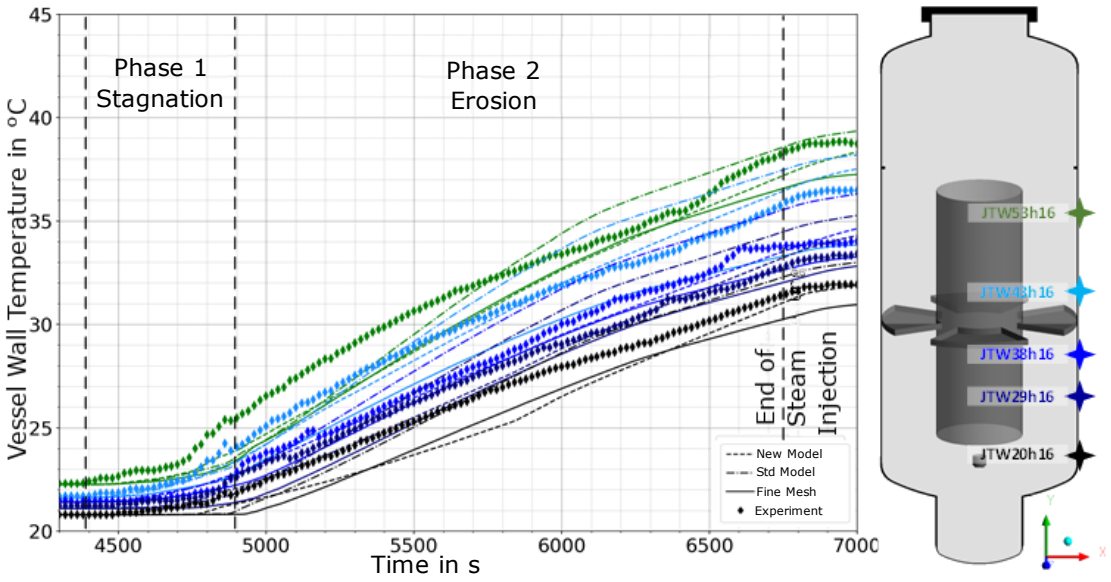

Figure D.5: THAI-HM2 Development of the lower vessel wall temperature

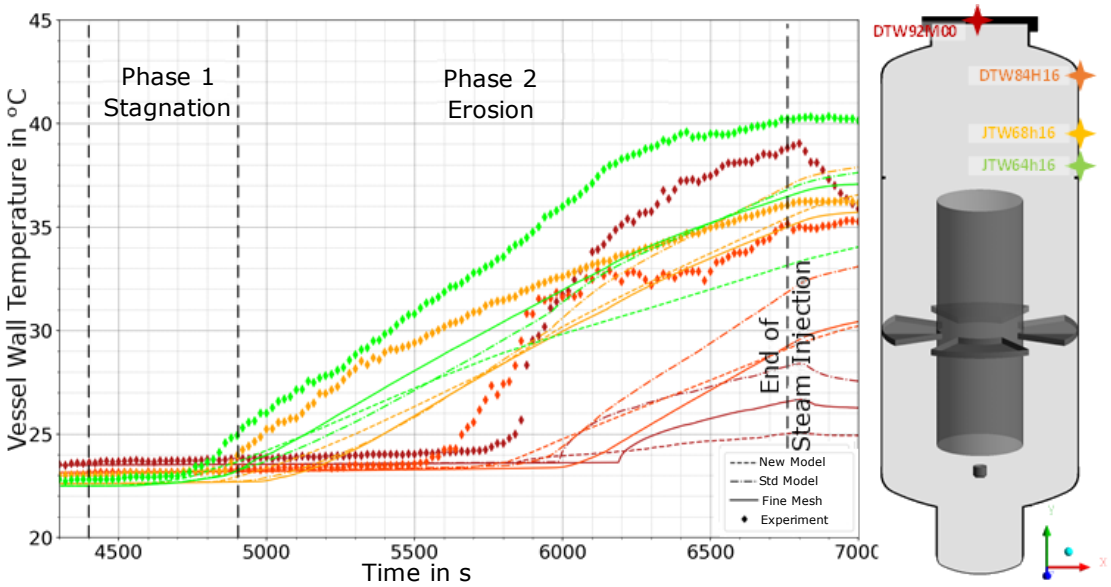

Figure D.6: THAI-HM2 Development of the upper vessel wall temperature

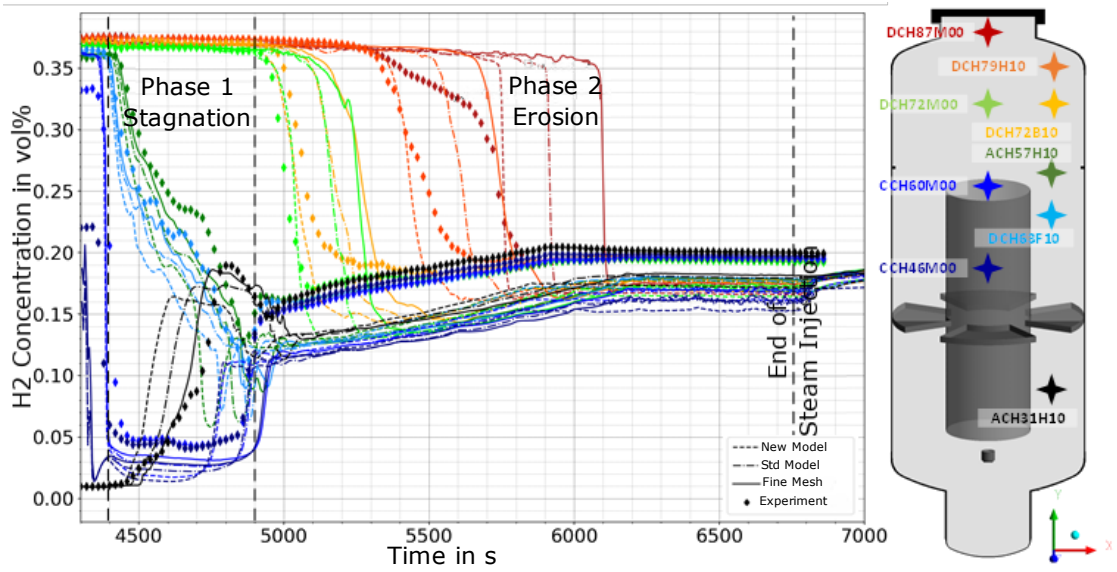

Figure D.7: THAI-HM2 Development of the hydrogen distribution during the mixture transient